University of Trento
Department of Physics

Non-Hermitian and Non-Linear Dynamics in Integrated Silicon Photonic Resonators.

Salamat Ali

A thesis submitted to the
Dipartimento di Fisica
Università degli Studi di Trento
Under the supervision of
Prof. Lorenzo Pavesi
In fulfillment of the requirements for the Degree of
Philosophiae Doctor in Physics

Co-Supervisors:
Prof. Iocopo Corosotto
Dr. Stefano Biasi

Members of the Committee:
Associate Prof. Francesco Da Ros – Technical University of Denmark
Associate Prof. Francesco Dell Olio – Politecnico di Bari, Italy
Associate Prof. Luca Tubiana – University of Trento, Italy

38th PhD cycle
December 2025

Acknowledgements

When I started my PhD, I was not sure I would ever reach this moment. Now, while writing this thesis, I feel deeply grateful to my supervisor, Prof. Lorenzo Pavesi, for pushing me forward whenever I was about to fall. I am thankful for his continuous trust in me, for allowing me the independence to work on my own, and for always watching over my progress and guiding me ahead. Thank you very much, Prof.!

I am also profoundly indebted to Dr. Stefano Biasi for his constant support and guidance throughout this PhD. In my early days, I would run to his office with all kinds of questions, and he never refused a single call or request for help.

My sincere thanks go to the ever-straightforward Ricardo Franchi for his honest corrections whenever I made mistakes. I am also grateful to Bülent for his help in the lab and for always reminding me to follow the simple, logical steps—especially when I overlooked them.

I would also like to express my gratitude to Prof.Icopo Corosotto for being a supportive co-supervisor, for checking in on my progress from time to time, and for helping me navigate through the many questions that arose along the way.

I would also like to sincerely thank the members of the committee for taking the time to review my thesis and for their valuable suggestions, which greatly contributed to the improvement of this work.

Finally, I want to extend my thanks to all those around me whose paths happened to cross mine. Whether objectively or subjectively, knowingly or unknowingly, I learned something valuable from each encounter.

Contents

List of Tables

Abstract

The exponential growth of data-centric computing has imposed fundamental limitations on electronic computing systems, with power dissipation and heat generation emerging as major barriers. At the system level, data movement between memory and processing units now consumes more energy and time than computation itself, a challenge further intensified by the latency and bandwidth constraints of electrical interconnects caused by resistive–capacitive delays and signal integrity issues. At the device level, transistors approaching atomic length scales suffer from increased leakage, variability, and reduced energy efficiency, signaling the physical limits of conventional scaling.

In this context, integrated photonics offers a compelling alternative, providing low-loss, high-bandwidth, and low-latency information transport with reduced energy per bit, and enabling scalable parallelism through wavelength-division multiplexing to alleviate the interconnect and power constraints of modern electronic architectures.

Motivated by the fundamental power, bandwidth, and data-movement limitations of electronic computing, integrated photonics has emerged not only as an enabling technology for energy-efficient interconnects but also as a platform for realizing new computational and signal-processing paradigms. In particular, the deliberate engineering of loss, coupling, and nonlinearity in photonic systems—traditionally viewed as detrimental—has opened new opportunities through non-Hermitian and nonlinear device physics.

In this context, this thesis presents a comprehensive analytical, numerical, and experimental investigation of non-Hermitian and nonlinear photonic devices based on silicon microring resonators and waveguide couplers. Using temporal coupled-mode theory, transfer-matrix methods, and reduced-order models, we develop quantitative frameworks that connect physical coupling mechanisms, intrinsic loss, and nonlinear feedback to experimentally observable spectral and dynamical behavior. These models are validated through systematic characterization of foundry-fabricated devices. First, an optimized 3×3 silicon waveguide coupler is designed and experimentally demonstrated as a compact and reconfigurable photon-routing primitive. Full nine-port characterization reveals controlled outer-to-outer crossing, equal three-way splitting, and arbitrary output distri-

butions, with extracted coupling and detuning parameters quantifying fabrication-induced non-idealities. Second, a p-n integrated silicon microring is studied in the non-linear regime, where coupled carrier and thermal dynamics give rise to self-pulsing oscillations. By electrically tuning the free-carrier lifetime via reverse bias, the self-pulsing frequency is widely and rapidly controlled, reaching oscillation frequencies up to $\sim 190\,\mathrm{MHz}$.

The thesis then investigates non-Hermitian Taiji microrings and Taiji-based coupled-resonator optical waveguides (CROWs), revealing how intentional asymmetry competes with parasitic backscattering to shape spectral response and transport. A reduced coupled-mode "hopping" model is introduced to extract practical design rules, demonstrating that robust non-Hermitian operation requires the engineered inter-resonator coupling to exceed roughness-induced backscattering. Finally, a dynamically reconfigurable microring circuit is presented that enables continuous and programmable control of mode coupling. This platform allows on-demand transitions between diabolic points and exceptional points, coherent suppression of backscattering, and electrically tunable optical chirality approaching unity.

Together, these results establish experimentally validated device-level frameworks for understanding and controlling asymmetry, loss, non-linearity, and coupling in silicon photonic systems. By transforming traditionally parasitic mechanisms into tunable resources, this work advances scalable and reconfigurable non-Hermitian photonic architectures for integrated signal processing, routing, and dynamical control.

Declaration of generative AI and AI-assisted technologies in the writing process. *During the preparation of the thesis, the author used ChatGPT in order to improve language. After using this tool, the author reviewed and edited the content as needed and takes full responsibility for the content of the publication.*

Introduction

From the earliest forms of long-distance communication, light has served as a fundamental carrier of information. Ancient optical signaling systems—such as beacon fires, heliographs, and line-of-sight visual codes—enabled the transmission of discrete information well before the emergence of electronic technologies. With the development of written language and organized transport, communication gradually became decoupled from physical proximity, culminating in the telegraph and telephone, which marked the transition to electrically mediated information transmission.

By the mid-twentieth century, electronics had become the dominant platform for communication and information processing. Integrated circuits enabled information to be encoded, manipulated, and transmitted using controlled electrical signals, while advances in semiconductor fabrication led to rapid increases in device density and speed. The exponential scaling of transistor counts and the concurrent reduction in power density, formalized by Moore's law and Dennard scaling, drove unprecedented growth in electronic communication capacity [1, 2].

As device dimensions approached deep-submicron scales, however, electronic interconnects emerged as a primary bottleneck. Resistive–capacitive (RC) delays, cross-talk, and Joule heating imposed fundamental limits on bandwidth, latency, and energy efficiency, shifting the performance constraint from computation to data transport. This transition has renewed reliance on optical transmission, which now underpins modern information systems ranging from long-haul fiber networks to short-reach and on-chip interconnects.

The growing demand for fast and energy-efficient information transfer has reshaped technologies far beyond communication itself. Transportation systems, healthcare infrastructure, and large-scale industrial and urban networks increasingly rely on dense, real-time data exchange to maintain performance and stability [3, 4]. At the same time, the slowdown of Moore's law and the rising cost of data movement have exposed fundamental limits of electronic hardware [3, 5]. A prominent manifestation of these limits is the *memory wall*, in which the performance gap between processors and memory continues to widen, making data transport a dominant bottleneck. In data centers and AI accelerators, a substantial fraction of energy and latency is now consumed by moving data across memory hierarchies and interconnects rather than by computation itself [4, 6].

Integrated photonics offers a compelling pathway to address these limitations by implementing optical functionality on compact, chip-scale platforms. Using light as the information carrier enables high data rates, low latency, and reduced energy per bit, while minimizing electrical–optical conversion overheads [7–9]. Among available platforms, silicon photonics has emerged as a leading technology due to its CMOS compatibility and strong optical confinement, despite the presence of intrinsic loss and other non-conservative effects.

Rather than treating loss as a limitation, *non-Hermitian photonics* provides a framework in which gain, loss, and asymmetry are deliberately exploited as design parameters [10–12]. By engineering these effects, non-Hermitian systems enable unconventional spectral responses and directional light control beyond the constraints of passive Hermitian devices [10–12]. A central concept in this framework is the exceptional point (EP), where both eigenvalues and eigenvectors coalesce, giving rise to nontrivial dynamical and topological behavior [13]. Optical realizations of parity–time (PT) symmetry breaking and EPs have demonstrated controlled mode transitions, nonreciprocal transport, and enhanced sensitivity [14–18].

Alongside non-Hermiticity, optical non-linearity provides an additional and powerful degree of freedom for controlling light–matter interactions. In non-linear photonic systems, the system response depends on optical intensity, enabling effects such as bistability, self-pulsing, frequency conversion, and dynamical symmetry breaking [19–22]. When combined with non-Hermitian design, non-linearity can strongly amplify asymmetries, induce new operating regimes, and give rise to rich dynamical behavior that is inaccessible in linear systems [23–25].

These combined effects have been extensively explored in integrated resonant platforms, particularly microring and microdisk resonators coupled to waveguides. Such structures naturally enhance optical non-linearities through strong field confinement while simultaneously allowing precise engineering of loss, gain, and coupling. Both active and passive implementations have demonstrated unidirectional transport, linewidth control, non-linear mode interaction, and topological mode conversion near exceptional points [26–30]. Coupled-resonator optical waveguides (CROWs) further extend these concepts to scalable lattices, enabling the study of asymmetric transport, non-linear mode competition, and collective interference effects in non-Hermitian systems [31, 32].

Furthermore, dynamic encircling of exceptional points has revealed asymmetric mode evolution and topologically protected state transfer [33, 34], while EP-enhanced sensitivity has been exploited for ultra-responsive optical sensing [35, 36]. In non-linear regimes, these effects can be further amplified, leading to threshold-dependent responses and enhanced controllability of system dynamics.

While exceptional-point physics, PT-symmetry breaking, and chiral scattering phenomena—including Taiji-type non-Hermitian ring configurations—are now well established experimentally [15, 16, 18, 26], most demonstrations remain proof-of-principle, with limited emphasis on device-level engineering constraints. Key open challenges include quantitative calibration of non-Hermitian parameters such as asymmetric couplings, robustness against fabrication-induced disorder, scalable circuit integration, and electrically reconfigurable control of coupling. Similarly, carrier- and thermally induced self-pulsing in silicon microring resonators has been widely reported [37–39], yet often without a unified framework linking optical non-linearity to electrical control in a reproducible and quantitatively validated manner. The approach developed in this thesis addresses these gaps by combining electrically tunable non-Hermitian design with systematic, port-resolved characterization and quantitative modeling, enabling controlled exploration of non-linear dynamics, asymmetry, reconfigurability, and scalability in integrated photonic circuits.

Resonant building blocks such as microring resonators, directional couplers, and coupled-resonator optical waveguide lattices therefore provide compact and versatile platforms for realizing advanced non-Hermitian and non-linear functionalities in integrated photonic circuits [40–42].

Motivation. As silicon photonic systems grow in scale and functional complexity, their performance increasingly depends on understanding how coupling, loss, non-linearity, and fabrication-induced variations shape device behavior. Compact and reconfigurable routing elements, such as 3×3 waveguide couplers [43], are essential for large photonic fabrics, yet their practical utility is limited by asymmetric coupling, propagation mismatch, and sensitivity to fabrication imperfections. Accurate, experimentally validated multiport models are therefore required to transform these couplers from components into reliable routing primitives. At the same time, high-confinement silicon microrings exhibit strong non-linear carrier–thermal feedback, leading to behaviors such as bistability and self-pulsing that offer opportunities for tunable oscillators and neuromorphic photonic elements. Realizing these functionalities demands a predictive understanding of how detuning, intrinsic loss, and electrical bias interact to shape non-linear dynamical states. Non-Hermitian resonator structures, including the Taiji ring (a simple microring with S-Shape waveguide inscribed in it) [44] and Taiji-based CROWs [45], further highlight the role of asymmetry and parasitic backscattering in determining system response.

These devices rely on a delicate balance between intentional and unintentional coupling pathways to access exceptional points, chiral mode evolution, and robust non-reciprocal transport—behaviors that require quantitative models linking physical imperfections to non-Hermitian spectral signatures. Building on this perspective, a photonic micro ring circuit that demonstrates controlled and tunable mode coupling can enable programmable non-Hermitian interactions, including continuous transitions between diabolic points and exceptional points and the realization of on-demand optical chirality. Achieving such levels of reconfigurability calls for experimentally controlled platforms capable of modulating effective coupling with high precision. Across these varied systems, a common need emerges: to develop device-level frameworks that explain how asymmetry, loss, non-linear feedback, and tunable coupling shape the observable behavior of silicon photonic components. By addressing this need, one can convert mechanisms traditionally viewed as parasitic into functional resources for scalable, high-performance, and reconfigurable photonic systems.

Scope and approach. This thesis combines analytical modeling, numerical simulation, and experimental characterization to study non-Hermitian photonic and non-linear microring resonator devices implemented in foundry-fabricated silicon platforms. Analytically, I employ temporal coupled-mode theory, transfer-matrix methods, and reduced-order models that capture the essential coupling and non-linear dynamics [46–48]. Experimentally, my work focuses on: (i) *Taiji microrings* and *Taiji-CROWs* to investigate non-Hermitian intra-ring coupling and inter-ring transport; (ii) *three-waveguide (*3×3*) couplers* as compact, reconfigurable routing primitives; (iii) *p-n-integrated microrings* to explore carrier- and thermo-optical non-linearities, including self-pulsing and its tunability through electro-optic control [21, 49]; and (iv) a *reconfigurable microring-resonator circuit* that enables symmetric and asymmetric mode control on-chip.

Structure of the thesis. This thesis is organized into four main device- and function-oriented chapters, each describing specific contributions:

Chapter 1. I begin by introducing the fundamentals of silicon photonics. Starting from Maxwell's equations, I build the foundations for understanding light transport in integrated waveguides and introduce the concept of power flow. I then review coupled-waveguide theory and introduce microring resonators as the key building blocks of integrated photonics. This leads to the definitions of Hermitian and non-Hermitian photonic systems. As examples, I describe a Hermitian microring resonator operating at a diabolic point and the non-Hermitian Taiji microring that supports exceptional-point dynamics. The chapter concludes with an overview of the current state and open challenges in non-Hermitian silicon photonics.

Chapter 2. In this chapter, I present design and experimentally demonstrate an optimized 3×3 silicon waveguide coupler for optimized photon routing. I demonstrate the device supports (i) outer-to-outer crossing, (ii) equal three-way splitting, and (iii) arbitrary output distributions. I report full experimental characterization across all nine input–output paths and explain the results using a compact coupled-mode model. From the fits, I extract coupling and detuning parameters and quantify fabrication-induced non-idealities. This establishes a simple and tunable routing primitive for large-scale integrated photonic circuits.

Chapter 3. In this chapter I investigate a p-n integrated silicon microring that exhibits self-pulsing (SP) behavior due to coupled carrier–thermal feedback at high optical powers. By applying a reverse bias, I deduce the free-carrier lifetime and thus suppress the carrier non-linearity, enabling fast and wide tunability of the SP frequency. Experimentally, I achieved oscillations up to $\sim 190\,\mathrm{MHz}$ at $-5\,\mathrm{V}$ bias, consistent with a coupled carrier–thermal model. These results demonstrate a compact, bias-tunable pulse source suitable for on-chip non-linear dynamics and photonic signal processing.

Chapter 4. I then develop a theoretical and experimental framework for understanding Taiji microrings and Taiji-CROWs using coupled-mode theory (CMT) and transfer-matrix analysis. I first characterize individual Taiji microrings to reveal how backscattering and small detunings shape their transmission spectra. Building on this, I study a two-ring Taiji-CROW connected by a link resonator. By fitting measured spectra with a reduced "hopping" CMT model, I derive a practical design rule: robust operation requires a minimum ratio between the intended inter-resonator coupling and the parasitic backscattering rate. This provides clear tolerance targets for mitigating roughness-induced limitations in larger ring arrays.

Chapter 5. In this chapter, I present the *Dynamically Reconfigurable Unified Microresonator* (DRUM), consisting of a ring coupled to two independently tunable side waveguides equipped with Mach–Zehnder interferometers (MZIs) and phase shifters (PS). This architecture allows independent, promotion and then control over the amplitude and phase of counter-propagating mode coupling, enabling a continuous transition between diabolic points (DPs) and exceptional points (EPs). I experimentally demonstrate coherent suppression of backscattering to realize an ideal DP, as well as tunable chirality reaching normalized values of ± 1 at EPs. Measured results are in excellent agreement with temporal CMT predictions, establishing a compact and reconfigurable platform for exploring (non-)Hermitian dynamics on-chip.

Chapter 6. Finally, I present a summary of the main results and discuss future perspectives and directions for further research.

Chapter 1

Non-Hermitian Silicon Photonics

1.1 Introduction

As transistor dimensions continued to shrink, the dominant cost of computation shifted from the switching of individual devices to the movement of information across and between chips. Global electronic interconnects increasingly dictated system latency and energy consumption, while wiring congestion and resistive–capacitive effects imposed fundamental constraints on bandwidth and overall efficiency [3, 5, 6]. These limitations have consequently motivated the exploration of photonic interconnects, which intrinsically exhibit low crosstalk, high bandwidth density, and the potential for attojoule-class signaling when carefully engineered [4].

Against this backdrop, *silicon photonics* leverages CMOS-compatible fabrication to translate the fast, low-loss transport familiar from optical fibers into *on-chip* components. In this platform, light is guided, split, combined, and filtered by passive building blocks (waveguides, directional couplers, multimode interferometers) and controlled by active elements (modulators, detectors), all realized within the same manufacturing ecosystem as electronics [4, 7–9]. The silicon-on-insulator (SOI) stack provides a strong index contrast (Si vs. SiO_2), enabling tight bends and compact functional elements such as microring resonators (MR), Mach–Zehnder interferometers (MZI), and multimode-interference couplers (MMI) [40–42, 50].

Building on these foundations, *non-Hermitian photonics* explicitly harnesses engineered gain, loss, aymmetric coupling and openness—rather than treating them as imperfections—to access phenomena such as parity–time symmetry, exceptional points, and non-Hermitian topological effects. These phenomena open new degrees of freedom for on-chip control of light and motivate their implementation in silicon-compatible architectures [51–

54].

This chapter first reviews the essentials of silicon photonics including nonlinearities in silicon, then introduces the core concepts of non-Hermitian physics, traces key photonic demonstrations such as microring resonator, and finally surveys current challenges and future outlook [51–54].

1.2 Fundamentals of Silicon Photonics

1.2.1 Why Silicon Photonics?

Silicon photonics has emerged as a leading platform in integrated optics because it combines the scalability of modern semiconductor technology with the precision and flexibility of photonic design. Its full compatibility with complementary metal–oxide–semiconductor (CMOS) fabrication enables wafer-scale production with high yield, reproducibility, and low cost [4, 8, 9, 55]. This scalability ensures that once a photonic design is validated, it can be mass-produced using the same industrial processes that revolutionized microelectronics [1, 2, 5]. The ability to fabricate complex optical systems using existing foundries makes silicon photonics not only a research platform but a practical route to commercialization [8, 9].

A defining feature of silicon photonics is the high refractive index contrast between crystalline silicon ($n_{\mathrm{Si}} \approx 3.48$) and its silicon dioxide cladding ($n_{\mathrm{SiO_2}} \approx 1.44$) at telecom wavelengths around $\lambda = 1.3$–$1.55\ \mu$m, enabling strong optical confinement in submicron waveguides [7]. This contrast allows tight optical confinement, enabling light to be guided through structures only a few hundred nanometers wide [40]. As a result, extremely compact devices such as MR, MZI, and grating couplers can be integrated densely on a single chip [40, 56, 57]. The high confinement also enhances non-linear effects, providing a pathway to study intensity-dependent phenomena in compact geometries [21, 58]. Thus, the index contrast of silicon is a key enabler for both miniaturization and enhanced optical functionality [7, 40].

Equally important is the maturity of the silicon photonics ecosystem. Over the past two decades, a comprehensive catalog of passive and active components has been established, including waveguides, couplers, resonators, modulators, and photodetectors, all compatible with standard CMOS processes [8, 40, 55]. This maturity reduces the barriers between design and fabrication, allowing to focus on new optical functionalities rather than basic material or process development [9]. Consequently, silicon photonics offers a

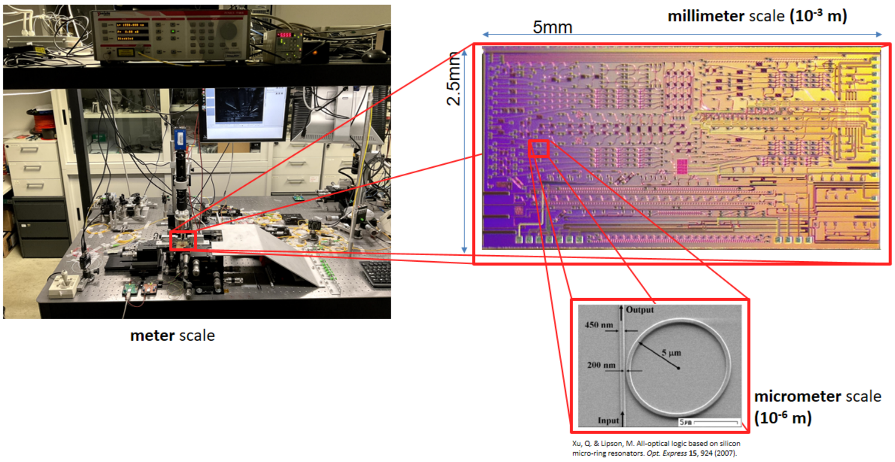

Figure 1.1: **From tabletop optics to Integrated Silicon Photonics**. Top-left: meter-scale experimental setup with an external laser coupled to the chip (e.g., via lensed fiber or grating couplers) our lab picture. Right: zoom of millimetre-scale silicon photonic chip. Insets/highlights show micrometre-scale components—single-mode WG and MR

unified platform where new physics can be explored without sacrificing manufacturability or scalability [8, 9].

This technological readiness makes silicon photonics particularly well-suited for exploring non-Hermitian. The platform allows controlled engineering of loss, gain, and asymmetric coupling—key ingredients for realizing non-Hermitian Hamiltonians on chip [10, 11, 59]. By embedding such effects in established silicon architectures, one can investigate exotic optical behaviors such as exceptional points, non-reciprocity, mode conversion, and enhanced sensing within a stable and repeatable environment [12, 51]. Representative structures, including coupled-resonator optical waveguides (CROWs), Taiji ring resonators, and multiport couplers (e.g., 3×3 devices), provide natural testbeds for these phenomena [43, 60–65].

The experimental relevance of silicon photonics lies in its ability to translate abstract theoretical models into tangible, chip-scale devices. The same structures that describe non-Hermitian Hamiltonians in theory can be fabricated and characterized experimentally with high precision [10, 51]. As illustrated in Figure 1.1, the transition from meter-scale optical benches to millimeter-scale integrated chips demonstrates how silicon photonics bridges the gap between fundamental physics and scalable implementation [8, 9, 43].

1.2.2 Design Principles and Modeling

Designing non-Hermitian photonic circuits in silicon requires bridging the physical layout with its underlying mathematical description through coupled-mode theory and scattering matrix formalism. Non-Hermiticity can be introduced deliberately through several mechanisms: spatially distributed optical loss or gain (via absorption, carrier injection, or hybrid III–V integration) [66, 67], radiative leakage to external ports [68, 69], or dynamically modulated coupling that induces effective non-reciprocal energy transfer [70–76]. These mechanisms allow the implementation of tailored non-Hermitian Hamiltonians, where complex eigenfrequencies capture both resonance shifts and dissipative dynamics [51].

Typical design paradigms include parity–time (PT) symmetric dimers and lattices, exceptional-point (EP) encirclement schemes, and coherent perfect absorber (CPA)–laser configurations [77, 78]. In silicon photonics, such configurations can be realized using MR, CROW structures, or hybrid waveguide–resonator systems, where the balance and interplay between loss, coupling, and feedback determine the system's spectral response.

Temporal coupled-mode theory (TCMT) and transfer-matrix methods (TMM) are key modeling tools that connect the physical geometry of the device—such as waveguide separation and interaction length (which set the coupling strength), path-length or effective-index mismatch (which determines detuning), and the coupling to access waveguides or ports (which defines external loading)—to experimentally measurable quantities including transmission and reflection spectra, resonance linewidths, and quality factors [46, 79]. These analytical frameworks not only predict device performance but also reveal the location of scattering poles and zeros in the complex frequency plane- such as diabolical and exceptional points, providing insight into critical transitions between Hermitian and non-Hermitian regimes. Consequently, silicon photonics serves not only as a practical fabrication platform but also as a fertile ground for fundamental exploration of non-Hermitian physics at the chip scale.

1.2.3 Waveguides

In integrated photonic circuits the waveguide serves as the most fundamental and indispensable component, as it provides the physical pathway for guiding light into, within, and out of the photonic circuit.

A waveguide confines and transports optical energy through solutions of Maxwell's equations within a dielectric medium. In silicon photonics, waveguides are typically realized on a *silicon-on-insulator (SOI)* platform, which consists of a high-refractive-index silicon (Si) guiding layer atop a low-index silicon dioxide (SiO_2) substrate, with either air or oxide serving as the upper cladding.

The large refractive index contrast between silicon ($n_{\mathrm{Si}} \approx 3.48$ at $\lambda = 1550$ nm) and silicon dioxide ($n_{\mathrm{SiO_2}} \approx 1.44$) enables strong optical confinement within submicron-

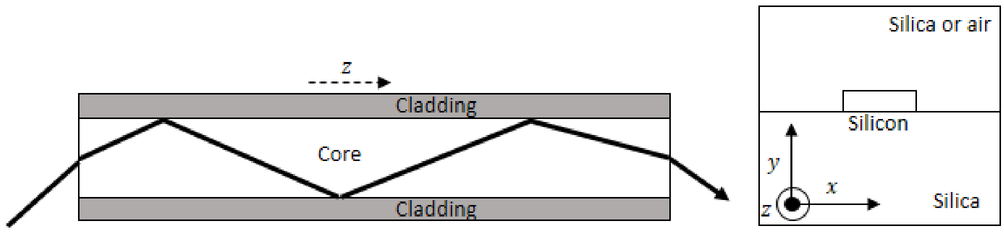

Figure 1.2: **Schematic of an optical waveguide** . (Left) Light enters from a region of lower refractive index into a higher-index core and propagates through the waveguide via total internal reflection. (Right) Cross-sectional view showing the waveguide core and cladding structure.

scale dimensions, allowing for tight bending radii, dense integration, and efficient mode manipulation. This tight confinement also enhances non-linear effects and facilitates compact device designs, making silicon waveguides a cornerstone for both classical and non-Hermitian photonic circuits.

A rectangular single-mode waveguide on this platform typically has a cross-section of width $w \approx 450$ nm and height $h \approx 220$ nm, supporting fundamental quasi-TE and quasi-TM modes. Light propagates along the longitudinal axis (z-direction), confined by total internal reflection at the Si/SiO_2 interfaces.

1.2.4 Light Transport in a Dielectric Slab Waveguide

In a lossless, translationally invariant dielectric waveguide (invariant along the z-axis), the monochromatic electromagnetic fields at an angular frequency ω satisfy the source-free Maxwell equations,

$$\nabla \times \mathbf{E} = i\omega\mu_0\mathbf{H}, \qquad \nabla \times \mathbf{H} = -i\omega\varepsilon_0 n^2(x, y)\,\mathbf{E}, \tag{1.1}$$

where μ_0 and ε_0 denote the permeability and permittivity of free space, and $n(x, y)$ represents the local refractive index profile of the waveguide structure.

For a waveguide uniform along z, guided modes can be expressed as separable field solutions of the form

$$\mathbf{E}(x, y, z) = \mathbf{E}_m(x, y)\, e^{i\beta_m z}, \qquad \mathbf{H}(x, y, z) = \mathbf{H}_m(x, y)\, e^{i\beta_m z}, \tag{1.2}$$

where β_m is the propagation constant (or longitudinal wavenumber) of the m^{th} guided mode, and $\mathbf{E}_m$, $\mathbf{H}_m$ are its corresponding transverse field distributions. Each guided mode satisfies the vector Helmholtz equation with appropriate boundary and radiation conditions at material interfaces.

The discrete set $\{\beta_m, \mathbf{E}_m, \mathbf{H}_m\}$ constitutes the orthogonal modal basis of the waveguide, satisfying the power orthogonality condition

$$\langle m, n\rangle = \frac{1}{4}\int \big(\mathbf{E}_m \times \mathbf{H}_n^* + \mathbf{E}_n^* \times \mathbf{H}_m\big)\cdot \hat{\mathbf{z}}\, dA = P_m\, \delta_{mn}, \tag{1.3}$$

where P_m denotes the power carried by mode m along the z-direction (per unit width for a 2D structure), and δ_{mn} is the Kronecker delta.

In high-index-contrast photonic platforms, such as silicon-on-insulator (SOI), modes are often classified as TE-like (transverse electric) or TM-like (transverse magnetic), depending on whether the dominant field component is electric (E_y) or magnetic (H_y). For a planar slab waveguide that is invariant along y, this polarization separation becomes exact: TE modes possess $E_y \neq 0$ with $E_x = E_z = 0$, whereas TM modes have $H_y \neq 0$ with $H_x = H_z = 0$.

Consider a symmetric SOI slab waveguide composed of a silicon (Si) core of refractive index $n_1 = 3.48$ and thickness t along x, surrounded by silicon dioxide (SiO_2) cladding of index $n_2 = 1.44$. Assuming TE polarization, the fields can be written as

$$\mathbf{E}(x,z) = \hat{\mathbf{y}}\, E_y(x) e^{i\beta z}, \qquad \mathbf{H}(x,z) = H_x(x)\,\hat{\mathbf{x}} + H_z(x)\,\hat{\mathbf{z}}. \tag{1.4}$$

Substituting these expressions into Maxwell's equations and eliminating H_x and H_z yields a scalar Helmholtz equation for the electric field component $E_y(x)$:

$$\frac{d^2 E_y}{dx^2} + \big(n^2(x) k_0^2 - \beta^2\big) E_y = 0, \tag{1.5}$$

where $k_0 = 2\pi/\lambda_0$ is the free-space wavenumber and λ_0 is the operating wavelength. For the core region ($|x| \le t/2$), define $k_x = \sqrt{n_1^2 k_0^2 - \beta^2}$, and for the cladding ($|x| > t/2$), define $\alpha = \sqrt{\beta^2 - n_2^2 k_0^2}$. Applying boundary conditions of field continuity at $x = \pm t/2$ yields the even TE_0 mode solution:

$$E_y(x) = \begin{cases} E_0 \cos(k_x x), & |x| \le t/2, \\ E_0 \cos(k_x t/2)\, e^{-\alpha(|x|-t/2)}, & |x| > t/2, \end{cases} \tag{1.6}$$

with the corresponding dispersion relation

$$k_x \tan\!\Big(\frac{k_x t}{2}\Big) = \alpha, \qquad k_x^2 + \alpha^2 = (n_1^2 - n_2^2) k_0^2. \tag{1.7}$$

The dimensionless frequency parameter

$$V = k_0 \, t \sqrt{n_1^2 - n_2^2}, \tag{1.8}$$

known as the normalized frequency or V-number, determines the number of supported modes. For a symmetric slab waveguide, TE modes exist for $V > m\pi$, where m is an integer. Thus, the structure supports a single guided mode (TE_0 only) when

$$V < \pi. \tag{1.9}$$

In this single-mode regime, the general field solution simplifies to

$$\mathbf{E}(x, y, z) = \hat{\mathbf{y}} \, E_0(x) e^{i\beta z}, \qquad \mathbf{H}(x, y, z) = \mathbf{H}_0(x) e^{i\beta z}, \tag{1.10}$$

where $E_0(x)$ is the TE_0 field profile and β is the effective propagation constant determined by Eq. (1.7).

The time-averaged Poynting vector, representing the local power flow density, is given by $\mathbf{S} = \frac{1}{2}\Re\{\mathbf{E} \times \mathbf{H}^*\}$. For the TE mode,

$$H_x = \frac{\beta}{\omega\mu_0} E_y, \qquad H_z = \frac{i}{\omega\mu_0} \frac{dE_y}{dx}, \qquad S_z = \frac{\beta}{2\omega\mu_0} |E_y(x)|^2. \tag{1.11}$$

The total guided power (per unit width along y) is then

$$P = \int_{-\infty}^{\infty} S_z \, dx = \frac{\beta}{2\omega\mu_0} \int_{-\infty}^{\infty} |E_y(x)|^2 \, dx. \tag{1.12}$$

The fraction of the optical power confined within the silicon core, often called the *confinement factor*, is expressed as

$$\Gamma_{\mathrm{TE}} = \frac{\displaystyle\int_{-t/2}^{t/2} |E_y|^2 \, dx}{\displaystyle\int_{-\infty}^{\infty} |E_y|^2 \, dx} = \frac{\dfrac{t}{2} + \dfrac{\sin(k_x t)}{4k_x}}{\dfrac{t}{2} + \dfrac{\sin(k_x t)}{4k_x} + \dfrac{\cos^2(k_x t/2)}{\alpha}}. \tag{1.13}$$

For an SOI waveguide with $t = 220$ nm, $n_1 = 3.48$ (Si), $n_2 = 1.44$ (SiO_2), and $\lambda_0 = 1550$ nm, the free-space wavenumber is $k_0 = 2\pi/\lambda_0 \approx 4.053{\times}10^6 \, \mathrm{m}^{-1}$. The corresponding normalized frequency is

$$V = k_0 t \sqrt{n_1^2 - n_2^2} \approx 2.83 < \pi,$$

confirming that the structure supports a single TE_0 mode.

Solving Eq. (1.7) numerically gives $k_x \approx 8.09 \times 10^6$ m^{-1} and $\alpha \approx 1.00 \times 10^7$ m^{-1}. The effective propagation constant and refractive index are then

$$\beta = \sqrt{n_1^2 k_0^2 - k_x^2} \approx 1.155 \times 10^7 \text{ m}^{-1}, \qquad n_{\text{eff}} = \beta / k_0 \approx 2.85.$$

Using Eq. (1.13), the optical power confinement factor is

$$\Gamma_{\text{TE}} \approx 0.78,$$

indicating that approximately 78% of the mode power is confined within the silicon core.

Assuming an input power of $P(0) = 1$ mW and a propagation loss coefficient α_{loss} (in nepers per meter, Np/m, describing exponential power attenuation along the waveguide), the transmitted power after a distance L is

$$P(L) = P(0)\, e^{-\alpha_{\text{loss}} L}.$$

For a typical SOI loss of 2 dB/cm, which corresponds to $\alpha_{\text{loss}} = 200 \text{ dB/m} \times \frac{\ln 10}{20} \approx$ 23.03 Np/m, the power after a 70 μm propagation length is

$$P(70\ \mu\text{m}) = 1 \text{ mW} \times e^{-23.03 \times 70 \times 10^{-6}} \approx 0.998 \text{ mW},$$

equivalent to an attenuation of only ~ 0.014 dB.

This analysis demonstrates that over micrometer-scale propagation lengths, the power loss in a high-quality SOI waveguide is negligible. The TE_0 mode propagates with nearly constant amplitude, with most of its optical energy confined within the silicon core, as quantified by Γ_{TE}.

1.2.5 Coupling and Mode Excitation

A major practical challenge in integrated photonics is the efficient transfer of light between an external optical source and the submicron waveguides on a silicon photonic chip and for the detection of light out of the chip. Typical laser sources are delivered through single-mode optical fibers whose fundamental mode area is orders of magnitude larger than that of a silicon waveguide. The mismatch in spatial extent and numerical aperture leads to poor mode overlap and significant insertion losses unless dedicated coupling structures are implemented.

For a quantitative comparison, the effective mode area of a standard single-mode fiber

(SMF-28) at 1550 nm is approximately

$$A_{\text{eff,fiber}} \approx 80-100\ \mu\text{m}^2,$$

corresponding to a mode-field diameter of about 10–11 μm. In contrast, the effective mode area of a single-mode silicon waveguide on an SOI platform is typically

$$A_{\text{eff,WG}} \approx 0.5-1\ \mu\text{m}^2,$$

nearly two orders of magnitude smaller due to the high index contrast between silicon ($n_{\text{Si}} \approx 3.48$) and silicon dioxide ($n_{\text{SiO}_2} \approx 1.44$). Direct butt-coupling from fiber to waveguide would therefore result in poor efficiency, as only a small fraction of the incident optical field would match the confined TE_0 mode supported by the waveguide.

To overcome this mode-size and phase-matching mismatch, *grating couplers* are commonly employed to couple light between an optical fiber and the on-chip waveguide. A grating coupler consists of a periodic modulation of the refractive index (or surface corrugation) with period Λ, designed to scatter the incident fiber mode into the guided mode at an appropriate angle. Efficient coupling occurs when the phase-matching condition between the in-plane momentum of the incident beam and the guided mode is satisfied:

$$k_0 n_{\text{fiber}} \sin\theta \pm \frac{2\pi}{\Lambda} = \beta, \tag{1.14}$$

where θ is the fiber tilt angle (typically 8–15°), n_{fiber} is the refractive index of the fiber mode, β is the propagation constant of the guided TE_0 mode, and the sign accounts for upward or downward diffraction. The grating period Λ and etch depth are optimized to maximize the overlap between the scattered field and the desired guided mode while minimizing reflections.

Once the phase-matching condition is met, the coupling efficiency into the fundamental guided mode can be described by the field overlap integral

$$\eta_{\text{in}} = \left| \frac{\iint \mathbf{E}_{\text{in}}(x,y) \cdot \mathbf{E}^*_{\text{wg}}(x,y)\, dx\, dy}{\sqrt{\iint |\mathbf{E}_{\text{in}}|^2 dx\, dy} \sqrt{\iint |\mathbf{E}_{\text{wg}}|^2 dx\, dy}} \right|^2, \tag{1.15}$$

where $\mathbf{E}_{\text{in}}$ is the incident electric field distribution from the fiber and $\mathbf{E}_{\text{wg}}$ is the guided mode field of the waveguide (for the single-mode case, $\mathbf{E}_{\text{wg}} = \mathbf{E}_0$). This expression follows directly from the power orthogonality relation introduced in Eq. (1.3) and quantifies the fraction of optical power projected from the input field onto the guided-mode basis.

For a single-mode TE waveguide, $\mathbf{E}_{\text{wg}}$ is dominated by its y-component $E_{0,y}(x,y)$, as obtained from Eq. (1.5). Therefore, the overlap integral effectively measures how well the polarization, spatial profile, and phase front of the incoming field match those of the TE_0 mode. Perfect overlap ($\eta_{\text{in}} = 1$) requires both mode-field and phase matching, which is practically limited by fabrication imperfections, reflection losses, and angular alignment.

If light is launched from a fiber with input power P_{in}, the optical power coupled into the on-chip TE_0 mode is $\eta_{\text{in}} P_{\text{in}}$. After propagating a distance L along the waveguide with attenuation coefficient α_{loss} (in Np/m), the remaining guided power is

$$P(L) = \eta_{\text{in}} P_{\text{in}} e^{-\alpha_{\text{loss}} L}. \tag{1.16}$$

If an identical grating coupler is used for out-coupling, characterized by efficiency η_{out}, the transmitted optical power at the output fiber is

$$P_{\text{out}} = \eta_{\text{in}} \eta_{\text{out}} P_{\text{in}} e^{-\alpha_{\text{loss}} L}. \tag{1.17}$$

For the 70 μm waveguide analyzed in the previous subsection ($\alpha_{\text{loss}} \approx 23.03$ Np/m), the propagation factor $e^{-\alpha_{\text{loss}} L} \approx 0.998$, indicating negligible internal loss. Hence, the overall efficiency is dominated by the coupling terms η_{in} and η_{out}. For instance, with grating couplers of $\eta_{\text{in}} = \eta_{\text{out}} = 0.6$, the total fiber-to-fiber transmission is approximately 0.36 mW for 1 mW input power; using optimized couplers with $\eta_{\text{in}} = \eta_{\text{out}} = 0.8$ increases transmission to ~ 0.64 mW.

Design strategies for efficient coupling.

- *Mode-size transformation:* The grating or taper geometry can be engineered to expand the on-chip TE_0 mode laterally and vertically, improving overlap with the larger fiber mode.
- *Phase matching:* The grating period Λ is chosen according to Eq. (1.14) to match the in-plane propagation constants.
- *Apodization and back-reflection minimization:* Gradual modulation of the grating duty cycle (apodization) and the use of anti-reflection coatings enhance unidirectional coupling efficiency.
- *Polarization alignment:* Proper alignment ensures that the incident polarization

(usually linear, horizontal) excites the TE_0 mode rather than higher-order or TM modes.

1.2.6 The Mach–Zehnder Interferometer (MZI)

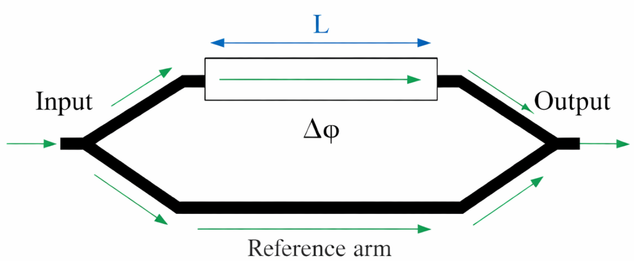

Figure 1.3: Schematics of The Mach–Zehnder Interferometer (MZI)

The Mach–Zehnder Interferometer (MZI) consists of two 50:50 beam splitters connected by two optical paths as shown in the Figure 1.3. An input electric field $E_{in} = E_0$ is divided equally, so each arm carries a field of amplitude $E_0/\sqrt{2}$. As the fields propagate, they accumulate a phase

$$\phi = \frac{2\pi n L}{\lambda_0}, \tag{1.18}$$

where n is the refractive index, L is the arm length, and λ_0 is the free-space wavelength. In the reference arm, the phase is

$$\phi_1 = \frac{2\pi n_0 L}{\lambda_0}, \tag{1.19}$$

while in the heated arm a micro-heater induces a refractive index change Δn through the thermo-optic effect, resulting in

$$\phi_2 = \frac{2\pi (n_0 + \Delta n) L}{\lambda_0}. \tag{1.20}$$

The resulting phase difference is

$$\Delta\phi = \phi_2 - \phi_1 = \frac{2\pi \Delta n L}{\lambda_0}, \tag{1.21}$$

with

$$\Delta n = \frac{dn}{dT}\Delta T, \tag{1.22}$$

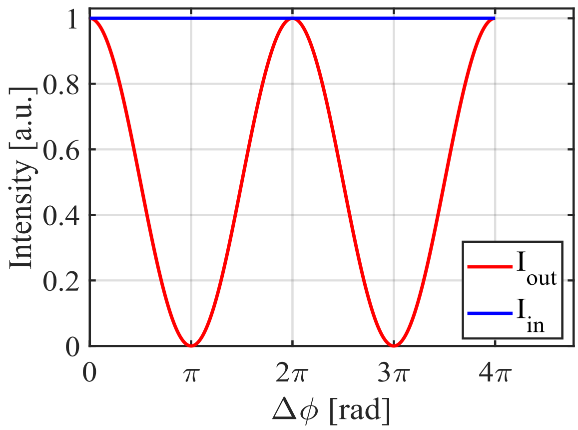

Figure 1.4: **Simulation.** Output intensity variation as a function of the phase difference $\Delta\phi$ in one arm of the Mach–Zehnder interferometer. The interference pattern follows $I_{\text{out}} = I_{\text{in}} \cos^2(\Delta\phi/2)$, illustrating how phase modulation controls the output transmission.

where $\frac{dn}{dT}$ is the thermo-optic coefficient and ΔT is the temperature rise in the heated arm.

At the second beam splitter, the two optical fields interfere, and the output field at output port is

$$E_{\text{out}} = \frac{1}{2}E_0\left(e^{-i\phi_1} + e^{-i\phi_2}\right), \tag{1.23}$$

resulting in the output intensity

$$I_{\text{out}} = I_{\text{in}} \cos^2\left(\frac{\Delta\phi}{2}\right) = I_{\text{in}} \cos^2\left(\frac{\pi\Delta n L}{\lambda_0}\right). \tag{1.24}$$

This expression shows that the output intensity depends only on the relative phase between the two arms as shown in the Figure 1.4. Constructive interference occurs when $\Delta\phi = 2m\pi$, giving maximum transmission, while destructive interference occurs when $\Delta\phi = (2m + 1)\pi$, resulting in zero output. A π phase shift is required to switch between maximum and minimum transmission, corresponding to

$$\Delta n_\pi = \frac{\lambda_0}{2L}. \tag{1.25}$$

Therefore, by controlling the heater power, and consequently the temperature and refractive index, the MZI provides a precise method for tuning optical intensity through thermo-optic phase modulation. In the last chapter, this MZI configuration will be used inside an integrated microring resonator to achieve chiral light routing.

1.2.7 Two Coupled Waveguides

When two silicon waveguides are brought in close proximity (typically separated by a few hundred nanometers), their evanescent fields overlap, allowing optical power to exchange between them. This phenomenon, known as *evanescent coupling*, forms the basis of directional couplers, multimode interference (MMI) devices, and microring–bus coupling sections in integrated silicon photonics, as shown in Figure 1.5.

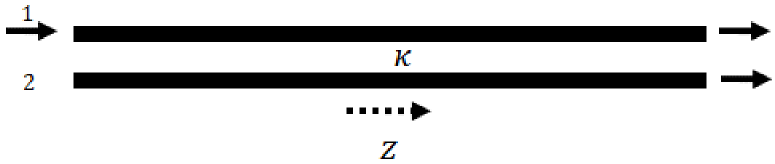

Figure 1.5: **Schematic of two evanescently coupled waveguides**. Optical power oscillates between the guides along the propagation direction z.

The total electric field in a system of two evanescently coupled waveguides can be expressed as a superposition of the guided modes of the isolated waveguides,

$$\mathbf{E}(\mathbf{r}, z) = A_1(z)\,\mathbf{E}_1(\mathbf{r})\,e^{i\beta_1 z} + A_2(z)\,\mathbf{E}_2(\mathbf{r})\,e^{i\beta_2 z}, \tag{1.26}$$

where $A_1(z)$ and $A_2(z)$ denote the complex modal amplitudes of the guided fields in waveguides 1 and 2, respectively, $\mathbf{E}_1(\mathbf{r})$ and $\mathbf{E}_2(\mathbf{r})$ are the normalized transverse electric-field profiles of their fundamental modes, and β_1 and β_2 are the corresponding propagation constants.

Assuming that each waveguide supports only its fundamental mode and that the coupling is sufficiently weak so that higher-order modes can be neglected, the evolution of the modal amplitudes along the propagation direction z is governed by the coupled-mode equations

$$\begin{aligned} \frac{dA_1}{dz} &= -i\frac{\Delta\beta}{2}A_1 - i\kappa A_2, \\ \frac{dA_2}{dz} &= -i\kappa A_1 + i\frac{\Delta\beta}{2}A_2, \end{aligned} \tag{1.27}$$

where $\Delta\beta = \beta_1 - \beta_2$ represents the propagation-constant mismatch between the two isolated waveguides, and κ is the coupling coefficient describing the evanescent interaction between the modes.

The evanescent coupling originates from the spatial overlap of the guided modes in the region where the waveguides are brought into close proximity.

Under the weak-coupling approximation, the coupling coefficient between two parallel waveguides is given by

$$\kappa = \frac{\omega}{4} \frac{\displaystyle\int \Delta\varepsilon(\mathbf{r})\, \mathbf{E}_1^*(\mathbf{r}) \cdot \mathbf{E}_2(\mathbf{r})\, \mathrm{d}A}{\sqrt{P_1 P_2}}, \tag{1.28}$$

where ω is the angular frequency of the optical field, $\mathbf{E}_1(\mathbf{r})$ and $\mathbf{E}_2(\mathbf{r})$ are the electric-field mode profiles of waveguide 1 and waveguide 2 calculated for the isolated (uncoupled) waveguides, and $\Delta\varepsilon(\mathbf{r})$ represents the permittivity perturbation induced by the presence of the adjacent waveguide. The integration is carried out over the transverse cross-sectional area A.

Here P_1 and P_2 denote the optical powers carried by modes 1 and 2, respectively. In general, the optical power carried by the m-th guided mode is defined as

$$P_m = \frac{1}{2} \mathrm{Re} \left\{ \int \left[\mathbf{E}_m(\mathbf{r}) \times \mathbf{H}_m^*(\mathbf{r}) \right] \cdot \hat{\mathbf{z}}\, \mathrm{d}A \right\}, \tag{1.29}$$

where $\mathbf{H}_m(\mathbf{r})$ is the magnetic-field profile associated with the m-th mode and $\hat{\mathbf{z}}$ denotes the unit vector along the propagation direction. With this power normalization, the coupling coefficient κ has units of inverse length and appears naturally in the coupled-mode equations written along the propagation direction z.

In matrix form:

$$\frac{d}{dz} \begin{bmatrix} A_1 \\ A_2 \end{bmatrix} = -i \begin{bmatrix} \Delta\beta/2 & \kappa \\ \kappa & -\Delta\beta/2 \end{bmatrix} \begin{bmatrix} A_1 \\ A_2 \end{bmatrix}. \tag{1.30}$$

Diagonalizing this matrix yields the normal-mode eigenvalues $\pm\Omega$, where

$$\Omega = \sqrt{\kappa^2 + \left(\frac{\Delta\beta}{2} \right)^2}. \tag{1.31}$$

These correspond to the even and odd supermodes of the coupled system with propagation constants $\beta_\pm = \bar{\beta} \pm \Omega$, where $\bar{\beta} = (\beta_1 + \beta_2)/2$.

If only waveguide 1 is excited at $z = 0$, i.e.,

$$A_1(0) = 1, \quad A_2(0) = 0,$$

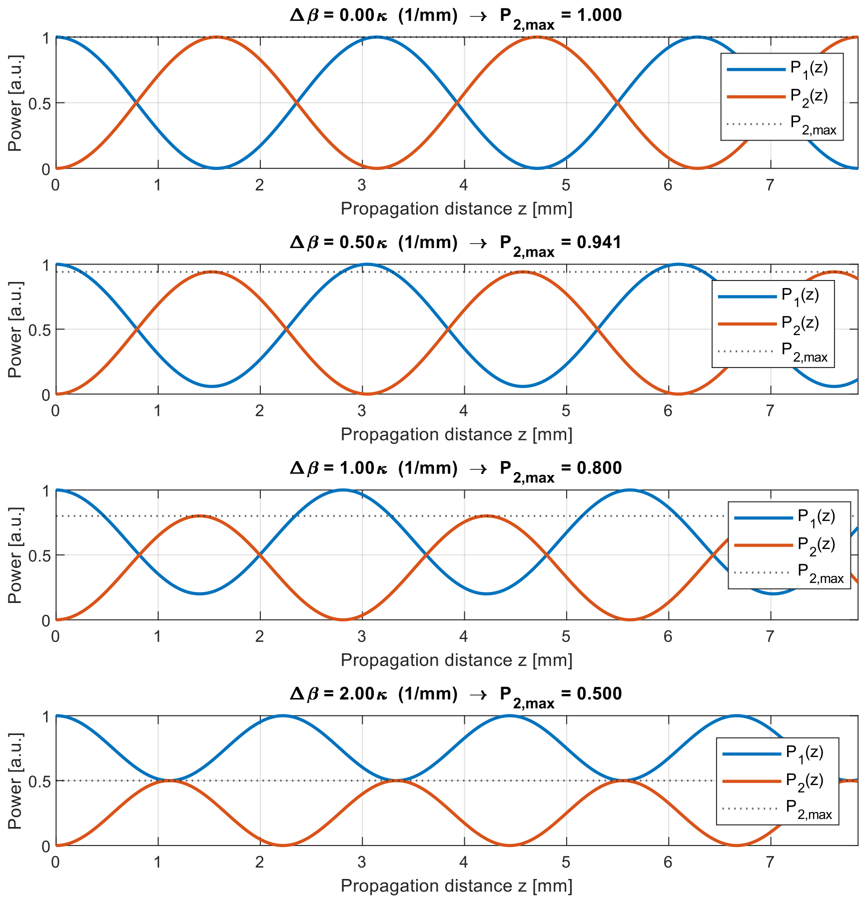

Figure 1.6: **Theory**. Power distribution in coupled waveguides at different detuning values shown in the title of the the subplots. Top to bottom for different values of detuning

the field amplitudes evolve as:

$$\boxed{\begin{aligned} A_1(z) &= \cos(\Omega z) - i\frac{\Delta\beta}{2\Omega}\sin(\Omega z), \\ A_2(z) &= -i\frac{\kappa}{\Omega}\sin(\Omega z). \end{aligned}} \tag{1.32}$$

The corresponding optical powers are

$$\boxed{\begin{aligned} P_1(z) &= |A_1(z)|^2 = 1 - \frac{\kappa^2}{\Omega^2}\sin^2(\Omega z), \\ P_2(z) &= |A_2(z)|^2 = \frac{\kappa^2}{\Omega^2}\sin^2(\Omega z), \end{aligned}} \tag{1.33}$$

satisfying total power conservation $P_1 + P_2 = 1$.

For identical waveguides ($\Delta\beta = 0$), the system simplifies to

$$P_1(z) = \cos^2(\kappa z), \quad P_2(z) = \sin^2(\kappa z),$$

and complete power transfer occurs after the *coupling length*

$$L_c = \frac{\pi}{2\kappa}. \tag{1.34}$$

When $\Delta\beta \neq 0$, the maximum transfer efficiency decreases to

$$P_{2,\max} = \frac{\kappa^2}{\kappa^2 + (\Delta\beta/2)^2}. \tag{1.35}$$

Power oscillation between the two guides results from interference between the even and odd supermodes, which propagate with $\beta_\pm = \bar{\beta} \pm \Omega$. The corresponding beat length is

$$L_\pi = \frac{\pi}{\beta_+ - \beta_-} = \frac{\pi}{2\Omega}. \tag{1.36}$$

This coupled-mode formalism provides the foundation for the design of directional couplers, ring–bus interfaces, and reconfigurable photonic circuits in silicon platforms, where κ and $\Delta\beta$ can be engineered by adjusting waveguide separation, width, or local refractive index modulation.

1.2.8 Non-Linear Optics

When an electric field is applied to an optical medium, it induces an electric dipole moment within the material. The resulting polarization **P**, defined as the induced dipole moment per unit volume, quantifies this response. In the linear (low-field) regime, the induced polarization is directly proportional to the applied electric field **E** [19, 20].

$$\mathbf{P} = \epsilon_0 \chi^{(1)} \mathbf{E},$$

where ϵ_0 is the vacuum permittivity and $\chi^{(1)}$ is the linear susceptibility, which in general is a complex quantity: $\chi^{(1)} = \chi'^{(1)} + i\chi''^{(1)}$. The real part $\chi'^{(1)}$ determines the phase velocity of light and hence the refractive index, while the imaginary part $\chi''^{(1)}$ accounts for absorption (or gain) within the material. The refractive index and absorption coefficient are related to $\chi^{(1)}$ through:

$$n = \sqrt{1 + \chi'^{(1)}}, \quad \alpha = \frac{\omega}{c}\chi''^{(1)}.$$

For silicon at telecom wavelengths, the imaginary part is negligible, resulting in a low propagation loss and a real refractive index of approximately $n_0 \approx \sqrt{1+\chi^{(1)}} \approx 3.48$ at $1.55\ \mu$m [19, 20, 80].

As the electric field increases the relationship between the induced dipole moment and the applied field is no longer linear. The material now responds as:

$$\mathbf{P} = \epsilon_0 \left(\chi^{(1)}\mathbf{E} + \chi^{(2)}\mathbf{E}^2 + \chi^{(3)}\mathbf{E}^3 + \cdots \right),$$

where $\chi^{(n)}$ are the n-th order susceptibilities. In centrosymmetric materials like crystalline silicon, which has a diamond lattice structure with inversion symmetry, even-order susceptibilities such as $\chi^{(2)}$ are zero [21]. This occurs because under spatial inversion ($\mathbf{r} \to -\mathbf{r}$), the material's atomic structure remains unchanged, and the induced polarization must reverse direction when the electric field $\mathbf{E}$ is inverted ($\mathbf{E} \to -\mathbf{E}$), i.e., $\mathbf{P}(-\mathbf{E}) = -\mathbf{P}(\mathbf{E})$. In the power-series expansion of $\mathbf{P}$ in terms of $\mathbf{E}$, this symmetry condition eliminates all even-order terms that would not change sign upon field reversal. As a result, bulk silicon lacks second-order non-linear processes such as second-harmonic generation or the Pockels effect, and its non-linear optical response is dominated by third-order effects associated with $\chi^{(3)}$. However, an effective $\chi^{(2)}$ non-linearity can be induced in silicon through symmetry-breaking mechanisms such as strain engineering, interface effects in silicon–silicon nitride or silicon–oxide heterostructures, and electric-field-induced second-harmonic generation [4, 81, 82].

The dominant non-linearities in silicon arise from the third-order susceptibility $\chi^{(3)}$, which is a complex tensor quantity:

$$\chi^{(3)} = \Re\{\chi^{(3)}\} + i\,\Im\{\chi^{(3)}\}.$$

The real part $\Re\{\chi^{(3)}\}$ governs refractive effects such as the Kerr-induced index change, whereas the imaginary part $\Im\{\chi^{(3)}\}$ accounts for non-linear absorption, predominantly two-photon absorption (TPA). Both parts are strongly wavelength dependent, and their interplay determines the balance between non-linear phase shift and non-linear loss in silicon devices [22]. Moreover, the free carriers generated by TPA modify the complex refractive index, introducing additional real and imaginary perturbations—free-carrier dispersion (FCD) and free-carrier absorption (FCA)—that dynamically couple back to the optical field.

1.2.8.1 Kerr Effect

The Kerr effect refers to the intensity-dependent modification of the refractive index arising from a third-order non-linear optical response. When an optical field of sufficiently high intensity propagates through a medium, it induces a non-linear polarization term proportional to the cube of the electric field amplitude. As a result, the refractive index acquires an intensity dependence,

$$n(I) = n_0 + n_2 I, \tag{1.37}$$

where n_0 is the linear refractive index, n_2 is the nonlinear refractive index coefficient, and I denotes the optical intensity, defined as the time-averaged power per unit area of the guided mode. The latter is related to the real part of the third-order susceptibility $\chi^{(3)}$ as

$$n_2 = \frac{3\,\Re\{\chi^{(3)}\}}{4 n_0^2 \epsilon_0 c}. \tag{1.38}$$

For crystalline silicon at $\lambda \approx 1.55$ μm, $n_2 \approx 4.5 \times 10^{-18}$ m^2/W [21, 22]. The Kerr effect becomes significant when the optical intensity is high and absorptive processes do not suppress the non-linear phase accumulation. In tightly confined silicon-on-insulator (SOI) waveguides with sub-micron mode areas, the non-linear interaction strength is quantified by

$$\gamma = \frac{\omega n_2}{c A_{\text{eff}}}, \tag{1.39}$$

where A_{eff} is the effective mode area. For $A_{\text{eff}} \sim 0.1$–1 μm^2, γ can reach hundreds of W^{-1}m^{-1}, enabling pronounced non-linear effects even at milliwatt power levels [22, 80].

The Kerr-induced refractive index change underlies key non-linear processes such as self-phase modulation (SPM), cross-phase modulation (XPM), and four-wave mixing (FWM) in integrated waveguides [40, 58]. While the Kerr response in silicon is ultrafast and purely refractive, it is typically accompanied by competing carrier- and absorption-related non-linearities in practice.

1.2.8.2 Two-Photon Absorption

The imaginary part of $\chi^{(3)}$ leads to two-photon absorption (TPA), a non-linear absorption process where two photons of energy $\hbar\omega$ are simultaneously absorbed to excite one electron–hole pair across the indirect bandgap ($2\hbar\omega > E_g$). The intensity-dependent, loss

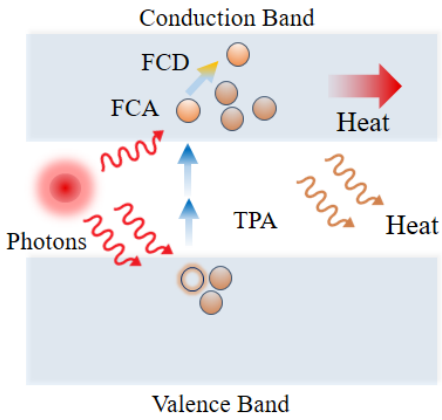

Figure 1.7: Schematic illustration of the two-photon absorption (TPA) process.

is expressed as

$$\frac{dI}{dz} = -(\alpha + \beta_{\mathrm{TPA}} I) I,$$

where α is the linear absorption coefficient and β_{TPA} is the TPA coefficient, related to $\Im\{\chi^{(3)}\}$ by

$$\beta_{\mathrm{TPA}} = \frac{3\omega}{2n_0^2\epsilon_0^2c^2}\Im\{\chi^{(3)}\}.$$

At $\lambda = 1.55\ \mu$m, β_{TPA} typically lies between 0.44 and 0.9 cm/GW [22, 83]. TPA is responsible for non-linear losses that limit the efficiency of Kerr-based processes but simultaneously generate free carriers that trigger secondary non-linearities.

1.2.8.3 Free-Carrier Effects: FCD and FCA

Two-photon absorption generates free carriers (electrons and holes), whose density N evolves as

$$\frac{dN}{dt} = \frac{\beta_{\mathrm{TPA}} I^2}{2\hbar\omega} - \frac{N}{\tau_{fc}},$$

where τ_{fc} is the carrier lifetime. These carriers alter both the real and imaginary parts of the refractive index, respectively through free-carrier dispersion (FCD) and free-carrier absorption (FCA). Empirical relations at 1.55 μm [22, 84] are

$$\Delta n_{\mathrm{fc}} = -(8.8\times10^{-22}N_e + 8.5\times10^{-18}N_h^{0.8}), \qquad \Delta\alpha_{\mathrm{fc}} = 8.5\times10^{-18}N_e + 6.0\times10^{-18}N_h,$$

with carrier concentrations in cm^{-3} and α in cm^{-1}. The FCD term Δn_{fc} produces a negative index shift (blue detuning), while FCA $\Delta\alpha_{\mathrm{fc}}$,introduces additional optical loss. Since carriers persist for nanoseconds to microseconds, they contribute a non-instantaneous, cumulative non-linearity that couples to both optical and thermal dynamics.

1.2.8.4 Thermal non-linearity

Absorption due to two-photon absorption (TPA) and free-carrier absorption (FCA) generates excess energy in the silicon core, which is subsequently released through carrier–phonon and phonon–phonon interactions, leading to localized heating. This temperature rise gives rise to a slow thermo-optic effect, resulting in a refractive-index change

$$\Delta n_{\mathrm{th}} = \frac{dn}{dT}\,\Delta T,$$

where $\frac{dn}{dT} \approx 1.86\times 10^{-4}\ \mathrm{K}^{-1}$ [22, 80]. Because the thermal relaxation time in micron-scale waveguides and resonators ranges from microseconds to milliseconds, the thermo-optic non-linearity dominates under continuous-wave (CW) or high-duty-cycle operation. It can lead to optical bistability, resonance hysteresis, and self-pulsing behaviors observed in silicon microrings [58].

1.2.8.5 Combined non-linear Response

The total change in the effective refractive index is therefore a superposition of Kerr, carrier, and thermal contributions:

$$\Delta n_{\mathrm{eff}} = n_2 I - \Delta n_{\mathrm{fc}} + \Delta n_{\mathrm{th}}.$$

In high-confinement waveguides this variation modifies the propagation constant $\beta = 2\pi n_{\mathrm{eff}}/\lambda$, leading to power-dependent phase shifts and spectral broadening. In microring resonators, the high-Q cavity (The quality factor Q characterizes how long light remains stored in the cavity and is defined as the ratio between the resonance frequency and its linewidth, $Q = \omega_0/\Delta\omega$.) enhances the internal intensity by orders of magnitude, amplifying all non-linear effects. The interplay of instantaneous Kerr and delayed carrier/thermal non-linearities gives rise to complex dynamics, including resonance shifts, optical bistability, self-pulsation, and frequency-comb formation [22, 56, 58].The modulation of these self-pulsing frequencies through electro-optic control will be discussed in detail in Chapter 3. These combined effects make silicon a unique platform for studying both ultrafast and slow non-linear optical phenomena on a CMOS-compatible chip.

1.2.9 Microring Resonators

A silicon microring resonator (MRR) is a closed waveguide loop, typically with radii of a few µm, side-coupled to one or more bus waveguides on a silicon-on-insulator (SOI) platform. The large Si/SiO_2 index contrast enables tight bends and dense, CMOS-compatible integration with mature fabrication processes [8, 9, 40]. At resonant frequencies, circulating fields build up and interfere coherently, enabling narrowband filtering, switching, delay, modulation, and enhanced light–matter interactions in a compact footprint [40, 41].

MRRs have been demonstrated as compact notch and add–drop filters on SOI [56]; analyzed as resonant channel add/drop elements via coupled-mode theory [85]; and arranged as coupled-resonator optical waveguides (CROWs) for on-chip routing and dispersion engineering [60, 86]. They underpin micrometre-scale electro-optic modulators exploiting free carriers [87], as well as performance-enhanced coupled-ring modulators [88]. Ultrahigh-Q silicon microrings provide narrow-linewidth refractive-index and biosensing [89]. non-linear applications include two-photon generation in silicon rings [90] and microcomb generation in monolithic microresonators [58, 91]. At the system level, a microprocessor communicating optically via integrated MRRs highlights platform maturity [9]. More recently, dispersion- and topology-aware multiport couplers and coupled-resonator networks have been engineered for asymmetric transport and exceptional-point physics [43, 65].

Light couples into a microring through a directional coupler as shown in the Figure 1.8 , which splits the input field between the through path and the circulating mode inside the ring. Once inside, the intracavity field acquires a round-trip phase $\phi_{\mathrm{rt}} = \beta(\omega)L$ and experiences attenuation determined by intrinsic losses (e.g., scattering, absorption) and out-coupling to the bus waveguides [40]. Resonance occurs when the round-trip phase matches an integer multiple of 2π ($\phi_{\mathrm{rt}} = 2\pi m, m \in \mathbb{Z}$), allowing successive passes to add constructively and leading to strong field buildup in the cavity [40, 41]. At the output, interference between the directly transmitted field and the out-coupled cavity field produces Lorentzian or Fano-like line shapes, with depth and linewidth governed by the balance between intrinsic loss and external loading (critical, under-, or over-coupling) [40, 46]. Furthermore, active mechanisms such as free-carrier plasma dispersion and the thermo-optic effect in silicon, along with non-linear responses including Kerr and two-photon absorption, provide dynamic tuning and open access to non-linear optical phenomena [8, 21, 49].

1.2.9.1 Temporal coupled-mode theory (TCMT).

The temporal coupled-mode theory (TCMT) [92–94], which will be employed throughout this thesis, provides an effective description of the optical field dynamics in driven resonator systems. It describes how energy is coupled into, stored within, and dissipated from a resonant cavity under continuous excitation. Physically, the theory applies to an

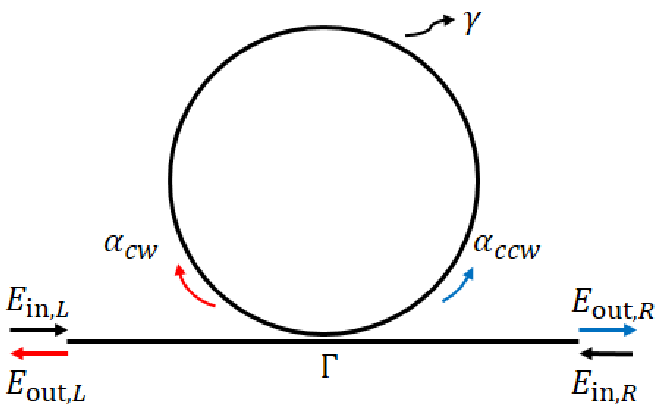

Figure 1.8: **Schematics of the microring resonator coupled to a bus waveguide.** The incoming and outgoing fields are denoted by the subscripts "in" and "out", while the labels L and R indicate left and right sides, respectively.

open through-flow system, where an external optical drive injects power into the cavity, the field circulates internally, and energy is continuously exchanged between the resonator and the bus waveguides through coupling and loss channels.

In this driven regime, the intracavity field reaches a steady or quasi-steady state in which the total stored energy remains constant on average. The internal dynamics are then governed by the balance between input coupling, intrinsic dissipation, and output extraction. Within TCMT, these processes are characterized by the coupling rate Γ, intrinsic loss rate γ, and the total decay rate $\gamma_t = \Gamma + \gamma$. To ensure the validity of the temporal description, all physical rates governing these energy exchanges must remain much smaller than the optical resonance frequency ω_0, namely

$$\max\{\Gamma, \gamma, |\Delta|\} \ll \omega_0, \tag{1.40}$$

where $\Delta = \omega - \omega_0$ is the detuning between the drive frequency ω and the cavity ω_0.

Working in those limitation , let us now consider an input electric field $E_{\text{in},L}$ with complex amplitude $\mathcal{E}_{\text{in},L}$ entering the bus waveguide from the left port, as illustrated in Fig. 1.8. The field is expressed as

$$E_{\text{in},L} = \mathcal{E}_{\text{in},L}\, e^{-i\omega t},$$

This field couples to the microring resonator positioned adjacent to the bus waveguide, thereby exciting the counter-clockwise (CCW) mode. The circulating field inside the ring can then be written in complex form as

$$\alpha_{\text{ccw}} = a_{\text{ccw}}\, e^{-i\omega t}.$$

In the coupled-mode picture, the temporal evolution of the CCW and CCW mode amplitude inside the microring is governed by following set of the equations:

$$i\,\frac{d}{dt}\begin{bmatrix}\alpha_{\text{ccw}}\\ \alpha_{\text{cw}}\end{bmatrix}=\begin{bmatrix}\omega_0-i\gamma_t & 0\\ 0 & \omega_0-i\gamma_t\end{bmatrix}\begin{bmatrix}\alpha_{\text{ccw}}\\ \alpha_{\text{cw}}\end{bmatrix}-\sqrt{2\Gamma}\begin{bmatrix}E_{\text{in},L}\\ E_{\text{in},R}\end{bmatrix}. \tag{1.41}$$

The output fields from the left and right ports are related to the input fields through the following relations:

$$E_{\text{out},R}=E_{\text{in},L}+i\sqrt{2\Gamma}\,\alpha_{\text{ccw}}, \tag{1.42}$$

$$E_{\text{out},L}=E_{\text{in},R}+i\sqrt{2\Gamma}\,\alpha_{\text{cw}}. \tag{1.43}$$

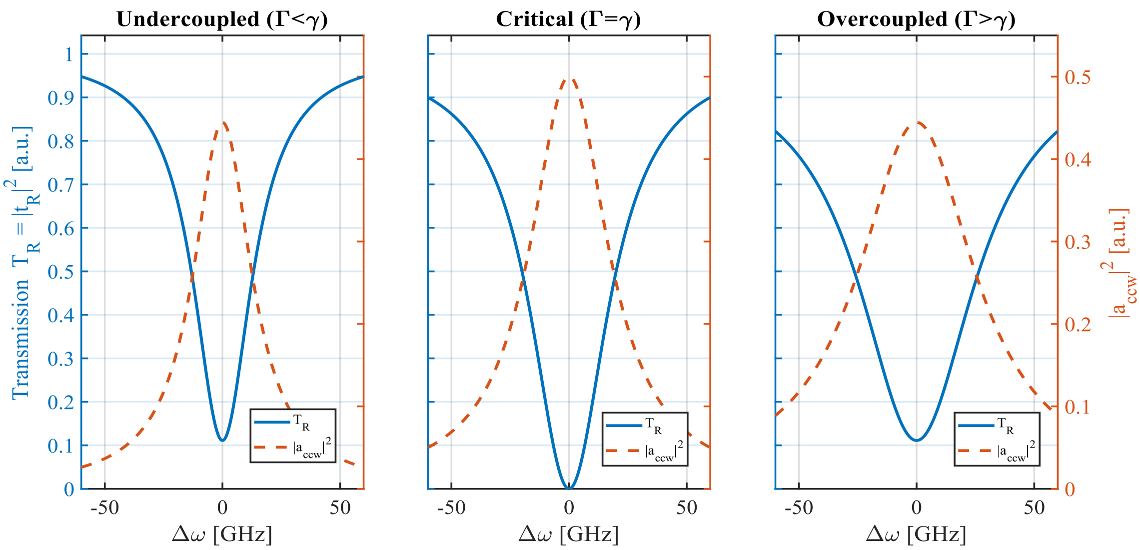

Figure 1.9: **Theoretical response of a microring resonator in the undercoupled, critical, and overcoupled regimes.** All frequency-related quantities are expressed in GHz. Here, Γ denotes the coupling rate between the bus waveguide and the microring, and γ is the intrinsic loss rate of the ring. The three panels (left to right) correspond to $\Gamma = 0.5\,\gamma$ (undercoupled), $\Gamma = \gamma$ (critical coupling), and $\Gamma = 2\,\gamma$ (overcoupled). The coupled-mode-theory calculations are performed using normalized parameters $\gamma = 1$, $\omega_0 = 0$, and left input field amplitude $E_{\text{in},L} = 1$. A physical frequency scale is introduced by mapping one normalized frequency unit to 10 GHz. The horizontal axis shows the detuning $\Delta\omega = \omega-\omega_0$ in GHz, swept over the range $\Delta\omega \in [-6\gamma, 6\gamma]$. Each panel displays the power transmission $T_R = |t_R|^2$ (solid blue) and the intracavity counter-clockwise field intensity $|a_{\text{ccw}}|^2$ (dashed orange) as functions of detuning.

Now our idea is to find the transmission through the "through" port. By dividing Eq. (1.42) by $E_{\text{in},L}$ we obtain

$$\frac{E_{\text{out},R}}{E_{\text{in},L}}=1+i\sqrt{2\Gamma}\,\frac{\alpha_{\text{ccw}}}{E_{\text{in},L}}\equiv t_R. \tag{1.44}$$

We define the transmission to the right as $T_R = |t_R|^2$.

Hence our transmission t_R takes following form:

$$t_R = 1 + i\frac{2\Gamma}{\omega_0 - \omega - i\gamma_t}, \tag{1.45}$$

When the laser is tuned at $\omega = \omega_0$ and the ring is set at critical coupling $\gamma = \Gamma$, the transmission to the right becomes

$$t_R = 0. \tag{1.46}$$

and the ring field amplitude inside the ring becomes

$$a_{\text{ccw}} = -\frac{\mathcal{E}_{\text{in,L}}}{i\sqrt{2\Gamma}}. \tag{1.47}$$

This condition corresponds to complete destructive interference in the through port with incoming field through a bus waveguide, resulting in zero transmission at resonance, as showed in the middle panel of Figure 1.9. At the same time, the amplitude of the field inside the microring builds up to maximum. The left and right panels in the Figure 1.9 show the transmission and amplitude inside the ring correspond to the cases $\Gamma = 0.5\gamma$ (undercoupled) and $\Gamma = 2\gamma$ (overcoupled), evaluated using normalized parameters $\gamma = 1$, $\omega_0 = 0$, and left excitation amplitude $E_{\text{in},L} = 1$. The buildup of the field inside the microring under this condition allows us to characterize the resonator in terms of its quality factor, photon lifetime, and linewidth , which I will define now.

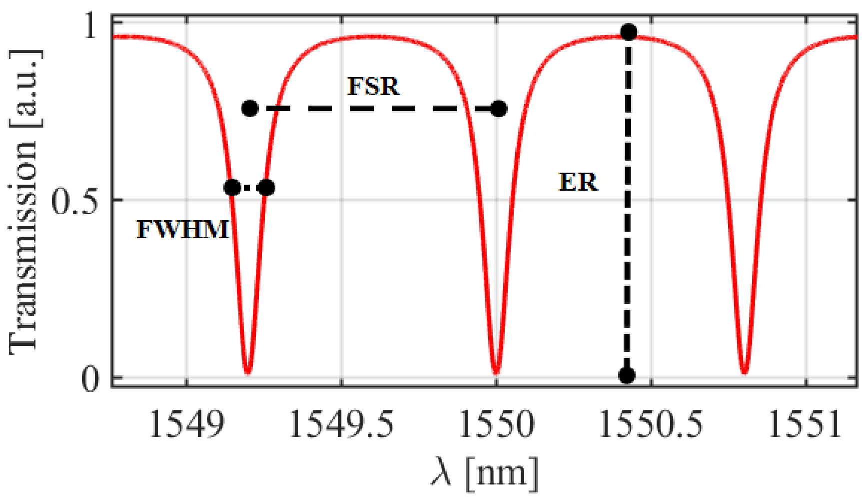

Figure 1.10: Free spectral range (FSR), full width at half maximum (FWHM), and extinction ratio (ER) from the transmission spectrum.

The quality factor, Q of a resonator describes how efficiently it stores optical energy relative to its losses. It is defined as the ratio of the stored energy to the energy lost per optical cycle:

$$Q = \omega_0 \frac{\text{Energy stored}}{\text{Power loss}} = \frac{\omega_0}{2\gamma_t}, \tag{1.48}$$

Where ω_0 is the resonance angular frequency, and $\gamma_t = \Gamma + \gamma$ is the total decay rate that accounts for both intrinsic loss (γ) and coupling loss (Γ).

The full width at half maximum (FWHM) of the resonance is related to the decay rate by

$$\Delta\omega_{\text{FWHM}} = 2\gamma_t, \tag{1.49}$$

and in frequency units,

$$\Delta f_{\text{FWHM}} = \frac{\Delta\omega_{\text{FWHM}}}{2\pi} = \frac{\gamma_t}{\pi}. \tag{1.50}$$

The photon lifetime τ_{ph} represents the characteristic time over which the stored energy decays to $1/e$ of its initial value. It is inversely proportional to the total loss rate:

$$\tau_{\text{ph}} = \frac{1}{2\gamma_t}. \tag{1.51}$$

Using the definition of Q, it can also be expressed as

$$\tau_{\text{ph}} = \frac{Q}{\omega_0}. \tag{1.52}$$

During this time, the photon circulates inside the ring multiple times before decaying. The number of round trips N_{rt} that a photon completes can be estimated by comparing its lifetime with the round-trip time $T_{\text{rt}} = \frac{L}{v_g}$, where $L = 2\pi R$ is the ring circumference and v_g is the group velocity:

$$N_{\text{rt}} = \frac{\tau_{\text{ph}}}{T_{\text{rt}}} = \frac{v_g}{2\gamma_t L}. \tag{1.53}$$

For a silicon microring resonator operating near $\lambda_0 = 1550$ nm, the angular frequency is

$$\omega_0 = \frac{2\pi c}{\lambda_0} \approx 1.22 \times 10^{15} \text{ rad/s}.$$

Assuming a measured linewidth of $\Delta f_{\text{FWHM}} = 20$ GHz, the total decay rate is

$$\gamma_t = \pi\, \Delta f_{\text{FWHM}} = \pi \times 20 \times 10^9 \approx 6.28 \times 10^{10} \text{ rad/s}.$$

The quality factor is then

$$Q = \frac{\omega_0}{2\gamma_t} = \frac{1.22 \times 10^{15}}{2 \times 6.28 \times 10^{10}} \approx 9.7 \times 10^3.$$

The corresponding photon lifetime is

$$\tau_{\text{ph}} = \frac{1}{2\gamma_t} \approx 7.96 \times 10^{-12}\ \text{s}.$$

Another important parameter of the microring resonator is the Free Spectral Range (FSR), which represents the frequency spacing between two consecutive resonance modes. It is given by

$$\Delta f_{\text{FSR}} = \frac{v_g}{L} = \frac{c}{n_g L} = \frac{c}{2\pi n_g R}. \tag{1.54}$$

In wavelength units, the FSR can be approximated as

$$\Delta\lambda_{\text{FSR}} \approx \frac{\lambda_0^2}{n_g L}. \tag{1.55}$$

The ratio between the FSR and the resonance linewidth determines the finesse $\mathcal{F}$ of the resonator:

$$\mathcal{F} = \frac{\Delta f_{\text{FSR}}}{\Delta f_{\text{FWHM}}} = \frac{1.14\ \text{THz}}{20\ \text{GHz}} \approx 57. \tag{1.56}$$

A higher finesse indicates better spectral selectivity and stronger field confinement within the microring cavity.

1.2.9.2 Backscattering in Microring Resonators

Sidewall roughness and microscopic interface disorder in integrated microring resonators unavoidably induce coupling between the two degenerate counter-propagating eigenmodes, as first modeled in [95, 96]. This parasitic mode conversion manifests as resonance splitting, coherent hybridization of clockwise (CW) and counter-clockwise (CCW) fields, and excess insertion loss, consistently observed and quantified in [97]. Such symmetry-breaking reduces Q and degrades extinction ratios in filtering applications [96], and compromises the spectral stability required for laser stabilization, frequency-comb formation, and routing systems that rely on high coherence rings [98]. From a fundamental perspective, uncontrolled backscattering obscures the intrinsic modal topology of the ring and hinders faithful realization of physical effects that rely on directional purity — including non-Hermitian degeneracies, chirality, and reciprocity breaking — as made explicit in recent chiral and EP-based suppression schemes [99, 100].

The origin and impact of CW–CCW coupling were first captured analytically using coupled-mode theory, which connected resonance doublets to Rayleigh-type scattering induced by nanoscale roughness [95]. Classical mitigation strategies consequently aimed at suppressing the underlying disorder. Surface smoothing through optimized etching and thermal oxidation was shown to reduce the intrinsic backscattering strength [96]. Deterministic scatterer placement was later explored to gain controlled coupling between the two modes and restore spectral symmetry, rather than allowing random perturbations to dictate hybridization [97]. In parallel, geometric countermeasures — such as asymmetric rings, angled bus couplers, and split-ring topologies — were introduced to lift the degeneracy between CW and CCW trajectories and thereby minimize coherent back-reflection at the design level [101].

A more recent class of works does not attempt to eliminate scattering, but instead exploits coherent interference to neutralize its effect. Svela *et al.* showed that adding a precisely engineered auxiliary scatterer can destructively interfere with the intrinsic roughness-induced coupling and recover a single Lorentzian peak, effectively erasing the backscattering signature [98]. A conceptually distinct non-Hermitian strategy was later implemented using low-loss Mie scatterers to create a chiral exceptional point in silicon microrings; in that regime, mode coalescence enforces unidirectionality and suppresses CW–CCW hybridization without post-fabrication tuning [99]. Complementarily, Li and Bogaerts introduced a cancellation design that suppresses resonance splitting by engineering the contra-propagating coupling pathways such that destructive interference occurs intrinsically at the device level [100]. Along the same direction of "cancellation rather than elimination," Aslan *et al.* demonstrated that the backscattering channel itself can be coherently controlled and tuned in situ, enabling suppression or deliberate enhancement of the CW–CCW coupling by phase-matched auxiliary perturbations [45]. In our this work the engineered perturbation allows the system to transition continuously between Hermitian and non-Hermitian coupling regimes, granting tunable chirality and access to exceptional-point dynamics, while at the same time providing a control knob to erase or reinstate the spectral signatures of backscattering without modifying the fabricated device.

Backscattering in a microring resonator can be modeled by introducing complex coupling terms between the two counter-propagating modes (CW and CCW). In a fabricated device, inevitable sidewall and surface roughness induce coherent backscattering; alternatively, a preferential backscattering channel can be intentionally engineered, as will be shown later. In either case, optical power circulating in one direction is scattered into the opposite direction. Experimentally, this intermodal coupling manifests as resonance doublets in the through- and drop-port transmission spectra. Fig. 5.4(a) in Chapter 5 shows the asymmetric doublet that results from non- hermitian backscattering couplings.Whereas the hermitian backscattering results in symmetric doublet.

To model this behavior we use time-domain coupled-mode theory for the two intracavity amplitudes, including both backscattering and coupling to the bus waveguide. The dynamics are governed by

$$i\,\frac{d}{dt}\begin{bmatrix}\alpha_{\mathrm{CCW}}\\ \alpha_{\mathrm{CW}}\end{bmatrix}=\begin{bmatrix}\omega_0-i\,\gamma_{\mathrm{t}} & -i\,\beta_{\mathrm{BS},12}\\ -i\,\beta_{\mathrm{BS},21} & \omega_0-i\,\gamma_{\mathrm{t}}\end{bmatrix}\begin{bmatrix}\alpha_{\mathrm{CCW}}\\ \alpha_{\mathrm{CW}}\end{bmatrix}-\sqrt{2\Gamma}\begin{bmatrix}E_{\mathrm{in},L}\\ E_{\mathrm{in},R}\end{bmatrix}. \tag{1.57}$$

Here $\beta_{\mathrm{BS},12}$ and $\beta_{\mathrm{BS},21}$ are the complex backscattering coefficients. For reciprocal (Hermitian) backscattering we use

$$\beta_{\mathrm{BS},21}=-\beta^*_{\mathrm{BS},12}, \tag{1.58}$$

In contrast, a non-Hermitian backscattering channel corresponds to a violation of these equalities, i.e.

$$\beta_{\mathrm{BS},21}\neq-\beta^*_{\mathrm{BS},12}, \tag{1.59}$$

which generally produces asymmetric CW↔CCW coupling and enables chiral or EP-mediated transport regimes as shown in Fig. 5.4 in Chapter 5.

In the coming sections, we will demonstrate in detail how backscattering—whether originating from fabrication-induced disorder or from intentionally engineered coupling—transfers energy between counter-propagating modes, converting CCW into CW and vice versa. The discussion will proceed from Hermitian backscattering in a conventional microring resonator to non-Hermitian backscattering, allowing a clear distinction between the two regimes.

1.3 Non-Hermitian Physics: Concepts and Tools

1.3.1 Hermitian vs Non-Hermitian

The law of conservation of energy states that, in a closed system, the total energy remains constant over time. In other words, the energy of a system can only change if energy enters or leaves the system.

As a simple example, consider a simple harmonic oscillator (SHO) consisting of a mass m attached to a spring of stiffness constant k, placed on a frictionless surface. The *system* comprises the mass, the spring, the frictionless surface, and the fixed support to which the other end of the spring is attached. When the mass is displaced from its equilibrium position and released, it oscillates back and forth, continuously converting the potential energy stored in the spring into the kinetic energy of the moving mass.

In an ideal, perfectly frictionless system, the total mechanical energy remains constant over time. The notion of *time* here refers to the continuous evolution of the system during which kinetic and potential energies exchange periodically. The relative increase and decrease of the kinetic and potential energies are perfectly balanced—the evolution of the system back and forth in energy space is symmetric. In this relative sense, the dynamics of the system appear *timeless*: the process of energy exchange repeats indefinitely and identically, as if time itself does not exist within the confines of the system's energy balance. The total energy of the oscillator is given by

$$E(t) = T + V = \frac{1}{2}m\dot{x}^2 + \frac{1}{2}kx^2, \tag{1.60}$$

where $T = \frac{1}{2}m\dot{x}^2$ is the kinetic energy associated with the velocity of the mass, and $V = \frac{1}{2}kx^2$ is the potential energy stored in the spring due to displacement from equilibrium. In the absence of dissipation, $E(t)$ remains constant, and the system exhibits perfect periodic reversibility.

This idealized symmetry is related to the concept of *time-reversal symmetry*, which exists in both classical and quantum mechanics. In a closed system with no dissipation or external driving, the dynamics are governed by a Hermitian Hamiltonian with real eigenvalues corresponding to physically observable energies. Such a Hamiltonian generates a unitary time-evolution operator,

$$U(t) = e^{-iHt/\hbar}, \tag{1.61}$$

which satisfies the unitarity condition

$$U^\dagger(t)U(t) = U(t)U^\dagger(t) = \mathbb{I}. \tag{1.62}$$

Unitarity ensures that the norm of the quantum state—and by analogy, the total energy in the classical oscillator—remains conserved throughout the evolution.

In the classical picture, this manifests as a reversible trajectory in phase space: if time is reversed, the system precisely retraces its path. In the quantum picture, unitarity implies deterministic and reversible dynamics—the system can evolve forward or backward in time without loss or gain of information or energy. Thus, Hermitian Hamiltonians not only conserve energy but also embody the fundamental symmetry of time itself. Their evolution is unitary in the quantum domain and energy-conserving in the classical sense, revealing a profound correspondence between Hermiticity, conservation laws, and temporal reversibility [102, 103].

However, in a realistic scenario, this idealization does not hold - perfect time symmetry does not hold. As the mass slides, friction from the surface and air resistance gradually dissipate energy from the system. Consequently, the amplitude of oscillation decreases over time, and the system eventually comes to rest, having transferred its mechanical energy to the surrounding environment in the form of heat and sound. The damped oscillator can be described by the equation of motion

$$m\ddot{x} + b\dot{x} + kx = 0, \tag{1.63}$$

where b is the damping coefficient. The total energy,

$$E(t) = \frac{1}{2}m\dot{x}^2 + \frac{1}{2}kx^2, \tag{1.64}$$

decays according to

$$\frac{dE(t)}{dt} = -b\dot{x}^2, \tag{1.65}$$

indicating that the rate of energy loss is proportional to the square of the velocity. The negative sign reflects that energy is continuously dissipated into the environment, breaking time-reversal symmetry. If time were reversed, the system would not retrace its trajectory, as the lost energy cannot be recovered without external input. In the language of Hamiltonian dynamics, this breaking of energy conservation corresponds to the transition from a Hermitian to a *non-Hermitian* system. The effective Hamiltonian of such a system can be expressed as

$$H_{\text{eff}} = H_0 - i\Gamma, \tag{1.66}$$

where H_0 is the Hermitian (energy-conserving) part and Γ represents loss or gain. The imaginary component $-i\Gamma$ introduces exponential decay or amplification in the system's evolution, corresponding to non-unitary dynamics.

In photonic systems, such as optical microrings, this non-Hermitian behavior emerges naturally through intrinsic and coupling losses. For instance, the effective Hamiltonian for the clockwise (CW) and counter-clockwise (CCW) modes of a symmetric microring resonator can be written as the effective Hamiltonian given in Eq. (1.41) governing the intracavity field dynamics is given by

$$H_{\text{eff}} = \begin{bmatrix} \omega_0 - i\gamma_t & 0 \\ 0 & \omega_0 - i\gamma_t \end{bmatrix} = (\omega_0 - i\gamma_t)\, I, \tag{1.67}$$

A Hamiltonian H is said to be *Hermitian* if it satisfies

$$H^\dagger = H, \tag{1.68}$$

where $H^\dagger$ denotes the complex conjugate transpose of H. Taking the adjoint of H_{eff}, we obtain

$$H_{\text{eff}}^\dagger = \begin{bmatrix} \omega_0 + i\gamma_t & 0 \\ 0 & \omega_0 + i\gamma_t \end{bmatrix}. \tag{1.69}$$

It is clear that

$$H_{\text{eff}}^\dagger \neq H_{\text{eff}} \quad \text{since} \quad -i\gamma_t \neq +i\gamma_t \text{ for } \gamma_t > 0. \tag{1.70}$$

Nevertheless, since both CW and CCW modes have the same resonance frequency ω_0 and decay at the same rate γ_t, and there is no coupling term between them, the two modes evolve independently and identically. Therefore, although the original H_{eff} does not satisfy the Hermitian conjugate condition, it can be regarded as an *effectively Hermitian Hamiltonian* because the uniform decay affects both modes equally and does not alter their relative dynamics. Physically, the system behaves as two identical, uncoupled, exponentially decaying oscillators with no energy exchange between the CW and CCW modes. Hence, the system exhibits *trivial non-Hermiticity*—the global energy decays exponentially, but the relative dynamics of the modes remain time-symmetric.

The transition from Hermitian to non-Hermitian dynamics thus marks a shift from perfectly reversible, energy-conserving evolution to open, dissipative behavior where time symmetry is broken. This fundamental distinction underlies a wide range of phenomena in optics and photonics, including mode coalescence, exceptional points, and asymmetric energy flow in coupled resonator systems [10–12, 15, 16, 23, 35, 36, 59, 79, 104–106].

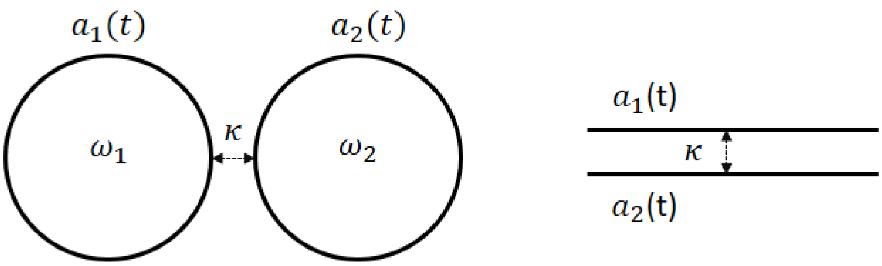

Figure 1.11: **Schematic of two evanescently coupled photonic resonators (Left) (or waveguides (Right).** The modal amplitudes are $a_1(t)$ and $a_2(t)$, the resonance frequencies are ω_1 and ω_2, and the two modes are coupled with a Hermitian coupling coefficient κ.

In a coupled photonic system such as two evanescently coupled resonators or two coupled waveguides as shown in Figure 1.11. let $a_1(t)$ and $a_2(t)$ denote the complex modal amplitudes. In the lossless, reciprocal case the coupled-mode equations take the form

$$i\frac{d}{dt}\begin{pmatrix} a_1 \\ a_2 \end{pmatrix} = \begin{pmatrix} \omega_1 & \kappa \\ \kappa^* & \omega_2 \end{pmatrix}\begin{pmatrix} a_1 \\ a_2 \end{pmatrix}, \tag{1.71}$$

where $\omega_1, \omega_2 \in \mathbb{R}$ are the isolated resonance frequencies and κ is the complex coupling coefficient. Reciprocity in a passive, time-reversal symmetric, lossless structure implies $\kappa \in \mathbb{R}$, so that

$$H = \begin{pmatrix} \omega_1 & \kappa \\ \kappa & \omega_2 \end{pmatrix} = H^\dagger. \tag{1.72}$$

This is exactly the generic Hermitian two-level Hamiltonian with $\alpha = \omega_1$, $\delta = \omega_2$, $\beta = \kappa$.

The total optical power

$$P(t) = |a_1(t)|^2 + |a_2(t)|^2, \tag{1.73}$$

obeys

$$\frac{dP}{dt} = 0, \tag{1.74}$$

so power is conserved. The supermode frequencies are real and given by the eigenvalues

$$\Omega_\pm = \frac{\omega_1 + \omega_2}{2} \pm \sqrt{\left(\frac{\omega_1 - \omega_2}{2}\right)^2 + |\kappa|^2}, \tag{1.75}$$

The expressions derived for the Hermitian or non–Hermitian exchange of energy between the counter–propagating modes are physically meaningful only in the *driven* regime, where energy is continuously supplied to the resonator and a nonzero intracavity field is sustained. In this regime the system behaves as an open through–flow channel: input power is injected, redistributed internally by the coupling, and extracted by loss/output. In particular, the distinction between *Hermitian* and *non–Hermitian* coupling is *manifested only through this redistribution of energy under sustained drive*; it is the manner of energy exchange (reciprocal versus phase–biased or unidirectional) that operationally distinguishes the two cases. Once the external drive is switched off and the fields free–decay to zero, the total energy simply undergoes exponential extinction; the internal exchange terms vanish trivially with the amplitudes, and the phase–dependent routing between modes ceases to have operational significance. Thus, Hermitian versus non–Hermitian behavior in this context is not a property of the late–time decay tail, but of the driven steady or quasi–steady operating regime in which internal energy circulation is sustained.

1.3.2 Diabolic and Exceptional points

In a fabricated microring, inevitable sidewall and surface roughness induce coherent backscattering between the clockwise (CW) and counterclockwise (CCW) propagating modes [107–109]. Alternatively, the scattering process can be intentionally engineered to realize *preferential* or asymmetric backscattering, for example through tailored scatterers or asymmetric resonator geometries, as demonstrated in dedicated non-Hermitian microring designs [105, 110]. In both cases, optical power circulating in one direction is partially scattered into the counterpropagating mode, leading to an effective intermodal coupling.

Experimentally, this coupling manifests as a splitting of the resonance into doublets in the through- and drop-port transmission spectra, as well as asymmetric reflection spectra when the backscattering is direction dependent [107, 108, 110].

To model this behavior, we use time-domain coupled-mode theory for the two counterpropagating intracavity amplitudes, including backscattering and coupling to the bus waveguide. The dynamics and input–output relations are governed by the following pair of equations [111]

$$i\,\frac{d}{dt}\begin{bmatrix}\alpha_{\mathrm{CCW}}\\ \alpha_{\mathrm{CW}}\end{bmatrix}=\begin{bmatrix}\omega_0-i\,\gamma_{\mathrm{t}} & -i\,\beta_{\mathrm{BS},12}\\ -i\,\beta_{\mathrm{BS},21} & \omega_0-i\,\gamma_{\mathrm{t}}\end{bmatrix}\begin{bmatrix}\alpha_{\mathrm{CCW}}\\ \alpha_{\mathrm{CW}}\end{bmatrix}-\sqrt{2\Gamma}\begin{bmatrix}E_{\mathrm{in},L}\\ E_{\mathrm{in},R}\end{bmatrix}, \tag{1.59}$$

and the input–output relations

$$\begin{bmatrix}E_{\mathrm{out},R}\\ E_{\mathrm{out},L}\end{bmatrix}=\begin{bmatrix}E_{\mathrm{in},L}\\ E_{\mathrm{in},R}\end{bmatrix}+i\sqrt{2\Gamma}\begin{bmatrix}\alpha_{\mathrm{CCW}}\\ \alpha_{\mathrm{CW}}\end{bmatrix}. \tag{1.60}$$

while $\beta_{\mathrm{BS},12}$ and $\beta_{\mathrm{BS},21}$ are the complex backscattering couplings between CCW and CW. For a Hermitian (reciprocal) coupling we write

$$\beta_{\mathrm{BS},12}=|\beta|\,e^{+i\theta},\qquad \beta_{\mathrm{BS},21}=-|\beta|\,e^{-i\theta}. \tag{1.76}$$

Let $\kappa=\sqrt{2\Gamma}$ and at exact resonance $\Delta\omega=0$. Solving Eq. (1.59) in steady state gives

$$a_{\mathrm{CCW}}=\frac{\kappa}{D}\left(i\gamma_t\,\mathcal{E}_{\mathrm{in},L}-i\,\beta_{\mathrm{BS},12}\,\mathcal{E}_{\mathrm{in},R}\right), \tag{1.77}$$

$$a_{\mathrm{CW}}=\frac{\kappa}{D}\left(i\gamma_t\,\mathcal{E}_{\mathrm{in},R}-i\,\beta_{\mathrm{BS},21}\,\mathcal{E}_{\mathrm{in},L}\right), \tag{1.78}$$

with the (phase-independent) denominator

$$D=\gamma_t^2-\beta_{\mathrm{BS},12}\beta_{\mathrm{BS},21}=\gamma_t^2+|\beta|^2. \tag{1.79}$$

Equation (1.79) shows that magnitude effects of backscattering enter via $|\beta|$; the coupling phase θ appears only in the numerators.

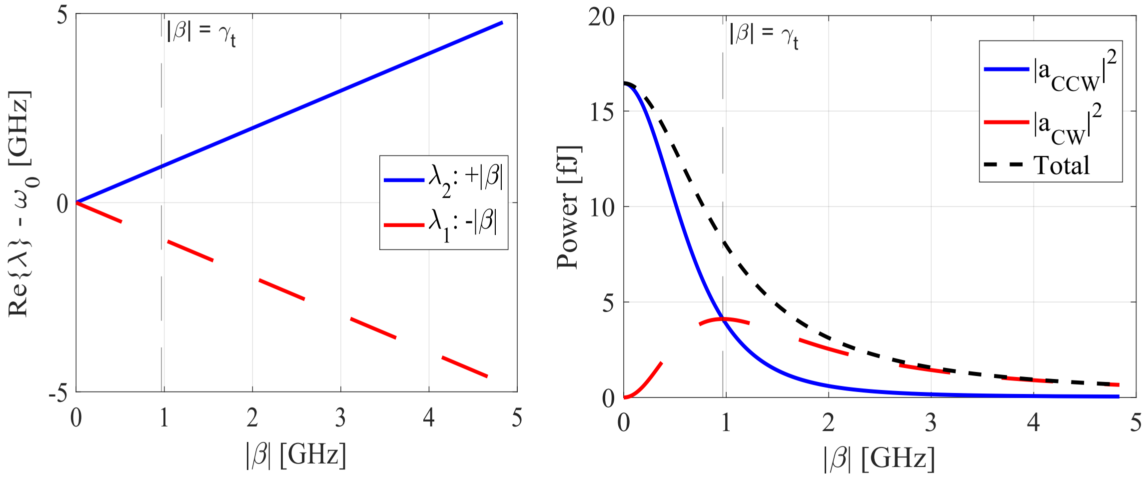

Figure 1.12: **Theory.** Left panel: Eigenfrequency splitting as a function of Hermitian coupling magnitude $|\beta|$, swept from 0 to 5 γ_t. Right panel: resonant circulating energies of the CCW mode, CW mode, and their sum versus $|\beta|$ under single-sided excitation; the vertical marker denotes $|\beta| = \gamma_t$. Common parameters for both panels: ω_0 = 193,414 GHz, γ_t = 0.967 GHz, $\Gamma = \gamma_i$ = 0.484 GHz, and input power P_{in} = 0.100 mW.

We then define the intracavity powers

$$P_{\text{CCW}} = |a_{\text{CCW}}|^2, \qquad P_{\text{CW}} = |a_{\text{CW}}|^2, \qquad P_{\text{tot}} = P_{\text{CCW}} + P_{\text{CW}}.$$

For the single-sided excitation - from the left ($\mathcal{E}_{\text{in},R} = 0$, $\mathcal{E}_{\text{in},L} \neq 0$), power circulating in CCW and CW become

$$P_{\text{CCW}} = \frac{\kappa^2\,\gamma_t^2\,|\mathcal{E}_{\text{in},L}|^2}{(\gamma_t^2 + |\beta|^2)^2}, \qquad P_{\text{CW}} = \frac{\kappa^2\,|\beta|^2\,|\mathcal{E}_{\text{in},L}|^2}{(\gamma_t^2 + |\beta|^2)^2}, \tag{1.80}$$

$$\boxed{P_{\text{tot}} = \frac{\kappa^2\,(\gamma_t^2 + |\beta|^2)\,|\mathcal{E}_{\text{in},L}|^2}{(\gamma_t^2 + |\beta|^2)^2}} \tag{1.81}$$

Both modal powers share the same enhancement factor, so P_{CCW} and P_{CW} reach their maxima at $|\beta| = \gamma_t$.

Under critical coupling ($\Gamma = \gamma$), one has $\gamma_t = 2\Gamma$ and $D = (2\Gamma)^2 + |\beta|^2$. The apparent peak occurs at $|\beta| = \gamma_t = 2\Gamma$.

Their *ratio* is therefore

$$\boxed{\frac{P_{\text{CCW}}}{P_{\text{CW}}} = \frac{\gamma_t^2}{|\beta|^2} = \left(\frac{\gamma_t}{|\beta|}\right)^2}, \tag{1.82}$$

which is independent of the input amplitude and the coupling phase θ. Equivalently, the power *fractions* in the two counterpropagating modes are

$$\boxed{\frac{P_{\mathrm{CCW}}}{P_{\mathrm{tot}}} = \frac{\gamma_t^2}{\gamma_t^2 + |\beta|^2}, \qquad \frac{P_{\mathrm{CW}}}{P_{\mathrm{tot}}} = \frac{|\beta|^2}{\gamma_t^2 + |\beta|^2}}, \tag{1.83}$$

so the modal partition is governed solely by the ratio "loss : coupling" (γ_t : $|\beta|$). This means (in weak backscattering) as shown in the right panel of Fig. 1.12 $|\beta| \ll \gamma_t$: $P_{\mathrm{CCW}} \gg P_{\mathrm{CW}}$ and the ring predominantly stores energy in the driven (CCW) mode; the CW component is a small leakage set by $|\beta|/\gamma_t$. In the case of $|\beta| = \gamma_t$: the two powers are equal, $P_{\mathrm{CCW}} = P_{\mathrm{CW}}$, i.e., the ring circulates the same power in both directions. In stronger intermodal coupling $|\beta| > \gamma_t$: the CW share exceeds the CCW share, $P_{\mathrm{CW}} > P_{\mathrm{CCW}}$; intermodal scattering dominates over damping.

Thus, by *tweaking either* the total loss γ_t (e.g., via absorption, radiation, or external coupling Γ) *or* the backscattering strength $|\beta|$ (set by surface roughness or engineered scatterers), one can continuously steer the power distribution between the counterpropagating modes , In particular, increasing $|\beta|$ at fixed γ_t transfers a larger fraction of power into the CW mode; increasing γ_t at fixed $|\beta|$ suppresses the CW content and restores CCW dominance.

In the Hermitian case with $\beta_{\mathrm{BS},21} = -\beta^*_{\mathrm{BS},12}$ and $H = \begin{bmatrix} \omega_0 - i\gamma_t & -i\beta_{\mathrm{BS},21} \\ -i\beta_{\mathrm{BS},12} & \omega_0 - i\gamma_t \end{bmatrix}$, taking $\beta_{\mathrm{BS},12} = |\beta|e^{i\theta}$ gives eigenvalues $\lambda_{1,2} = \omega_0 - i\gamma_t \mp |\beta|$, i.e., a symmetric real-frequency splitting $\pm|\beta|$ at a common decay rate γ_t. Under single-sided excitation from the left at exact resonance, $\mathcal{E}_{\mathrm{in},R} = 0$ and $\omega = \omega_0$, the steady-state traveling-wave amplitudes reduce to $a_{\mathrm{CCW}} = \kappa\, i\gamma_t\, \mathcal{E}_{\mathrm{in},L}/D$ and $a_{\mathrm{CW}} = \kappa\,(\pm i|\beta|)\, \mathcal{E}_{\mathrm{in},L}/D$, with $D = \gamma_t^2 + |\beta|^2$ for this sign convention. Consequently, the modal power ratio is $P_{\mathrm{CCW}}/P_{\mathrm{CW}} = (\gamma_t/|\beta|)^2$, independent of the coupling phase and common prefactors, so the power partition is governed solely by the competition between total loss and intermodal coupling as shown in the right panel of Fig. 1.12. This connects directly to the spectral picture: at $|\beta| = 0$ the eigenvalues as can be seen in the left panel of Fig. 1.12 are degenerate also known as the diabolical point and only the driven traveling wave (CCW) carries power as we saw this in earlier subsection 1.2.9 . As $|\beta|$ increases, the eigenfrequencies split while the total intracavity build-up at ω_0 decreases as $1/D$, yet the CCW/CW partition remains fixed by $(\gamma_t/|\beta|)^2$; and precisely at $|\beta| = \gamma_t$ the powers become equal, $P_{\mathrm{CCW}} = P_{\mathrm{CW}}$, because the drive at ω_0 projects equally onto the two split hybrids even though the overall stored energy is reduced by the larger D.

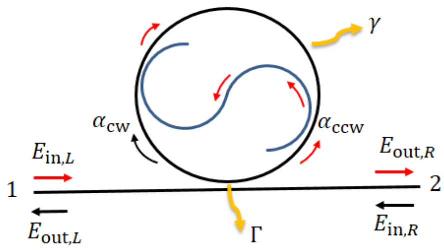

Figure 1.13: **Schematic of the Taiji Microring Resonator (TMR).** The indices R and L denote excitation from the right and left sides, respectively, while ports 1 and 2 correspond to the designated input/output channels. The fields E_{in} and E_{out} represent the injected and extracted optical fields.

1.3.3 Taiji Microring as Non-Hermitian Device

The Taiji microring resonator (TMR) extends the simple microring by introducing an intentional path imbalance or asymmetric coupling that enables effective non-Hermitian interactions between the counter-propagating modes, thereby functioning as a non-Hermitian device [23, 24, 61, 62]. This is realized by inscribing an S-shaped waveguide inside the ring, as shown in Fig. 1.13, which acts as an internal feedback channel. The resulting geometry breaks the spatial symmetry between the clockwise (CW) and counterclockwise (CCW) modes, allowing tunable non-reciprocal coupling within a passive photonic platform. The feedback branch re-injects part of the circulating field in a direction-dependent manner, leading to complex intermodal coupling that manifests as both frequency and linewidth splitting.

The TMR has been exploited in several ways. TMR is employed to realize 2D topological laser for the preferential chirality and suppression of the backscattering [112, 113]. Calabrese *et al.* reported unidirectional reflection in an integrated Taiji microresonator [61]. Muñoz de las Heras *et al.* proposed a non-linear Taiji resonator supporting unidirectional lasing, where Kerr non-linearity enhances direction-dependent gain competition [114]. Subsequent experimental work confirmed non-linearity-induced reciprocity breaking and asymmetric transmission [24]. Franchi *et al.* analyzed how bus-induced loss and Fabry–Pérot interference modify the linear and non-linear response of Taiji devices [115]. More recently, Biasi *et al.* directly measured the complex eigenvalues of Taiji resonators using an interferometric method, quantifying the non-Hermitian coupling strength and phase [116]. Moreover, the TMR has been proposed for high-sensitivity sensing near exceptional points [62]. Building upon these studies, the dynamical behavior of the ideal Taiji microring can be formulated within the temporal coupled-mode theory (TCMT) framework, following the same notation for the counter-propagating modes as

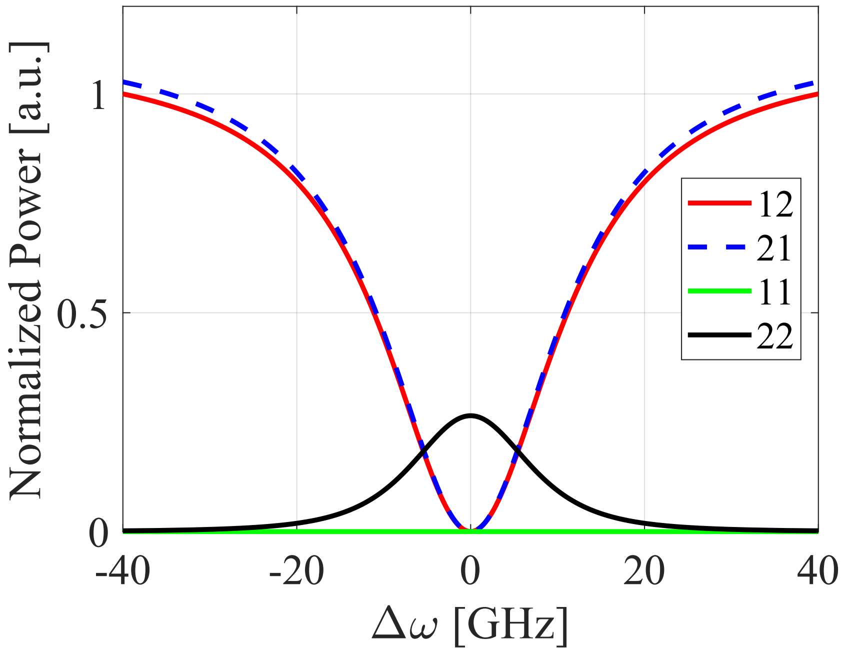

Figure 1.14: **Theory: Taiji microring resonator (TMR) transmission and reflection spectra.** The total loaded loss is $\gamma_t = \gamma + \Gamma + 2\Gamma_S$ with $\gamma = 4.144$ GHz, $\Gamma = 5.973$ GHz, and $\Gamma_S = 1.000$ GHz. Taiji coupling of magnitude is set to $|\beta_t| = \Gamma$ with phase $\phi_t = 5.897$ rad is included as the only coupling mechanism, while intrinsic backscattering is set to ($\beta_{12} = \beta_{21} = 0$). The detuning axis is defined as $\Delta = \omega - \omega_0$ with $\omega_0 = 2.89465$ THz.

introduced earlier:

$$i\frac{d}{dt}\begin{pmatrix}\alpha_{\mathrm{CCW}}\\ \alpha_{\mathrm{CW}}\end{pmatrix} = \begin{pmatrix}\omega_0 - i\gamma_t & -i\beta_t\\ 0 & \omega_0 - i\gamma_t\end{pmatrix}\begin{pmatrix}\alpha_{\mathrm{CCW}}\\ \alpha_{\mathrm{CW}}\end{pmatrix} - \sqrt{2\Gamma}\begin{pmatrix}E_{\mathrm{in},L}\\ E_{\mathrm{in},R}\end{pmatrix}, \tag{1.84}$$

$$\begin{pmatrix}E_{\mathrm{out},R}\\ E_{\mathrm{out},L}\end{pmatrix} = \begin{pmatrix}E_{\mathrm{in},L}\\ E_{\mathrm{in},R}\end{pmatrix} + i\sqrt{2\Gamma}\begin{pmatrix}\alpha_{\mathrm{CCW}}\\ \alpha_{\mathrm{CW}}\end{pmatrix}, \tag{1.85}$$

where Γ is the extrinsic decay rate, and the total loss rate is given by $\gamma_t = \gamma + \Gamma + 2\Gamma_S$. Here, γ represents the intrinsic decay rate due to absorption and scattering losses, while Γ_S denotes the coupling rate between the microring and the S-shaped waveguide. The term β_t is the effective coupling rate from α_{CW} to α_{CCW}. Specifically,

$$\beta_t = 4\Gamma_S e^{i\phi}, \tag{1.86}$$

where ϕ is the phase accumulated by the field as it propagates through the S-shaped waveguide.

The corresponding Hamiltonian for the TMR is

$$H = \begin{pmatrix} \omega_0 - i\gamma_t & -i\beta_t \\ 0 & \omega_0 - i\gamma_t \end{pmatrix}. \tag{1.87}$$

From the Hamiltonian in Eq. 1.87, it is evident that the coupling between the counter-propagating modes is asymmetric, as indicated by the presence of the off-diagonal term. The eigenvalue problem for H yields

$$\lambda_1 = \lambda_2 = \omega_0 - i\gamma_t, \quad v_1 = v_2 = \begin{pmatrix} 1 \\ 0 \end{pmatrix}. \tag{1.88}$$

These results show that the eigenvalues are degenerate while the eigenvectors also coincide, indicating their coalescence. Since $|\langle v_1 | v_2 \rangle| = 1$, the two eigenstates are linearly dependent. The simultaneous degeneracy of eigenvalues and eigenvectors signifies that the system operates at an exceptional point (EP)—a hallmark of non-Hermitian physics. Therefore, the TMR not only exhibits asymmetric (non-Hermitian) coupling between the counter-propagating modes but also inherently resides at an exceptional point under these idealized conditions.

Following the TCMT formulation, the steady-state intracavity field amplitudes for the counter-propagating modes can be expressed as

$$a_{\mathrm{CCW}} = \frac{i\sqrt{2\Gamma}}{-i\Delta\omega + \gamma_t}\,\mathcal{E}_{\mathrm{in},L} - \frac{i\sqrt{2\Gamma}\,\beta_t}{(-i\Delta\omega + \gamma_t)^2}\,\mathcal{E}_{\mathrm{in},R}, \tag{1.89}$$

$$a_{\mathrm{CW}} = \frac{i\sqrt{2\Gamma}}{-i\Delta\omega + \gamma_t}\,\mathcal{E}_{\mathrm{in},R}. \tag{1.90}$$

Using the input–output relations in Eq. 1.85, the corresponding transmission and reflection coefficients can be derived for excitation from both sides of the resonator. The power transmission from left to right (T_{LR}) and from right to left (T_{RL}) are identical and given by

$$T_{LR} = \frac{|\mathcal{E}_{L\to R}|^2}{|\mathcal{E}_{\mathrm{in},L}|^2} = T_{RL} = \frac{|\mathcal{E}_{R\to L}|^2}{|\mathcal{E}_{\mathrm{in},R}|^2} = 1 - \frac{4(\gamma_t - \Gamma)\Gamma}{\Delta\omega^2 + \gamma_t^2}, \tag{1.91}$$

which shows the Lorentzian dependence of the transmission on the frequency detuning $\Delta\omega$.

The reflections at the left and right ports, denoted as R_L and R_R, are

$$R_L = \frac{|\mathcal{E}_{L\to L}|^2}{|\mathcal{E}_{\text{in},L}|^2} = 0, \tag{1.92}$$

$$R_R = \frac{|\mathcal{E}_{R\to R}|^2}{|\mathcal{E}_{\text{in},R}|^2} = \frac{4\Gamma^2|\beta_t|^2}{(\Delta\omega^2 + \gamma_t^2)^2} = \frac{4\Gamma^2(4\Gamma_S)^2 e^{-2\,\text{Im}[\phi]}}{(\Delta\omega^2 + \gamma_t^2)^2}, \tag{1.93}$$

where we used $\beta_t = 4\Gamma_S e^{i\phi}$ and $|\beta_t|^2 = (4\Gamma_S)^2|e^{i\phi}|^2 = (4\Gamma_S)^2 e^{-2\,\text{Im}[\phi]}$, since for a complex phase $\phi = \phi_R + i\phi_I$ one has $|e^{i\phi}|^2 = |e^{i\phi_R}e^{-\phi_I}|^2 = e^{-2\phi_I} = e^{-2\,\text{Im}[\phi]}$.

Equation 1.93 indicates that the right-side reflection arises from the non-Hermitian coupling β_t between the counter-propagating modes and depends exponentially on the imaginary part of the phase ϕ accumulated in the S-shaped feedback waveguide. In contrast, the left reflection R_L vanishes, consistent with the unidirectional nature of coupling in the Taiji configuration.

As shown in Fig. 1.14, the Taiji-coupled microring exhibits asymmetric forward and backward spectral responses under the fitted loss and coupling parameters. A non-zero Taiji coupling ($|\beta_t| = \Gamma$, $\phi_t = 5.897$ rad)- parameters used from the Table 1.1 induce mixing between CW and CCW modes even in the absence of intrinsic backscattering (intentionaly set to) ($\beta_{12} = \beta_{21} = 0$). The system is in a lossy (non-Hermitian) regime, with total loaded decay rate $\gamma_t = \gamma + \Gamma + 2\Gamma_S$, where $\gamma = 4.144$ GHz (intrinsic), $\Gamma = 5.973$ GHz (bus coupling), and $\Gamma_S = 1.000$ GHz (S-waveguide-induced loss). Under these conditions, the transmission dip and the residual reflection are determined by the interference between the driven CW mode and the Taiji-induced coupling into the CCW mode. Unlike the lossless critical-coupling limit, finite intrinsic and coupling-induced losses prevent perfect unidirectional reflection, but still produce clear asymmetry: excitation from the right couples light to the CCW mode through the Taiji branch, producing a measurable reflection, whereas excitation from the left does not induce a reciprocal coupling process. The increased total decay rate compared to a bare microring arises from the embedded S-shaped branch.

1.3.4 Taiji Microring Resonator Experimental Results and Discussion

A TMR resonator was characterized at the operating wavelength $\lambda_0 = 1536.04$ nm by fitting the measured transmission and reflection spectra to the TCMT of Eq. 1.84, adding extra terms on the off–diagonal couplings: an intrinsic contra–directional backscattering β_{12}, an independent counter backscattering β_{21}, and the Taiji S–link coupling β_t. Our

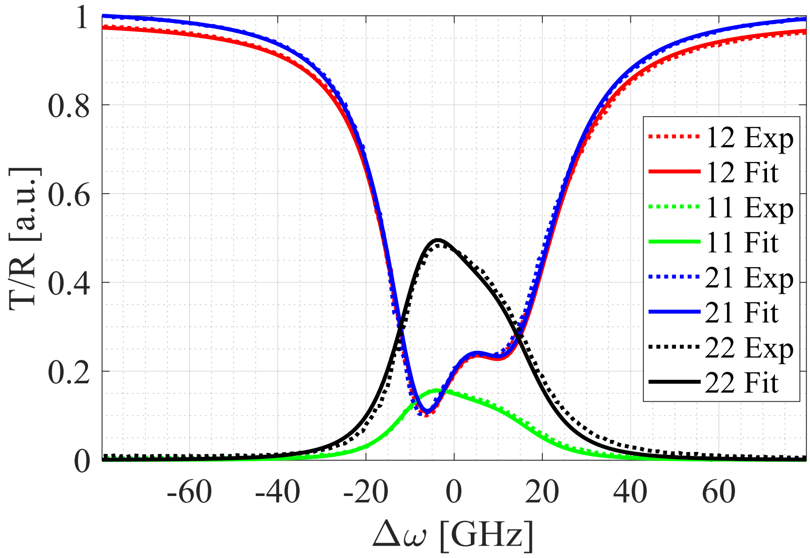

Figure 1.15: **Measured (dotted) and fitted (solid) spectra of the Taiji microring.** Excitation is applied from port 1 and port 2, and the corresponding transmission (12, 21) and reflection (11, 22) responses are shown. The data demonstrate reciprocal transmission and strongly asymmetric reflection, consistent with the fitted model.

choice of phases for the each complex couplings are given in the Table 1.1 which also provides the fit parameters. In our fitting procedures, all four experimental output signals corresponding to each input-output combination were used simultaneously to increase the overall confidence in the fitting. This combined fitting was performed with the parameters allowed to vary freely. The fit was done to the four scattering channels (transmission and reflection from ports 1 and 2), shown in Fig. 1.15, returned the parameters summarized in Table 1.1.

Let us now express the transmission (T) and reflection (R) coefficients corresponding to excitations from ports 1 and 2. As before, the first subscript denotes the excited port, while the subsequent second digit indicates the detected port. $\Delta = D - \omega_0$ and $\gamma_\mathrm{t} = \gamma + \Gamma + 2\Gamma_S$. With the shorthand

$$\mathcal{D}(\Delta) \;=\; \beta_{12}\,(\beta_{21} + \beta_t) + \left(\Delta + i\,\gamma_\mathrm{t}\right)^2,$$

Table 1.1: Extracted Taiji fitting parameters at λ_0 = 1536.04 nm. All coupling and loss parameters are reported in units of GHz, while phases are given both in radians and in multiples of π.

Parameter	**Extracted value**
Backscattering magnitude	$\lvert\beta_{12}\rvert = 8.55 \pm 0.02$ GHz
Backscattering phase	$\phi_{12} = 4.37 \pm 0.02$ rad $(1.39 \pm 0.01)\,\pi$
Counter backscattering magnitude	$\lvert\beta_{21}\rvert = 14.54 \pm 0.03$ GHz
Counter backscattering phase	$\phi_{21} = 4.69 \pm 0.02$ rad $(1.49 \pm 0.01)\,\pi$
Taiji (S–link) coupling magnitude	$\lvert\beta_t\rvert = 1.22 \pm 0.01$ GHz
Taiji (S–link) coupling phase	$\phi_t = 5.90 \pm 0.03$ rad $(1.88 \pm 0.01)\,\pi$
Resonance center	$\omega_0 = 2.89 \pm 0.01$ THz
Total loaded loss	$\gamma_{\mathrm{t}} = 12.12 \pm 0.03$ GHz
Loss partitions	$\Gamma_S = 1.00 \pm 0.01$ GHz $\Gamma = 5.97 \pm 0.02$ GHz $\gamma = 4.14 \pm 0.02$ GHz
Normalization factors	$n_b = 0.99 \pm 0.01$, $n_{b1} = 1.02 \pm 0.01$

the complex amplitudes are then

$$
\begin{aligned}
t_{12}(\Delta) &= \frac{\beta_{12}(\beta_{21}+\beta_t) + \big(\Delta + i\,\gamma_{\mathrm{t}}\big)\big(\Delta - 2i\Gamma + i\,\gamma_{\mathrm{t}}\big)}{\mathcal{D}(\Delta)}, && (1.94)\\
r_{11}(\Delta) &= \frac{-\,2\,\beta_{12}\,\Gamma}{\mathcal{D}(\Delta)}, && (1.95)\\
t_{21}(\Delta) &= \frac{\beta_{12}(\beta_{21}+\beta_t) + \big(\Delta + i\,\gamma_{\mathrm{t}}\big)\big(\Delta - 2i\Gamma + i\,\gamma_{\mathrm{t}}\big)}{\mathcal{D}(\Delta)}, && (1.96)\\
r_{22}(\Delta) &= \frac{-\,2\,(\beta_{21}+\beta_t)\,\Gamma}{\mathcal{D}(\Delta)}. && (1.97)
\end{aligned}
$$

The measured powers with normalizations are

$$
T_{12} = n_b\,|t_{12}|^2, \quad R_{11} = n_b\,|r_{11}|^2, \qquad T_{21} = n_{b1}\,|t_{21}|^2, \quad R_{22} = n_{b1}\,|r_{22}|^2.
$$

Since $t_{12} \equiv t_{21}$ analytically, reciprocity follows immediately:

$$
\boxed{T_{12} = \frac{n_b}{n_{b1}}\,T_{21} \quad \approx \quad T_{21}} \qquad (1.98)
$$

because $n_b \approx n_{b1} \approx 1$.

From the expressions above,

$$
R_{11} \propto |\beta_{12}|^2, \qquad R_{22} \propto |\beta_{21}+\beta_t|^2.
$$

Using the fitted parameters from Table 1.1, we obtain the backscattering magnitudes

$$|\beta_{12}| = 8.55\ \text{GHz}, \qquad |\beta_{21} + \beta_t| = \left| |\beta_{21}|e^{i\phi_{21}} + |\beta_t|e^{i\phi_t} \right| \approx 15.01\ \text{GHz}.$$

we obtain

$$\frac{R_{22}}{R_{11}} \approx \frac{n_{b1}}{n_b}\,\frac{|\beta_{21} + \beta_t|^2}{|\beta_{12}|^2} \approx \frac{1.0220}{0.9948} \times \left(\frac{15.0139}{8.5481}\right)^2 \approx 3.17 > 1,$$

i.e., the model predicts and the data confirm $R_{22} > R_{11}$.

Because the contra-directional coupling channels are complex and not phase-aligned ($\phi_{12} \approx 1.39\pi$, $\phi_{21} \approx 1.49\pi$, $\phi_t \approx 1.88\pi$), the hybrid supermodes formed by the combined interactions $\{\beta_{12}, \beta_{21}, \beta_t\}$ acquire *unequal* effective decay rates. Quantitatively, the port-1–weighted combination entering the 11 pathway has a large effective coupling strength $|\beta_{21} + \beta_t| \approx 15.01$ GHz, whereas the port-2 pathway samples only $|\beta_{12}| \approx 8.55$ GHz.

In the *transmission* spectra, this non-Hermitian modal imbalance produces an *asymmetric resonance doublet*: the dip associated with the more strongly coupled supermode is broader and shallower (superradiant), while its companion mode is narrower and deeper (subradiant). The resulting spectral skewness is *deterministic*, being set by the controlled complex interference among β_{12}, β_{21}, and β_t, and does not rely on fabrication-induced disorder. Meanwhile, the cross-port responses T_{12} and T_{21} remain reciprocal, differing only through the normalization factors n_b and n_{b1}.

The S–link coupling obeys the relation

$$\beta_t = 4\Gamma_S e^{i\phi},$$

from which the S–link coupling rate is extracted as

$$\Gamma_S = \frac{|\beta_t|}{4} \approx 0.30\ \text{GHz}, \qquad \phi \approx \phi_t \approx 1.88\,\pi.$$

Comparing with the dissipative S–link loading from the linewidth partition ($\Gamma_S \approx 1.00$ GHz in $\gamma_\text{t} = \gamma + \Gamma + 2\Gamma_S$), the S–section contributes both *coherent* contra–directional coupling and *dissipative* loading. Tuning the S-path (length or thermo-optic phase) rotates β_t in the complex plane, steering its interference with β_{12} and β_{21} to control the 22/11 contrast and which transmission lobe in the doublet is narrower vs. broader—all while maintaining 12 = 21 reciprocity.

For excitation from port 2, the normalized intracavity modal amplitudes are

$$a_1(\Delta) = i\sqrt{2}\,(\beta_{21} + \beta_t)\sqrt{\Gamma}\,\left[\beta_{12}(\beta_{21} + \beta_t) + (\Delta + i\gamma_t)^2\right]^{-1}, \tag{1.99}$$

$$a_2(\Delta) = -\sqrt{2\Gamma}\,(\Delta + i\gamma_t)\,\left[\beta_{12}(\beta_{21} + \beta_t) + (\Delta + i\gamma_t)^2\right]^{-1}, \tag{1.100}$$

so the total normalized energy in the ring is

$$U(\Delta) \propto |a_1|^2 + |a_2|^2.$$

With detuning $\Delta = D - \omega_0$ and total loaded loss $\gamma_t = \gamma + \Gamma + 2\Gamma_S$, the common denominator of all channels in our model is

$$\mathcal{D}(\Delta) = \beta_{12}\,(\beta_{21} + \beta_t) + (\Delta + i\gamma_t)^2. \tag{1.101}$$

The complex poles of the scattering response are obtained by setting the denominator $\mathcal{D}(\Delta) = 0$, yielding

$$\Delta_\pm \;=\; -i\gamma_t \;\pm\; \sqrt{-\beta_{12}(\beta_{21} + \beta_t)}. \tag{1.102}$$

These poles determine the complex eigenfrequencies of the effective non-Hermitian two-mode system and directly govern the resonance structure observed in transmission and reflection spectra.

An *exceptional point* (EP), characterized by the simultaneous coalescence of eigenvalues *and* eigenvectors, occurs when the square-root term in Eq. (1.102) vanishes, i.e.,

$$\boxed{\beta_{12}(\beta_{21} + \beta_t) = 0} \qquad \Longleftrightarrow \qquad \text{either } \beta_{12} = 0 \text{ or } \beta_{21} + \beta_t = 0. \tag{1.103}$$

At this condition, the two poles collapse into a double root

$$\Delta_{\mathrm{EP}} = -i\gamma_t, \tag{1.104}$$

and the effective 2×2 non-Hermitian Hamiltonian becomes defective, admitting a Jordan normal form rather than a diagonal representation.

At the EP, the characteristic denominator reduces to

$$\mathcal{D}(\Delta) = (\Delta + i\gamma_t)^2. \tag{1.105}$$

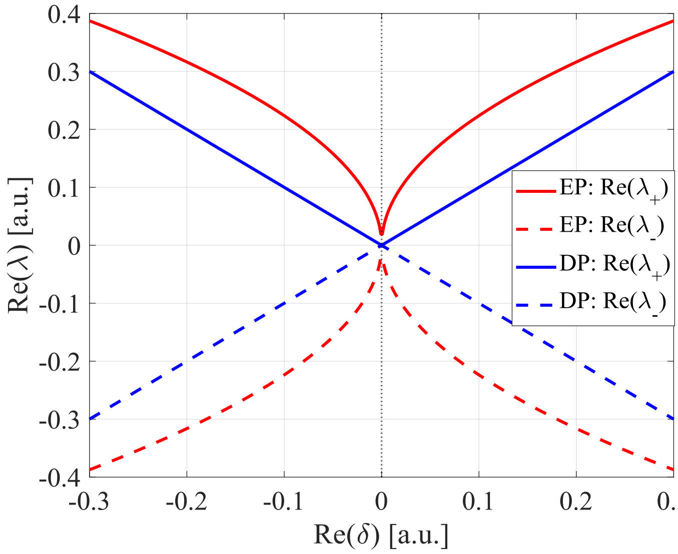

Figure 1.16: Eigenvalue splitting as a function of perturbation strength, comparing exceptional-point (EP) and diabolic-point (DP) regimes. The EP exhibits a square-root response, while the DP shows a linear splitting.

Using the fitted channel expressions,

$$t_{12}(\Delta) = \frac{\beta_{12}(\beta_{21} + \beta_t) + (\Delta + i\gamma_t)(\Delta - 2i\Gamma + i\gamma_t)}{\mathcal{D}(\Delta)}, \tag{1.106}$$

$$r_{11}(\Delta) = \frac{-2\beta_{12}\Gamma}{\mathcal{D}(\Delta)}, \qquad r_{22}(\Delta) = \frac{-2(\beta_{21} + \beta_t)\Gamma}{\mathcal{D}(\Delta)}, \tag{1.107}$$

and imposing the EP condition (1.103), the transmission simplifies to

$$t_{12}^{(\mathrm{EP})}(\Delta) = \frac{(\Delta + i\gamma_t)(\Delta - 2i\Gamma + i\gamma_t)}{(\Delta + i\gamma_t)^2} = 1 - \frac{2i\Gamma}{\Delta + i\gamma_t}. \tag{1.108}$$

Equation (1.108) describes a *single-pole* resonance, demonstrating the complete collapse of the mode doublet at the exceptional point.

The reflection response depends on which coupling channel is nulled:

$$\begin{aligned} \text{EP via } \beta_{12} = 0: \quad & r_{11}^{(\mathrm{EP})} \equiv 0, \qquad r_{22}^{(\mathrm{EP})}(\Delta) = -\frac{2(\beta_{21} + \beta_t)\Gamma}{(\Delta + i\gamma_t)^2}, \\ \text{EP via } \beta_{21} + \beta_t = 0: \quad & r_{22}^{(\mathrm{EP})} \equiv 0, \qquad r_{11}^{(\mathrm{EP})}(\Delta) = -\frac{2\beta_{12}\Gamma}{(\Delta + i\gamma_t)^2}. \end{aligned} \tag{1.109}$$

Thus, at the EP one reflection channel is completely suppressed, while the opposite channel exhibits a second-order pole, reflecting the chiral and direction-dependent nature of the non-Hermitian coupling.

Accordingly, the Taiji spectrum shown in Fig. 1.14 (obtained by setting $\beta_{12} = 0$, $\beta_{21} = 0$, and $\beta_t \neq 0$) corresponds exactly to the first exceptional point. The resonance doublet collapses into a single unsplit dip; the reflection coefficient r_{11} is identically zero, while r_{22} remains finite. This behavior directly signatures eigenvalue and eigenvector coalescence.

The nature of this degeneracy is revealed by perturbing the system away from the EP and comparing it with a diabolic point (DP), as illustrated in Fig. 1.16. In the Taiji platform, a physically relevant perturbation corresponds to a controlled imbalance in the backscattering channels $\beta_{12} = \beta_{\mathrm{Bs},12}$, which we parameterize as hermitian perturbation

$$\beta_{\mathrm{Bs},12} = -\beta^*_{\mathrm{Bs},21} \equiv \delta, \tag{1.110}$$

where δ is taken to be a small real parameter. This form preserves the anti-Hermitian structure of the perturbation and naturally arises from weak, direction-dependent scattering processes.

Introducing the perturbation in Equation (1.102) into the EP condition Equation (1.103), the square-root term in the pole expression (1.102) becomes proportional to δ, yielding

$$\Delta_\pm - \Delta_{\mathrm{EP}} \;\propto\; \sqrt{\delta}. \tag{1.111}$$

As a result, even an infinitesimal perturbation leads to a pronounced splitting of the complex eigenvalues, reflecting the characteristic square-root response of an exceptional point.

By contrast, when the microring is prepared at a diabolic point (DP), where the coupling matrix remains Hermitian and the eigenvectors are orthogonal, the same perturbation produces a linear eigenvalue response,

$$\Delta_\pm - \Delta_{\mathrm{DP}} \;\propto\; \delta. \tag{1.112}$$

This difference shown in Fig. 1.16 between the square-root scaling at the EP and the linear scaling at the DP underlies the enhanced sensitivity and non-trivial topology of exceptional points in non-Hermitian Taiji microring resonators.

In the final chapter, we will show that this same EP behavior is observed experimentally in the dynamically reconfigurable unitary microring resonator (DRUM) by the control of the model coupling externally applied electric power.

1.4 Challenges and Future Directions

A primary obstacle for non-Hermitian (NH) silicon photonics is the absence of native optical gain in silicon. Realizing controlled gain–loss distributions typically requires heterogeneous bonding of III–V materials, erbium- or ytterbium-doped dielectrics, or parametric gain in non-linear waveguides, all of which introduce process complexity, thermal parasitics, and deviations from the ideal linear NH Hamiltonian [8, 21]. Moreover, gain elements inherently bring saturation dynamics, amplified spontaneous emission, thermal drift, and carrier-induced refractive-index changes that distort the target non-Hermitian spectra. Maintaining a stable, bias-controlled PT-symmetric point or exceptional point (EP) in the presence of such non-linearities remains a nontrivial engineering and materials challenge [51]. Future progress therefore hinges on developing CMOS-compatible gain media with lower noise, improved thermal handling, and more predictable small-signal behavior, alongside passive methods for engineering controlled loss that do not compromise device reproducibility.

Noise, stability, and metrology near EPs. Although exceptional points offer enhanced sensitivity, they are simultaneously accompanied by amplified noise, increased susceptibility to fabrication disorder, and linewidth broadening [11, 12]. Thermal fluctuations, free-carrier dispersion, and back-reflections in silicon perturb the delicate balance of gain and loss, shifting EP conditions and generating instability.

Fabrication tolerance and calibration. Precise control of coupling coefficients, waveguide widths, asymmetric scattering, and spatial gain/loss profiles is essential in NH photonic designs. However, nanometer-scale variations in etch depth or gap spacing significantly perturb the intended NH Hamiltonian, causing device-to-device variability and shifts in the exceptional point location [8, 40]. As a result, post-fabrication calibration is unavoidable. Thermal tuning, carrier-injection trimming, and bias-dependent refractive-index tuning are emerging as indispensable tools for restoring PT symmetry or compensating asymmetric loss/gain imbalances [51]. At the circuit level, on-chip reference structures and inverse-design-assisted calibration strategies may become necessary to ensure reproducible NH behavior across wafers.

Most current NH demonstrations involve single resonators, dimers, trimers, or small coupled cavities. Extending NH physics to large-scale circuits—switch meshes, photonic processors, or multi-stage signal-conditioning networks—remains an open challenge. Cascading multiple NH elements introduces nonlocal interactions mediated by thermal effects, carrier diffusion, and back-reflections, complicating the preservation of a designed NH spectrum under feedback. Ensuring that EP-enhanced performance survives within a larger architecture requires circuit topologies that mitigate parasitic resonances and maintain directional biasing. Recent demonstrations of EP-assisted switching and nonreciprocal modulation in silicon indicate promising paths toward NH-enabled photonic fabrics [54], but full-scale integration will require both system-level models and fabrication-tolerant designs.

Chapter 2

Coupled Waveguides - Light Routing with a silicon 3 × 3 waveguide coupler

2.1 Introduction

In free space, an electromagnetic wave expands in three dimensions without constraint, and its intensity decays according to the inverse-square law. In other words, such waves are solutions of Maxwell's equations in media free of charges and current densities. A waveguide, by contrast, is a structure that confines and directs the propagation of electromagnetic waves along a specific path. The field inside a waveguide evolves in discrete propagation modes, which are solutions of the Helmholtz equation under the boundary conditions imposed by the guide's geometry and refractive index contrast. While waves in free space spread isotropically, waveguides restrict and channel this energy, enabling controlled light–matter interactions.

Coupled arrays of integrated waveguides provide a versatile platform to explore and deploy diverse phenomena, including non-Hermitian transport, quantum walks, and photonic neural computation [15, 117–121]. A central challenge in such systems is the deterministic *routing* of optical power among multiple paths. Conventional approaches rely on multimode interferometers (MMIs) [50], directional couplers [64], and ring-based devices [88]. Robustness in these schemes can be further improved through techniques such as adiabatic passage and shortcut-to-adiabaticity protocols [122–124].

For n-port functionality, one strategy is to cascade multiple 2×2 elements; alternatively, one may directly couple n single-mode waveguides [65, 125–127]. Beyond silicon photonics, 3×3 couplers have been investigated in platforms such as lithium niobate ($LiNbO_3$), indium phosphide (InP) MMIs, and related material systems. However, these implementations often lack thermal tunability or target distinct operating regimes, which motivates a dedicated study of silicon-based 3×3 couplers with a comprehensive theory–experiment comparison.

In this chapter, we demonstrate a compact silicon 3×3 waveguide coupler that (i) crosses signals between the outer guides while leaving the central guide essentially unperturbed, (ii) enables nearly *uniform* three-way splitting, and (iii) provides *reconfigurable* routing via a micro-heater over the middle guide. By globally fitting all nine input–output combinations to a coupled-mode model, we retrieve wavelength- and power-dependent coupling and detuning parameters and quantify small fabrication asymmetries.

2.2 Light Routing with a silicon 3 × 3 waveguide coupler

2.2.1 Experimental Samples and Setup

The 3×3 waveguide coupler device as shown in Figure 2.1 is based on 450 nm × 220 nm silicon waveguides embedded in a silica cladding. The input and output ports are provided by grating couplers. These allow coupling only the Transverse Electric (TE) mode. The waveguide cross section is designed to ensure single-mode operation. The device was fabricated in a run at the IMEC/Europractice facility as part of a multi-project wafer program. The coupling region of the device has waveguide lengths of 60 µm and an inter-waveguide gap of 0.25 µm. Note that the gap and length of the coupling region rule the energy exchange that occurs via the evanescent field. In addition, the device is tunable via current injection through a micro-heater positioned above the central waveguide. Alternatively, one can use a p-n junction across the waveguide to achieve a faster tuning. The metal used for the microheater is Titanium Nitride (TiN), which operates as a 345 Ω resistor. The micro-heater is operated with an injected electrical current from 0 mA to 16 mA.

We explore the transmission through the output ports under two distinct conditions: (1) in the absence of electrical current flow through the microheater, where the device is passive, and (2) with an injected electrical current, where the device is active. Measurements are performed using a tunable continuous-wave laser in the 1490–1640 nm range. Optical power is defined at the chip input and calibrated by subtracting fiber-to-chip coupling losses extracted from reference waveguides fabricated on the same chip. The input polarization is adjusted to the TE mode using a fiber polarization controller and confirmed by maximizing the signal. Device temperature is stabilized to within ±0.01°C using a thermoelectric controller. Port-resolved transmission spectra are recorded using calibrated

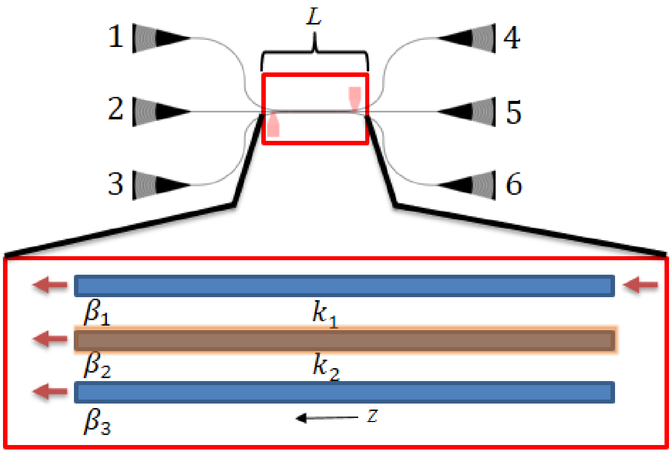

Figure 2.1: **The 3×3 coupler device.** The three grating couplers on the right (triangles labeled 4–6) serve as the input ports, while the three on the left (triangles labeled 1–3) serve as the output ports. These ports are interconnected by a 3×3 directional coupler of length L. The light orange pads denote the electrical contacts used for current injection. The red rectangle highlights the three equally spaced and equal-length coupled waveguides, with a micro-heater (transparent brown layer) fabricated on the central waveguide for thermal tuning.

photodetectors. Coupling parameters and refractive index mismatches are extracted by fitting the measured spectra coupled-mode-theory model. A write-board (Measurement Computing USB-3106) with an amplification stage controls the current applied to the micro-heater. The optical chip is placed on a thermostat holder whose temperature is controlled by a proportional-integral-derivative controller connected to a Peltier cell and a 10kΩ thermistor.

2.3 Theory and Design

We examine a configuration of three coupled waveguides, which are equally spaced and of equal lengths, as shown in Fig 2.1. We employ coupled mode theory (CMT), a method highly effective for characterizing the behavior of weakly coupled three-waveguide directional couplers with a constant coupling coefficient [128, 129]. Additionally, the theory assumes that the external waveguides do not interact with each other due to the exponential decay of their coupling fields.

We aim to establish a general method, as described in [129], to relate the electric field at the waveguides entry at $z = 0$ to the electric field at their exit, at $z = L$, where z represents the propagation direction of the wave and L is the length of the coupling section of the waveguides in the structure, as shown in Fig 2.1. To achieve this, we construct a transformation matrix, T, to show the field propagation in three coupled waveguides in the following way:

$$\mathbf{E}(z = L) = T\mathbf{E}(z = 0)\,. \tag{2.1}$$

Due to the lateral separation between the waveguides, the segments of each waveguide from the grating couplers (numbered pads in Figure 2.1) to the coupling section are assumed to be negligible in influencing light propagation. To obtain T, we begin by defining the coupling matrix M, which encapsulates the interactions within the system using the following set of differential equations [130–132],

$$-i\frac{d\mathbf{E}(z)}{dz} = M\mathbf{E}(z) \tag{2.2}$$

Here, $\mathbf{E}(z)$ is a vector associated with the electric field for each waveguide as a function of propagation distance z, i.e., $\mathbf{E}(z) = [E_1(z); E_2(z); E_3(z)]$. M is the coupling matrix governing the interactions in the coupled system [132],

$$M = \begin{bmatrix} \beta_1 & k_1 & 0 \\ k_1 & \beta_2 & k_2 \\ 0 & k_2 & \beta_3 \end{bmatrix}$$

Where β_n are the propagation constants for each waveguide (from top to bottom: $n = 1, 2, 3$), k_1 is the coupling coefficient between the top and middle waveguides, and k_2 is the coupling coefficient between the middle and bottom waveguides. The coupling coefficients are related to the fields overlap from the waveguides. The couplings between the waveguides are assumed to be Hermitian, and the coefficients are considered to be real and positive.

We then compute the eigenvalues λ_i and the eigenvectors v_i of the M matrix. These calculated eigenvalues λ_i and associated eigenvectors v_i of matrix M form the foundational components for the transformation matrix T. By using the eigenvectors, we construct the modal matrix M_g which is the transpose of the matrix formed by the eigenvectors.

The evolution matrix U is calculated using the expression:

$$U = e^{-iDz}\,, \tag{2.3}$$

where D is the diagonal matrix of the eigenvalues. The exponential term e^{-iDz} represents the evolution of the three supermodes of the system under the influence of the eigenvalues

λ_i over the spatial coordinate z.

Finally, the transformation matrix T takes the following form:

$$T = M_g U M_g^{-1} \,. \tag{2.4}$$

Through the construction of this transformation matrix T, we establish a linear relation that maps the field from the initial position $z = 0$ to the final position $z = L$, thereby providing a systematic approach to calculate the outputs of the fields.

In general, the knowledge of T allows relating any input to any output. In the specific example we are showing in Fig. 2.1, matrix T has a simplified expression. In fact, given the symmetry of the external waveguides, we can assume $\beta_1 = \beta_3$. In addition, we define $\Delta\beta = \beta_2 - \beta_1 = \beta_2 - \beta_3$. Additionally, we account for fabrication errors in the structure, making $\Delta\beta$ an intrinsic property of our static device. Using these definitions, the coupling matrix takes the following form:

$$M_1 = \begin{bmatrix} 0 & k_1 & 0 \\ k_1 & \Delta\beta & k_2 \\ 0 & k_2 & 0 \end{bmatrix} \tag{2.5}$$

It is worth noting that changing the sign of $\Delta\beta$ does not affect the output intensities of the structure. Note that the microheater placed on top of the central waveguide (Fig. 2.1) allows tuning β_2, i. e. $\Delta\beta$.

We then compute the transformation matrix T_1 for matrix M_1 by following the procedure outlined in equations (2.1) to (2.4). Consequently, T_1 takes the following form:

$$T_1 = \begin{bmatrix} a_{41} & a_{51} & a_{61} \\ a_{42} & a_{52} & a_{62} \\ a_{43} & a_{53} & a_{63} \end{bmatrix} , \tag{2.6}$$

where a_{ij} are the complex amplitude coefficients with the first and second index referring to the input and output ports, respectively. The explicit form of T_1 is reported in the appendix. Assuming that there is no loss and the incident light is distributed among the waveguides, the following conditions hold true for each column of matrix T_1:

$$|a_{i1}|^2 + |a_{i2}|^2 + |a_{i3}|^2 = 1 \,,$$

where $i = 4, 5, 6$ refer to each input port. This is the equation of a sphere in a 3-dimensional space defined by a_{i1}, a_{i2}, and a_{i3}. Thus, we have many solutions for the values of a_{i1}, a_{i2}, and a_{i3} that represent the points on the surface of this sphere. The specific solutions or points on the sphere depend on how a_{i1}, a_{i2}, and a_{i3} are functionally related to k_1, k_2, and $\Delta\beta$. These parameters are real in our model.

Now, let us analyze a simple symmetric scenario when light is injected in port 4. We set $\Delta\beta = 0$ and $k_1 = k_2 = k$ (three perfectly equal waveguides with the same gap between adjacent waveguides). If we want to achieve a complete transfer of the input signal from port 4 to port 3, we have to tune the 3×3 coupler parameters such that:

$$|a_{41}(L)|^2 = |a_{42}(L)|^2 = 0\,, \quad |a_{43}(L)|^2 = 1\,. \tag{2.7}$$

This condition is met for discrete values of the coupling coefficient k given by:

$$k_m := (2m-1)\,\frac{\pi}{\sqrt{2}L}, \quad \text{where } m = 1, 2, 3, \ldots \tag{2.8}$$

Figure 2.2 illustrates the outputs for ports 1, 2, and 3 when the input signal is injected into ports 4 (gray color scale) or 5 (cool scale) or 6 (autumn scale) as a function of the coupling $k_2 = k_1 = k$ value ranging from 0 to $\frac{\pi}{\sqrt{2}L}$ at $z = L = 60\,\mu$m. We can represent the outputs as a point laying on a sphere, where the axis of the sphere are nothing else than the field mode intensities in each output waveguides. Consequently, the points representing different combinations of input to outputs, normalized and summed to unity following the energy conservation, form a surface on a unit sphere. Notice that, when the coupling between the waveguides is equal to zero ($k = 0$, darker hues), the light remains in the same waveguide. Consequently, $|a_{41}| = 1$, $|a_{52}| = 1$ and $|a_{63}| = 1$ (left, top and right corners of the eighth of the sphere).

In Fig. 2.2 (c), it is observed that when the system is excited from port 4, with increasing k, the light passes from the top waveguide to the middle waveguide, fully reaching the bottom one at $k = \frac{\pi}{\sqrt{2}L}$ (from left to top corners of the sphere in Figure 2.2 (a)). Due to the symmetry of the structure, the line corresponding to the excitation from port 6 is similar to the one corresponding to the excitation from port 4, and so the output field starts from the top corner and reaches the left corner of the sphere, see autumn color scale line in Figure 2.2. On the other hand, as shown in Fig. 2.2(d), when light is fed from port 5 (middle waveguide), increasing k, the electromagnetic wave passes symmetrically from the middle waveguide to the external (top and bottom) waveguides reaching the combination $(|a_{i1}|^2, |a_{i2}|^2, |a_{i3}|^2) = (0.5, 0, 0.5)$ at $k = \frac{\pi}{2\sqrt{2}L}$. As can be seen from the cool color scale curve in Figure 2.2, after this point the light gradually returns to the

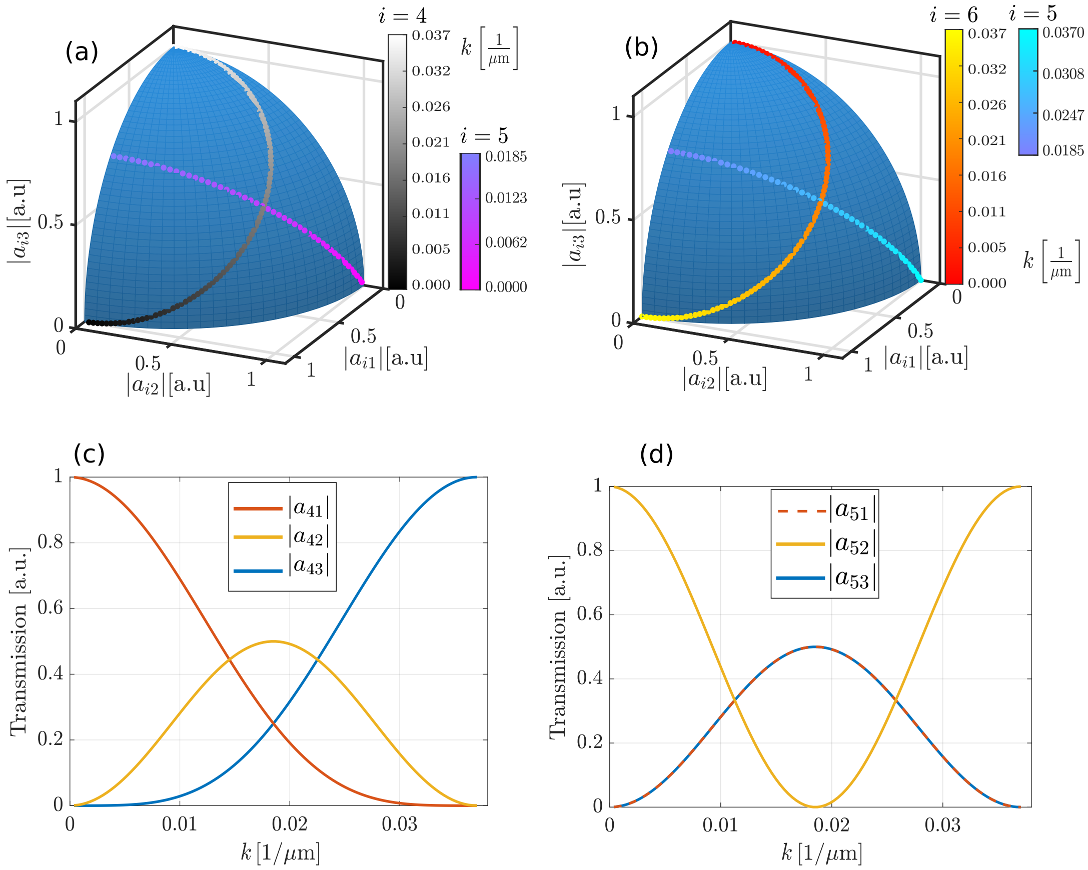

Figure 2.2: **Theory.** Three dimensional visualization of the output combinations of the structure for a single excitation from ports $i = 4, 5, 6$ as a function of the coupling parameter $k = k_1 = k_2$, ranging from 0 to $k = \frac{\pi}{\sqrt{2}L}$, where $L = 60\,\mu$m. Panel (a) shows the outputs for excitation from port $i = 4$ (gray scale color), varying from $k = 0$ to $k = \frac{\pi}{\sqrt{2}L}$, along with the excitation from port $i = 5$ (violet scale color) for k ranging from 0 to $k = \frac{\pi}{2\sqrt{2}L}$. Panel (b) shows the output for excitation from port $i = 6$ (cyan scale color), varying from $k = 0$ to $k = \frac{\pi}{\sqrt{2}L}$, along with the excitation from port $i = 5$ (violet scale color) for k ranging from $k = \frac{\pi}{2\sqrt{2}L}$ to $k = \frac{\pi}{\sqrt{2}L}$. Panels (c) and (d) show the transmission outputs for excitation from ports 4 and 5, respectively. Note: the output combinations for excitation from port 6 can be inferred from panel (c) by replacing $|a_{43}|$ with $|a_{61}|$, $|a_{42}|$ with $|a_{62}|$ and $|a_{41}|$ with $|a_{63}|$

.

central waveguide, exiting from port 2 for $k = \frac{\pi}{\sqrt{2}L}$. Note also that in this figure the lines corresponding to the excitation from port 6 and the second half of the excitation from port 5 have been plotted in panel (b) to give a clearer picture.

It is worth noting that Figure 2.2 shows a very specific case, where the structure is symmetric and $\Delta\beta = 0$ (three equal waveguides). However, the solutions presented here are general and can be used in cases where the structure is asymmetric and the waveguides are different.

We report here the analytical functions derived from the matrix M_1 used in Eq. (2.5). These functions are the elements of the transformation matrix T_1 mentioned in Eq. (2.6): Let us define $\alpha = \sqrt{\Delta\beta^2 + 4(k_1^2 + k_2^2)}$ for simplification.

$$a_{41} = \frac{1}{2(k_1^2 + k_2^2)\alpha}\left[e^{-\frac{1}{2}i(\Delta\beta+\alpha)z}\left(\Delta\beta k_1^2(-1 + e^{i\alpha z}) + (k_1^2 + e^{i\alpha z}k_1^2 + 2e^{\frac{1}{2}i\alpha z}k_2^2)\alpha\right)\right], \quad (2.9)$$

$$a_{42} = -\frac{2ie^{-\frac{1}{2}i\Delta\beta z}k_1 \sin\left(\frac{1}{2}\alpha z\right)}{\alpha}, \quad (2.10)$$

$$a_{43} = \frac{1}{2(k_1^2 + k_2^2)\alpha}\left[e^{-\frac{1}{2}i(\Delta\beta+\alpha)z}k_1k_2\left(\Delta\beta(-1 + e^{i\alpha z}) + (1 - 2e^{\frac{1}{2}i(\Delta\beta+\alpha)z} + e^{i\alpha z})\alpha\right)\right], \quad (2.11)$$

$$a_{51} = -\frac{2ie^{-\frac{1}{2}i\Delta\beta z}k_1 \sin\left(\frac{1}{2}\alpha z\right)}{\alpha}, \quad (2.12)$$

$$a_{52} = e^{-\frac{1}{2}i\Delta\beta z}\left(\cos\left(\frac{1}{2}\alpha z\right) - \frac{i\Delta\beta \sin\left(\frac{1}{2}\alpha z\right)}{\alpha}\right), \quad (2.13)$$

$$a_{53} = -\frac{2ie^{-\frac{1}{2}i\Delta\beta z}k_2 \sin\left(\frac{1}{2}\alpha z\right)}{\alpha}, \tag{2.14}$$

$$a_{61} = \frac{1}{2(k_1^2 + k_2^2)\alpha}\left[e^{-\frac{1}{2}i(\Delta\beta+\alpha)z}k_1 k_2\left(\Delta\beta(-1 + e^{i\alpha z}) + (1 + e^{i\alpha z} - 2e^{-\frac{1}{2}i(\Delta\beta+\alpha)z})\alpha\right)\right], \tag{2.15}$$

$$a_{62} = -\frac{2ie^{-\frac{1}{2}i\Delta\beta z}k_2 \sin\left(\frac{1}{2}\alpha z\right)}{\alpha}, \tag{2.16}$$

$$a_{63} = \frac{1}{2(k_1^2 + k_2^2)\alpha}\left[e^{-\frac{1}{2}i(\Delta\beta+\alpha)z}\left(\Delta\beta k_2^2(-1 + e^{i\alpha z}) + (k_2^2 + e^{i\alpha z}k_2^2 + 2k_2^2 k_1^2 e^{\frac{1}{2}i(\Delta\beta+\alpha)z})\alpha\right)\right], \tag{2.17}$$

The transformation matrix T takes a simple form when the coupling is symmetric ($k_1 = k_2 = k$) and detuning is zero ($\Delta\beta = 0$):

$$T = \begin{pmatrix} \cos^2\left(\frac{kz}{\sqrt{2}}\right) & -\frac{i\sin\left(\sqrt{2}kz\right)}{\sqrt{2}} & -\sin^2\left(\frac{kz}{\sqrt{2}}\right) \\ -\frac{i\sin\left(\sqrt{2}kz\right)}{\sqrt{2}} & \cos\left(\sqrt{2}kz\right) & -\frac{i\sin\left(\sqrt{2}kz\right)}{\sqrt{2}} \\ -\sin^2\left(\frac{kz}{\sqrt{2}}\right) & -\frac{i\sin\left(\sqrt{2}kz\right)}{\sqrt{2}} & \cos^2\left(\frac{kz}{\sqrt{2}}\right) \end{pmatrix} \tag{2.18}$$

2.3.1 Results and Discussion

Figure 2.3 shows the experimental results and fitting parameters obtained using the theoretical model for an input signal at ports 4, 5, and 6. Panels (a) through (c) show the output transmission at the different output ports as a function of input wavelength and their fit when there is no electrical current applied to the micro-heater. In our fitting procedures, all nine experimental output signals corresponding to each input-output combination were used simultaneously to increase the overall confidence in the fitting. This combined fitting was performed with the parameters allowed to vary freely. For the device with no current applied, the sum of the normalized Squared Residuals (SSR) with respect to the model was found to be $SSR = 1.1 \times 10^{-5}$, while when current is applied, $SSR = 5.3 \times 10^{-3}$. During the fitting, the experimental data were normalized to the sum of the transmissions at the output ports for each input. Therefore, an SSR much smaller than 1 means a very good agreement between the model and the measured data. Since the designed structure is composed of three equal waveguides with the same gap, we simplify the general equation using the assumption $\Delta\beta = \beta_2 - \beta_1 = \beta_2 - \beta_3$. In addition, we allow for $k_1 \neq k_2$ to account for fabrication errors. The extracted parameters are illustrated in Panel (d). We observe that the coupling coefficients k_1 and k_2, although slightly different, increase with increasing wavelengths.

This is particularly noticeable at longer wavelengths. This phenomenon can be attributed to the enhanced mode spreading within the waveguides. Since the mode confinement in each waveguide decreases for longer wavelengths, there is a greater extent of mode overlap across the waveguides, facilitating stronger coupling.

Despite the structures being designed to exhibit identical coupling between the waveguides, we observed a slight difference between the extracted k_1 and k_2. This suggests the presence of imperfections arising from the fabrication processes and results in a nonzero $\Delta\beta$ term. Note that $\Delta\beta \simeq 0.05$ $1/\mu$m is easily explained by fabrication errors. In fact, it corresponds to a change in waveguide width of about 7 nm (see Fig. 2.6. This value is in agreement with the value of the standard deviation of the waveguide width declared by IMEC. Additionally, the observed decrease in $\Delta\beta$ as a function of increasing wavelength is coherent with the relationship $\Delta\beta = \frac{2\pi}{\lambda}(n_{\text{eff},2} - n_{\text{eff},1})$, where $n_{\text{eff},i}$ is the effective refractive index of the waveguide number i and λ is the wavelength. As shown in Panels (a)-(d) of Fig. 2.3, changing the wavelength changes the parameters of the structure. This gives rise to a variation of the ratio between the intensities at the output ports.

Let us now focus on two specific situations highlighted by the colored boxes in Fig. 2.3. The first case is represented by the gray box at $\lambda = 1560$ nm and corresponds to $\Delta\beta \simeq 0.029 \pm 1.56 \times 10^{-5}$ $1/\mu$m, $k_1 = 0.022 \pm 5.25 \times 10^{-6}$ $1/\mu$m, and $k_2 = 0.021 \pm 5.67 \times 10^{-6}$ $1/\mu$m. By injecting light into any of the input ports (4, 5, 6), the intensities at the output ports (1, 2, 3) are almost equal, indicating that the optical power is equally split among the output channels, as shown in Panels (a)-(c). This equal distribution of optical power demonstrates the symmetric behavior of the system at this specific wavelength, where each output port receives approximately one-third of the input power, ensuring balanced operation.

In contrast, for the second case at $\lambda = 1637$ nm, the power distribution exhibits selective routing behavior. When light is injected into port 4, the signal is routed to port 3, as shown

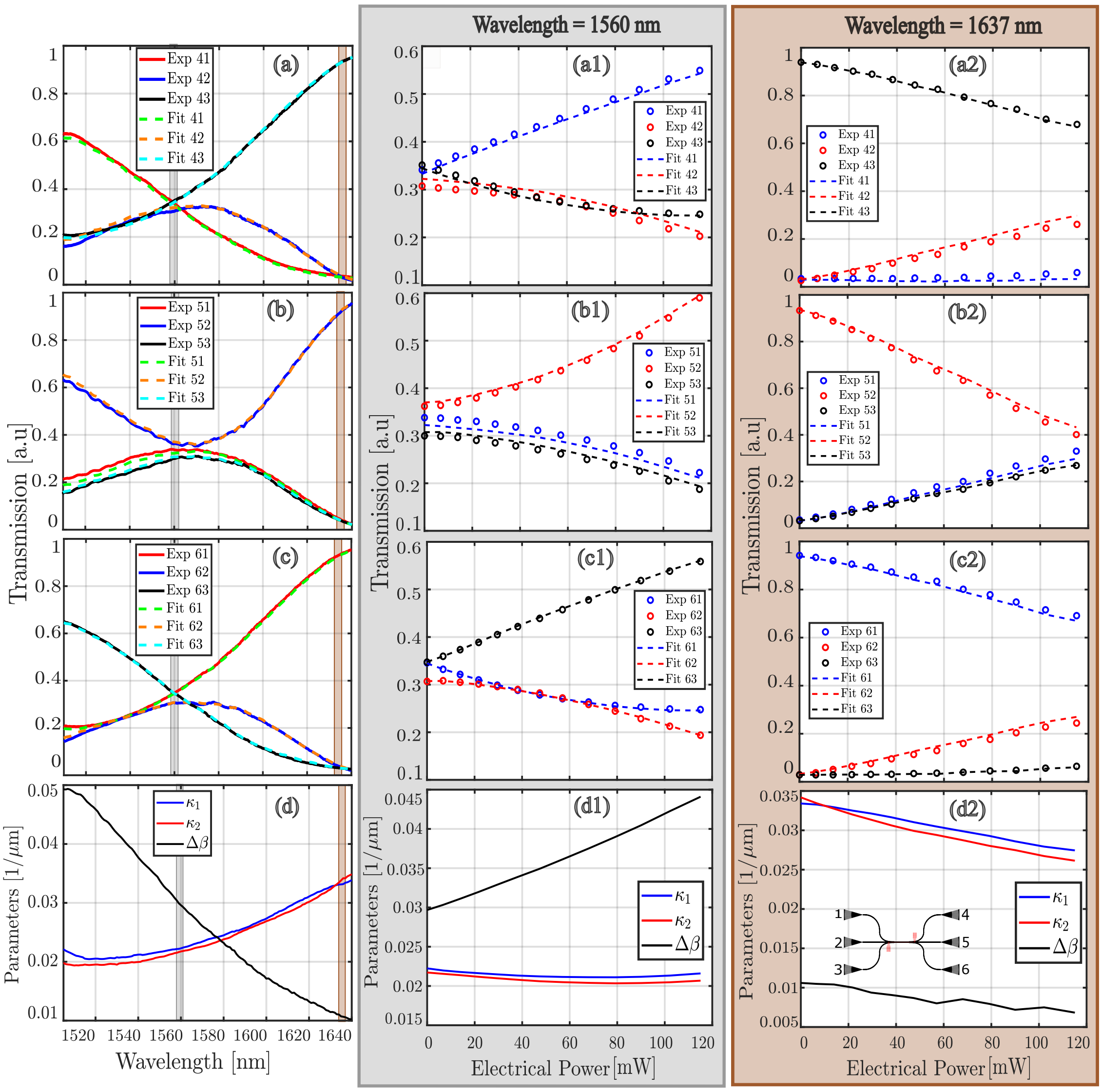

Figure 2.3: **Experimental Results and Extracted Parameters.** Panels (a) to (c) show the measured transmission spectra (solid lines) and fit (dashed lines) for single excitation from ports 4, 5, and 6, respectively. Panel (d) provides the values of k_1, k_2, and $\Delta\beta$ extracted from the fit for a passive device (no electrical power applied). Panels (a1) to (c1) [Panels (a2) to (c2)] depict the measured (empty circles) and fit (dashed lines) output intensities at λ = 1560 nm [λ = 1637 nm], as indicated with a grey [brown] bar in the top Panels, as a function of the power delivered to the micro-heater. Panels (d1) and (d2) display variations in k_1, k_2, and $\Delta\beta$ extracted from the fit as a function of the power delivered to the micro-heater. The numbering in the legend: the first number refers to the input port and the second to the output port.

in Panel (a), while the intensities at ports 1 and 2 approach zero . Similarly, injecting light into port 5 routes the signal to port 2, with the output at the ports 1 and 3 reduced to nearly zero, as depicted in Panel (b). When light is injected into port 6, the signal is directed to port 1, with output at ports 2 and 3 simultaneously approaching zero, as illustrated in Panel (c). This selective routing indicates that at $\lambda = 1637$ nm, the system preferentially directs power to specific output ports based on the input port used, enabling cross-routing between the external waveguides.

Starting from these initial states, as we increase the electrical power delivered to the micro-heater, the parameters of the system are altered, leading to a redistribution of the output field ratios, as illustrated in Panels (a1)-(d1) and (a2)-(d2). Panel (a1) demonstrates that at an electrical power of 115.08 mW, the intensity at port 1 reaches 55%, while port 2 settles at 20% and port 3 decreases to 25% . When light is injected from port 5, as shown in Panel (b1) with an electrical power of 115.08 mW, port 2 now has the output value of 60%, while ports 1 and 3 are reduced to values around 20%. Similarly, in Panel (c1), we observe behavior akin to that in Panel (a1): when light is initially coupled to one of the external waveguides, more light remains in the same waveguide, while less light couples to the others as the electrical power is increased. This is due to the design symmetry. Note that the experimental points in the graphs are well-fitted by the theoretical model (dashed lines). The extracted parameters from the fit are shown in Panel (d1). Notice that $\Delta\beta$ increases to 0.045 $1/\mu$m from 0.030 $1/\mu$m with the application of approximately 115 mW of electrical power. Since the micro-heater is positioned over the central waveguide, this is expected because the increase of $\Delta\beta$ means a faster increase of the effective refractive index of the central waveguide with respect to that of the external waveguides. Additionally, at 1560 nm, the coupling coefficients k_1 and k_2 remain almost constant as a function of the electrical power. This stability is attributed to the high confinement of the optical mode within the waveguide at this particular wavelength, which remains relatively stable despite the temperature changes induced by the micro-heater. Panels (a2)-(d2) of Fig. 2.3 show the results at $\lambda = 1637$ nm. At this wavelength, when the light enters from port 4 exits almost entirely through port 3, the light from port 5 exits through port 2, and the light from port 6 exits through port 1 (see Panels (a), (b), and (c)). In essence, light traverses (crosses) between the external waveguides while remaining confined within the middle waveguide. However, when the micro-heater is activated, the light distribution at the output ports changes for the same input. As a result, some of the light that previously exited through one of the external waveguides (port 1 or port 3) is now routed through the middle waveguide and exits at port 2. Additionally, only a very small percentage of the input light exits from the same waveguide (i.e., output port 1 (3) for input port 4 (6)) as illustrated in Panels (a2) and (c2). In fact, for these two cases, the observed distribution of light at the output ports is 70% , 25% and 5% at 115 mW of electrical power. On the other hand, when the light is injected into the middle waveguide (port 5), some of the light that previously exited through the same waveguide (port 2) is equally routed through the external waveguides and exits at port 1 and port 3 (see Panels (b2)). The observed distribution of light at the output ports is 40%, 30% and 30% at 115 mW of electrical power.

Panel (d2) shows the parameters extrapolated from the fit for $\lambda = 1637$ nm. Here we see that at longer wavelength, both k_1 and k_2 values exhibit a decrease as the electrical power increases. This trend is not observed at $\lambda = 1560$ nm (see Panel (d1)). This can be explained by the fact that, at longer wavelengths, the light confinement inside the waveguide is lower and consequently the coupling coefficients are more sensitive to the variation of the effective refractive index of the waveguide. Panel (d1) shows an increasing $\Delta\beta$ as a function of the injected electrical power, while Panel (d2) shows a decreasing behavior. The behavior of $\Delta\beta$ in Panel (d1) could be explained by the fact that β decreases as a function of wavelength (making the $\Delta\beta$ variation less pronounced), and by the fact that the optical mode of the waveguide is less confined and therefore less affected by local temperature variations. On the contrary, the slight decrease of $\Delta\beta$ as a function of power in Panel (d2) cannot be explained in this way. This behavior may be due to either an imperfect noisy fit or to the fact that coupled mode theory is valid for small couplings and well-confined waveguide modes. In the present case, where the coupling is high and the confinement of the light is low, the parameters obtained are not directly related to those of the ideal case.

In Fig. 2.4 Panel (a), the output intensities are shown for signal input at ports 4, 5, and 6. Output intensities are normalized and mapped onto the surface of a sphere as a function of wavelengths and injected electrical power. The various colors, as shown in the color bars, represent an increase in wavelength, while the size of the dots, from smaller to bigger, indicates the increase of the injected electrical power. The distribution of points on the sphere surface illustrates the range of output combinations achievable by the system.

From a fit of the experimental data, the characteristic device parameters are extracted. Figure 2.4 (b) shows a wavelength dependent $\Delta\beta$ value increase with rising injected electrical power. Furthermore, Fig. 2.4 Panel (c) reveals that at injected electrical power lower than 60 mW, as the wavelength increases, the coupling constant values —though slightly different— are consistently increasing. However, at higher injected power levels, not only the difference between k_1 and k_2 widens for lower wavelengths, but also k_1 and k_2 decrease before rising again with further increases in wavelength. This unexpected increase of the coupling coefficients at short wavelengths as the injected power increases

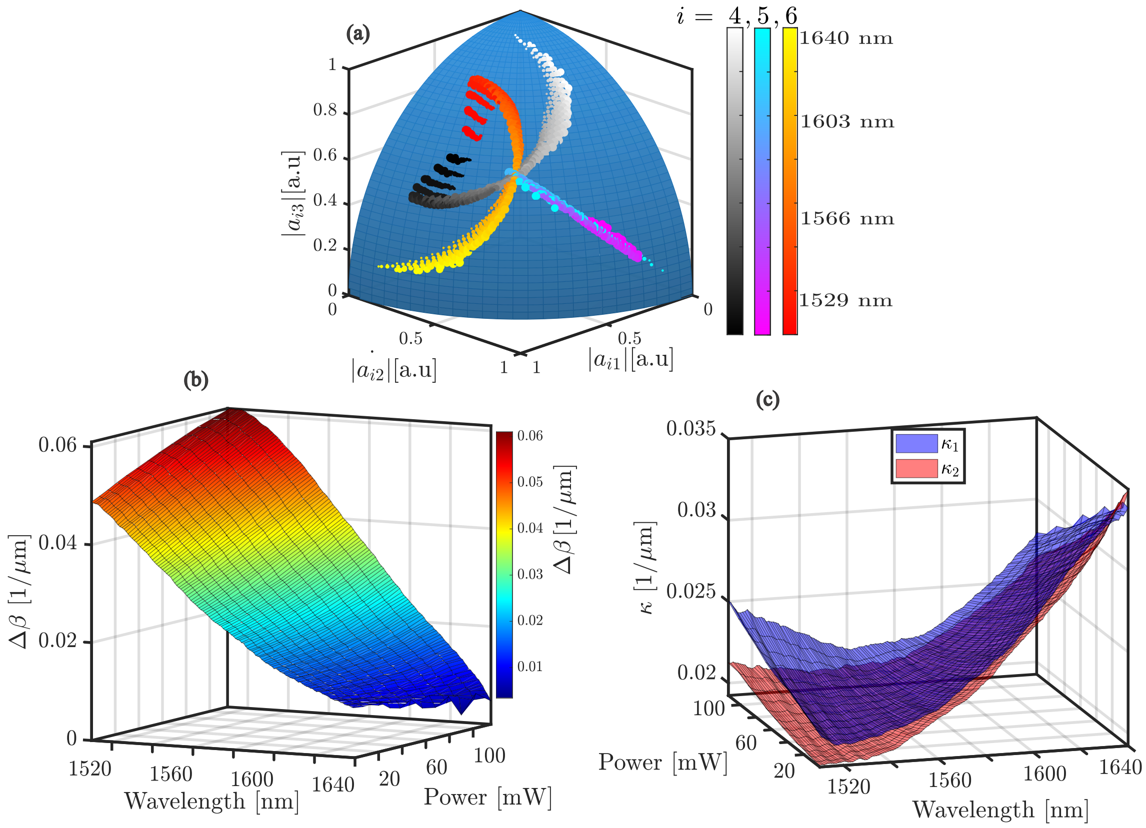

Figure 2.4: **Representations on a Sphere and Extracted Parameters.** Panel (a) displays the experimental outputs for combinations 4, 5, and 6, mapped onto the surface of a sphere as a function of increasing wavelength values and injected electrical power from smaller to larger dots. Panels (b) and (c) present the extracted $\Delta\beta$ values and coupling coefficients, respectively, derived from simultaneous fits of the output signals.

could be due to the simplified model used to fit the data. In fact, we have assumed that $\beta_1 = \beta_3$ and that the micro-heater is symmetrically positioned on top of the central waveguide. However, as can be observed from Figures 2.3 (d) and 2.4 (c), at lower wavelength we detect an asymmetry in the structure. This asymmetry is more relevant at shorter wavelengths because the optical mode is more confined and thus more sensitive to local perturbations. For these reasons, at shorter wavelengths, the fabrication errors e.g., in the symmetry of the waveguides and position of the micro-heater) and the simplified model make the parameters obtained from the fit less physically meaningful.

2.3.2 Optical Power Loss

To evaluate the impact of power loss as a result of microheater heating when electrical power is applied, we measured the sums of the transmitted signals from the three outputs (41+42+43, 51+52+53, and 61+62+63) and normalized them to their values at zero applied electrical power. Figure 2.5 (a) illustrates how these sums evolve for 1560 nm, when changing the applied electrical power. As depicted, random variations of about 3.3 % are observed. These variations are attributed to several factors: (i) mechanical relaxation of the fiber holders during repeated measurements as the current increased from 0 to 16 mA, (ii) random fluctuations due to noise, and (iii) variations of the Fabry-Perot (FP) oscillations resulting from reflections at the waveguide ends. This FP interference is shown in the broad spectral sum transmissions shown in Figure 2.5 (b) whose overall lineshape reflects the grating transmission. At longer wavelengths, the signal-to-noise ratio is lower, and the FP fringes are more prominent compared to shorter wavelengths. The propagation losses are estimated to be approximately 2 dB cm^{-1} at 1550 nm, according to the foundry data. Given the short length of the 3×3 coupler waveguides (about 310 µm), the device losses are negligible. We also observed a grating insertion loss of less than 3 dB.

2.4 Conclusion

In this chapter, we investigated, both theoretically and experimentally, a 3×3 waveguide coupler device capable of routing light signals between three input ports (4, 5, 6) and three output ports (1, 2, 3) in various configurations. For a specific coupling condition or wavelength, we demonstrated that the device can cross the signals between the external waveguides — that is, from input port 4 to output port 3 and from input port 6 to output port 1 — while allowing the central waveguide signal to pass through. Additionally, the device supports other routing functionalities, such as a balanced split of one input into all

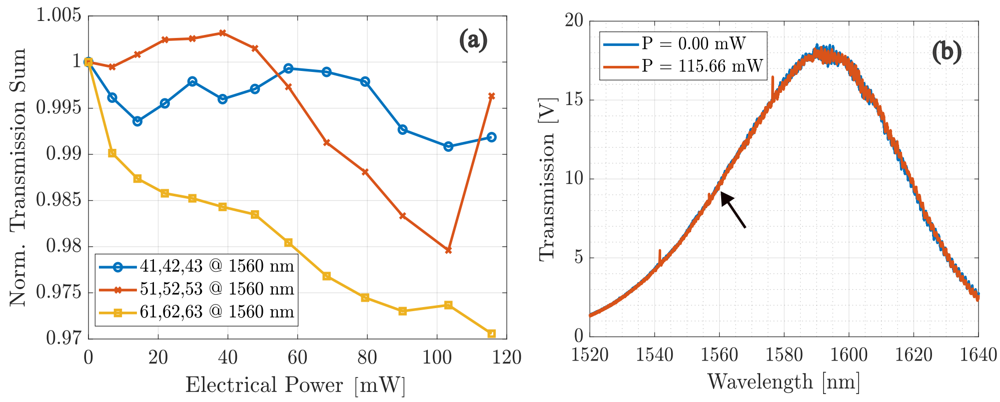

Figure 2.5: **Thermal tuning response of the 3×3 coupler.** (a) Sum of the three output powers (41+42+43, 51+52+53, and 61+62+63), each normalized to its value at zero electrical power, plotted as a function of the microheater power for λ = 1560 nm. (b) Measured spectrum of 51+52+53 for two heater powers, P = 0 mW and P = 115.19 mW. The arrow indicates the wavelength used in panel (a).

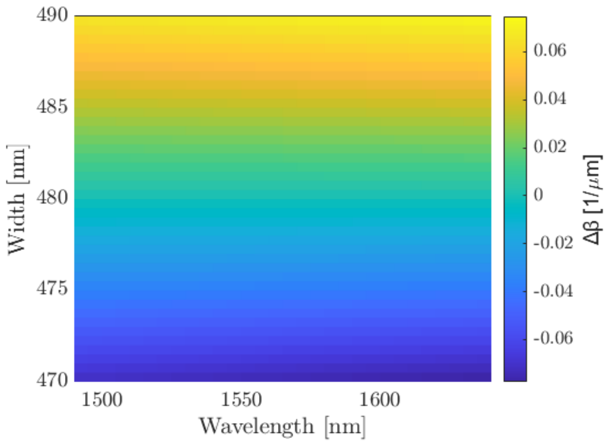

Figure 2.6: Simulation results showing the variation of $\Delta\beta$ (the propagation constant difference) as a function of waveguide width and operating wavelength.

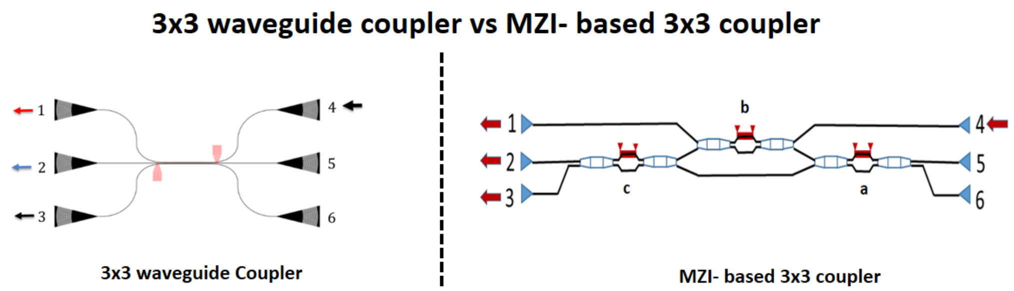

Device	3x3 waveguide Coupler	MZI- based 3x3 coupler
Footprint (Area)	320 μm^2 (35 times smaller)	11400 μm^2
Power Consumption	115 mW for cross routing	279 mW for cross routing
Scalability	Easier to scale due to one heater	Difficult due to cascading MZI stages

Figure 2.7: Comparison between the proposed 3×3 coupler and a Mach–Zehnder Interferometer (MZI)-based 3×3 coupler.

three output ports (1, 2, 3), provided an appropriate choice of coupling values or operating wavelength is made.

When a micro-heater atop the central waveguide is activated, it thermally modifies the propagation constant of the central waveguide, inducing an effective modal index mismatch with the external waveguides and dynamically altering the coupling coefficients. This enables reversible re-routing of optical signals among different output ports. Through our theoretical model, we extracted the key device parameters (coupling coefficients and propagation constants) as functions of both the injected electrical power and the signal wavelength, providing a complete parameter map for the routing behaviors achievable in the 3×3 coupler.

To assess the impact of thermal tuning on device loss, we analyzed the sums of the transmitted optical powers from the three outputs under applied heating and normalized them to the unheated case. Across the tuning range, the total transmission remained stable within fluctuations of approximately 3.3%, originating primarily from mechanical relaxation during repeated measurements, noise-induced variations, and Fabry–Perot oscillations at the chip facets. Foundry specifications estimate propagation losses at $2\,\mathrm{dB\,cm^{-1}}$ near 1550 nm; given the short length of the device (~310 µm), these losses are negligible. The measured grating insertion loss remained below 3 dB, confirming that the routing performance is preserved without significant loss penalty under thermal actuation.

Comparable functionalities can also be realized with multi-mode interferometers or Mach–Zehnder interferometers. However, the 3×3 coupler offers a compact footprint, simple design, and excellent tunability, making it especially promising for integration into more complex photonic circuits such as photonic neural networks or quantum interference architectures. Furthermore, because three coupled waveguides constitute a three-level system, the same platform may serve future applications in quantum photonics using path-encoded qutrit states [133].

Chapter 3

Optical Non-Linear Control in Microring Resonators - Investigation of Self Pulsing in p-n Mircoring Resonators

3.1 Introduction

Silicon microring resonators (MRRs) are foundational building blocks in integrated photonics, offering compact footprints, CMOS-compatible fabrication, and strong scalability for applications ranging from optical interconnects and wavelength-division multiplexing to sensing and all-optical signal processing [40, 55, 134, 135]. Implemented on silicon-on-insulator (SOI) platforms, MRRs benefit from the large refractive-index contrast between silicon and silica, which enables tight optical confinement and high quality factors. These properties make microrings highly effective for wavelength-selective filtering, modulation, and enhancing light–matter interactions in non-linear regimes [136, 137].

At high optical intracavity intensities, silicon MRRs exhibit pronounced non-linear behaviour because absorption and refractive-index changes occur simultaneously and on different time scales. In particular, self-pulsing (SP) emerges when the coupled dynamics of two-photon absorption (TPA), free-carrier generation, free-carrier dispersion (FCD), free-carrier absorption (FCA), and thermo-optic (TO) resonance shifting form a delayed non-linear feedback loop that destabilizes the steady state [38, 84, 138]. TPA generates electron–hole pairs, modifying the refractive index through plasma dispersion (FCD) [84] and introducing additional loss through FCA, while the associated absorption also heats the resonator, shifting the resonance via the thermo-optic coefficient of silicon [138, 139]. Because carriers typically evolve on nanosecond time scales and thermal relaxation occurs more slowly, the competition between these mechanisms can drive sustained limit-cycle oscillations in the transmitted power without any external modulation [38, 140]. Such self-generated oscillations provide a compact route to on-chip microwave-to-radiofrequency tone generation and non-linear signal processing, leveraging the intrinsic dynamics of the cavity rather than external electronic drivers [141].

A particularly powerful approach to control these nonlinear dynamics is to embed a p–n junction—consisting of p-type and n-type doped regions separated by an intrinsic silicon region—into the microring resonator. Electrical biasing of this junction modifies the carrier dynamics by either injecting carriers under forward bias or sweeping them out under reverse bias, thereby altering both the free-carrier–induced loss and the effective carrier lifetime that sets the fast timescale of the nonlinear feedback [21, 49]. Such electrical control enables direct tuning of carrier recombination and extraction processes, which are otherwise fixed by material properties and device geometry

While self-pulsing has been extensively studied in passive silicon microring resonators driven by the interplay of thermo-optic and free-carrier nonlinearities [38, 56], systematic experimental demonstrations of electrically enhanced, high-frequency self-pulsing under reverse-bias operation remain comparatively limited. In particular, key questions remain open regarding the attainable oscillation frequency range and the quantitative relationship between applied bias voltage, effective free-carrier lifetime, and the resulting nonlinear dynamical response in practical p-n-integrated microring geometries [21].

To date, self-pulsing under reverse-bias conditions has been reported only in a small number of experimental works. Notably, Shetewy *et al.* demonstrated self-pulsing in a p-n-integrated silicon microring resonator, observing oscillation frequencies up to $\sim$ 30 MHz under relatively small reverse-bias voltages (1–100 mV) [142]. Earlier characterization of the same platform reported self-pulsing frequencies up to $\sim$ 20 MHz under similar operating conditions [143]. Other diode-integrated microring studies, including those by Morichetti *et al.* and Guha *et al.*, employed reverse bias primarily for carrier extraction or photodetection; although thermo-optic relaxation oscillations in the kHz–MHz range were observed, high-frequency free-carrier-driven self-pulsing comparable to the Shetewy results was not reported [144, 145]. Complementing these experimental efforts, Hamerly *et al.* provided a theoretical analysis indicating that reverse bias can reduce the free-carrier lifetime sufficiently to enable carrier-driven oscillatory instabilities, although no experimental self-pulsing data were presented [146]. The studied literature indicates that the highest experimentally verified self-pulsing frequency under reverse bias to date is on the order of $\sim$ 30 MHz, and a systematic exploration of self-pulsing scaling at larger reverse-bias voltages remains absent.

In this chapter, we address this gap by investigating self-pulsing in a p-n embedded silicon microring resonator operated deep in the nonlinear regime at on-chip optical powers up to 36 mW. Experimentally, we demonstrate electrically tunable self-pulsing with oscillation frequencies reaching $\sim$ 190 MHz under a -5 V reverse bias. By varying the reverse-bias voltage while keeping the laser detuning and input power fixed, we observe a systematic acceleration of the oscillation frequency, directly revealing electrical control over the nonlinear limit cycle. To interpret these observations, we develop a temporal coupled-mode theory model augmented by coupled carrier and thermal rate equations, and we quantitatively link the bias-induced increase in self-pulsing frequency to a reduction of the effective free-carrier lifetime resulting from enhanced carrier sweep-out. We then extract the free carrier life time by matching the experimental SP frequencies to theoretical ones at same power and detuning. Our method stands different from the previous studies of pump and prope method in extracting free carrier life time.

The chapter is organized as follows. We first introduce the theoretical framework describing the coupled optical, thermal, and free-carrier dynamics in silicon microring resonators. We then present low-power measurements that characterize the linear optical response under forward- and reverse-bias conditions and provide calibrated parameters for the dynamical model. Next, we explain the physical mechanism of self-pulsing with support from numerical simulations and stability maps in detuning–power space. We then describe the fabricated p-n embedded microring device and the experimental setup used for time- and frequency-domain measurements. Finally, we present high-power experimental results under reverse-bias operation, extract the voltage-dependent free-carrier lifetime, and show how the reduction of τ_{fc} quantitatively accounts for the observed increase in self-pulsing frequency.

3.2 Theoretical Modeling

We model a silicon microring resonator with resonance frequency ω_0 coupled to a bus waveguide, as shown in Fig. 3.1, using temporal coupled-mode theory (TCMT). The intracavity field amplitude is denoted by $a(t)$, where $|a|^2$ represents the stored energy in the cavity. The input field is S_{in} with corresponding power $P_{\mathrm{in}} = |S_{\mathrm{in}}|^2$.

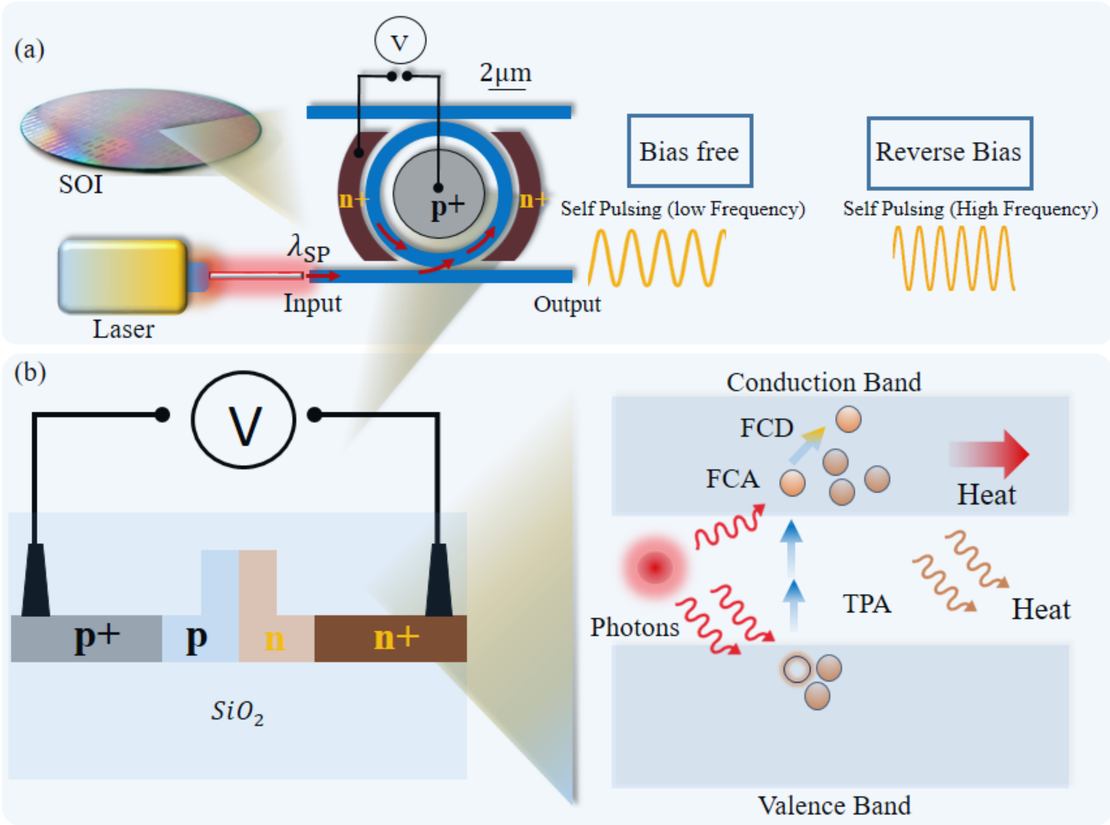

Figure 3.1: **Self-pulsing (SP) in a lateral p-n embedded silicon microring resonator.** **(a)** Schematic of the device and measurement concept. A continuous-wave laser excites the microring; the embedded p-n junction enables electrical biasing that programs the self-pulsing frequency. **(b)** Cross-sectional view of the silicon waveguide in SiO_2 matrix and schematic p-n junction profile. The physical origin of SP, arising from the interplay of carrier and thermal nonlinearities, is shown on the right.

The time evolution of the intracavity field is given by [38, 147, 148]:

$$\frac{da}{dt} = \left[i\Delta\omega_{\mathrm{NL}} - \frac{\gamma_{\mathrm{t}}}{2} \right] a + i\sqrt{\gamma_{\mathrm{coup}}}\, S_{\mathrm{in}}, \tag{3.1}$$

where the total loss rate γ_{t} consists of coupling loss, radiation loss, linear absorption, and non-linear loss due to TPA and FCA:

$$\gamma_{\mathrm{t}} = 2\gamma_{\mathrm{coup}} + \gamma_{\mathrm{rad}} + \gamma_{\mathrm{abs,lin}} + \gamma_{\mathrm{TPA}}|a|^2 + \gamma_{\mathrm{FCA}} N. \tag{3.2}$$

The non-linear detuning $\Delta\omega_{\mathrm{NL}}$ incorporates both thermo-optic and free-carrier dispersion effects:

$$\Delta\omega_{\mathrm{NL}} = \omega_0 - \omega - \frac{\omega_0}{n_g} \left(\frac{dn}{dT} \Delta T + \frac{dn}{dN} N \right), \tag{3.3}$$

where ΔT is the local temperature rise, N is the free-carrier density, and n_g is the group

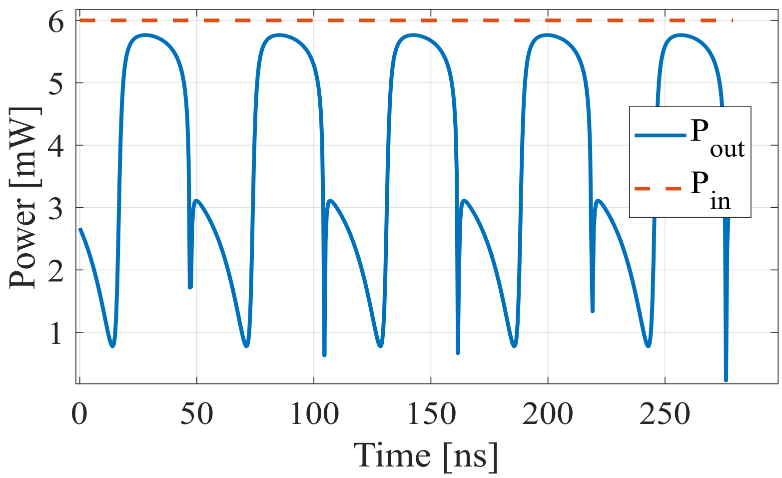

Figure 3.2: **Theoretical Model Simulation.** Time-domain trace of the microring response. The orange curve shows the constant input power of 6 mW (detuning: −70 GHz), while the output power exhibits self-pulsing behavior, visible as oscillations in time at the through port.

index.

The dynamics of the temperature and free-carrier density are governed by:

$$\frac{d\Delta T}{dt} = -\frac{\Delta T}{\tau_{\mathrm{th}}} + \alpha_{\mathrm{th}}\left(\gamma_{\mathrm{abs,lin}} + \gamma_{\mathrm{TPA}}|a|^2 + \gamma_{\mathrm{FCA}}N\right)|a|^2, \tag{3.4}$$

$$\frac{dN}{dt} = -\frac{N}{\tau_{\mathrm{fc}}(V_R)} + \alpha_{\mathrm{fc}}|a|^4. \tag{3.5}$$

where τ_{th} and $\tau_{fc}(V_R)$ denote the thermal and free-carrier lifetimes, respectively. The free-carrier lifetime decreases with increasing reverse-bias voltage V_R due to enhanced carrier sweep-out. The coefficients α_{th} and α_{fc} depend on the silicon TPA coefficient β_{Si}, the FCA cross-section σ_{Si}, and the thermal conductivity.

Equations (3.1)–(3.5) form a closed system describing the coupled evolution of the intracavity field, free-carrier density, and temperature. The optical energy stored in the cavity generates free carriers through two-photon absorption (TPA), and it contributes to heating through both free-carrier absorption (FCA) and TPA-related absorption. These processes modify the refractive index via the free-carrier dispersion (FCD) effect and the thermo-optic effect, respectively, thereby shifting the resonance frequency through Eq. (3.3). The resulting detuning variation alters the intracavity field according to Eq. (3.1), completing a non-linear feedback loop that couples the optical, thermal, and carrier dynamics.

Reverse bias enters the model through the carrier lifetime $\tau_{\mathrm{fc}}(V_R)$ and the carrier-induced refractive-index change $dn/dN(V_R)$: increasing the magnitude of the reverse bias $|V_R|$

reduces τ_{fc} by accelerating carrier sweep-out, thereby shortening the feedback delay that sustains self-pulsing [21, 49, 149].

3.2.1 Numerical solution procedure for intracavity dynamics and self-pulsing analysis

For a fixed input optical power P_{in}, the laser angular frequency ω is swept across the cavity resonance by varying the detuning $\Delta\omega = \omega - \omega_0$, where ω_0 is the cold-cavity resonance frequency. For each detuning point, the system dynamics are described by two slow state variables: the temperature rise $\Delta T(t)$ inside the resonator and the effective free-carrier density $N(t)$. These variables evolve according to coupled rate equations, while the intracavity optical energy $|a(t)|^2$ is assumed to reach its steady-state value instantaneously and is therefore obtained algebraically at each time step rather than through a differential equation.

The effective detuning experienced by the intracavity field is given by equation 3.3. For a given $(\Delta T, N)$ and laser frequency ω, the steady-state intracavity optical energy $|a|^2$ is obtained by solving a cubic polynomial equation. Where we substitude $u = |a|^2$.

$$Au^3 + Bu^2 + Cu + D = 0, \tag{3.6}$$

with coefficients

$$D = -\left|\kappa S_{\text{in}}\right|^2, \tag{3.7}$$

$$\begin{aligned} C = {} & \frac{1}{4}\gamma_{\text{coup}}^2 + \frac{1}{4}\gamma_{\text{rad}}^2 + \frac{1}{4}\gamma_{\text{abs,lin}}^2 + \frac{1}{2}\gamma_{\text{coup}}\gamma_{\text{rad}} + \frac{1}{2}\gamma_{\text{coup}}\gamma_{\text{abs,lin}} + \frac{1}{2}\gamma_{\text{rad}}\gamma_{\text{abs,lin}} \\ & + \frac{1}{2}\left(\gamma_{\text{coup}} + \gamma_{\text{rad}} + \gamma_{\text{abs,lin}}\right) c_4 N + \frac{1}{4}c_4^2 N^2 + \Delta\omega_{\text{NL}}^2, \end{aligned} \tag{3.8}$$

$$B = \frac{1}{2}c_3\left(\gamma_{\text{coup}} + \gamma_{\text{rad}} + \gamma_{\text{abs,lin}} + c_4 N\right), \tag{3.9}$$

$$A = \frac{1}{4}c_3^2. \tag{3.10}$$

Here γ_{coup}, γ_{rad}, and $\gamma_{\text{abs,lin}}$ are the coupling, radiation, and linear-absorption loss rates, respectively. The coefficient c_3 accounts for the two-photon-absorption (TPA) induced intensity-dependent loss and is defined as

$$c_3 = \Gamma_{\text{TPA}}\,\beta_{\text{Si}}\,\frac{c^2}{n_g^2\,V_{\text{TPA}}}, \tag{3.11}$$

where Γ_{TPA} is the modal overlap factor for TPA, β_{Si} is the TPA coefficient of silicon, n_g is the group index, and V_{TPA} is the effective TPA mode volume. The coefficient c_4 describes free-carrier absorption (FCA) and is given by

$$c_4 = \Gamma_{\text{FCA}}\,\sigma_{\text{Si}}\,\frac{c}{n_g}, \tag{3.12}$$

where Γ_{FCA} is the FCA overlap factor and σ_{Si} is the free-carrier absorption cross section.

Free carriers are generated through TPA with a rate proportional to the intracavity intensity squared. The corresponding free-carrier generation coefficient c_2 is defined as

$$c_2 = \Gamma_{\text{FCA}}\,\beta_{\text{Si}}\,\frac{c^2}{2\hbar\omega_0\,n_g^2\,V_{\text{FCA}}^2}, \tag{3.13}$$

where $\hbar$ is the reduced Planck constant, ω_0 is the cavity resonance angular frequency, and V_{FCA} is the effective mode volume associated with free-carrier generation.

Moreover, $\kappa = i\sqrt{\gamma_{\text{coup}}}$ is the coupling amplitude and $S_{\text{in}} = \sqrt{P_{\text{in}}}$ is the input field amplitude. Among the three possible roots of the resulting cubic equation, the physically meaningful solution is taken as the real and positive root.

Once $|a(t)|^2$ is determined, the slow dynamics of the system are evaluated through the coupled rate equations

$$\frac{d\Delta T}{dt} = -\frac{\Delta T}{\tau_{\text{th}}} + \Gamma_{\text{th}}\,\frac{\gamma_{\text{abs,lin}} + c_3|a|^2 + c_4 N}{\rho_{\text{Si}} C_{p,\text{Si}} V_{\text{th}}}\,|a|^2, \tag{3.14}$$

$$\frac{dN}{dt} = -\frac{N}{\tau_{\text{fc}}} + c_2|a|^4, \tag{3.15}$$

where τ_{th} and τ_{fc} are the thermal and free-carrier lifetimes, respectively, ρ_{Si} is the silicon density, $C_{p,\text{Si}}$ is the specific heat capacity, V_{th} is the effective thermal volume, and Γ_{th} is the thermal overlap factor. These equations are integrated in time using Runge–Kutta method over a fixed simulation window, and the final state $(\Delta T, N)$ at a given detuning is used as the initial condition for the next detuning point, implementing a continuation scheme.

This continuation strategy directly reflects the experimental measurement procedure. In the experiment, the laser wavelength is swept quasi-continuously across the resonance, with each detuning point reached from the previous one on a timescale that is slow compared to the thermal and carrier relaxation times. As a result, the microring does not reinitialize at each wavelength; instead, its internal state—characterized by the accumulated temperature shift ΔT and carrier density N—evolves smoothly and retains memory of the previous operating point. Consequently, the system follows a history-dependent trajectory in phase space, and the observed transmission at a given detuning depends on the direction and rate of the wavelength sweep.

The continuation scheme employed in the simulations therefore reproduces the experimental conditions, ensuring that the calculated steady states correspond to those accessed during a realistic wavelength sweep rather than to isolated, independently initialized solutions.

From the resulting time trace $|a(t)|^2$, a stationary regime is identified by discarding the initial transient and retaining the final portion of the signal. The mean intracavity energy is computed over this stationary window, and the oscillation amplitude is defined as the maximum deviation of $|a(t)|^2$ from its mean value. If this amplitude exceeds a predefined threshold, the system is identified as being in the self-pulsing regime. The self-pulsing frequency is then extracted by computing the Fourier transform of the stationary part of the signal, searching for the dominant spectral peak within a predefined frequency window, and converting the corresponding angular frequency to MHz. In this way, for each detuning value and fixed input power, the model yields the steady-state transmission, the intracavity energy, and the self-pulsing frequency, allowing a direct comparison between thermal–free-carrier non-linear dynamics and experimentally observed oscillatory behavior.

3.3 Self-Pulsing in Silicon Microring Resonators

Self-pulsing (SP) in silicon microring resonators (MRRs) is a non-linear dynamical phenomenon in which the output optical intensity oscillates in time, despite being driven by a continuous-wave (CW) input as shown in the Fig. 3.2.

Consider applying a high-power continuous-wave input signal at a fixed wavelength λ chosen close to the cold-cavity resonance λ_r. As illustrated in Fig. 3.3, when λ is sufficiently close to resonance, light couples efficiently into the microring and the intracavity energy $|a(t)|^2$ increases. The high optical intensity activates nonlinear absorption, primarily two-photon absorption, which generates free carriers and induces a carrier-related refractive-index change $\Delta n_{\mathrm{FC}}(t)$. On the fast carrier timescale set by the free-carrier lifetime τ_{fc}, this effect produces a blueshift of the effective resonance wavelength

$$\lambda_{r,\mathrm{eff}}(t) = \lambda_r + \delta\lambda_{r,N}(t) + \delta\lambda_{r,\Delta T}(t), \tag{3.16}$$

thereby reducing the detuning between λ and $\lambda_{r,\mathrm{eff}}(t)$ and sustaining strong coupling into the resonator.

As the optical field remains high, absorption processes deposit energy into the silicon

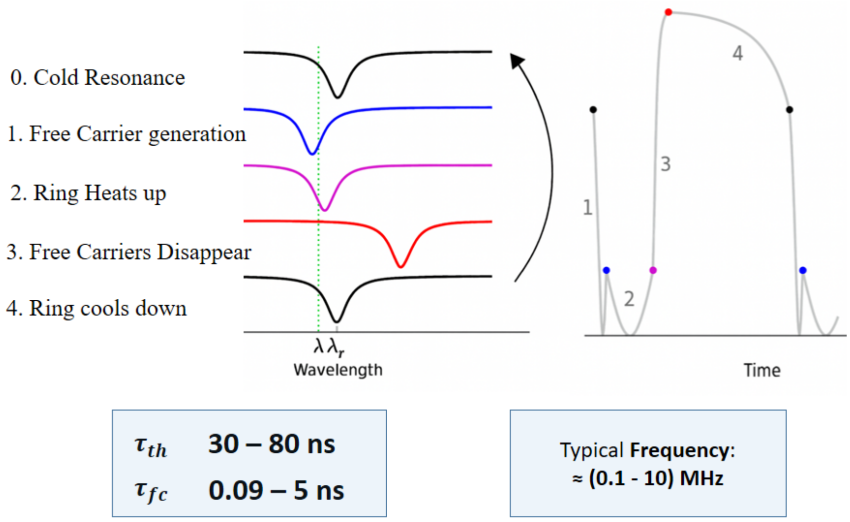

Figure 3.3: Variation in free-carrier density shifts the microring resonance toward shorter wavelengths, while temperature-induced refractive index changes shift it toward longer wavelengths. The interplay of these two effects, occurring on different time scales, leads to amplitude fluctuations that give rise to self-pulsing in the microring resonator. Figure adapted from [150] with modifications.

lattice, leading to a gradual temperature increase. On the slower thermal timescale τ_{th}, the resulting thermo-optic refractive-index change $\Delta n_{\text{th}}(t)$ induces a redshift $\delta\lambda_{r,\Delta T}(t)$ of the resonance. As shown schematically in Fig. 3.3, this thermo-optic redshift eventually compensates and overcomes the carrier-induced blueshift. At this point, the effective resonance wavelength moves away from the fixed input wavelength, the detuning increases, and the amount of light coupled into the ring is reduced.

Once the intracavity energy decreases, free-carrier generation is suppressed and the existing carriers recombine on the timescale τ_{fc}, causing the carrier-induced contribution $\delta\lambda_{r,N}(t)$ to relax toward zero. The resonance position is then governed primarily by the thermal contribution, $\lambda_{r,\text{eff}}(t) \approx \lambda_r + \delta\lambda_{r,\Delta T}(t)$. With little optical power coupled into the ring, no additional heating occurs and the resonator slowly cools down on the thermal relaxation timescale τ_{th}. As the device cools, the thermo-optic redshift diminishes and the resonance moves back toward λ. When sufficient spectral overlap is restored, the intracavity field builds up again, closing the cycle.

This sequence of a fast carrier-induced blueshift followed by a slower and ultimately dominant thermo-optic redshift gives rise to sustained relaxation oscillations of the intracavity intensity $|a(t)|^2$, carrier density $N(t)$, and temperature shift $\Delta T(t)$. These dynamics are fully consistent with the physical picture summarized in Fig. 3.3. Experimentally and numerically, such self-pulsing behavior is observed only above a sufficient input-power threshold: as shown in the right column of Fig. 3.4, at an input power of 4 mW the system

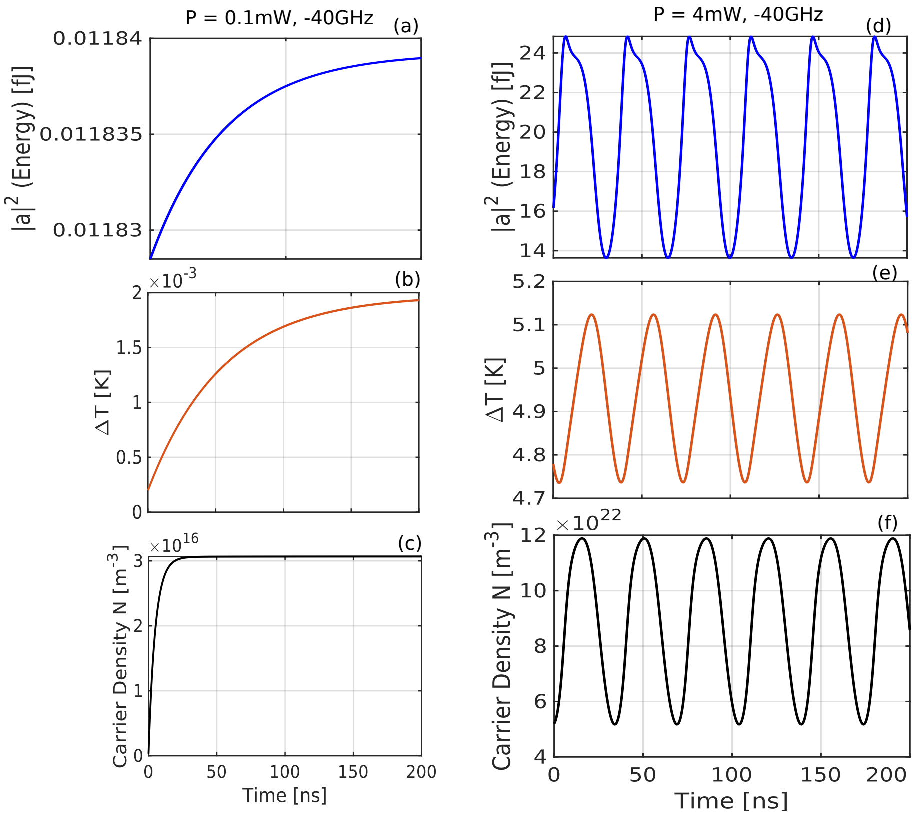

Figure 3.4: **Theoretical Model Simulation.** Time traces of intracavity energy ($|a|^2$), temperature change (ΔT), and carrier density (N) for two different input powers at the same detuning value. The left panels (a-c) corresponds to an input power of 0.1 mW, and the right panels (d-f) corresponds to 4 mW, both at a detuning of -40 GHz.

exhibits clear periodic oscillations, whereas at low input power (left column of the same figure) the intracavity field remains stable and self-pulsing does not occur.

The emergence of self-pulsing as a function of input power and laser–cavity detuning is summarized in the SP map shown in Fig. 3.5. This diagram identifies the regions of stable continuous-wave operation and those where self-pulsing occurs. At low power and small detuning, the system remains stable. As either the input power increases or the detuning is pushed further to the red side of the resonance, the non-linear detuning becomes strong enough to destabilize the steady state, driving the system into the oscillatory regime.

Beyond identifying the regions where self-pulsing occurs, the SP map in Fig. 3.5 also provides insight into how the oscillation frequency evolves as a function of input power and detuning. From the figure, it is observed that for a fixed detuning value, increasing the input power generally leads to a decrease in the self-pulsing frequency. This is because higher optical power enhances free-carrier and thermal effects, which increase the non-linear detuning and slow down the recovery dynamics, resulting in longer oscillation periods.

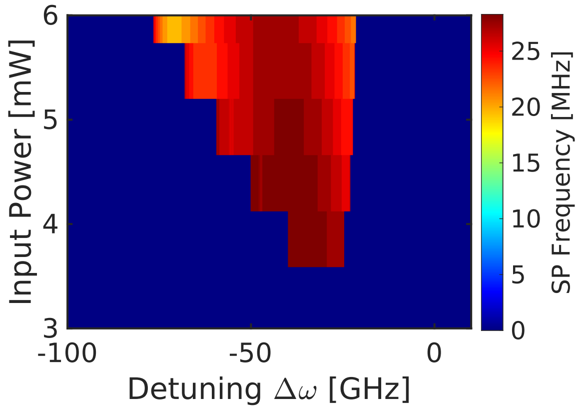

Figure 3.5: **Theoretical Model Simulation.** Self-pulsing (SP) map showing regions of stable and oscillatory behavior as a function of input power and laser–cavity detuning. The simulations are performed using the parameter values listed in Table 3.6.

In addition, the width of the self-pulsing window in detuning expands as the input power increases. At low power, only a narrow range of detuning values near the red side of the resonance supports oscillations. As the power is raised, the non-linear refractive index changes become stronger, and the system is pushed deeper into the unstable regime, allowing self-pulsing to persist over a broader range of detuning.

For a constant power level (i.e., along a horizontal slice in the SP map), the self-pulsing frequency does not remain constant across detuning. Instead, it first increases gradually as the detuning moves away from the resonance, reaches a maximum at an intermediate detuning value, and then decreases again before vanishing at the boundary of the SP region where the oscillation amplitude approaches zero. This characteristic rise-and-fall trend of the SP frequency is consistently observed across all power levels .

3.4 The Device

The investigated device is a silicon microring resonator (Si-MRR) fabricated on a silicon-on-insulator (SOI), as illustrated in Fig. 3.1(a). This MRR has been fabricated by a multi-project wafer service at a CMOS foundry (IMEC, Belgium) run on an SOI wafer of 220 nm thickness. The microring had a designed diameter of 14.5 µm, a waveguide width of 0.5 µm, and a coupling distance of 0.39 µm is between microring and bus waveguide, is configured in an add-drop geometry, where the input and output bus waveguides are side-coupled to the ring to enable both through- and drop-port measurements. The waveguides support the fundamental Transverse Electric (TE), ensuring single-mode operation for all optical measurements.

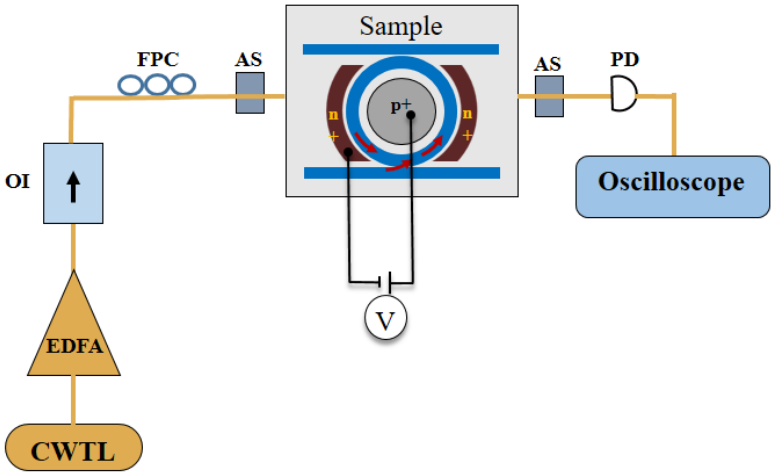

Figure 3.6: **Schematic of the experimental setup.** The set up starts from a continuous-wave tunable laser (CWTL), an Erbium-doped fiber amplifier (EDFA), an optical isolator (OI), a fiber polarization controller (FPC), two alignment stages (ASs), an InGaAs photodetector (PD), and an oscilloscope.

To provide electrical control, a lateral p-n junction encircles the microring, except in the coupling regions, in order to minimize carrier diffusion losses and preserve optical quality. As shown in Fig. 3.1(b), the doping profile consists of lightly doped p- and n-type regions positioned adjacent to the optical mode, together with heavily doped p^+ and n^+ regions that form low-resistance electrical contacts. In the AMF silicon photonics platform, the lightly doped p and n regions typically exhibit doping concentrations on the order of 10^{16}–10^{17} cm^{-3}, while the p^+ and n^+ contact regions are doped to 10^{19}–10^{20} cm^{-3}. This lateral p-n geometry enables efficient carrier sweep-out under reverse bias while maintaining high optical quality factors.

Electrical connections are made to the p^+ and n^+ terminals using metal pads linked to a source-measure unit (SMU). This configuration allows precise application of forward and reverse bias voltages, enabling two distinct regimes: Forward bias ($V > 0$) injects carriers into the waveguide, increasing free-carrier density and thereby modifying the refractive index via free-carrier dispersion (FCD) and increasing optical absorption via free-carrier absorption (FCA). Reverse bias ($V < 0$) sweeps carriers out of the waveguide, reducing the carrier lifetime τ_{fc}, lowering FCA-induced losses, and enabling high-speed modulation of the cavity dynamics.

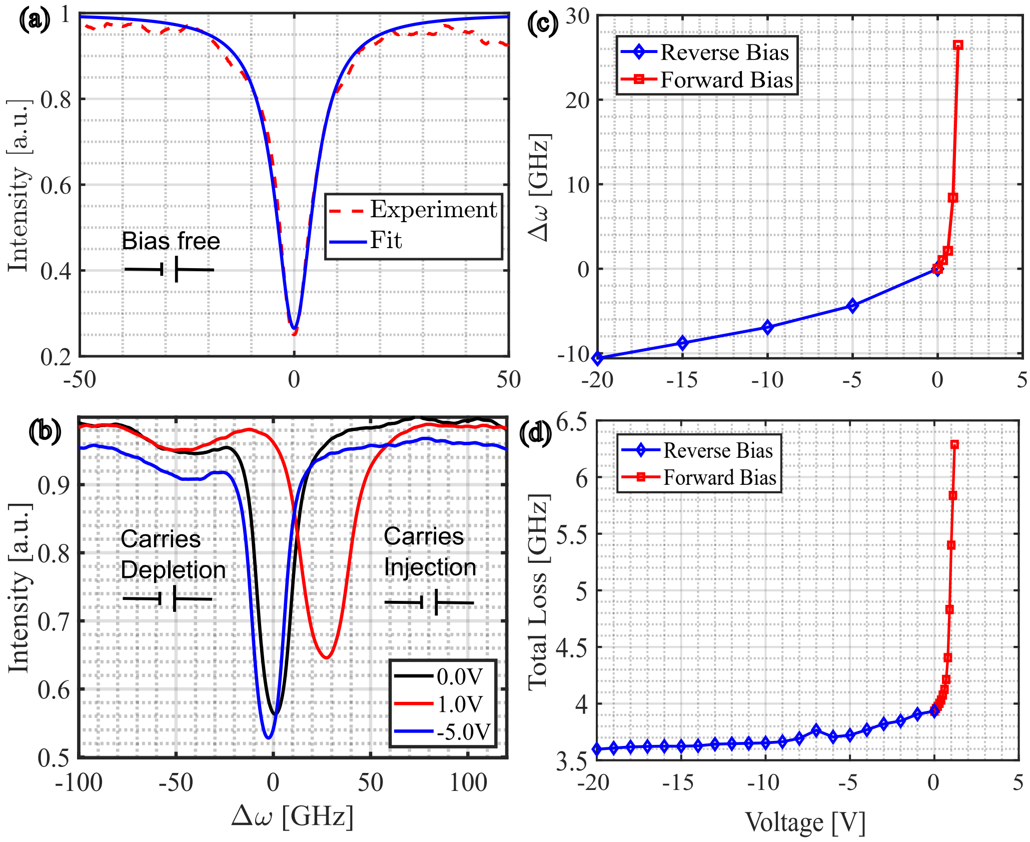

Figure 3.7: **Experimental results: Linear optical response of the silicon microring resonator under low input power.** **(a)** Normalized transmission spectrum as a function of frequency detuning ($\Delta\omega$) in the unbiased (0 V) condition. Experimental data (solid line) and Lorentzian fit (dashed line) show good agreement. **(b)** Bias-dependent transmission spectra under reverse (-5.0 V, blue) and forward ($+1.0$ V, red) conditions, illustrating carrier depletion and injection effects. Blueshift due to carrier depletion and redshift due to free-carrier injection are observed. **(c)** Resonance shift ($\Delta\omega$) versus applied voltage, showing asymmetric tuning: a blueshift under reverse bias and a redshift under forward bias. **(d)** Total optical loss as a function of applied voltage.

3.5 Experimental Setup

The optical setup consists of a tunable continuous-wave (CW) laser source whose TE-polarized output is coupled into the input waveguide using gratings. The laser is scanned through 1549 nm to 1556 nm wavelength with fixed power. The transmitted optical signals in through port are collected using high-speed photodetectors and analyzed in both the frequency and time domains using a real-time oscilloscope. The p-n junction bias voltage is varied from 1.2 V (forward bias) to -20 V (reverse bias) during the linear and non-linear optical scans using the DC voltage source.

The sample was excited using a continuous-wave tunable laser (Yenista TUNICS T-100S), operating in the third telecom window within the 1475–1575 nm range. The laser power was amplified by an Erbium-doped fiber amplifier (EDFA). An optical isolator was inserted after the laser to suppress back-reflections that could induce power instabilities or damage the source. A fiber polarization controller (FPC) was then used to set the polarization to the transverse electric (TE) mode, which is the only guided mode in the single-mode integrated waveguides used in this work.

The light was coupled to the chip using a precision alignment stage (AS). The chip was mounted on a copper block driven by a Peltier cell and heat sink for thermal stabilization. A 10 kΩ thermistor measured the temperature, and a PID controller held it stable under a constant-current bias of approximately 500 μA, ensuring resonant wavelength stability. A near-infrared camera (IRC) assisted during the alignment. The transmitted light was collected on the opposite side using a second alignment stage and detected using a Thorlabs InGaAs photodetector (1.2 GHz bandwidth). Time traces were acquired on an oscilloscope connected to a MATLAB® acquisition script.

For the given measurments, optical power is defined at the chip input and calibrated by subtracting fiber-to-chip coupling losses on the same chip. The input polarization is adjusted to the TE mode using a fiber polarization controller and confirmed by maximizing the signal. Device temperature is stabilized to within ±0.01°C using a thermoelectric controller. Port transmission spectra are recorded using calibrated photodetectors. Resonance positions, linewidths, and asymmetric coupling parameters are extracted by fitting the measured spectra coupled-mode-theory model.

3.6 Results

3.6.1 Low Power Measurements

Figures 3.7(a–d) present the linear transmission characterization of the device. The measurements were performed at a low input power of 0.0239 mW launched into the bus waveguide, ensuring operation in the linear regime. For this device, measured on a different chip, the resonance wavelength is located at $\lambda_0 = 1543.0940$ nm.

From the experimental spectra, we extract a loaded quality factor of $Q = 41\,706.24$, corresponding to a photon lifetime of 34.17 ps. The resonance exhibits a full width at half maximum (FWHM) of 0.0370 nm, equivalent to 4.6583 GHz, and an extinction ratio of 5.85 dB.

Under forward bias (+1.2 V), the resonance exhibits a clear redhift (moving to higher

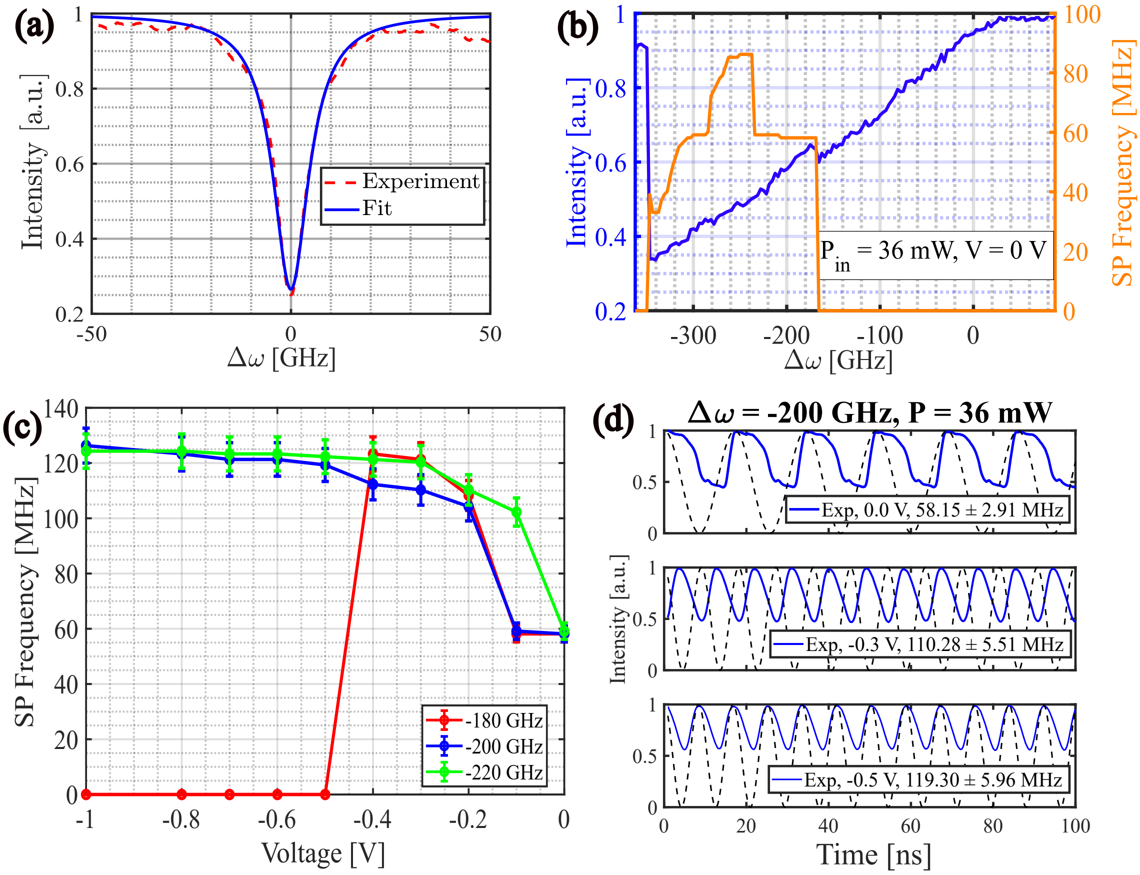

Figure 3.8: **Experimental Results (a)** Linear fit with experiment at 0 V baised. **(b)** non-linear resonance shift and corresponding SP frequencies versus detuning under zero-bias (0 V) at a fixed input power. **(c)** Self-pulsing frequencies as a function of the applied reverse-bias voltage for three detuning values at an input power of 36 mW. **(d)** Experimental time traces for a detuning of −200 GHz at three selected reverse-bias voltages: 0, −0.3, and −0.5 V.

values relative to 0) of ≈ 27 GHz relative to the unbiased case as shown in (panel b and c), whereas under reverse bias (−20 V) the resonance shows a blueshift (moving to lower values relative to 0) of ≈ 10 GHz (panel c), yielding a bidirectional electrical tuning span of ≈ 37 GHz across the explored voltage range. The total optical loss, extracted from the experimental spectra via the FWHM method, decreases from ∼ 4 GHz at 0 V to ∼ 3.5 GHz at −20 V, while it increases to ∼ 6.5 GHz at +1.2 V as shown in (panel d).The loss increase under forward bias arises from carrier injection that elevates the free-carrier density N, thereby enhancing free-carrier absorption (FCA) and carrier-induced scattering resulting in the decrease of the Q factor. Conversely, reverse bias depletes and sweeps out carriers, reducing FCA and narrowing the linewidth (lower FWHM) increasing the Q factor, while the accompanying reduction in N .

To enable a reliable analysis of the device (same device but in different chip) behavior at

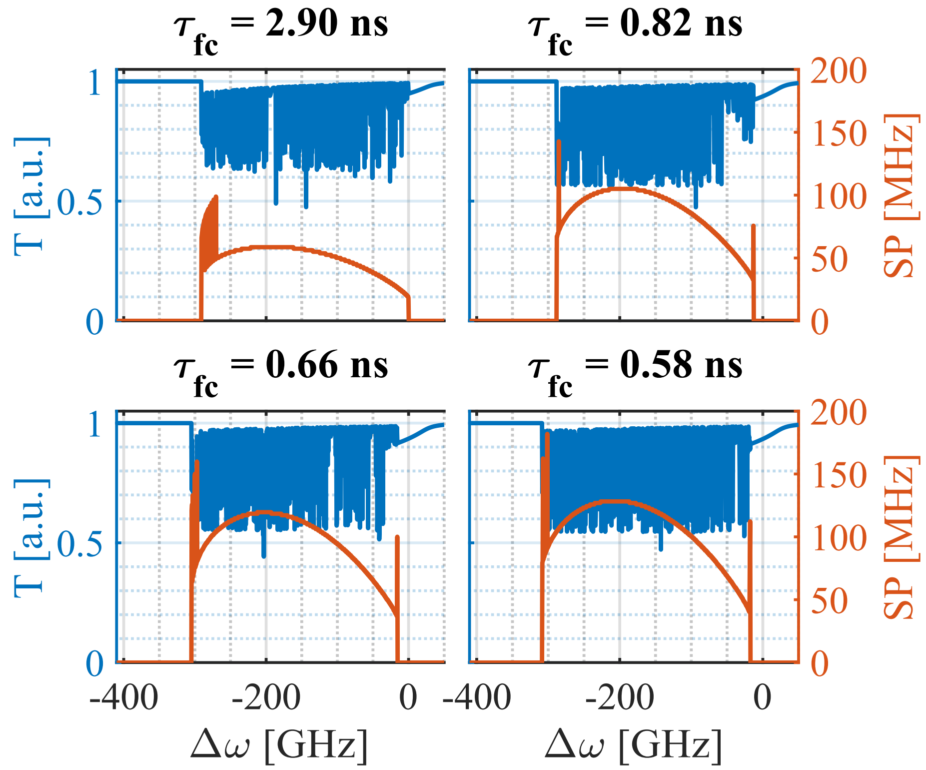

Figure 3.9: Transmission and self-pulsing (SP) frequency maps for several extracted values of the free-carrier lifetime τ_{fc}. Unless stated otherwise, the parameters used in the sweep correspond to those listed in Table 3.6, with the following values extracted from fitting experimental data with model: $dn/dN = -1.01 \times 10^{-27}\,\mathrm{m}^3$ and $\tau_{th} = 38.12\,\mathrm{ns}$.

high optical powers, we first characterize the microring in the low-power regime, where non-linear effects are negligible. This initial characterization provides accurate values for the coupling and loss coefficients, which are later used as fixed parameters when modeling the system under strong driving conditions.

Again we use an input power of only 0.0239 mW at the bus waveguide, we observe the expected transmission dip in the output spectrum, as shown in Fig. 3.8(a). Under zero-bias conditions, the silicon microring exhibits a resonance wavelength of 1549.72 nm and a measured quality factor of 41 885.24, corresponding to a photon lifetime of 34.46 ps.

The measured spectrum was fitted using the coupled-mode theory (CMT) model introduced above. From this fit, we extract the key linear parameters of the resonator: a radiative loss rate of $\gamma_{rad} = 4.58 \times 10^{10}$ rad/s (7.29 GHz), a linear absorption loss of $\gamma_{abs,lin} = 2.18 \times 10^{8}$ rad/s (0.03 GHz), and a coupling rate of $\gamma_{coup} = 1.54 \times 10^{10}$ rad/s (2.45 GHz), all extracted at a resonance wavelength of 1549.7 nm. The sum of squared errors normalized to their data points is 1.20×10^{-2}, confirming excellent agreement between the model and the measured transmission.

3.6.2 High Power Measurements and Self Pulsing Dynamics

3.6.2.1 Parameter Extraction and SP Model Fitting at 0 V

In the experiment, at an incident optical power of $P_{\text{in}} = 36\,\text{mW}$, the laser is initially tuned to the cold-cavity resonance wavelength of the microring. The laser wavelength is then scanned toward longer values. As the scan proceeds, nonlinear absorption inside the cavity generates free carriers and heat, causing the effective resonance wavelength to shift continuously toward higher wavelengths. At a critical laser wavelength, the steady-state transmission becomes unstable and self-pulsing (SP) dynamics emerge.

To quantitatively analyze the self-pulsing (SP) dynamics of the silicon microring resonator, a parameter-extraction procedure was performed using the experimental measurements acquired under zero reverse-bias conditions (0 V). The fitting strategy was designed to isolate and match only the self-pulsing frequencies, ensuring that the dynamical model accurately reproduces the oscillatory behaviour arising from the coupled thermal and free-carrier non-linearities. The fitting used three detuning values,

$$D = -200\text{ GHz},\ -210\text{ GHz},\ -215\text{ GHz},$$

representing the region where the device consistently exhibits SP oscillations with high signal-to-noise ratio.

3.6.2.2 Fitting Strategy

The particle swarm optimization (PSO) routine was used to extract the nonlinear dynamical parameters of the model [151]. In this fitting stage, all linear cavity parameters were kept fixed: the coupling coefficient γ_{coup}, the linear absorption γ_{abs}, and the radiation loss γ_{rad} were inserted as constant values obtained independently from the linear transmission fit was performed under zero reverse-bias conditions (0 V). Likewise, the thermo-optic coefficient was fixed to its calibrated value,

$$\frac{dn}{dT} = 1.86 \times 10^{-4}\ \text{K}^{-1},$$

[38] and was not included in the optimisation. The free-carrier dispersion coefficient, however, was treated as a fitting parameter and allowed to vary within a physically motivated range around its nominal value. As a result, the PSO explored a three-dimensional

non-linear parameter vector,

$$\mathbf{v} = \left[\tau_{\text{fc}},\ \frac{dn}{dN},\ \tau_{\text{th}}\right],$$

while the input optical power was fixed to the experimentally measured on-chip value ($P_{\text{in}} = 36$ mW). By separating the linear calibration from the non-linear optimisation, the SP-only fitting procedure isolates the dynamical carrier and thermal contributions without altering the independently validated linear cavity parameters.

The PSO was configured with 20 particles and 20 iterations. In the implementation, the detuning axis is first restricted to a sub-range $\{D_{\text{fit}}\}$, defined as

$$D_{\text{fit}} = \{D_i \mid i \in \{\texttt{idx\_cold}, \ldots, \texttt{idx\_last}\}\},$$

where `idx_cold` is the index of the last positive detuning value (the “cold” operating point just before crossing resonance), and `idx_last` is the index of the most negative of the three target detunings.

For each candidate parameter set $\mathbf{v}$, the model then sweeps sequentially along D_{fit}, using continuation in detuning: the steady-state solution at detuning D_i is used as the initial condition for the ODE at detuning D_{i+1}. This procedure ensures that the simulation follows the same non-linear resonance branch as the experiment, starting from the cold resonance and moving towards larger negative detuning.

Within this detuning sub-range, only three specific detuning values are selected as cost points, namely -200, -210, and -215 GHz. Their indices inside D_{fit} are stored in `idx_cost`, and the corresponding experimental SP frequencies are collected in a vector $\mathbf{y}_{\text{exp}}$. The model computes the SP frequency $\text{SP}_m(D_i; \mathbf{v})$ at all $D_i \in D_{\text{fit}}$, and then extracts only the three entries at `idx_cost` for the cost evaluation. Although the cost is evaluated at only three detunings, the predicted SP values at these points depend on the full continuation along D_{fit}; any mismatch of the dynamics at detunings above the target values (i.e. closer to resonance) can propagate through the continuation and indirectly degrade the agreement at -200, -210, and -215 GHz. This explains why the fit quality can appear noticeably worse near the detunings above and below the three selected points, and why the cost cannot be further reduced without losing the good agreement in the region where the SP oscillation is best defined. In practice, this trade-off is unavoidable: in order to correctly reproduce the non-linear branch and the SP behaviour at the three anchor detunings, the model must be continued from the cold resonance through a region where the fit to the experimental SP may be less accurate.

3.6.2.3 SP - Cost Function

The fitting procedure uses only the SP frequencies at the three selected detunings as explicit cost points. Denoting the experimental SP values as

$$\mathbf{y}_{\text{exp}} = \begin{bmatrix} \text{SP}(-200\ \text{GHz}) \\ \text{SP}(-210\ \text{GHz}) \\ \text{SP}(-215\ \text{GHz}) \end{bmatrix}, \qquad \mathbf{y}_{\text{model}}(\mathbf{v}) = \begin{bmatrix} \text{SP}_m(-200\ \text{GHz}; \mathbf{v}) \\ \text{SP}_m(-210\ \text{GHz}; \mathbf{v}) \\ \text{SP}_m(-215\ \text{GHz}; \mathbf{v}) \end{bmatrix},$$

the scalar SP-only cost function implemented in `objective_SP` is defined as the mean-squared error

$$J(\mathbf{v}) = \frac{1}{3}\left\|\mathbf{y}_{\text{exp}} - \mathbf{y}_{\text{model}}(\mathbf{v})\right\|^2 = \frac{1}{3}\sum_{k=1}^{3}\Big[\text{SP}_{\text{exp}}(D_k) - \text{SP}_m(D_k; \mathbf{v})\Big]^2,$$

with the SP frequencies used directly in megahertz, without any additional scaling. The reported best cost value cost = 0.324211 therefore quantifies the normalized squared error between experiment and model over these three anchor detuning points, after full continuation along the non-linear resonance branch from the cold detuning down to −215 GHz.

Table 3.1: From the SP-only fit at 0 V, together with the fixed thermo-optic coefficient and the linear cavity parameters extracted independently from the linear transmission fit.

Parameter	Symbol	Value	Description
Free-carrier lifetime	τ_{fc}	2.90 ns	Fitted non-linear carrier timescale
Free-carrier dispersion	$\frac{dn}{dN}$	-1.01×10^{-27} m^3	Fitted FCD coefficient
Thermal relaxation time	τ_{th}	38.16 ns	Fitted thermal timescale
Thermo-optic coefficient	$\frac{dn}{dT}$	1.86×10^{-4} K^{-1}	Fixed material constant
Coupling loss rate	γ_{coup}	1.54×10^{10} s^{-1}	Fixed from linear fit
Linear absorption rate	γ_{abs}	2.18×10^{8} s^{-1}	Fixed from linear fit
Radiation loss rate	γ_{rad}	4.58×10^{10} s^{-1}	Fixed from linear fit

3.6.2.4 Extraction of the Free-Carrier Lifetime as a Function of Reverse Bias

Once the 0 V parameter set is obtained from the SP-only PSO optimisation, the next step is to determine how the free-carrier lifetime τ_{fc} changes with applied reverse bias. The goal is to extract $\tau_{\text{fc}}(V)$ directly from the experimentally measured SP frequency at a fixed detuning of −200 GHz. This procedure is implemented in the second part of the code and is conceptually separate from the PSO fit: τ_{fc} is not re-optimised via PSO for each voltage, but instead is inferred by forward-model evaluation.

The code first constructs a dense detuning grid,

$$\Delta\omega_{\text{down}} = \{+50\text{ GHz} \rightarrow -400\text{ GHz}\},$$

and performs a full non-linear sweep from positive detuning down to −200 GHz, using the continuation strategy

$$\mathbf{x}_{i+1}(0) = \mathbf{x}_i(t_{\text{end}}),$$

where $\mathbf{x}(t) = [\Delta T(t), N(t)]$ are the thermal and carrier state variables. This ensures that the model follows the same non-linear resonance branch as in the experiment. The full sweep is executed once using the fitted 0 V parameters, including the extracted $\tau_{\text{fc}} = 2.90$ ns. This step provides a physically correct initial condition at −200 GHz,

$$\mathbf{x}_{200}^{(0)} = [\Delta T_{200},\ N_{200}],$$

which is then reused for all subsequent biased simulations.

To extract the voltage-dependent free-carrier lifetime $\tau_{\text{fc}}(V)$, the model is evaluated at a fixed detuning of −200 GHz while sweeping τ_{fc} over a discrete set of values. For each candidate lifetime, the system dynamics are integrated , which returns the corresponding steady-state self-pulsing frequency $\text{SP}_m(-200; \tau_{\text{fc}})$. In this way, an explicit mapping

$$\tau_{\text{fc}} \longmapsto \text{SP}_m(-200; \tau_{\text{fc}})$$

is constructed numerically.

In parallel, the experimentally measured self-pulsing frequencies at the same detuning of −200 GHz are obtained under various applied reverse-bias voltages as shown in the Fig 3.8(c). Table 3.2 summarizes the lifetimes used in the model sweep, the corresponding experimental SP frequencies, and the applied voltages for direct comparison.

The model–experiment comparison in Table 3.2 therefore provides a consistent basis for extracting $\tau_{\text{fc}}(V)$ and calibrating the voltage dependence of the free-carrier dynamics in the device.

The extracted lifetime $\tau_{\text{fc}}(V)$ is obtained by matching each experimental value with the corresponding model value at −200 GHz, i.e.,

$$\text{SP}_m(-200; \tau_{\text{fc}}(V)) \approx \text{SP}_{\text{exp}}(-200; V).$$

Because the model predicts an approximately monotonic decrease of τ_{fc} with increasing

Table 3.2: Deduced free-carrier lifetimes τ_{fc} with estimated uncertainties, corresponding experimental self-pulsing (SP) frequencies, and applied reverse-bias voltages at a detuning of −200 GHz.

Reverse Bias V (V)	**τ_{fc} (ns)**	**SP Frequency (MHz)**
0.0	2.90 ± 0.20	58
-0.1	2.68 ± 0.15	60
-0.2	0.82 ± 0.07	104
-0.3	0.76 ± 0.06	110
-0.4	0.74 ± 0.04	112
-0.5	0.66 ± 0.04	119
-0.6	0.65 ± 0.03	121
-0.8	0.64 ± 0.03	123
-1.0	0.58 ± 0.03	126

reverse bias, and because continuation ensures the correct non-linear state at −200 GHz, the resulting $\tau_{fc}(V)$ curve is smooth and physically consistent. The extracted data show a strong voltage-dependent reduction in free-carrier lifetime, from $\tau_{fc} = 2.90$ ns at 0 V down to $\tau_{fc} \approx 0.58$ ns at −1 V.

This approach is justified by the fact that the SP frequency is primarily determined by the fast carrier-recovery timescale in the non-linear limit cycle, while the other non-linear and linear parameters are held fixed from the 0 V optimisation. Thus, τ_{fc} becomes the sole degree of freedom required to explain the voltage-dependent SP behaviour. The excellent agreement between model predictions and experimental SP frequencies demonstrates that the voltage-tuned carrier extraction in the p-n junction is the dominant mechanism governing the observed shift in the limit-cycle frequency.

3.6.2.5 High Power Results and Discussion

The extracted free-carrier lifetime at 0 V, $\tau_{fc} \approx 2.9$ ns, is consistent with carrier recombination dynamics in p-n-integrated silicon photonic devices and sets the fast nonlinear timescale governing the high-frequency component of the self-pulsing oscillation. In contrast, the thermal relaxation time, $\tau_{th} \approx 38$ ns, is an order of magnitude slower and provides the delayed feedback responsible for the relaxation-type limit-cycle dynamics characteristic of self-pulsing.

The extracted dispersion coefficient,

$$\frac{dn}{dN} = -1.01 \times 10^{-27}\ \mathrm{m}^3,$$

lie within the established physical ranges for silicon at telecom wavelengths.

This SP-only fitting procedure establishes a physically reliable baseline for the subsequent analysis of reverse-bias tuning. Since the thermal response is voltage-independent, the extracted τ_{th} at 0 V provides a fixed reference, while voltage-dependent variations in τ_{fc} can be quantified and modelled as a function of applied bias in the following sections.

Figures 3.8(a–d) shows experimental results of how a reverse bias across the embedded p–i–n junction controls self-pulsing (SP) in the silicon microring. The results are obtained at a fixed input power $P_{\text{in}} = 36$ mW, while the reverse bias is varied from 0 to -1 V.

As shown in panel (b), at $V = 0\,\text{V}$, tuning the laser toward the cavity resonance initially induces a non-linear shift in the resonance frequency. At moderate detuning, self-pulsing (SP) oscillations emerge, with the oscillation frequency increasing as the detuning is further increased. Beyond a critical detuning of approximately $-345\,\text{GHz}$, the SP abruptly disappears as the transmission trace exhibits a sharp jump back to unity, indicating that the ring has moved out of resonance and the intracavity energy has collapsed. This behavior confirms that sustained SP oscillations require sufficient optical energy to remain trapped inside the resonator. At $V = 0\,\text{V}$, the SP frequencies occur only within a distinct detuning window of roughly 180 GHz, beyond which the system relaxes back to a stable, non-oscillatory state.

Panel (c) focuses on the scenario where the detuning values are fixed at -180 GHz, -200 GHz, and -220 GHz. For all three detuning points, the SP frequency increases monotonically with increasing in reverse bias, exhibiting an approximately linear dependence over the displayed bias interval. We also observe that for the initial detuning of the -180 GHz, the SP disappears at the -0.5 V. The differing slopes for each detuning reflect operating-point sensitivity: variations in the steady-state intracavity power and its derivatives with respect to detuning weight the carrier-mediated feedback differently, producing distinct frequency–bias characteristics at each operating point.

Panel (d) shows the time-domain traces at a fixed detuning of $-200\,\text{GHz}$, clearly illustrating the acceleration of SP dynamics. The oscillation frequency increases from $58.15\,\text{MHz} \pm 2.91\,\text{MHz}$ at $0\,\text{V}$, to $110.28\,\text{MHz} \pm 5.51\,\text{MHz}$ at $-0.3\,\text{V}$, and further to $119.30\,\text{MHz} \pm 5.96\,\text{MHz}$ at $-0.5\,\text{V}$. The pronounced initial frequency jump, followed by a more gradual rise, suggests mild saturation effects. This behaviour is consistent with the interpretation that once $\tau_{fc}(V)$ approaches other limiting internal timescales, further reductions in carrier lifetime produce only diminishing increases in the limit-cycle frequency.

Figure 3.10 compares the experimentally measured self-pulsing (SP) frequencies (orange square markers) as a function of the applied reverse-bias voltages listed in Table 3.2 with the model predictions (solid blue line), which describe the SP frequency as a function of the free-carrier lifetime. In the same figure, the *SP theory fit* (dashed magenta line) corresponds to a fit obtained using Eq. 3.18. The strong agreement between the experimental data and the theoretical model demonstrates that the SP frequency is governed by the free-carrier lifetime, τ_{fc}. This dependence is strongly non-linear: relatively modest reductions in τ_{fc}, from 3 ns to approximately 0.5 ns, result in substantial increases in the SP frequency. The blue curve further illustrates a model-based extrapolation of the SP frequencies over a broader range of free-carrier lifetimes.

As can be observed in Fig. 3.10, as the free-carrier lifetime τ_{fc} is reduced, the self-pulsing (SP) frequency f_{SP} increases and shoots up for shorter carrier lifetimes. This behaviour is consistent with the fact that the carrier population governs the strength and speed of the free-carrier dispersion (FCD) modulation in silicon: a faster carrier decay enables quicker refractive-index recovery, thereby shortening the characteristic oscillation period and increasing the SP frequency.

To capture this dependence, we model the SP frequency using a reduced two-time-scale description in which the free-carrier lifetime τ_{fc} and the thermal relaxation time τ_{th} jointly determine the oscillation rate. The scaling relation takes the form

$$f_{\mathrm{SP}}(\tau_{\mathrm{fc}}) = \frac{A}{\sqrt{\tau_{\mathrm{th}}\,\tau_{\mathrm{fc}}}}, \tag{3.17}$$

where τ_{th} is the effective thermal relaxation time of the microring, τ_{fc} is the free-carrier lifetime, and A is a dimensionless prefactor capturing geometric constants, non-linear interaction strength, and higher-order corrections in the simplified analytical model. In Eq. (3.17), f_{SP} is expressed in hertz and the lifetimes are expressed in seconds.

For practical comparison to the experiment, we express the lifetimes in nanoseconds and the frequencies in megahertz.

$$f_{\mathrm{SP}}^{(\mathrm{MHz})}\big(\tau_{\mathrm{fc}}^{(\mathrm{ns})}\big) = \frac{10^3 A}{\sqrt{\tau_{\mathrm{th}}^{(\mathrm{ns})}\,\tau_{\mathrm{fc}}^{(\mathrm{ns})}}}, \tag{3.18}$$

where $\tau_{\mathrm{th}}^{(\mathrm{ns})}$ and $\tau_{\mathrm{fc}}^{(\mathrm{ns})}$ are expressed in nanoseconds. Equation (3.18) is then fitted to the experimental SP frequencies in the range 0.30 ns $\leq \tau_{\mathrm{fc}}^{(\mathrm{ns})} \leq$ 3 ns, where the oscillations are stable and well resolved.

Using particle swarm optimization (PSO), the best-fit parameters are found to be

$$A = 0.596, \qquad \tau_{\mathrm{th}}^{(\mathrm{ns})} = 38.036\ \mathrm{ns}. \tag{3.19}$$

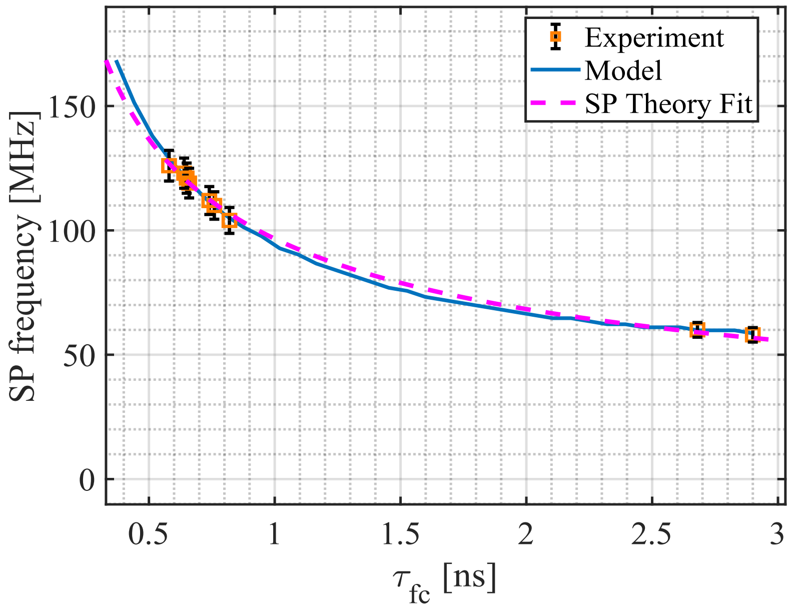

Figure 3.10: Extracted free-carrier lifetimes obtained by fitting the experimentally measured self-pulsing (SP) frequencies at a fixed detuning of −200 GHz and an input power of $P = 36$ mW. The blue curve represents the model-generated SP frequencies evaluated over an extended range of free-carrier lifetimes. The magenta curve shows the theoretical SP-frequency model of Eq. (3.18), fitted to the experimental data.

The extracted thermal relaxation time of $\tau_{th} \approx 38$ ns is fully consistent with the expected thermal response time of the silicon microring at 0 V reverse bias. This agreement indicates that the reduced SP model captures the dominant interplay between thermal and free-carrier dynamics and accurately reflects the operating physical regime of the device.

Figure 3.11 shows the deduced free-carrier lifetime τ_{fc} as a function of the applied reverse-bias voltage $|V_{rev}|$, fitted exponential saturation model in [152]. The model has following form

$$\tau_{fc}(V) = \tau_{fc,sat} + (\tau_{fc0} - \tau_{fc,sat})\, e^{-V/V_\tau}, \tag{3.20}$$

where τ_{fc0} is the low-bias free-carrier lifetime, $\tau_{fc,sat}$ is the saturated lifetime at large reverse bias, and V_τ is the characteristic voltage determining the rate at which the transition between these two regimes occurs.

Fitting Eq. (3.20) to the experimental data yields

The extracted parameters in Table 3.3 indicate that at zero applied voltage the microring exhibits a relatively slow free-carrier recombination time of $\tau_{fc0} \approx 3.12$ ns, consistent with the intrinsic carrier lifetime of the waveguide region in the absence of an electric field.The

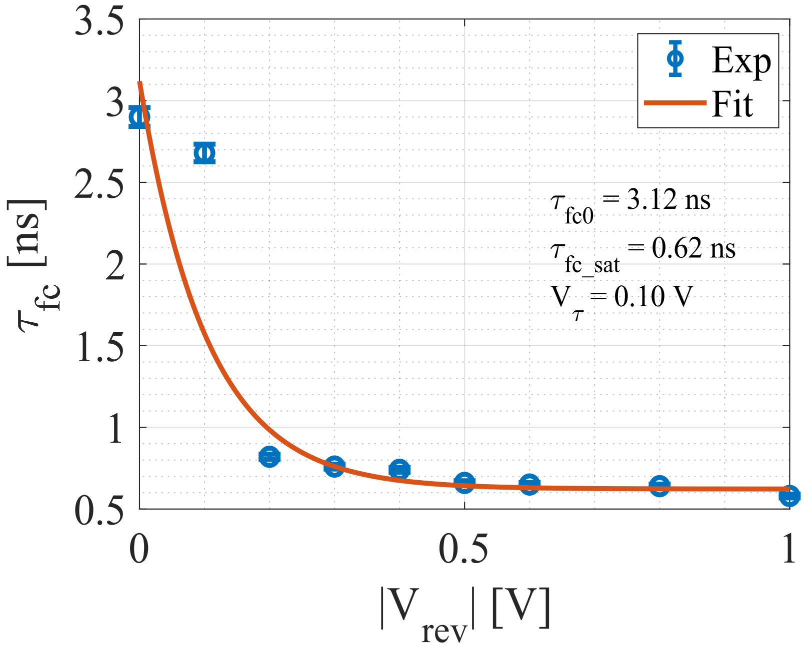

Figure 3.11: Free-carrier lifetime plotted as a function of the applied reverse-bias voltage. The extracted life time is fitted lifetime–voltage model. The extracted parameters are given inside the plot. Measurements correspond to a detuning of −200 GHz and an input power of $P = 36\,\text{mW}$.

Table 3.3: Extracted parameters from the τ_{fc}–voltage fit.

Parameter	**Value**
τ_{fc0} (low-bias lifetime)	3.12 ns
$\tau_{fc,sat}$ (saturated lifetime)	0.62 ns
V_τ (characteristic voltage)	0.10 V

saturation value $\tau_{fc,sat} \approx 0.62$ ns represents the limit imposed by the fastest field-assisted extraction achievable in this device geometry.

The characteristic voltage $V_\tau \approx 0.10$ V quantifies the voltage scale over which the lifetime transitions from its intrinsic value to its field-assisted saturated value; this small value indicates that even modest reverse biases significantly improve carrier extraction efficiency. Overall, the fitted curve shows excellent agreement with the experimental τ_{fc}–voltage trend and accurately captures the enhanced free-carrier sweep-out dynamics induced by the applied reverse bias.

Then, in Fig. 3.9, we plot the transmission through the through-port together with the corresponding self-pulsing (SP) frequencies for four representative values of the extracted free-carrier lifetime τ_{fc}. The maps are generated by sweeping the laser frequency from higher to lower values.

The resulting diagrams highlight the detuning windows in which SP oscillations emerge

Table 3.4: Extracted non-linear transmission-fit parameters for -1 V . The fit is over all detuning range as shown in Fig 3.12

Parameter	Value
Radiative loss rate	$\gamma_{\mathrm{rad}} = 3.63 \times 10^{10}\,\mathrm{rad/s}$ (5.78 GHz)
Absorption loss rate	$\gamma_{\mathrm{abs}} = 1.69 \times 10^{10}\,\mathrm{rad/s}$ (2.69 GHz)
Coupling rate	$\gamma_{\mathrm{coup}} = 7.58 \times 10^{9}\,\mathrm{rad/s}$ (1.21 GHz)
Total loss rate	$\gamma_{\mathrm{tot}} = 6.08 \times 10^{10}\,\mathrm{rad/s}$ (9.68 GHz)
Free-carrier lifetime	$\tau_{\mathrm{fc}} = 0.100\,\mathrm{ns}$
Thermal relaxation time	$\tau_{\mathrm{th}} = 35.69\,\mathrm{ns}$
Carrier-induced index change	$\mathrm{d}n/\mathrm{d}N = -1.0864 \times 10^{-27}\,\mathrm{m}^3$

and subsequently disappear as τ_{fc} is varied.The can be seen at the either edges of the SP maps by just looking over the detuning values. Though the window of SP appearance on the edges is narrow but it give plausible picture of the phenomena. As the free-carrier lifetime decreases, these SP windows progressively shrink in width across the detuning axis. At the same time, the SP frequencies within the remaining windows increase, reflecting the faster carrier dynamics associated with shorter τ_{fc}. This behavior illustrates how the interplay between carrier sweep-out and optical feedback reshapes the stability landscape of the system as the effective carrier lifetime is reduced.

3.6.2.6 Full detuning sweep fit for -1 V and High SP Frequencies

Figure 3.12 shows the experimental transmission and self-pulsing (SP) frequency over the full detuning sweep at a reverse bias of -1 V, together with the corresponding theoretical fit. The parameters extracted from the fit are summarized in Table 3.4. The particle swarm optimization (PSO) fitting procedure yields a best cost value of 0.20, indicating good agreement between the model and the experimental data. The fitted curves closely overlap with the experimentally observed SP detuning windows. In addition, the SP window exhibits a noticeable detuning lag relative to the transmission jump to unity when compared to the 0 V case where the SP cease at the same detuning value where the transmission jumps back to the unity.

Under a reverse bias of -1 V, the disappearance of self-pulsing (SP) occurs at a smaller detuning than the recovery of the transmission to unity, indicating that the condition for dynamical instability is lost while a nonlinear steady state still persists. The effective cavity detuning can be expressed as

$$\Delta_{\mathrm{eff}} = \Delta_{\mathrm{laser}} - \Delta_{\mathrm{th}}(T) - \Delta_{\mathrm{fc}}(N), \tag{3.21}$$

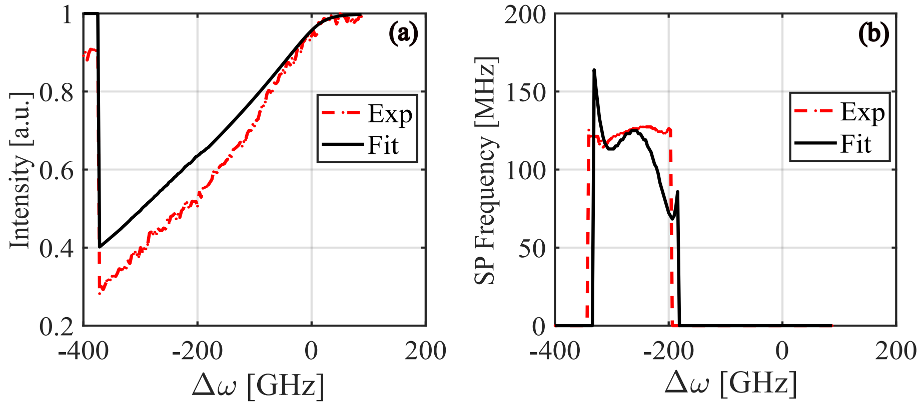

Figure 3.12: Experimental transmission spectra panel (a) and self-pulsing (SP) frequency panel (b) as a function of detuning for a reverse bias of −1 V. Red dashed curves represent the experimental data, while black solid curves correspond to the theoretical fit, showing good agreement across the full detuning sweep.

where Δ_{laser} is the laser detuning, while $\Delta_{\text{th}}(T)$ and $\Delta_{\text{fc}}(N)$ denote the thermally induced and free-carrier–induced resonance shifts, respectively. A pushed transmission branch only requires the existence of a nonlinear steady-state solution of the coupled field–carrier–thermal rate equations, characterized by a nonzero dependence of Δ_{eff} on the intracavity power $P = |a|^2$. In contrast, SP corresponds to a Hopf instability of this steady state and arises when the delayed nonlinear feedback provided by the carrier and thermal dynamics causes the real part of an eigenvalue of the Jacobian to become positive, $\text{Re}(\lambda_{\max}) > 0$. Under reverse bias, carrier sweep-out reduces the effective carrier lifetime τ_{fc} and enhances free-carrier absorption, thereby increasing the effective cavity loss and suppressing the delayed feedback strength required for the Hopf instability. As a result, the condition $\text{Re}(\lambda_{\max}) > 0$ is no longer satisfied at smaller detuning, leading to the disappearance of SP. However, because the thermal nonlinearity evolves on a much slower timescale ($\tau_{\text{th}} \gg \tau_{\text{fc}}$), the nonlinear steady-state solution remains stable over a wider detuning range, allowing the transmission to remain in the pushed branch until the steady state collapses via a saddle-node bifurcation, at which point the transmission jumps back to unity. In contrast, at 0 V bias the longer carrier lifetime preserves sufficient delayed feedback such that the Hopf bifurcation and the collapse of the nonlinear steady state occur at nearly the same detuning, causing SP to disappear simultaneously with the transmission recovery.

From the transmission fit in the non-linear regime, we extract a radiative loss rate of $\gamma_{\text{rad}} = 3.63 \times 10^{10}$ rad/s, an effective absorption loss of $\gamma_{\text{abs}} = 1.69 \times 10^{10}$ rad/s, and a coupling rate of $\gamma_{\text{coup}} = 7.58 \times 10^{9}$ rad/s. Compared to linear resonator characterization ($\gamma_{\text{rad}}^{(\text{lin})} = 4.58 \times 10^{10}$ rad/s, $\gamma_{\text{abs,lin}}^{(\text{lin})} = 2.18 \times 10^{8}$ rad/s, and $\gamma_{\text{coup}}^{(\text{lin})} = 1.54 \times 10^{10}$ rad/s), the non-linear fit reveals a reduction of the radiative loss by approximately 21% and of the coupling rate by approximately 51%, while the effective absorption loss increases by nearly two orders of magnitude.

Despite these pronounced changes in individual loss channels, the total cavity loss remains nearly conserved. The total loss rate extracted from the non-linear transmission fit is $\gamma_{\mathrm{tot}}^{(-1\mathrm{V})} = 6.08 \times 10^{10}\,\mathrm{rad/s}$, which differs by only $\sim 1\%$ from the linear value $\gamma_{\mathrm{tot}}^{(\mathrm{lin})} = 6.14 \times 10^{10}\,\mathrm{rad/s}$. This indicates that, although the individual loss mechanisms are significantly modified under reverse bias, the non-linear dynamics primarily redistribute dissipation among radiation, coupling, and absorption channels. So the asummption of keeping the total loss same from the linear fit still hold true for the fit of -1 V.

At -1 V, the free-carrier lifetime is $\tau_{\mathrm{fc}} = 0.100\,\mathrm{ns}$, and the thermal relaxation time is $\tau_{\mathrm{th}} = 35.69\,\mathrm{ns}$, while the carrier-induced refractive index change is characterized by $\mathrm{d}n/\mathrm{d}N = -1.0864 \times 10^{-27}\,\mathrm{m}^3$. These values can be directly compared with the parameters obtained at 0 V, listed in Table 3.1.

Quantitatively, the carrier-induced refractive index coefficient changes by only $\sim 7.6\%$, increasing in magnitude from $\mathrm{d}n/\mathrm{d}N = -1.01 \times 10^{-27}\,\mathrm{m}^3$ at 0 V to $\mathrm{d}n/\mathrm{d}N = -1.0864 \times 10^{-27}\,\mathrm{m}^3$ at -1 V, confirming that the plasma-dispersion response remains largely bias-independent. Similarly, the thermal relaxation time decreases by only $\sim 6.5\%$, from $\tau_{\mathrm{th}} = 38.16$ ns at 0 V to $\tau_{\mathrm{th}} = 35.69$ ns at -1 V, indicating that the thermal dynamics are only weakly affected by the applied reverse bias. In contrast, the free-carrier lifetime is reduced by more than an order of magnitude, highlighting that the dominant effect of reverse bias is the acceleration of carrier dynamics rather than modifications to thermal or refractive material parameters.

This demonstrates that reverse bias primarily modifies the carrier dynamics without significantly altering the intrinsic optical properties of the resonator. While the individual loss channels are strongly redistributed—most notably through enhanced effective absorption and reduced external coupling—the total cavity loss remains nearly unchanged, validating our assumption of a bias-independent total loss in the non-linear fitting procedure.This redistribution of loss channels can be consistently interpreted within the coupled-mode framework of the bus–ring interface. In particular, the observed reduction in external loss under reverse bias corresponds to a decrease in the effective coupling between the bus waveguide and the ring resonator. In the language of coupled-waveguide theory, reverse bias modifies the local refractive index via free-carrier depletion, thereby changing the propagation constant of the ring mode relative to that of the bus waveguide. This induces a finite propagation-constant mismatch, $\Delta\beta = \beta_{\mathrm{bus}} - \beta_{\mathrm{ring}}$, which suppresses power transfer between the two guides. As shown by the coupled-mode equations, a nonzero $\Delta\beta$ reduces the maximum coupling efficiency according to $P_{2,\mathrm{max}} = \kappa^2/(\kappa^2 + (\Delta\beta/2)^2)$, effectively weakening the external coupling without requiring a change in the physical gap or overlap

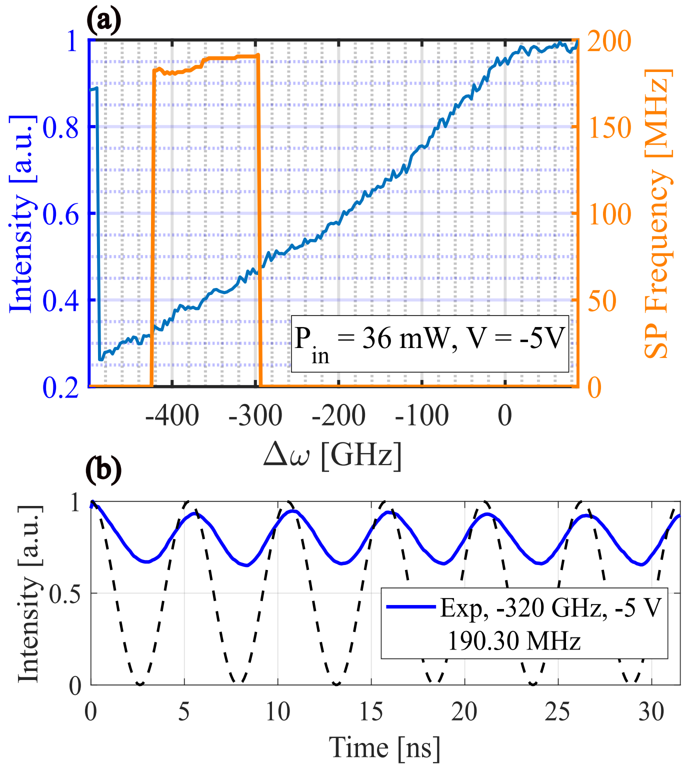

Figure 3.13: Panel (a) shows the experimental transmission spectra and self-pulsing (SP) frequency as a function of detuning for a reverse bias of −5 V. Panel (b) shows the experimental temporal waveform measured at a selected detuning of −320 GHz within the SP detuning window at −5 V, confirming stable self-pulsing dynamics in the time domain.

integral. Consequently, while the intrinsic absorption increases due to enhanced carrier-related loss mechanisms, the reduced evanescent coupling compensates for this change, leaving the total cavity loss nearly unchanged. This explains why reverse bias primarily alters the carrier dynamics—manifested as a persistent reduction in the free-carrier lifetime—while preserving a bias-independent total loss, thereby justifying the assumptions employed in the nonlinear detuning-sweep fitting procedure. Whereas persistant substantial reduction in free-carrier lifetime under reverse bias at the total detuning sweep fit at -1 V validates also our previous results where the carrier life time is decreased.

Figure 3.13(a) shows the experimental transmission and self-pulsing (SP) frequency map measured at an input power of 36 mW, with the laser swept over the indicated detuning range under a reverse bias of −5 V. Compared to the 0 V and −1 V cases, the SP frequency window is noticeably shifted toward larger negative detuning values. In addition, the SP frequency drops to zero already at a detuning of approximately −200 GHz. At the same time, the overall SP frequency range over the detuning values is compressed at the same time SP frequencies reaching up to 190 MHz. Consistently, the transmission resonance dip is also shifted toward lower detuning values compared to the 0 V and −1 V cases, reflecting the stronger bias-induced modification of the intracavity dynamics.

Panel (b) shows the experimentally measured temporal waveform at a selected detuning of −320 GHz within the self-pulsing (SP) window at a reverse bias of −5 V. The time trace exhibits a smooth and nearly sinusoidal oscillation with a frequency of approximately 190 MHz, confirming stable self-pulsing behavior in the time domain. Notably, the asymmetry observed in the oscillations at lower reverse biases is no longer present, and the temporal waveform becomes nearly sinusoidal. This transition reflects a suppression of higher-order nonlinear contributions associated with the delayed free-carrier dynamics. At high reverse bias, rapid carrier sweep-out significantly shortens the free-carrier lifetime, reducing the phase lag between the intracavity optical field and the carrier-induced refractive index change. As a consequence, the system dynamics are dominated by a single oscillation frequency with reduced waveform distortion. Upon further increasing the reverse bias to −7 V, self-pulsing is no longer observed over the entire detuning range. At this bias, the free-carrier lifetime is sufficiently reduced that the carrier-induced refractive index modulation becomes too weak to destabilize the steady-state solution. Consequently, the system remains in a stable fixed point, as the carrier-mediated nonlinear feedback is unable to overcome cavity losses and damping required to sustain a Hopf instability.

3.7 Comparison to previous work

Unlike prior diode-integrated silicon resonator studies, where the free-carrier lifetime is obtained from pump–probe measurements, relaxation-time fitting, or treated as a phenomenological parameter, in this work $\tau_{\mathrm{fc}}(V)$ is directly extracted from the measured self-pulsing frequency under fixed optical power and laser–cavity detuning. Table 3.5 shows this work to the previous work comparison in the extraction of the free carrier life time and the methods used to do so.

3.8 Conclusion

In this chapter, we investigated optical non-linear control in a p-n embedded silicon microring resonator, with a focus on self-pulsing (SP) driven by the coupled dynamics of two-photon absorption (TPA), free-carrier effects (FCD/FCA), and thermo-optic (TO) resonance shifting. Using a temporal coupled-mode theory (TCMT) framework augmented with carrier and thermal rate equations, we established a unified dynamical model in which the intracavity field, carrier density, and temperature form a non-linear delayed-feedback

Table 3.5: Comparison of silicon microring resonator studies on self-pulsing (SP), free-carrier lifetime (τ_{fc}) treatment, and reverse-bias control of oscillation dynamics.

Reference	Device / Junction (Si Microring)	SP Studied	Method to Estimate τ_{fc}	Reverse-Bias Control of SP Frequency	Operating Conditions (Power & Detuning)	Reverse-Bias Range	Highest Reported SP Frequency
[146]	Silicon ring cavities with free-carrier dynamics (theoretical, PIN-controlled carrier sweep-out discussed)	Yes (free-carrier oscillations and instability regimes)	τ_{fc} treated as a key tunable parameter in nonlinear dynamical coupled-mode theory	Predicted influence via carrier lifetime reduction (no direct experimental bias sweep)	Systematically analyzed versus pump power and detuning in stability maps	Not experimentally specified (theoretical treatment)	Not the primary metric (focus on oscillation conditions and instability thresholds)
[152]	Silicon microring with lateral diode (free-carrier removal platform)	Indirect (multistability and dynamical relaxation near instability)	τ_{fc} implicitly included in carrier–thermal dynamical model and fitted to relaxation behavior	No explicit SP-frequency tuning via reverse bias demonstrated	Nonlinear dynamics analyzed over detuning and input power regimes	Reverse bias applied for carrier removal (exact SP tuning range not the focus)	SP frequency not explicitly reported (focus on relaxation dynamics)
[142]	PIN-integrated silicon microring resonator on chip	Yes (self-pulsing oscillator)	Qualitative lifetime reduction due to carrier sweep-out under reverse bias	Yes, SP frequency increases with reverse bias	Power and detuning considered, but not strictly fixed during bias–frequency scaling	Small reverse-bias regime (few volts)	~10–30 MHz (multi-MHz self-pulsing regime)
[153]	Silicon microring resonator (carrier–thermal nonlinear dynamics model)	Yes (oscillatory and instability regimes modeled)	Temporal coupled-mode theory with carrier rate equation (τ_{fc} as fitting/model parameter)	No electrical bias control of SP frequency	Detailed detuning-dependent nonlinear dynamics and stability analysis	No junction bias (passive nonlinear microring model)	Frequency scale determined by model parameters (not bias-tuned experimentally)
[39]	PN-junction embedded silicon microring resonator (CMOS SOI platform)	Yes (experimental SP and bistability)	τ_{fc} calculated from interface recombination model and fitted in CMT-based simulations (e.g., ~3 ns to ~30 ps with probe)	No; reverse bias suppresses SP by strongly shortening carrier lifetime	Explicit mapping of SP versus input power (8–11 dBm) and wavelength detuning	Reverse bias applied (e.g., probe condition around ~-1 V)	~10–18 MHz
This Work	Lateral PN-integrated silicon microring resonator (SOI, CMOS-compatible)	Yes (stable and bias-tunable self-pulsing)	Direct extraction via SP-frequency-to-model matching using nonlinear temporal coupled-mode theory with $\tau_{fc}(V)$ as the only varying parameter	Yes; monotonic increase of SP frequency with reverse bias at fixed optical power and selected detuning values	Explicitly measured at fixed input power (e.g., 36 mW) and controlled laser–cavity detuning sweeps	0 V to ~-5 V (reverse bias)	Up to ~190 MHz

loop. This model reproduces the transition from stable continuous-wave operation to limit-cycle oscillations and captures the characteristic dependence of SP on input power and laser–cavity detuning.

Low-power measurements provided a consistent linear calibration of the resonator response, enabling extraction of the coupling and loss rates and validating the baseline operating point of the device under forward- and reverse-bias conditions. In the high-power regime (P_{in} = 36 mW), we experimentally observed robust SP oscillations over a finite red-detuned window. At fixed optical power and detuning, applying reverse bias across the p-n junction produced a systematic acceleration of the SP dynamics: the oscillation frequency increased monotonically with increasing reverse bias, directly demonstrating electrical control of the non-linear limit cycle. This trend is consistent with carrier sweep-out in the depletion regime, which reduces FCA and, more importantly, shortens the effective free-carrier lifetime, thereby reducing the feedback delay that sets the oscillation period.

By first fitting the unbiased (0 V) SP response using a constrained SP-only particle swarm optimization procedure, we established a physically consistent parameter set that isolates the key non-linear timescales of the system. The extracted values, $\tau_{fc} \approx 2.90$ ns and $\tau_{th} \approx 38$ ns, confirm the expected two-time-scale nature of SP in silicon microrings: fast carrier dynamics shape the high-frequency modulation, while slower thermal relaxation provides the restoring mechanism required for relaxation-type oscillations. Holding the remaining parameters fixed, we then extracted the voltage-dependent free-carrier lifetime

$\tau_{\mathrm{fc}}(V)$ directly from the measured SP frequency at a fixed detuning. The inferred lifetime decreases sharply with modest reverse bias and saturates at sub-nanosecond values, quantitatively linking the observed frequency enhancement to electrically accelerated carrier removal. A simple saturation model accurately describes this behaviour and highlights that relatively small reverse biases already push the device close to its carrier-extraction limit.

Finally, mapping the model response for representative extracted lifetimes showed that decreasing τ_{fc} reshapes the non-linear stability landscape: the SP detuning window narrows while the achievable oscillation frequency increases. This trade-off provides a practical design and operating guideline for electrically tunable non-linear oscillators based on silicon microrings: reverse bias enables higher-speed SP operation, but over a reduced detuning range.

Overall, the results demonstrate that p-n integration provides an effective electrical knob to control self-pulsing in silicon microring resonators by tuning the free-carrier lifetime, enabling compact, bias-tunable on-chip oscillators. These findings are directly relevant for integrated microwave photonics, optical signal processing, and non-linear frequency generation, and they motivate future work on extending the controllable bias range, improving thermal engineering to stabilize or broaden the oscillation window, and exploring injection-locking or synchronization schemes for low-noise, application-oriented SP sources.

Table 3.6: List of all parameters used in the simulations shown in Fig. 3.4 and Fig. 3.5.

Symbol	Description	Value	Units	Source
c	Speed of light	3.0×10^{8}	$\mathrm{m\,s^{-1}}$	Constant
$\hbar$	Reduced Planck constant	$1.054\,571\,8 \times 10^{-34}$	$\mathrm{J\,s}$	Constant
λ_r	Resonant wavelength	1549.7	nm	Exp
ω_0	Resonant frequency	$2\pi c/\lambda_r$	$\mathrm{rad\,s^{-1}}$	Exp
γ_{rad}	Radiative loss rate	4.58×10^{10}	$\mathrm{rad\,s^{-1}}$	Fit
$\gamma_{\mathrm{abs,lin}}$	Linear absorption rate	2.18×10^{8}	$\mathrm{rad\,s^{-1}}$	Fit
γ_{coup}	Bus coupling rate	1.54×10^{10}	$\mathrm{rad\,s^{-1}}$	Fit
κ	Field coupling amplitude	$i\sqrt{\gamma_{\mathrm{coup}}}$	$\mathrm{s^{-1/2}}$	Fit
n_g	Group index	3.476	–	[148]
σ_{Si}	FCA cross section	1×10^{-21}	$\mathrm{m^2}$	[148]
ρ_{Si}	Silicon density	2330	$\mathrm{kg\,m^{-3}}$	[38]
C_p^{Si}	Silicon heat capacity	700	$\mathrm{J\,kg^{-1}\,K^{-1}}$	[38]
Γ_{FCA}	FCA modal overlap	0.9996	–	Simulation
Γ_{TPA}	TPA modal overlap	0.9964	–	Simulation
Γ_{th}	Thermal overlap	0.9355	–	Simulation
V_{FCA}	Free-carrier volume	2.36×10^{-18}	$\mathrm{m^3}$	Simulation
V_{TPA}	TPA volume	2.59×10^{-18}	$\mathrm{m^3}$	Simulation
V_{th}	Thermal volume	3.19×10^{-18}	$\mathrm{m^3}$	Simulation
β_{Si}	TPA coefficient	8.4×10^{-12}	$\mathrm{m\,W^{-1}}$	[148]
τ_{fc}	Free-carrier lifetime	5×10^{-9}	s	Bias dependent
dn/dN	Plasma-dispersion coefficient	-1.73×10^{-27}	$\mathrm{m^3}$	[148]
τ_{th}	Thermal relaxation time	55×10^{-9}	s	Fit
dn/dT	Thermo-optic coefficient	1.86×10^{-4}	$\mathrm{K^{-1}}$	[148]
c_4	FCA loss coefficient	$\Gamma_{\mathrm{FCA}}\sigma_{\mathrm{Si}}c/n_g$	$\mathrm{m^3\,s^{-1}}$	Derived
c_3	TPA loss coefficient	$\Gamma_{\mathrm{TPA}}\beta_{\mathrm{Si}}c^2/(n_g^2 V_{\mathrm{TPA}})$	$\mathrm{(J\,s)^{-1}}$	Derived
c_2	Carrier generation coefficient	$\Gamma_{\mathrm{FCA}}\beta c^2/(2\hbar\omega_0 V_{\mathrm{FCA}}^2 n_g^2)$	$\mathrm{m^{-3}\,J^{-2}\,s^{-1}}$	Derived

Chapter 4

Non-Hermitian Coupled Microring Resonator Circuits - Taiji- CROW

4.1 Introduction

In the previous chapters, we explored active control of optical effects in silicon photonics through both thermo-optic and electro-optic mechanisms. The first approach, implemented using a 3×3 coupled-waveguide structure with an integrated microheater, demonstrated dynamic tuning and routing of light among different waveguides via thermal modulation in linear regime. The second approach employed a p-n integrated microring resonator, where carrier injection and depletion under reverse bias enabled electro-optic tuning of the resonance condition and control over the self-pulsing frequencies arising from non-linear interactions.

Building on these foundations, we now turn to a new frontier in integrated photonics: the realization of *Hermitian* and *non-Hermitian* behavior through engineered coupling in microring resonator circuits. In contrast to purely index-based modulation or symmetrical evanescent coupling, these systems intentionally incorporate directional coupling to reshape the underlying Hamiltonian of the device. Such control expands the design space of silicon photonics, enabling phenomena such as chiral light transport, linewidth redistribution, and the emergence of exceptional points within CMOS-compatible platforms.

This shift from conventional refractive-index engineering to Hamiltonian-level control is closely aligned with broader efforts to emulate concepts from condensed-matter physics in photonic structures. The discovery of the integer quantum Hall effect, revealing quantized Hall conductance as a hallmark of topological order [154], inspired analogous explorations in optical systems, where coupled microring resonators can be arranged into periodic lattices that mimic electronic tight-binding models. Such photonic lattices reproduce features such as Hofstadter's butterfly [155] and support unidirectional edge transport without requiring magnetic fields, as shown in a range of seminal works [156–161].In these photonic lattices, synthetic gauge phases are introduced within each unit cell, giving rise to optical edge states that are resilient to disorder and backscattering. Early demonstrations achieved such synthetic magnetic fields using two-dimensional plaquettes composed of four site MRs connected via auxiliary coupling rings [156, 157].

However, in realistic nanophotonic platforms, surface roughness and fabrication imperfections couple the forward (CW) and backward (CCW) propagating modes, degrading chirality and compromising the topological protection of optical modes by mediating spin-mixing inside each site resonator. To preserve directional transport in topological microring lattices, one must operate in a regime where the designed complex coupling pathways and gain-selection mechanisms overwhelm disorder-induced backscattering. Imposing a synthetic gauge flux in coupled-ring arrays and selectively amplifying the chiral edge band has enabled the realization of topological chiral lasers whose edge emission remains robust against disorder [162–167]. In these systems, the suppression of backscattering is not solved inside the ring itself, but rather at the network level by enforcing a spectrally isolated unidirectional edge supermode that survives perturbations.

A distinct and complementary strategy is to modify the internal scattering channels of each site resonator so that the device itself becomes asymmetric at the modal level. A key element in this direction is the *Taiji microring resonator* — a ring resonator incorporating an internal S-shaped waveguide that implements directional CW $\rightarrow$ CCW conversion while suppressing the reverse process [168]. The S-bend therefore acts as an internal non-Hermitian directional coupler, creating controllable chirality that recycles backscattered amplitude into the lasing spin, thereby mitigating detrimental spin-mixing in topological microring matrices [25, 105, 158, 169, 170]. This Taiji-based mitigation has been theoretically proposed and analysed to stabilize single-pseudospin lasing in topological CROWs even in the presence of realistic disorder [170]. Nevertheless, practical implementation remains sensitive to fabrication tolerances and refractive-index fluctuations, which can partially offset the intended nonreciprocity and shift the resonance condition [62, 170].

In this chapter, we present the analysis, design, and experimental realization of a coupled microring resonator circuit based on Taiji resonators — referred to as the **Taiji-CROW** (Taiji- Coupled Resonator Optical Waveguide). The system consists of two taiji microrings connected by an intermediate link ring, forming a minimal non-Hermitian photonic system with tailored inter-ring coupling and asymmetric intra-ring scattering. By systematically quantifying the ratio between inter-resonator coupling and parasitic backscattering from

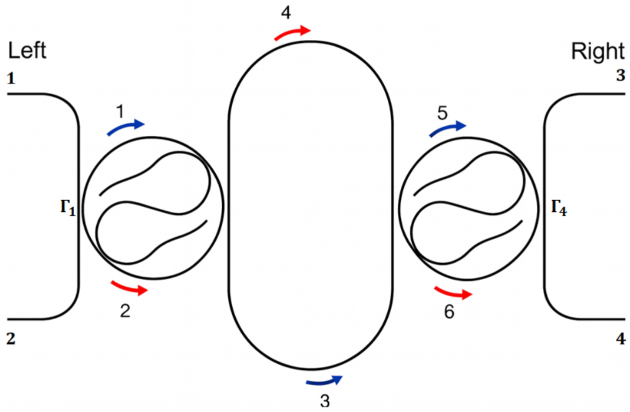

Figure 4.1: **The Taiji–CROW device.** Two Taiji microrring resonators (left and right) are coupled via a middle "link" microresonator. Starting from the left Taiji ring, the CW (CCW) mode is indicated by a numbered black (red) arrow beneath the resonator. The same color coding is preserved through the coupled-resonator chain: $1 \rightarrow 3 \rightarrow 5$ correspond to CW (black), and $2 \rightarrow 4 \rightarrow 6$ correspond to CCW (red).

the experimental results through fitting the model, we derive design rules for achieving robust chiral coupling and preserving non-Hermitian features in silicon photonic circuits. These results provide practical guidelines for implementing scalable topological and non-Hermitian photonic architectures within CMOS-compatible integrated platforms.

4.2 The Physical System and Theoretical Model

Figure 4.1 shows the Taiji-CROW structure, composed of two Taiji microring resonators (MRs) coupled through a central link MR and interfaced with two parallel bus waveguides that define four optical I/O ports at their terminations. Each Taiji resonator integrates an S-shaped waveguide that enforces directional mode conversion: the clockwise (CW) mode is coupled into the counter-clockwise (CCW) mode, while the reverse process (CCW→CW) is strongly suppressed. This asymmetric intermodal coupling breaks Hermitian reciprocity and renders the Taiji resonators intrinsically non-Hermitian [44, 111, 168].

Within the TCMT, the propagating modes obey the differential equation [111]:

$$i\frac{d\boldsymbol{\alpha}}{dt} = \mathbf{H}\boldsymbol{\alpha} - \mathbf{E}\,. \tag{4.1}$$

where bold symbols are vectors or matrices. $\boldsymbol{\alpha}$ is the vector associated with the field amplitude of the modes in each MR where the elements are α_j, with j=1, ..., 6 as in Fig.4.1. $\mathbf{E}$ is the vector associated with the input electric fields, such that

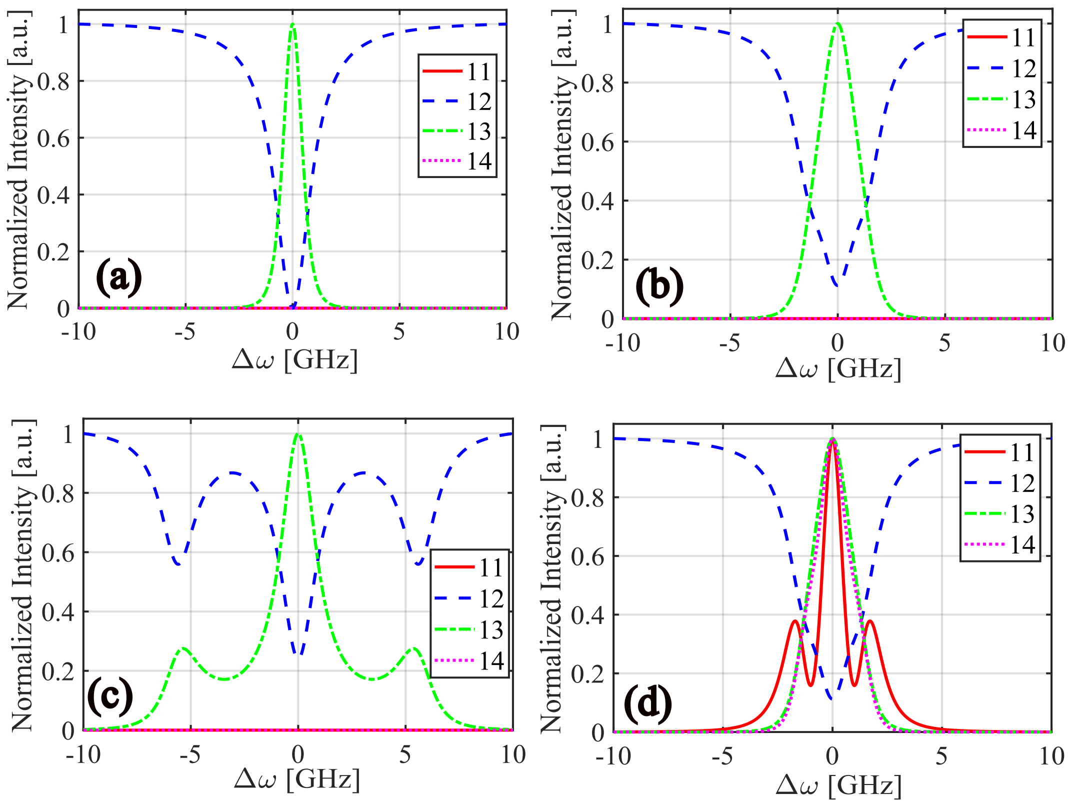

Figure 4.2: **Simulation: Transmission and reflection spectra under excitation from port 1.** The Taiji–CROW is simulated with the S-waveguide coupling disabled and with no intrinsic backscattering unless otherwise stated. In the legends, the first digit denotes the input port and the second digit denotes the output port. This convention is used throughout this chapter unless stated otherwise. Panels (a)–(c) show spectra for three values of the normalized coupling ratio $\beta/\gamma_t = 0.04$, 1, and 4, all with zero backscattering, $\beta_{bs} = 0\,\mathrm{GHz}$. Panel (d) corresponds to $\beta/\gamma_t = 1$ with a finite backscattering amplitude of $\beta_{bs} = 0.01\,\mathrm{GHz}$ applied uniformly to all rings and Taiji coupling set to $\beta_{t,1} = \beta_{t,2} = 0.04\,\mathrm{GHz}$. The directional coupling coefficients are defined as β_{ij} (GHz) and are chosen equal as $\beta_{13} = \beta_{24} = \beta_{35} = \beta_{46} \equiv \beta$ (GHz), with backward couplings satisfying $\beta_{ji} = -\beta_{ij}^*$. The backscattering couplings are taken identical, $\beta_{12} = \beta_{34} = \beta_{56} \equiv \beta_{bs}$ (GHz), with the corresponding reverse couplings given by $\beta_{21} = \beta_{43} = \beta_{65} = -\beta_{bs}^*$. The resonant frequencies are set equal, $\omega_1 = \omega_2 = \omega_3 = 0\,\mathrm{GHz}$, and the detunings are defined as $\Delta\omega = \omega - \omega_i$ (GHz).

$$\mathbf{E} = \begin{bmatrix} \sqrt{2\Gamma_1}\, E_{\mathrm{in},2} \\ \sqrt{2\Gamma_1}\, E_{\mathrm{in},1} \\ 0 \\ 0 \\ \sqrt{2\Gamma_4}\, E_{\mathrm{in},3} \\ \sqrt{2\Gamma_4}\, E_{\mathrm{in},4} \end{bmatrix}. \tag{4.2}$$

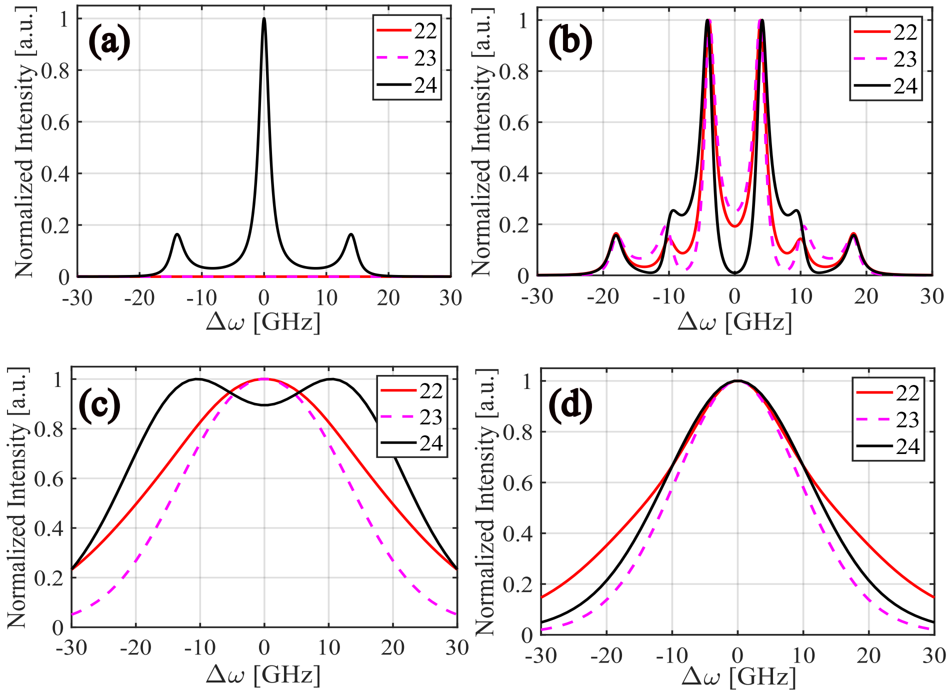

Figure 4.3: **Theory simulation of the Taiji–CROW response under excitation from port 2.** In the legends, the first digit denotes the input port and the second digit denotes the output port. This convention is used throughout this chapter unless stated otherwise. All parameters are expressed in units of GHz. The inter-resonator coupling is set to $\beta_{13} = 10$ with $\beta_{35} = \beta_{13}$, $\beta_{24} = \beta_{35}$, and $\beta_{46} = \beta_{24}$. Backscattering is $\beta_{12} = 4$ and Hermitian symmetry is imposed via $\beta_{21} = -\beta_{12}^*$, $\beta_{31} = -\beta_{13}^*$, $\beta_{43} = -\beta_{34}^*$, $\beta_{65} = -\beta_{56}^*$, $\beta_{53} = -\beta_{35}^*$, $\beta_{42} = -\beta_{24}^*$, and $\beta_{64} = -\beta_{46}^*$. The S-branch couplings satisfy $\Gamma_{S2} = \Gamma_{S1}$ and $\Gamma_{S3} = \Gamma_{S1}$, and the Taiji couplings satisfy $\beta_{t2} = \beta_{t1}$. Rings 1 and 4 are coupled to the bus waveguides with $\Gamma_1 = \Gamma_4 = \gamma_{\text{int}} + 2\Gamma_S$, where $\gamma_{\text{int}} = 0.5$. The total losses are $\gamma_{t,1} = \gamma_{t,3} = \Gamma_1 + \gamma_{\text{int}} + 2\Gamma_S$ and $\gamma_{t,2} = 2\Gamma_1 + \gamma_{\text{int}}$. Panels: (a) $\Gamma_S = 0$ and backscattering disabled; (b) $\Gamma_S = 0$ and backscattering enabled ($\beta_{12} = 4$); (c) backscattering disabled and Taiji coupling enabled with $\Gamma_S = 4$ (i.e. $\beta_{t1} = \beta_{t2} = 4\Gamma_S$); (d) both backscattering ($\beta_{12} = 4$) and Taiji coupling ($\Gamma_S = 4$) enabled.

Here Γ_1 and Γ_4 are the coupling coefficients (coupling rates) between the bus waveguide and the taiji MR. The 6×6 Hamiltonian $\mathbf{H}$ in Eq. (4.1) can be written as

$$\mathbf{H} = \begin{bmatrix} \omega_1 - i\gamma_{t,1} & -i\beta_{21} & -i\beta_{31} & 0 & 0 & 0 \\ -i\beta_{t,1} - i\beta_{12} & \omega_1 - i\gamma_{t,1} & 0 & -i\beta_{42} & 0 & 0 \\ -i\beta_{13} & 0 & \omega_2 - i\gamma_{t,2} & -i\beta_{43} & -i\beta_{53} & 0 \\ 0 & -i\beta_{24} & -i\beta_{34} & \omega_2 - i\gamma_{t,2} & 0 & -i\beta_{64} \\ 0 & 0 & -i\beta_{35} & 0 & \omega_3 - i\gamma_{t,3} & -i\beta_{65} \\ 0 & 0 & 0 & -i\beta_{46} & -i\beta_{56} - i\beta_{t,2} & \omega_3 - i\gamma_{t,3} \end{bmatrix}. \tag{4.3}$$

where ω_i are the MR resonance frequencies (i=1,2 and 3 for the left taiji MR, the link MR and the right taiji MR, respectively), $\gamma_{t,i}$ are the total loss rates (includes intrinsic and extrinsic damping rates) and β_{ij} are the intermodal coupling coefficients. Here, the single digit subscripts 1, 2 and 3 are used to represent MRs, while two-digit subscripts refer to the coupling between different modes; for example, β_{21} coupling of α_2 to α_1 whereas $\beta_{t,1}$ and $\beta_{t,2}$ shows the coupling from α_1 to α_2 and α_5 to α_6 respectively through the S-shape waveguide. **H** in (4.1) refers to general Hamiltonian with system with backscattering and coupling from the S shape waveguides and assumes that all the waveguides are single-mode. It is also worth mentioning that $\gamma_{t,i}$ and Γ_i are real numbers while β_{ij} are complex numbers. The input and output fields are related by [111]:

$$\begin{bmatrix} E_{\text{out},1} \\ E_{\text{out},2} \end{bmatrix} = \begin{bmatrix} E_{\text{in},2} \\ E_{\text{in},1} \end{bmatrix} + i\sqrt{2\Gamma_1} \begin{bmatrix} \alpha_1 \\ \alpha_2 \end{bmatrix}, \tag{4.4a}$$

$$\begin{bmatrix} E_{\text{out},3} \\ E_{\text{out},4} \end{bmatrix} = \begin{bmatrix} E_{\text{in},4} \\ E_{\text{in},3} \end{bmatrix} + i\sqrt{2\Gamma_4} \begin{bmatrix} \alpha_6 \\ \alpha_5 \end{bmatrix}, \tag{4.4b}$$

where in the steady state the propagating modes and electric fields are in the form of $\alpha = ae^{-i\omega t}$ and $E = \varepsilon e^{-i\omega t}$, respectively.

To understand how light propagates through the Taiji-CROW, we first set the backscattering to zero and compute the output response as a function of the frequency detuning $\Delta\omega = \omega - \omega_1$ for the case $\omega_1 = \omega_2 = \omega_3$. The inter-resonator coupling is fixed to $\beta_{13} = 10\,\text{GHz}$ with the relations $\beta_{35} = \beta_{13}, \beta_{24} = \beta_{35}$, and $\beta_{46} = \beta_{24}$. When backscattering is introduced, it is set to $\beta_{12} = 4\,\text{GHz}$, with the Hermitian relations $\beta_{21} = -\beta^*_{12}, \beta_{31} = -\beta^*_{13}, \beta_{43} = -\beta^*_{34}$, $\beta_{65} = -\beta^*_{56}, \beta_{53} = -\beta^*_{35}, \beta_{42} = -\beta^*_{24}$, and $\beta_{64} = -\beta^*_{46}$. The S-shaped waveguide coupling losses are defined as $\Gamma_{S2} = \Gamma_{S1}$ and $\Gamma_{S3} = \Gamma_{S1}$, and the S-coupling strength is set to $\beta_{t2} = \beta_{t1}$. Rings 1 and 3 are coupled to the bus waveguides with losses $\Gamma_1 = \Gamma_4 = \gamma_{\text{int}} + 2\Gamma_S$ in the critical-coupling regime, with intrinsic loss fixed at $\gamma_{\text{int}} = 0.5\,\text{GHz}$.

We first analyse the case where light is injected from port 1, which does not couple to the S-shaped waveguide, and therefore the S-coupling is not engaged in this excitation path.The directional coupling coefficients are defined as β_{ij} and are chosen equal as $\beta_{13} = \beta_{24} = \beta_{35} = \beta_{46} \equiv \beta$, with backward couplings satisfying $\beta_{ji} = -\beta^*_{ij}$. Ring 1 and 3 are coupled to the bus waveguides with $\Gamma_1 = \Gamma_4$ and their total losses are given by $\gamma_{\mathrm{t},1} = \gamma_{\mathrm{t},3} = \gamma_{\mathrm{t}} = \Gamma_1 + \gamma_{\mathrm{int}} + 2\Gamma_S$ and link microring has total loss of $\gamma_{\mathrm{t},2} = 2\Gamma_1 + \gamma_{\mathrm{int}}$. The transmission is studied in three regimes by varying the ratio between the inter-resonator coupling and the total loss. In the weak-coupling regime $\beta/\gamma_t = 0.04$, shown in Fig. 4.2(a), transmission occurs only to port 3 at resonance, while ports 2 and 4 show no signal except for a dip at port 2. Increasing the coupling to $\beta/\gamma_{\mathrm{t}} = 1$ leads to peak broadening, indicating the onset of modal interaction [panel (b)]. When the coupling is further increased to $\beta/\gamma_{\mathrm{t}} = 4$, three resonance peaks emerge symmetrically around zero detuning, and transmission still occurs exclusively through port 3, with no signal at ports 1 or 4 [panel (c)].

When a finite backscattering amplitude of $\beta_{\mathrm{bs}} = 0.01$ GHz is applied uniformly to all rings at $\beta/\gamma_t = 1$, and the Taiji coupling is simultaneously turned on with $\beta_{t,1} = \beta_{t,2} = 0.04$ GHz, counter-propagating modes are activated and additional resonant peaks emerge, leading to nonzero transmission at ports 11 and 14 as shown in Fig. 4.2(d). This behavior signifies the onset of reflection and reciprocal coupling induced by backscattering.

In Fig. 4.3, we compute the response under the same detuning condition when the input is instead injected into port 2 and the monitored outputs are ports 22, 23, and 24. The same coupling relations and loss parameters are used. Before analysing the effect of the S-shaped Taiji coupling, we validate the model by first studying the passive backscattering–free configuration with $\beta_{t1} = \beta_{t2} = 0$. Backscattering is then introduced, followed by the activation of the S waveguide coupling.

In panels (a) and (b) the S-shaped waveguide loss is disabled ($\Gamma_S = 0$ GHz), and therefore the S-shaped waveguide coupling is also zero, through the relation $\beta_{t1} = \beta_{t2} = 4\Gamma_S = 0$ GHz. The total ring losses are $\gamma_{\mathrm{t},1} = \gamma_{\mathrm{t},3} = \Gamma_1 + \gamma_{\mathrm{int}} + 2\Gamma_S$ (GHz) and $\gamma_{\mathrm{t},2} = 2\Gamma_1 + \gamma_{\mathrm{int}}$ (GHz). All microrings are biased to the same resonance frequency (GHz) in the critical-coupling regime. When $\beta/\gamma_t = 10$, with $\Gamma_1 = \Gamma_4 = 0.5$ GHz and $\gamma_{\mathrm{int}} = 0.5$ GHz, and backscattering disabled, no signal is observed at ports 22 and 23. The only transmission appears at port 24, exhibiting three distinct resonance peaks associated with the three-ring chain.

When backscattering is enabled, modal splitting occurs: port 22 exhibits reflection with each of the three peaks splitting into doublets, and the same behaviour is observed at ports 23 and 24 [panel (b)]. Activating the Taiji coupling produces a broad spectral feature at port 24 and in the reflection at port 22, while the doublet structure at port 22 remains. Although the S-shaped coupling increases the total loss and broadens the peaks, it still induces preferential routing towards ports 23 and 22 as it can be seen in panel (c). In contrast, panel (d) corresponds to the case where only the S-shaped coupling is enabled and backscattering remains zero.

These results confirm that backscattering is the sole mechanism responsible for reciprocal mode coupling and spectral splitting, whereas the Taiji geometry selectively suppresses and reshapes these effects through non-Hermitian, direction-dependent coupling.

In 4.3 the backscattering terms are given by β_{12} and β_{21} which couple the counter-propagating modes inside ring 1, β_{34} and β_{43} inside the link ring, and β_{56} and β_{65} inside ring 3. These parameters are complex in general (setting phase and strength of the disorder-induced coupling). In our sign convention (consistent with Eq. (4.3)) the Hermitian relation used in the simulations is

$$\beta_{21} = -\beta_{12}^*, \qquad \beta_{43} = -\beta_{34}^*, \qquad \beta_{65} = -\beta_{56}^*,$$

while the non-Hermitian backscattering corresponds to any violation of these equalities, i.e. to the general case $\beta_{21} \neq -\beta_{12}^*$, $\beta_{43} \neq -\beta_{34}^*$, or $\beta_{65} \neq -\beta_{56}^*$.

while all inter-ring couplings ($\beta_{13}, \beta_{24}, \beta_{35}, \beta_{46}$ and their Hermitian counterparts) and adding Taiji S-waveguide couplings (β_{t1}, β_{t2}) in $\mathbf{H}$ give the non hermitianity. The effect of Backscattering can be clearly seen in the panel 4.2(d) shows new peaks at the previously dark ports 1 and 4 (reflection and cross). Similarly in the excitation from port 2 in (Fig. 4.3)(b). Here the simulations explicitly set a finite backscattering in ring 1 (β_{12} with $\beta_{21} = -\beta_{12}^*$) together with the inter-ring couplings β_{13}, β_{24}, β_{35}, β_{46}. With $\Gamma_S = 0$ (hence $\beta_{t1} = \beta_{t2} = 0$), panels (a)–(b) isolate the action of $\mathbf{H}$: doublets appear at ports 22, 23, and 24, and reflection becomes nonzero at port 22. Activating the Taiji S-coupling ($\Gamma_S > 0$ so $\beta_{t1} = \beta_{t2} = 4\Gamma_S$) in panels (c)–(d) . The result is a broadened, directionally biased response: while backscattering still seeds reflection and splitting, the non-Hermitian, one-way transfer induced by the S-waveguide re-weights the port distribution (enhancing ports 22/23 and reshaping port 24).

The phenomenology above matches the established picture: random sidewall disorder couples CW and CCW modes, producing doublets and reflection [95, 96]. Deterministic scatterers and topology-level asymmetries were introduced to control or reduce this hybridization [97, 101]. More recently, coherent suppression strategies either cancel the effective backscattering via engineered destructive interference [98], or reshape the eigenbasis through non-Hermitian chiral exceptional points so that CW–CCW mixing is

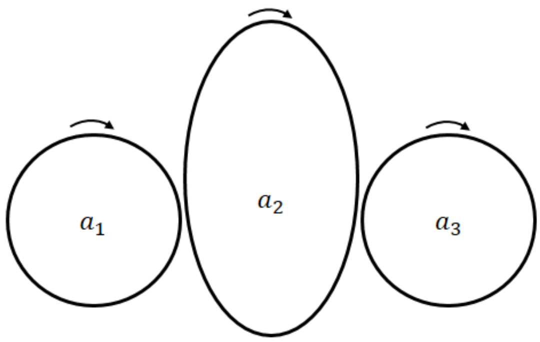

Figure 4.4: Three-ring CROW configuration with each having single mode a_1,a_2 and a_3

intrinsically quenched [99], with complementary cancellation designs demonstrated in silicon microrings [100].

4.3 Off Resonance Condition

To analyze the case in which the link microring is off resonance (its resonance frequency differs from the adjacent Taiji microring resonators, TMRs), we consider the Taiji-CROW with S waveguide coupling disabled by setting $\Gamma_S = 0$ in both TMRs and neglect backscattering this results in a coupled rings configuration as shown in the Fig 4.4. We first assume all microrings share the same isolated resonance frequency ω_0 and then detune only the middle (link) ring. We denote the inter-ring coupling rate, identified with J in the simplified model below, and γ_t the total decay rate.

Let the system be driven at $\omega_d = \omega_0$ so that the outer rings are on resonance, and define the detunings $\Delta_i = \omega_d - \omega_i$ and the decay rates γ_i for rings $i = 1, 2, 3$. Using temporal coupled-mode theory (phasor $e^{-i\omega_d t}$), the steady-state equations are

$$0 = \left(i\Delta_1 - \tfrac{\gamma_1}{2}\right)a_1 - iJ\,a_2 + s_{\text{in}}, \tag{4.5}$$

$$0 = \left(i\Delta_2 - \tfrac{\gamma_2}{2}\right)a_2 - iJ\,(a_1 + a_3), \tag{4.6}$$

$$0 = \left(i\Delta_3 - \tfrac{\gamma_3}{2}\right)a_3 - iJ\,a_2, \tag{4.7}$$

and we choose $\Delta_1 = \Delta_3 = 0$ while allowing $\Delta_2 \neq 0$. Solving the middle equation for a_2 gives

$$a_2 = \frac{iJ}{i\Delta_2 - \gamma_2/2}\,(a_1 + a_3), \tag{4.8}$$

Taking magnitudes yields

$$|a_2| = \frac{|J|}{\sqrt{\Delta_2^2 + (\gamma_2/2)^2}} \, |a_1 + a_3|. \tag{4.9}$$

A sufficient condition to render the middle ring effectively off-resonant (negligible intra-cavity energy compared to the outers) is

$$|\Delta_2| \gg \max\Big(J, \ \tfrac{\gamma_2}{2}\Big), \tag{4.10}$$

since in that regime $\sqrt{\Delta_2^2 + (\gamma_2/2)^2} \approx |\Delta_2|$ and $|a_2| \approx (J/|\Delta_2|)\,|a_1 + a_3| \ll |a_{1,3}|$. In round-trip phase language, if $\phi_i(\omega_d) = \beta(\omega_d)L_i$ with resonance at $\phi_i = 2\pi m$, keep the outers on resonance $\phi_{1,3} = 2\pi m$ and set $\phi_2 = 2\pi m + \delta\phi$ such that $|\delta\phi|$ exceeds the loaded linewidth in radians; this corresponds to $|\Delta_2|$ exceeding the loaded half-linewidth $\gamma_2/2$ by a comfortable margin.

This generic model can be directly mapped to the Taiji–CROW model we previously developed with parameters $J = \beta = 5\,\text{GHz}$, $\gamma_1 = \gamma_2 = \gamma_3 = \gamma_t = 0.2\,\text{GHz}$.

As shown in Fig. 4.5(a), when the excitation is applied at port 2 and the system is operated at a moderate coupling strength with the link ring tuned to the same resonance as the outer rings ($\omega_2 = 0$), the output at port 4 exhibits three distinct transmission maxima as a function of the laser detuning. These three peaks correspond to the three hybridized supermodes of the coupled-ring system when all rings are on resonance and actively participate in the coupling.

In contrast, Fig. 4.5(b) shows the response when the resonance of the link ring is shifted by setting $\omega_2 = 10$ GHz.

the intracavity amplitude in the link ring is suppressed when $|J/\Delta_2| \ll 1$, i.e., when the link ring is strongly detuned relative to the drive. This suppression is directly visible in panel (b): the small peak adjacent to the two dominant peaks corresponds to the residual contribution of the link ring, whose modal participation is already significantly reduced compared to the on-resonance case.

This off-resonant condition of the middle ring can also be interpreted in the phase domain. Writing the round-trip phase as

$$\phi_i(\omega_d) = \beta(\omega_d)L_i, \tag{4.11}$$

with resonance whenever $\phi_i = 2\pi m$ for integer m, the outer two rings are kept on resonance

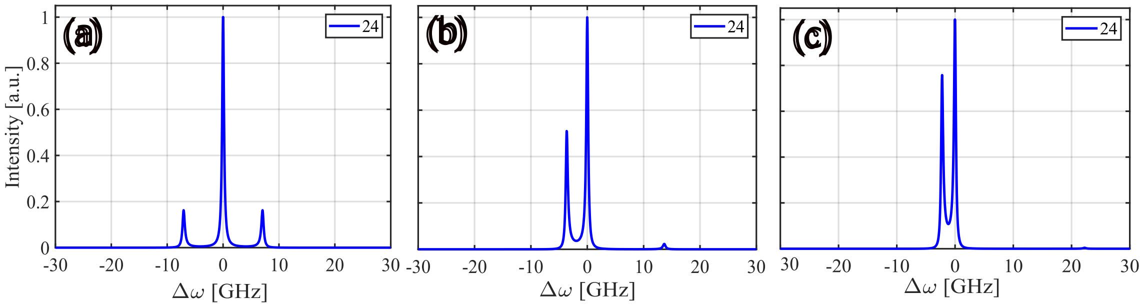

Figure 4.5: **Off-resonance response of the Taiji–CROW with zero backscattering and S-waveguide coupling disabled.** All units are in GHz. Panel (a) corresponds to $\omega_2 = 0$, panel (b) to $\omega_2 = 10$, and panel (c) to $\omega_2 = 20$. The simulation parameters are $\beta = 5$, $\gamma_t = 0.2$, $\Gamma_1 = \Gamma_4 = 0.1$, and intrinsic loss $\gamma_{\text{int}} = 0.1$.

by enforcing $\phi_{1,3} = 2\pi m$, while the link ring is detuned by imposing

$$\phi_2 = 2\pi m + \delta\phi, \tag{4.12}$$

where $|\delta\phi|$ exceeds the loaded linewidth in radians. This phase shift corresponds directly to the frequency detuning Δ_2 used above, and the condition $|\delta\phi| \gg \gamma_2/2$ is equivalent to the requirement $|\Delta_2| \gg \gamma_2/2$ for suppressing the middle-ring buildup.

By further increasing the detuning of the middle ring (larger values of ω_2), the suppression factor $J/|\Delta_2|$ becomes even smaller, driving the middle ring effectively into the off-resonant regime. In this limit, its intracavity energy becomes negligible compared to that of the outer rings, and the small peak on the right side of the two dominant peaks disappears. The spectrum then reduces to only two main peaks, reflecting that the two outer rings remain dynamically coupled while the detuned link ring no longer participates.

This numerical behavior is in full agreement with the theoretical condition derived earlier, namely that the link ring is effectively absent from the coupling chain when

$$|\Delta_2| \gg \max\left(J, \frac{\gamma_2}{2}\right), \tag{4.13}$$

or equivalently in the phase picture when $|\delta\phi| \gg$ linewidth, so that the middle-ring field is suppressed and its influence on the composite spectrum vanishes.

4.4 Taiji - CROW Hopping model

When the link MR is far off resonance and coupling is modest, the full model reduces to an effective "hopping" model connecting the two taiji rings as shown in the 4.6. In the

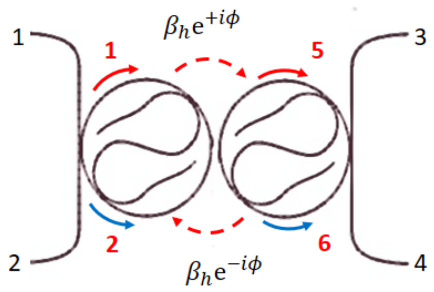

Figure 4.6: **Equivalent hopping–model representation of the Taiji–CROW.** The system consists of two coupled Taiji microrings in the regime where the link microring is detuned (off resonance). The arrows between the two TMRs indicate the effective hopping pathways. The intracavity modes are labeled by their node indices $(1, 2, 5, 6)$.

reduced basis $\boldsymbol{\alpha} = [\alpha_1, \alpha_2, \alpha_5, \alpha_6]$, the 4×4 Hamiltonian reads

$$\mathbf{H}_h = \begin{bmatrix} \omega_1 - i\gamma_{t,1} & -i\beta_{\mathrm{BS},21} & -i\beta_{51} & 0 \\ -i\beta_{t1} - \beta_{\mathrm{BS},12} & \omega_1 - i\gamma_{t,1} & 0 & -i\beta_{62} \\ -i\beta_{15} & 0 & \omega_3 - i\gamma_{t,3} & -i\beta_{\mathrm{BS},65} \\ 0 & -i\beta_{26} & -i\beta_{t2} - \beta_{\mathrm{BS},56} & \omega_3 - i\gamma_{t,3} \end{bmatrix}, \tag{4.14}$$

with complex hoppings $\beta_{15} = \beta_h e^{i\phi}$, $\beta_{51} = -\beta_h e^{-i\phi}$, $\beta_{26} = -\beta_h e^{-i\phi}$, $\beta_{62} = \beta_h e^{i\phi}$. With ϕ being the hopping phase taken with a positive sign for β_{15} and β_{62} and with a negative sign for β_{51} and β_{26}. For the case without backscattering and with the S-waveguide coupling disabled, the transmission of the two coupled microring system at port 4 reduces to the following form:

$$t_{24} = -\frac{2e^{i\phi}\beta_h \Gamma}{-\beta_h^2 + (\Delta\omega + i\gamma_t)^2}, \tag{4.15}$$

where β_h is the hopping (inter–ring coupling) amplitude and ϕ is the associated hopping phase. The detuning is defined as $\Delta\omega = \omega - \omega_0$, with ω_0 the common resonance frequency of the two microrings. The parameter γ_t denotes the total loss rate of an individual ring (intrinsic loss plus coupling loss to the bus waveguide). The spectra plotted in Fig. 4.8 include the transmission through port 4, $|t_{24}|^2$, together with the additional channels labelled “21”, “22”, and “23”; in the configuration shown, channels “22” and “23” are identically zero and are included for completeness.

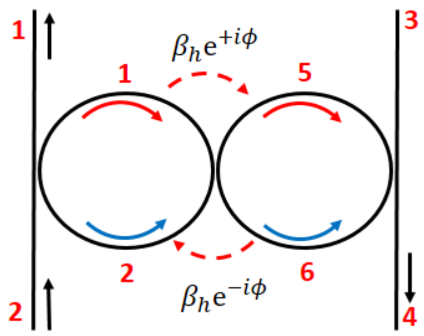

Figure 4.7: **Schematic of two coupled microring resonators with hopping amplitude and phase.** Ports 1–4 denote the input/output terminals depending on the excitation direction, while nodes 1–2–6–5 represent the intracavity modes of the two rings.

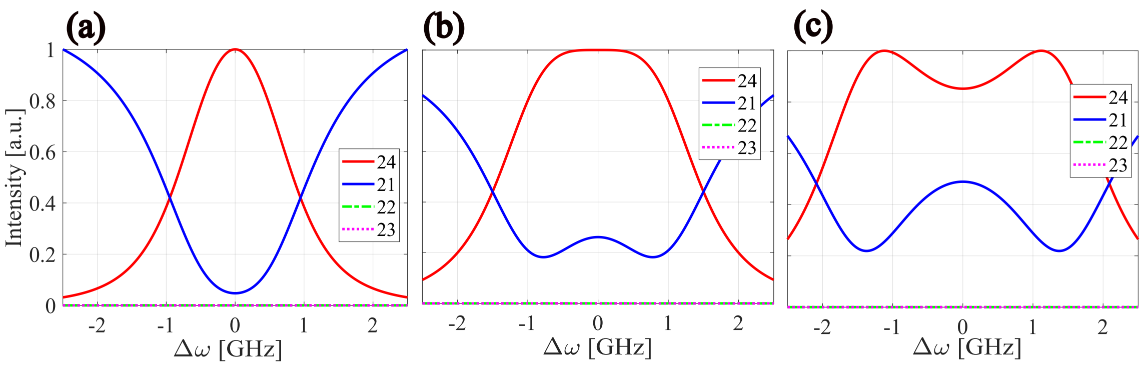

Figure 4.8: **Transmission spectra for ports 21–24 computed using the hopping model.** Panels (a)–(c) correspond to coupling ratios $\beta_h/\gamma_t \in \{0.5, 1, 1.5\}$, respectively. The S-waveguide coupling is disabled ($\beta_t = 0$) and backscattering is neglected ($\beta_{\mathrm{BS},12} = \beta_{\mathrm{BS},56} = 0$). Each plot shows the port-4 transmission $|t_{24}|^2$ together with the additional channels 21, 22, and 23; under the shown conditions, channels 22 and 23 remain zero over all detuning. The horizontal axis is the detuning $\Delta\omega = \omega - \omega_0$.

4.5 Experimental Details

Taiji-CROW devices were designed in silicon photonics with a waveguide cross section of 450 nm x 220 nm embedded in a silica cladding. Taiji MRs have a ring-shaped geometry with a radius of 20 μm and are point-coupled to a bus waveguide with a gap of 263 nm. Their inner S-shaped waveguide is formed by connecting two semicircles with a radius of 9 μm. The gap between the semicircles of the S-shaped waveguide and the external rim of the Taiji MR is 296 nm. At both ends of the S-shaped waveguide there is an inverse taper to ensure no back-reflections. The link MR has a racetrack geometry obtained by joining two pairs of straight sections with two semicircles. The radius of the semicircles and the length of the straight sections are chosen to obtain two configurations of the link MR:

(i) with the same perimeter as the taiji MR and (ii) with twice the perimeter of the taiji MR. Specifically, in the first, the radius of the semicircle is 10 μm, while in the second, it is 25 μm. The gap between the taiji MRs and the link MR is 263 nm, the same as between the taiji MR and the bus waveguide, hence $\Gamma_1 = \Gamma_2 = \Gamma_3 = \Gamma_4$ by design. In the two configurations of the link MR, the length of the straight sections has been changed to have the link MR on or off resonance with the taiji MRs. The devices were fabricated by IMEC/Europratice within a multi-project wafer run.

The optical responses of the devices were measured using an interferometric optical setup that allows simultaneous measurement of transmission and reflection in both excitation directions [111]. The output of a fiber-coupled continuous-wave (CW) tunable laser (Yenista OPTICS, TUNICS-T100S) is divided into two arms by a 50/50 fiber splitter. Each arm is equipped with a variable optical attenuator (VOA), a fiber polarization controller, an optical circulator, and a photodetector. At the end of each arm, light is coupled to the device input port through a single-mode stripped fiber. For spectral measurements, we operated the CW tunable laser at 3 mW with the VOA set to ensure a linear response, which resulted in a power of about 30 μW in the device. Further details of the optical setup are provided in [111].

For the given measurements, the optical power is defined at the chip input and calibrated by subtracting the fiber-to-chip coupling losses measured on the same chip. The input polarization is adjusted to the TE mode using a fiber polarization controller. By applying controlled stresses and torsions to the fiber, the state of polarization of the light at the fiber output before the input port of the ring—is modified. Since the coupling efficiency to the ring depends strongly on the polarization at the grating couplers, the polarization controller is tuned to maximize the transmitted signal, thereby ensuring optimal TE excitation.

The device temperature is stabilized within ±0.01°C using a thermoelectric controller. Port transmission spectra are recorded using calibrated photodetectors. Resonance positions, linewidths, and asymmetric coupling parameters are extracted by fitting the measured spectra with a coupled-mode-theory model.

4.6 Results and Discussion

Figure 4.9 shows the fitted results for the (24) and (22) port configurations of the Taiji CROW device. In these measurements, the link MR is out of resonance with respect to the Taiji MRs, and therefore the hopping model was used to fit the data. The extracted parameters are listed in Table 4.1.

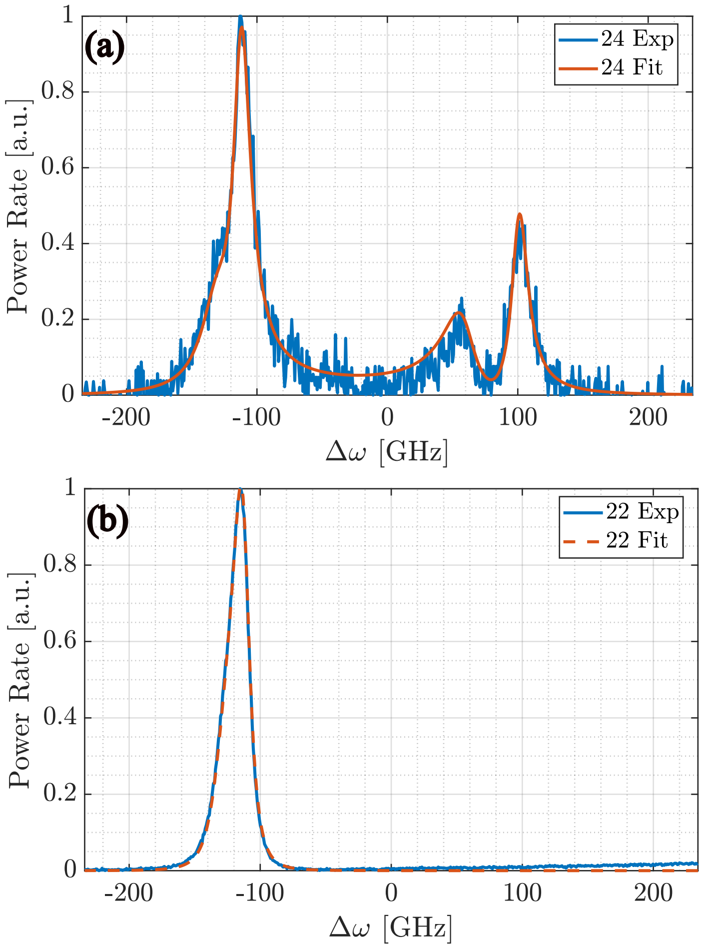

Figure 4.9: **Experimental spectra and hopping–model fits under excitation from port 2.** Panels (a) and (b) show the measured responses at ports 24 and 22, respectively. Because the link microring is off resonance, the reduced hopping model is used for fitting (parameters in Table 4.1). Experimental data (markers) are overlaid with the fitted responses (solid lines), showing good agreement across the observed resonances at both output ports.

Table 4.1: Parameters extracted from the hopping-fit corresponding to Fig. 4.9.

Param.	**Value (GHz)**	**Param.**	**Value (GHz)**	**Param.**	**Value ($\times\pi$)**
Γ	8.16	$\lvert\beta_t\rvert$	9.21	$\arg(\beta_{t1})$	0.604
γ_t	14.0	$\lvert\beta_{\mathrm{BS},1}\rvert$	10.5	$\arg(\beta_{\mathrm{BS},1})$	1.99
ω_1	-123	$\lvert\beta_{\mathrm{BS},3}\rvert$	18.0	$\arg(\beta_{\mathrm{BS},3})$	2.00
ω_3	78.9	$\lvert\beta_{15}\rvert$	7.91	$\arg(\beta_{15})$	1.88
				$\arg(\beta_{24})$	1.00

In the fit we used: $\Gamma = \Gamma_1 = \Gamma_4$, $\gamma_t = \gamma_{t,1} = \gamma_{t,3}$, $\beta_{12} = \beta_{56}$, and $|\beta_{24}| = |\beta_{15}|$.

The extracted intrinsic frequencies deviate significantly from the nominally identical target design. In particular, the two Taiji MRs are fitted at $\omega_1 = -123$ GHz and $\omega_3 = 78.9$ GHz, i.e. they are separated by ~ 200 GHz — several orders of magnitude larger than any of the coherent coupling scales in Table 4.1. This large intrinsic spectral splitting between the two active rings is already a strong signature that the link MR, which is designed to lie spectrally between them, must be far off resonance relative to both. In other words, $|\omega_{\text{link}} - \omega_{1,3}| \gg \{|\beta_{15}|, |\beta_t|, \gamma_t\}$ is automatically satisfied under the retrieved values, justifying the use of the reduced two-site hopping model.

Consistently, the extracted coherent hopping magnitude between the two Taiji MRs, $|\beta_{15}| = 7.91$ GHz, is more than an order of magnitude smaller than the frequency mismatch ($\sim$ 200 GHz), placing the system deep in the off-resonant regime where the middle MR contributes only a perturbative virtual coupling. Likewise, the total loaded decay $\gamma_t = 14$ GHz is also far smaller than $|\omega_1 - \omega_3|$, further ensuring that no resolvable spectral participation of the link MR can occur within the linewidth of the observed hybrid resonances.

The fitted backscattering components, $|\beta_{\text{BS},1}| = 10.5$ GHz and $|\beta_{\text{BS},3}| = 18.0$ GHz, are non-negligible and comparable to both the hopping and the Taiji-induced coupling $|\beta_t| = 9.21$ GHz. This explains why the experimental line shapes show pronounced modal splitting and reflection: backscattering competes on equal footing with the deliberate coupling channels, hybridizing CW and CCW modes and breaking the intended single-directionality. The phases $\arg(\beta_t)$, $\arg(\beta_{15})$, $\arg(\beta_{\text{BS}})$ are nontrivial (non-zero and non-π), meaning that no symmetry enforces coherent cancellation; the system operates in a generic non-Hermitian coupling regime with complex-valued interference between hopping and backscattering pathways.

Taken together, the hierarchy

$$|\omega_1 - \omega_3| \gg \gamma_t \sim |\beta_{\text{BS}}| \sim |\beta_t| \gtrsim |\beta_{15}|$$

has two direct physical consequences: (i) the link MR is effectively frozen out, validating the reduced hopping model; (ii) the measured spectra are shaped primarily by the competition between non-Hermitian Taiji coupling and disorder-induced backscattering inside the two active Taiji MRs.

Finally, the fact that the hopping-fit reproduces the lineshapes even under these strongly asymmetric, fabrication-perturbed conditions confirms that the simplified model captures the actual transport physics once the link ring is spectrally decoupled. This agreement is a strong experimental validation of the off-resonant reduction used in the analysis.

The reduced hopping model description employed relies on the adiabatic elimination of the detuned link microring, which is valid only when a clear separation of frequency scales exists between the link ring and the outer rings. Quantitatively, this requires the detuning of the middle ring to satisfy

$$|\Delta_2| \gg J, \qquad |\Delta_2| \gg \gamma_2/2, \tag{4.16}$$

where J denotes the inter-ring coupling rate and γ_2 is the total decay rate of the link ring. Under these conditions, the intracavity field of the link ring remains small, scaling as $|a_2|/|a_{1,3}| \sim J/|\Delta_2|$, and its influence can be captured perturbatively as an effective second-order hopping between the outer rings.

The validity of these inequalities is verified directly from the experimentally extracted parameters summarized in Table 4.1. Using the fitted values, the detuning of the link ring satisfies $|\Delta_2| \sim |\omega_1|, |\omega_3| \approx 100$ GHz, while the dominant coupling rates are $|\beta_t| \approx 9.2$ GHz and the total decay rate is $\gamma_2 \approx \gamma_t \approx 14$ GHz. This yields $|\Delta_2|/J \gtrsim 10$ and $|\Delta_2|/(\gamma_2/2) \gtrsim 14$, confirming that the experimental system operates well within the off-resonant regime required for the hopping reduction to be valid.

Consistent with this expectation, the measured spectra exhibit suppression of the link-ring participation and convergence toward a two-mode response as the detuning is increased, in full agreement with the reduced-order model predictions.

The spectral measurements constrain different model parameters with varying degrees of identifiability. Resonance frequencies (ω_i) and total decay rates (γ_t) are strongly constrained by the measured peak positions and linewidths, respectively, and can be extracted robustly from the spectra. In contrast, coupling amplitudes and phases entering the effective hopping terms exhibit partial correlations, particularly between coupling strength and loss, as well as between the magnitude and phase of complex coupling coefficients. To mitigate these correlations and ensure stable fits, physically motivated constraints were imposed during the fitting procedure. Specifically, symmetry relations between equivalent ports were enforced (e.g., $\Gamma_1 = \Gamma_4$ and $\gamma_{t,1} = \gamma_{t,3}$), and selected coupling amplitudes were fixed or shared across equivalent pathways (see Table 4.1). With these constraints, the remaining free parameters are uniquely determined within experimental uncertainty, yielding consistent agreement between the reduced-order model and the measured spectra.

4.7 Conclusion

In this chapter we established, modeled, and experimentally validated a minimal non-Hermitian photonic circuit based on Taiji microrings—the Taiji-CROW—where asymmetric intra-ring conversion (CW→CCW) is engineered via an internal S-waveguide.

Starting from a full temporal coupled-mode description [Eqs. (4.1)–(4.3)], we identified how deliberate non-Hermitian couplings ($\beta_{\mathrm{t},1}, \beta_{\mathrm{t},2}$) and disorder-induced backscattering (β_{BS}) jointly shape port-resolved spectra and mode routing (Figs. 4.2 and 4.3). We then derived and tested the off-resonance reduction of the three-ring system to an effective two-site hopping model, proving that when the link ring satisfies

$$|\Delta_2| \gg \max\left(J, \frac{\gamma_2}{2}\right),$$

its intracavity field is suppressed and the transport is governed by an effective complex hopping ($\beta_h e^{i\phi}$) between the two Taiji rings (Figs. 4.5–4.6). The resulting closed-form transmission $t_{24}(\Delta\omega)$ captures the essential lineshape physics and provides an interpretable fitting framework (Fig. 4.8).

Experimentally, spectra under excitation from port 2 (Fig. 4.9) are quantitatively reproduced by the hopping-model fit (Table 4.1). The retrieved parameter hierarchy,

$$|\omega_1 - \omega_3| \gg \gamma_t \sim |\beta_{\mathrm{BS}}| \sim |\beta_t| \gtrsim |\beta_{15}|,$$

(1) confirms that the link ring is spectrally decoupled (deep off-resonance), thereby validating the reduced two-site description; and (2) shows that the observed lineshapes are set by the competition of non-Hermitian Taiji conversion with intra-ring backscattering in the two active Taiji MRs. The nontrivial phases $\arg(\beta_t)$, $\arg(\beta_{15})$, and $\arg(\beta_{\mathrm{BS}})$ further indicate that no symmetry enforces cancellation, placing the device in a generic complex-coupled regime where interference between coherent hopping and disorder pathways is decisive.

From the combined modeling and fits, a practical tolerance rule emerges:

$$\frac{|\beta_{\mathrm{BS}}|}{\Gamma} \lesssim 0.17,$$

so that for typical $|\beta_{\mathrm{BS}}| \sim 20$ GHz one should target $\Gamma \gtrsim 120$ GHz to suppress resolvable splitting. At the network level, keeping the link ring deliberately off resonance (via perimeter or thermal/electrical detuning) ensures that $|\Delta_2|$ comfortably exceeds both J and $\gamma_2/2$, guaranteeing the validity of the hopping reduction while minimizing parasitic participation of the link mode. Finally, achieving $|\beta_t| \gtrsim |\beta_{\mathrm{BS}}|$ is key to sustain direction-selective routing in the presence of realistic disorder.

Translating these constraints into fabrication targets, disorder-induced backscattering must satisfy $|\beta_{\mathrm{BS}}| \lesssim 0.17\,\Gamma$, implying that for $\Gamma \approx 120$ GHz the residual coherent coupling should remain below ~ 20 GHz to prevent resolvable doublets. In silicon platforms, this sets tolerances on sidewall roughness and etch-induced dimensional variations that govern Rayleigh backscattering. Moreover, the loaded Q must be co-designed with disorder levels: excessively high-Q cavities narrow Γ and render weak backscattering spectrally visible, whereas moderate linewidth broadening enhances robustness. These bounds therefore translate the non-Hermitian design rules into concrete co-design targets for scalable Taiji-CROW arrays.

The Taiji-CROW showcases how non-Hermitian intra-ring engineering can complement lattice-level topology: instead of relying solely on edge-band selection, one can reshape the *site* physics to recycle or quench backscattered spin. The methodology demonstrated here—(i) full TCMT modeling, (ii) regime mapping via controlled backscattering and Taiji coupling, (iii) off-resonance reduction, and (iv) parameter fitting to experiment—provides a scalable recipe for larger arrays. Immediate extensions include: (a) programmable detuning and gain to access chiral exceptional points and non-Hermitian band engineering; (b) active stabilization of ϕ to control synthetic gauge phases; (c) statistical co-design (layout + fabrication) to bound $|\beta_{\mathrm{BS}}|$ and maintain $|\beta_t|/|\beta_{\mathrm{BS}}|$ above unity; and (d) integration with PIN/thermal actuators for on-chip reconfigurability.

Chapter 5

Reconfigurable Microring for Hermitian and Non-Hermitian Photonics (DRUM)

Integrated silicon photonics provides an ideal framework for translating theoretical models into compact, passive on-chip architectures capable of precise parameter control. It not only offers a platform to test and validate the proposed model but also enables the exploration of new physical regimes and potential applications. By engineering the geometry and coupling conditions of passive structures such as microring resonators, one can emulate and manipulate complex physical behaviors—allowing both Hermitian and non-Hermitian functionalities to emerge within a single, scalable photonic platform.

This chapter presents dynamically reconfigurable unified Microresonator (DRUM) that transitions from an effectively Hermitian two-mode system (reciprocal intermode coupling) to a genuinely non-Hermitian system (asymmetric intermode coupling). We construct the Hamiltonians in the relevant regimes, solve for eigenvalues and eigenvectors, derive the through and reflection spectra, and identify the conditions for a diabolical point (DP) versus an exceptional point (EP). Along the way, we explain in plain physical terms what each mathematical result means at the measurable transmission and reflection ports. We will then present experimental results and validate them with the theoretical model we presented.

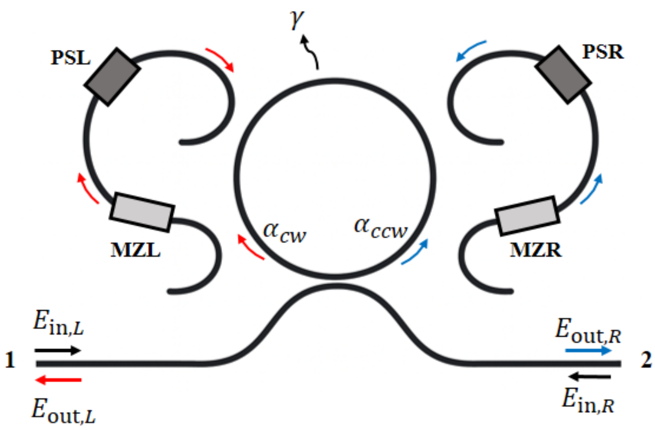

Figure 5.1: **Schematic of the DRUM device.** The ring resonator is coupled to two lateral lobes positioned on the left and right, which facilitate intermodal coupling. Each lobe contains a Mach–Zehnder interferometer, denoted as the left (MZL) and right (MZR) and incorporating a Phase Shifter Left (PSL) and a Phase Shifter Right (PSR), respectively. Ports 1 and 2 indicate the input and output waveguide ports.

5.1 The physical system and modeling

We consider a single-bus microring resonator (MR) side-coupled to a straight waveguide (see Fig. 5.1). The MR includes two passive *side lobes* (auxiliary arms) that mediate intermode coupling between the counter-clockwise (CCW) and clockwise (CW) modes. Each lobe contains a Mach–Zehnder interferometer (MZI) and a thermo-/electro-optic phase shifter, which together set the *magnitude and phase* of the effective CCW↔CW coupling (i.e., the complex coefficients β_{12} and β_{21} in our model) β_{12} represents energy transfer from CW mode to CCW mode, and β_{21} from CCW mode to CW mode through left and right lobe respectively. The bus waveguide provides left (L) and right (R) ports for coupling light in and out of the microring. In the passive, unbiased state the structure supports two *degenerate* traveling-wave modes at angular frequency ω_0 facilitated by the left right lobes. The slowly varying complex envelopes of the intracavity fields are denoted by $\alpha_{\text{ccw}}(t)$ and $\alpha_{\text{cw}}(t)$, respectively.

We denote the laser angular frequency by ω (rad/s) and the cold-cavity resonance angular frequency by ω_0 (rad/s); the laser–cavity detuning is $\Delta = \omega - \omega_0$ (rad/s). The external coupling rate from the ring to the bus is Γ (s^{-1}), while γ (s^{-1}) represents the intrinsic loss rate due to absorption, scattering, or radiation. The total decay rate is $\gamma_t = \Gamma + \gamma$ (s^{-1}). The input fields at the left and right bus ports are $E_{\text{in},L}$ and $E_{\text{in},R}$, and the corresponding output fields are $E_{\text{out},L}$ and $E_{\text{out},R}$. The uncoupled Hamiltonian is H_0, the intermode-coupling block is V, and the full system Hamiltonian is $H = H_0 + V$.

Let the port inputs be $E_{\text{in},L} = \mathcal{E}_{\text{in},L} e^{-i\omega t}$ and $E_{\text{in},R} = \mathcal{E}_{\text{in},R} e^{-i\omega t}$, and the intracavity fields be $\alpha_{\text{ccw}}(t) = a_{\text{ccw}} e^{-i\omega t}$ and $\alpha_{\text{cw}}(t) = a_{\text{cw}} e^{-i\omega t}$. In temporal coupled-mode theory (TCMT),

$$i\,\frac{d}{dt}\begin{bmatrix}\alpha_{\text{ccw}}\\ \alpha_{\text{cw}}\end{bmatrix} = \underbrace{\begin{bmatrix}\omega_0 - i\gamma_t & 0\\ 0 & \omega_0 - i\gamma_t\end{bmatrix}}_{H_0}\begin{bmatrix}\alpha_{\text{ccw}}\\ \alpha_{\text{cw}}\end{bmatrix} - \sqrt{2\Gamma}\begin{bmatrix}E_{\text{in},L}\\ E_{\text{in},R}\end{bmatrix}. \tag{5.1}$$

The input–output relations are

$$E_{\text{out},R} = E_{\text{in},L} + i\sqrt{2\Gamma}\,\alpha_{\text{ccw}}, \tag{5.2}$$

$$E_{\text{out},L} = E_{\text{in},R} + i\sqrt{2\Gamma}\,\alpha_{\text{cw}}. \tag{5.3}$$

Equations (5.1)–(5.3) set the convention that an input injected from one side of the bus couples into the *counter-propagating* intracavity mode of the ring.

The engineered (back)scattering between CCW and CW which is made through the passive designs of the lobs is captured by

$$V = \begin{bmatrix}0 & -i\,\beta_{12}\\ -i\,\beta_{21} & 0\end{bmatrix}, \qquad H \equiv H_0 + V. \tag{5.4}$$

Here $\beta_{12} = |\beta_{12}|e^{i\phi_1}$ parameterizes the CW→CCW modal conversion, while $\beta_{21} = |\beta_{21}|e^{i\phi_2}$ describes the CCW→CW conversion; the prefactor $-i$ follows the temporal coupled-mode theory (TCMT) phase convention used below.

For reciprocal, conservative coupling

$$\beta_{12} = -\beta_{21}^*, \tag{5.5}$$

so that $V = V^\dagger$ (effectively Hermitian in the coupling subspace). Passive perturbations often approximate this condition and yield standing-wave doublets (no chirality).

For convenience, we introduce the shorthand

$$\mathcal{D}(\Delta) = |\beta|^2 e^{i(\phi_1+\phi_2)} + \left(\Delta + i\,\gamma_{\text{t}}\right)^2,$$

Here we assume equal coupling magnitudes, $|\beta_{12}| = |\beta_{21}| \equiv |\beta|$, so that

$$\beta_{12}\beta_{21} = |\beta|^2 e^{i(\phi_1+\phi_2)}.$$

Using Eqs. 5.1, 5.3, and 5.2, and Eq. 5.4 the transmission and reflection coefficients at

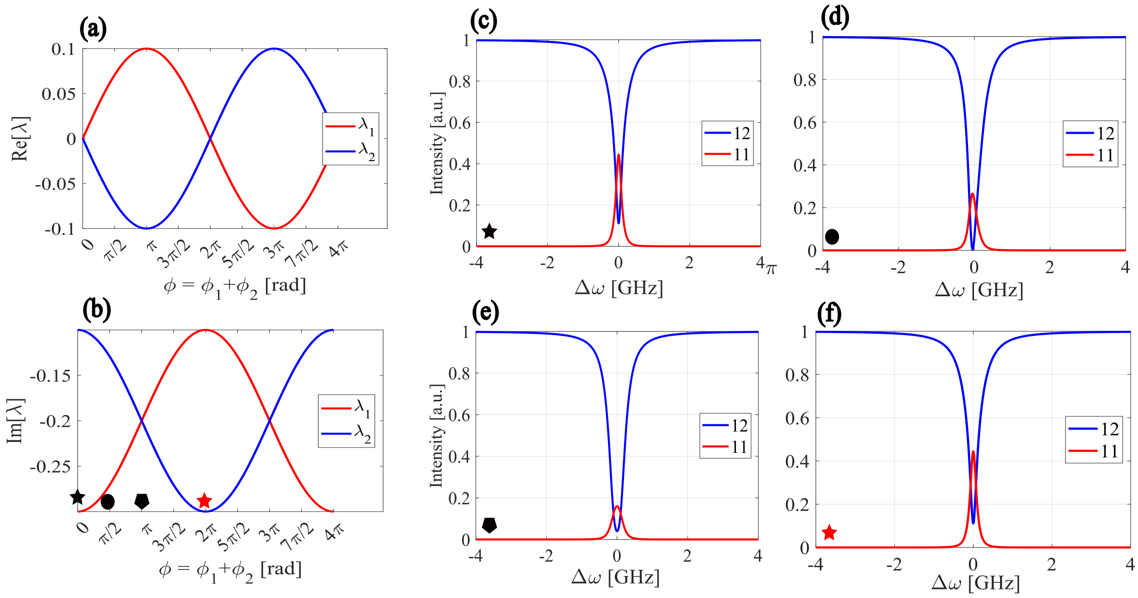

Figure 5.2: **Simulation:** Eigenvalues as a function of the phase ϕ (rad), along with the transmission and reflection spectra. For panels (a)–(b), the parameters are fixed to $\omega_0 = 0\,\text{GHz}$ (center frequency), $\gamma_t = 0.2\,\text{GHz}$ (total loss rate), and $\beta = 0.1\,\text{GHz}$. For panels (c)–(f), the system is set to the critical-coupling condition ($\Gamma = \gamma = 0.1\,\text{GHz}$); the total loss is $\gamma_t = 0.2\,\text{GHz}$, the external coupling rate is $\Gamma = 0.1\,\text{GHz}$, the intrinsic loss rate is $\gamma = 0.1\,\text{GHz}$, the coupling coefficients are $|\beta_{12}| = |\beta_{21}| = 0.1\,\text{GHz}$, and the phase ϕ is swept over $\{0, \pi/4, \pi/2, \pi\}$.

ports 1 and 2 can be expressed as follows.

$$t_{12}(\Delta) = \frac{\beta_{12}\beta_{21} + (\Delta + i\gamma_{\text{t}})\,(\Delta - 2i\Gamma + i\gamma_{\text{t}})}{\mathcal{D}(\Delta)}, \tag{5.6}$$

$$r_{11}(\Delta) = \frac{-2\beta_{12}\Gamma}{\mathcal{D}(\Delta)}, \tag{5.7}$$

$$t_{21}(\Delta) = t_{12}(\Delta), \tag{5.8}$$

$$r_{22}(\Delta) = \frac{-2\beta_{21}\Gamma}{\mathcal{D}(\Delta)}. \tag{5.9}$$

As can be seem from the above equations for one of the β_{12}

Figure 5.2(a–b) shows the evolution of the real and imaginary parts of the eigenvalues of the DRUM as a function of the total phase $\beta_{12}\beta_{21} = |\beta|^2 e^{i(\phi_1+\phi_2)}$ of the two complex coupling coefficients. The amplitudes are fixed to $|\beta_{12}| = |\beta_{21}| = 0.1\,\text{GHz}$, the total loss is set to $\gamma_{\text{t}} = 0.2\,\text{GHz}$. and the resonance is centered at $\omega_0 = 0$. At $\phi = 0$, the real parts of the eigenvalues are degenerate [panel (a)], corresponding to a single resonance dip in transmission at ω_0, as seen in panel (c). In the same condition, the imaginary parts are unequal [panel (b)], indicating that one mode experiences more loss than the other, which reflects in the asymmetry of the reflection spectrum.

As the phase increases toward $\phi = \pi/2$, the real eigenvalues split in opposite directions, indicating modal competition and frequency splitting. When the phase reaches $\phi = \pi$ [panel (e)], the doublet in transmission becomes only partially resolved. At this same phase, the imaginary parts remain non-degenerate [panel (b)], meaning the modes still experience unequal losses. As a result, the transmission and reflection spectra in panel (d) appear skewed: one mode is dominant while the other is suppressed, preventing a symmetric doublet from forming even though the real parts nearly re-cross at $\phi = \pi$.

By controlling the phase through an externally applied current $\phi(I)$ to the phase shifters on the arms of the DRUM, the device can be tuned into different operating states. This enables, for example, the generation of a symmetric mode splitting, which is advantageous for sensing applications.

5.2 Device Architecture and Experimental Methods

The DRUM device is implemented on a silicon-on-insulator (SOI) platform, comprising a silicon waveguide core with a cross section of 500 nm $\times$ 220 nm embedded in a silica cladding. The central microring resonator (MR) consists of a deformed ring composed of both straight and curved sections, with a total optical path length of 328.5 μm. The MR is side-coupled to a 410 μm-long bus waveguide via a 5 μm straight coupling region with a 216 nm gap. In addition, the MR is coupled to two lateral lobes through 6 μm-long straight coupling sections with a 204 nm gap, intentionally designed to provide slightly stronger coupling than the bus waveguide.

Each lobe has a total length of 574.6 μm between the two coupling points to the MR. Symmetric Mach–Zehnder interferometers (MZIs) are integrated within the lobes, with arm lengths of 122.8 μm, including 60 μm straight sections. Both the phase shifters (PSs) and the MZIs are thermally reconfigurable by means of 2 μm-wide titanium nitride (TiN) micro-heaters. The heater lengths are 150 μm for the PS and 60 μm for the MZI, corresponding to electrical resistances of 1035 Ω and 474 Ω, respectively. Devices were fabricated through the AMF/Europractice multi-project wafer service.

Grating couplers, located at the ends of the bus waveguide and the two side lobes, serve as input/output ports and enable independent characterization of each optical path. In this work, measurements are performed using only port 1 and port 2. The implemented layout

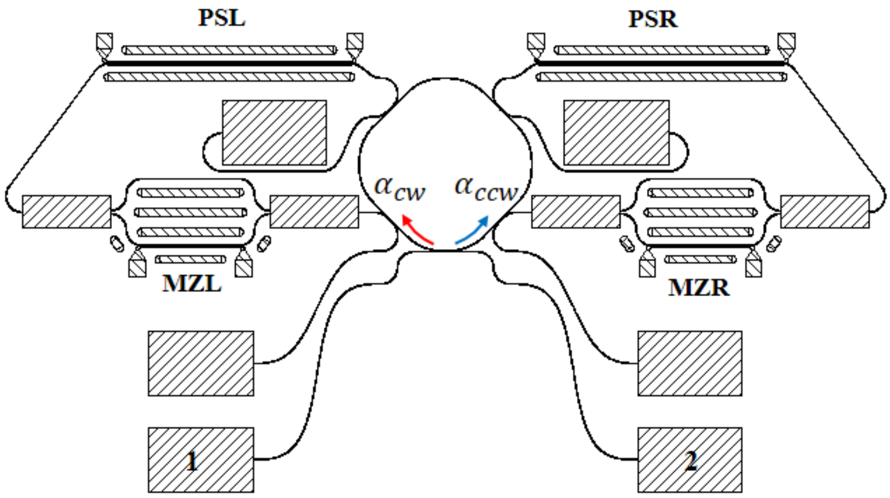

Figure 5.3: **DRUM design.** Layout of the DRUM device on an integrated silicon photonic chip.

is shown in (Fig. 5.3) .

To minimize thermal cross-talk, 5 μm-wide isolation trenches are etched on both sides of each micro-heater, as indicated by the hatched gray regions in Fig. 5.3. Additional isolation grooves prevent heat diffusion through the substrate and reduce undesired red-shifts of the resonance frequency. The main trenches are placed 5 μm away from the heaters, improving local tuning efficiency while maintaining stability across the device.

The optical response of the DRUM was characterized using an interferometric measurement setup capable of recording transmission and reflection spectra in both propagation directions. The output of a fiber-coupled, continuous-wave tunable laser is split into two arms by a 50:50 fiber splitter. Each arm contains a variable optical attenuator, a fiber polarization controller, an optical circulator, and a photodetector. Light is coupled into the photonic chip using a single-mode lensed (or cleaved) fiber aligned to the grating coupler. For spectral scans, the laser is operated at 3 mW, and the attenuator is adjusted to maintain linearity, resulting in approximately 30 μW of optical power coupled into the device. Further details of the optical setup are reported in [45].

To ensure reproducibility and quantitative comparison, all measurements follow a consistent calibration and analysis protocol. Optical power is defined at the chip input and calibrated by subtracting fiber-to-chip coupling losses measured on reference waveguides fabricated on the same chip. The input polarization is adjusted to the TE mode using a fiber polarization controller and verified by maximizing the transmitted signal. Device temperature is actively stabilized to within ±0.01°C using a thermoelectric controller. Port-resolved transmission spectra are recorded using calibrated photodetectors. Reso-

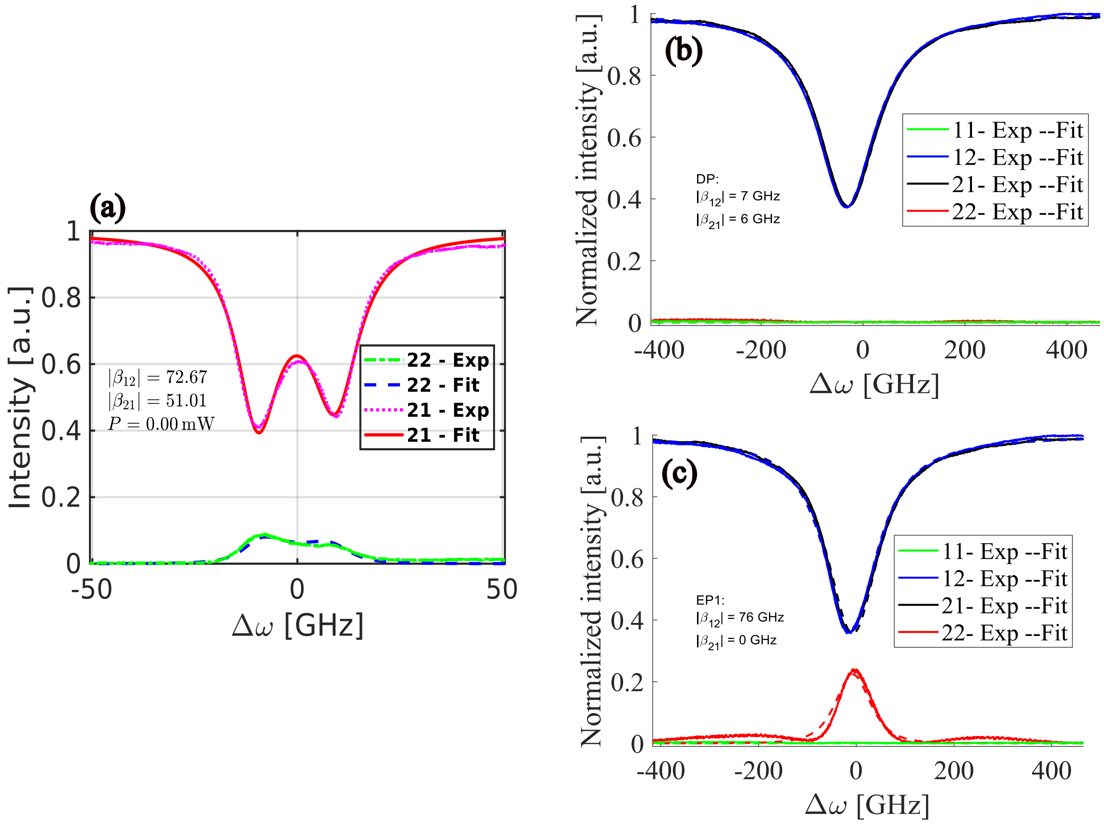

Figure 5.4: **Experimental Results**. DRUM structure response in (a) default condition, (b) Diabolic Point (DP), and (c) Exceptional Point (EP) state. The horizontal axis shows the detuning $\Delta\omega$ (GHz) and the vertical axis represents normalized intensity (a.u.). Solid curves correspond to experimental data and dashed curves to coupled-mode-theory fits. In panel (b), the DP condition is obtained for finite and nearly symmetric coupling coefficients $|\beta_{12}|$ and $|\beta_{21}|$ (GHz). In panel (c), the EP condition is realized by strongly asymmetric coupling, leading to simultaneous eigenfrequency and linewidth coalescence characteristic of non-Hermitian degeneracy.

nance frequencies, linewidths, and asymmetric coupling parameters are extracted by fitting the measured spectra to a coupled-mode-theory-based model.

5.3 Experimental Results - Diabolic Point (DP) to an Exceptional Point (EP)

Figure 5.4(a) shows the passive (default) state of the DRUM structure, where no current is applied to either the Mach–Zehnder interferometers (MZs) or the phase shifters (PSs). For the detuning set to $\Delta = 0$ during fitting, the transmission and reflection spectra exhibit an asymmetric resonance doublet. In particular, reflection coefficient r_{22} show finite, non-zero amplitudes.

This behaviour originates from the asymmetric intermodal coupling extracted from the fit, namely $|\beta_{12}| = 72.67$ GHz and $|\beta_{21}| = 51.01$ GHz at zero applied current ($P = 0$ mW). These values indicate that even in the fully passive state, the DRUM resonator permits energy exchange between the clockwise (CW) and counterclockwise (CCW) modes in an asymmetric manner.

To quantify the degree of this asymmetry, we define the optical chirality as

$$C = \frac{|\beta_{21}| - |\beta_{12}|}{|\beta_{12}| + |\beta_{21}|}, \tag{5.10}$$

which ranges from $C = -1$ (fully chiral, coupling only from CW to CCW) to $C = +1$ (fully chiral in the opposite direction), while $C = 0$ corresponds to reciprocal and symmetric coupling. Using the fitted coupling coefficients, we obtain $C = -0.175$, indicating a slight preference for coupling from the CCW to CW mode.

In addition to the coupling strengths, the fit reveals further intrinsic properties of the cavity. All the extracted parameters are given in the Table 5.1. The total loss rate is $\gamma_t = 42.29$ GHz, while the complex coupling phases are $\phi_{12} = 6.28$ rad and $\phi_{21} = 3.06$ rad. These non-trivial phases break time-reversal symmetry in the scattering pathways and contribute to the imbalance observed between the forward and backward propagating fields. The power during this measurement is $P = 0$ mW, and the sum of squared fitting error is SSE = 1.85×10^{-1}, confirming good agreement between experiment and model.

Overall, these results demonstrate that even in the absence of electrical bias, the DRUM resonator is not a perfectly reciprocal system. It inherently exhibits asymmetric backscattering, finite coupling phase differences, and weak optical chirality. This defines a non-Hermitian baseline state from which electrically induced chirality enhancement and exceptional point behaviour will be explored in the following sections.

Table 5.1: Parameter set for Default state of DRUM. Extracted from experimental fit

Parameter	**Symbol**	**Value**
Forward coupling	$\lvert\beta_{12}\rvert$	72.67 GHz
Backward coupling	$\lvert\beta_{21}\rvert$	51.01 GHz
Coupling phase (CW → CCW)	ϕ_{12}	6.28 rad
Coupling phase (CCW → CW)	ϕ_{21}	3.06 rad
Total loss rate	γ_t	42.29 GHz
Chirality	C	−0.175
Injected power	P	0 mW
Fit error	SSE	1.85×10^{-1}

From Eqs. 5.6–5.9, it is evident that both reflection coefficients r_{11} and r_{22} vanish only if the coupling terms satisfy $|\beta_{12}| = |\beta_{21}| = 0$. This condition corresponds to the diabolic point (DP), where CW and CCW modes are completely decoupled. Experimentally, this state is approached by applying current to both MZ_L and MZ_R to suppress the coupling. As shown in Fig. 5.4(b), the extracted coupling values become very small but not exactly zero, resulting in extremely weak reflections of the order of 10^{-3}. Which is negligible to see compare to the transmission extinction ratio. Therefore, this state is referred to as the near-zero coupling or DP- state. The extracted parameters from the fit are given in the Table 5.2. Since the extracted coupling values approach zero, no measurable reflection is observed at either port. According to the definition of chirality introduced above, this condition corresponds to a chirality value of 0, indicating a non-chiral regime with fully decoupled CW and CCW modes.

Table 5.2: Parameter set for DP condition. Extracted from experimental fit

Parameter	**Value**
Γ	13.60 GHz
γ_t	69.54 GHz
$\lvert\beta_{12}\rvert$	7.12 GHz
ϕ_{12}	2.20 Rad
$\lvert\beta_{21}\rvert$	5.99 GHz
ϕ_{21}	0.00
$\lvert\beta_{12,\mathrm{BS}}\rvert$	0.00
$\phi_{12,\mathrm{BS}}$	0.00
$\lvert\beta_{21,\mathrm{BS}}\rvert$	0.00
$\phi_{21,\mathrm{BS}}$	0.00

Figure 5.4(c) shows the experimentally measured spectra when only one of the coupling coefficients is suppressed, i.e., $|\beta_{21}| = 0$, while the other remains finite. This condition is achieved using an optimization algorithm that adjusts the MZ and PS currents during the experiment. In this case, the fitted values are $|\beta_{12}| = 76$ GHz and $|\beta_{21}| = 0$ GHz. Due to this highly asymmetric coupling, the system reaches an exceptional point (EP). As a result, a strong reflection appears at port 2 (non-zero r_{22}), while port 1 exhibits almost zero reflection ($r_{11} \approx 0$), demonstrating unidirectional reflectionlessness. Furthermore, using the definition of chirality, this condition yields a chirality value of -1, corresponding to a fully chiral regime in which the clockwise (CW) mode couples to the counterclockwise (CCW) mode, but not vice versa.

These experimental observations confirm that by appropriately tuning the currents in the MZs and PSs, the DRUM structure can be reconfigured from the passive state to either a diabolic point (DP) or an exceptional point (EP).

Although exceptional points exhibit square-root eigenvalue splitting, $\Delta\lambda \propto \sqrt{\varepsilon}$, in response to small perturbations [171], this mathematical sensitivity does not automatically

Table 5.3: Parameter set for EP condition. Extracted from experimental fit

Parameter	**Value**
Γ	13.13 GHz
γ_t	65.24 GHz
$\lvert\beta_{12}\rvert$	76.36 GHz
ϕ_{12}	5.19 Rad
$\lvert\beta_{21}\rvert$	0.00 GHz
ϕ_{21}	0.00
$\lvert\beta_{12,\mathrm{BS}}\rvert$	0.00
$\phi_{12,\mathrm{BS}}$	0.00
$\lvert\beta_{21,\mathrm{BS}}\rvert$	0.00
$\phi_{21,\mathrm{BS}}$	0.00

translate into enhanced measurement performance. The same non-Hermitian degeneracy responsible for the $\sqrt{\varepsilon}$ scaling also increases susceptibility to technical noise and linewidth fluctuations [172, 173]. Fluctuations in γ_t or in the effective coupling coefficients perturb the EP condition, inducing spectral jitter, excess linewidth broadening, and partial lifting of the degeneracy even in the absence of an external signal. Since practical sensing relies on resolvable spectral shifts relative to the resonance linewidth and noise floor, any increase in parametric responsivity may be offset—or even negated—by enhanced noise sensitivity [172]. Therefore, observable sensing enhancement near an EP is fundamentally constrained by linewidth stability and achievable signal-to-noise ratio, and cannot be inferred from eigenvalue scaling arguments alone. Active stabilization and careful noise engineering are essential when translating EP degeneracy into practical sensing performance.

5.4 Conclusion

In this chapter, we introduced and analyzed experimentally a dynamically reconfigurable unified microresonator (DRUM) on integrated silicon photonic chip. We have shown that the structure can transition from a Hermitian (reciprocal) to a non-Hermitian (asymmetric) coupling regime. Using temporal coupled-mode theory, we established a theoretical framework that explains how intermodal coupling between clockwise and counterclockwise modes can be precisely controlled through the complex coupling coefficients. This model allowed us to derive the eigenvalues, eigenvectors, and the transmission and reflection spectra, and to identify the physical conditions distinguishing a diabolic point (DP), where eigenvalues are degenerate but eigenvectors remain orthogonal, from an exceptional point (EP), where both eigenvalues and eigenvectors coalesce. Experimentally, we demonstrated that simple electrical control of the Mach–Zehnder interferometers and phase shifters enables tuning of the coupling strengths and phases, allowing the system to move continuously between passive asymmetric states, near-zero coupling (DP-like) states, and fully non-Hermitian exceptional point conditions. This tunability results in electrically programmable chirality, deterministic suppression of coherent backscattering, and directional asymmetry in reflection. The ability to reach and manipulate exceptional points provides a pathway to enhanced sensitivity and unconventional scattering responses. The concepts demonstrated here pave the way for applications such as exceptional-point-enhanced sensing, non-magnetic nonreciprocal photonic devices like isolators and circulators, direction-switchable chiral microring lasers, and synthetic gauge fields in resonator lattices. The DRUM platform offers a versatile and scalable approach for exploring Hermitian and non-Hermitian physics on a single photonic chip and establishes a foundation for future photonic systems that combine tunability, chirality, and non-Hermitian functionality.

Chapter 6

Conclusion and Future Outlook

This thesis has demonstrated how complex light–matter dynamics in integrated silicon photonics can be engineered, controlled, and exploited across linear photon routing, nonlinear dynamics, and non-Hermitian physics. Across multiple device platforms—including 3×3 waveguide couplers, p-n embedded microring resonators, DRUM structures, and Taiji-CROW—the work establishes how modal coupling, dissipation, phase, and nonlinearity can be deliberately designed and electrically tuned to access regimes beyond conventional reciprocal and linear photonics.

At the linear circuit level, a compact and thermally reconfigurable 3×3 waveguide coupler was theoretically modeled and experimentally validated, demonstrating flexible signal routing, wavelength-selective cross-connection, and balanced multiport splitting with minimal loss penalty. A complete parameter map linking electrical control to coupling coefficients and propagation constants was established, positioning the device as a practical building block for scalable photonic routing, multiport interferometry, and higher-dimensional path encoding.

At the nonlinear dynamical level, electrically tunable self-pulsing was realized and quantitatively controlled in a p-n silicon microring resonator. By combining temporal coupled-mode theory with carrier and thermal rate equations, a unified dynamical model was developed that captures the emergence of limit-cycle oscillations and their dependence on optical power, detuning, and electrical bias. The experiments directly demonstrate that reverse-bias control of the free-carrier lifetime provides a robust electrical knob to tune the oscillation frequency, linking carrier sweep-out physics to nonlinear temporal dynamics and enabling compact, bias-tunable on-chip oscillators. Beyond frequency control, this work reveals a clear physical distinction between nonlinear steady-state behaviour and dynamical instability: under reverse bias, self-pulsing is suppressed at smaller detuning while the nonlinear transmission branch remains stable. This demonstrates that electrical bias selectively quenches the delayed carrier-mediated feedback responsible for oscillatory dynamics without eliminating the underlying nonlinear steady state, thereby enabling independent control over oscillation onset and static nonlinear response. This selective control of nonlinear physics is significant because it enables independent tuning of static and dynamic nonlinear responses within the same device. This capability provides a new degree of freedom for the design of integrated nonlinear photonic systems, allowing stability, speed, and functionality to be dynamically balanced through electrical control rather than fixed by fabrication.

At the non-Hermitian level two complementary platforms—the dynamically reconfigurable unified microresonator (DRUM) and the Taiji-coupled resonator optical waveguide (Taiji-CROW)—were introduced and experimentally validated. In the DRUM, electrical control of Mach–Zehnder interferometers enables continuous tuning between Hermitian and non-Hermitian regimes, including access to diabolic points and exceptional points. This results in electrically programmable chirality, deterministic suppression of coherent backscattering, and direction-dependent reflection. In the Taiji-CROW, asymmetric intra-ring mode conversion combined with controlled disorder enables direction-selective transport in resonator lattices. An off-resonance reduction to an effective complex hopping model was derived and experimentally validated, yielding clear design rules for suppressing unwanted mode splitting and sustaining non-Hermitian routing in realistic devices.

Relative to existing literature, this work advances integrated photonics by unifying linear routing, nonlinear dynamics, and non-Hermitian physics within a common design and control framework. While prior studies have demonstrated these effects individually, this thesis shows that nontrivial photonic functionality emerges from the controlled interplay of coupling, loss, phase, and nonlinearity, rather than from geometry alone.

The goal of this thesis has been to move integrated photonics from passive light guiding toward actively controllable, dynamically reconfigurable, and physically rich photonic systems. Within this context, the work sits at the intersection of applied device engineering and fundamental photonic physics. It demonstrates that silicon photonics—despite material loss, disorder, and fabrication constraints—can reliably host nonlinear dynamics, non-Hermitian phenomena, and phase-controlled routing when these effects are deliberately co-designed.

Collectively, these results motivate future integrated photonic platforms that unify routing, oscillation, chirality, and nonreciprocity on a single chip, with electrical control enabling signal processing, sensing, and emerging quantum and neuromorphic functionalities through dynamically tunable coupling and dissipation.

6.1 Practical constraints and scalability

While the demonstrated non-Hermitian and nonlinear microring platforms show strong reconfigurability and controllable dynamics at the device level, several practical engineering constraints must be considered for large-scale circuit integration. First, thermo-optic tuning using integrated heaters and MZI phase shifters, as employed in the DRUM architecture, introduces non-negligible electric power consumption, which can become a limiting factor when scaling to dense CROW lattices or large photonic meshes. Second, thermal cross-talk between closely spaced resonators and coupled waveguides may induce unintended resonance detuning and coupling fluctuations, particularly in multi-ring configurations such as Taiji-CROW systems, where precise control of inter-resonator coupling and backscattering is required. A related practical constraint is the *footprint* of highly reconfigurable circuits: in the present architecture the dominant area contribution arises from the MZI sections and, more importantly, from the phase shifters, which sets a lower bound on the circuit size and limits dense co-integration with many resonators. In addition, because thermal phase shifters operate on comparatively slow time scales (typically kHz–ms), most tuning is intrinsically quasi-static; this is adequate for steady-state exploration of diabolic and exceptional point conditions, but it limits fast, time-domain modulation or rapid encircling protocols without alternative actuation mechanisms. From a scalability perspective, the device-level design rules derived in this thesis—specifically the requirement that engineered coupling exceeds disorder-induced backscattering and that loss and detuning are quantitatively calibrated—provide practical guidelines for extending these architectures to larger arrays. Future implementations in large-scale non-Hermitian photonic circuits will therefore benefit from low-power phase shifters, improved thermal isolation, more compact actuation schemes to reduce footprint, and fabrication processes that minimize roughness-induced backscattering to preserve robustness and reproducibility across many coupled resonators.

6.2 Future Outlook

The results of this thesis may open other research directions for advancing non-Hermitian integrated photonics. At the circuit level, scaling the demonstrated devices into larger non-Hermitian lattices, such as coupled-resonator optical waveguide (CROW) arrays or reconfigurable mesh networks, would allow exploration of collective phenomena including non-Hermitian topological transport and synthetic gauge fields. Combining these architectures with dynamic electrical control may lead to programmable nonreciprocal networks and reconfigurable optical isolators and circulators, enabling practical non-magnetic implementations of asymmetric light transport.

Another natural extension concerns the studied 3×3 coupler, which can be pushed toward the quantum regime by interfacing it with on-chip single-photon sources and single-photon detectors. In such a configuration, injecting single photons into any of the input ports would enable the preparation of arbitrary path-encoded qutrit states, where the quantum state evolves through the device according to an effective tunable Hamiltonian. The output ports can then be monitored using single-photon measurements to reconstruct the output probability distribution and investigate quantum interference and coherence in a multiport non-Hermitian platform. This would transform the 3×3 coupler from a classical routing element into a compact quantum photonic processor capable of programmable state evolution, quantum measurements, and photon routing. Moreover, the presence of engineered loss and tunable coupling in the device makes it an ideal testbed for exploring quantum manifestations of non-Hermitian physics, including non-unitary evolution, exceptional-point-enhanced quantum sensing, and chiral quantum transport in integrated photonic circuits.

Integrating non-linear and quantum effects into non-Hermitian silicon platforms may offer another research frontier. The interplay of non-linearity and EP dynamics could enable controllable self-oscillation, chaos, or soliton formation in CMOS-compatible photonics. Furthermore, implementing quantum states or entangled photons in non-Hermitian cavities may reveal fundamentally new behaviors in quantum non-Hermitian physics, including quantum EP sensing and chiral photon routing.

In this context, electrically tunable p–n junction silicon microring resonators represent a particularly promising direction for photonic reservoir computing. By exploiting voltage-controlled free-carrier dynamics, the carrier lifetime and refractive index inside the microring can be dynamically tuned, providing a nonlinear and memory-rich response to the input signal. The optical field circulating in the resonator acts as a nonlinear photonic reservoir whose internal states depend on the input waveform, detuning, and applied bias voltage. For constant optical power and detuning, the reservoir states can be mapped to the output intensity, while a trained linear readout layer extracts the desired computational output. This voltage-adaptive behavior enables task-dependent tuning of the reservoir through the carrier lifetime $\tau(V)$, offering a compact and CMOS-compatible hardware platform for high-speed optical computing, time-series prediction, and signal processing. When combined with non-Hermitian loss engineering and tunable dissipation, such p–n microring reservoirs could further enhance computational richness and stability, enabling adaptive and energy-efficient photonic information processing systems.

Finally, incorporating adaptive calibration and feedback circuits could make future non-Hermitian photonic systems robust to fabrication variations and environmental fluctuations. This would transform non-Hermitian photonics from a research paradigm into a practical engineering toolkit for advanced optical computing, signal processing, and sensing.

Publications

1. Optimized Photon Routing with a Silicon 3×3 Waveguide Coupler Device

Salamat Ali, Riccardo Franchi, Stefano Biasi, Bülent Aslan, and Lorenzo Pavesi.
Optics Express **33**, 14035–14047 (2025).

2. Electrically Tunable Self-Pulsing in a p-n Silicon Microring Resonator

Salamat Ali, Stefano Biasi, Bülent Aslan, and Lorenzo Pavesi.
(In preparation.)

3. On the Spectral Response of a Taiji-CROW Device

Bülent Aslan, Riccardo Franchi, Stefano Biasi, **Salamat Ali**, and Lorenzo Pavesi.
Optics Express **32**, 15177–15198 (2024).

4. Coherent Control of (Non-)Hermitian Mode Coupling: Tunable Chirality and Exceptional Point Dynamics in Photonic Microresonators

Bülent Aslan, Riccardo Franchi, Stefano Biasi, **Salamat Ali**, Davide Olivieri, and Lorenzo Pavesi.
Accepted for publication in Light Science & Applications.
(Previously available as a preprint on Research Square, 29 June 2025.)
`https://doi.org/10.21203/rs.3.rs-6420889/v1`

Bibliography

[1] Gordon E. Moore. “Cramming more components onto integrated circuits”. In: *Electronics* 38.8 (1965), pp. 114–117.

[2] Robert H. Dennard, Fritz H. Gaensslen, Hwa-Nien Yu, V. Leo Rideout, Ernest Bassous, and Andre R. LeBlanc. “Design of ion-implanted MOSFET’s with very small physical dimensions”. In: *IEEE Journal of Solid-State Circuits* 9.5 (1974), pp. 256–268.

[3] Shekhar Borkar and Andrew A. Chien. “The Future of Microprocessors”. In: *Communications of the ACM* 54.5 (2011), pp. 67–77.

[4] David A. B. Miller. “Attojoule Optoelectronics for Low-Energy Information Processing and Communications”. In: *Journal of Lightwave Technology* 35.3 (2017), pp. 346–396.

[5] M. Mitchell Waldrop. “The chips are down for Moore’s law”. In: *Nature* 530.7589 (2016), pp. 144–147.

[6] Mark Horowitz. “1.1 Computing’s energy problem (and what we can do about it)”. In: *2014 IEEE International Solid-State Circuits Conference Digest of Technical Papers (ISSCC)*. 2014, pp. 10–14.

[7] Richard Soref. “The Past, Present, and Future of Silicon Photonics”. In: *IEEE Journal of Selected Topics in Quantum Electronics* 12.6 (2006), pp. 1678–1687.

[8] David Thomson, Aaron Zilkie, John E. Bowers, T. Komljenovic, Graham T. Reed, L. Vivien, D. Marris-Morini, Eric Cassan, L. Virot, J.-M. Fédéli, et al. “Roadmap on silicon photonics”. In: *Journal of Optics* 18.7 (2016), p. 073003.

[9] Chen Sun et al. “Single-chip microprocessor that communicates directly using light”. In: *Nature* 528 (2015), pp. 534–538.

[10] Ramy El-Ganainy, Konstantinos G. Makris, Mercedeh Khajavikhan, Ziad H. Musslimani, Stefan Rotter, and Demetrios N. Christodoulides. “Non-Hermitian physics and PT symmetry”. In: *Nature Physics* 14.1 (2018), pp. 11–19.

[11] Mohammad-Ali Miri and Andrea Alù. “Exceptional points in optics and photonics”. In: *Science* 363.6422 (2019), eaar7709.

[12] Şahin Kaya Özdemir, Stefan Rotter, Florian Nori, and Lan Yang. “Parity–time symmetry and exceptional points in photonics”. In: *Nature Materials* 18 (2019), pp. 783–798.

[13] WD Heiss. “The physics of exceptional points”. In: *Journal of Physics A: Mathematical and Theoretical* 45.44 (2012), p. 444016.

[14] A. Guo, G.J. Salamo, D. Duchesne, R. Morandotti, M. Volatier-Ravat, V. Aimez, G.A. Siviloglou, and D.N. Christodoulides. “Observation of PT-symmetry breaking in complex optical potentials”. In: *Physical Review Letters* 103.9 (2009), p. 093902.

[15] Christian E. Rüter, Konstantinos G. Makris, Ramy El-Ganainy, Demetrios N. Christodoulides, Mordechai Segev, and Detlef Kip. “Observation of parity–time symmetry in optics”. In: *Nature Physics* 6.3 (2010), pp. 192–195.

[16] Bo Peng, Şahin Kaya Özdemir, Fuchuan Lei, Faraz Monifi, Mariagiovanna Gianfreda, Gui Lu Long, Shanhui Fan, Franco Nori, and Lan Yang. “Parity–time-symmetric whispering-gallery microcavities”. In: *Nature Physics* 10 (2014), pp. 394–398.

[17] Long Chang, Xiaoshun Jiang, Shiyue Hua, Cheng Yang, Jianming Wen, Liang Jiang, Guanyu Li, Guanghao Wang, Min Xiao, and L. Yang. “Parity–time symmetry and variable optical isolation in active–passive-coupled microresonators”. In: *Nature Photonics* 8.7 (2014), pp. 524–529.

[18] H. Hodaei, M.-A. Miri, M. Heinrich, D.N. Christodoulides, and M. Khajavikhan. “Parity-time–symmetric microring lasers”. In: *Science* 346.6212 (2014), pp. 975–978.

[19] Robert W. Boyd. *Nonlinear Optics*. 2nd. San Diego, CA: Academic Press, 2003.

[20] Govind P. Agrawal. *Nonlinear Fiber Optics*. 4th. San Diego, CA: Academic Press, 2007.

[21] David J. Moss, Roberto Morandotti, Alexander L. Gaeta, and Michal Lipson. “New CMOS-compatible platforms for nonlinear optics”. In: *Nature Photonics* 7 (2013), pp. 597–607.

[22] M. Borghi, C. Castellan, S. Signorini, A. Trenti, and L. Pavesi. “Nonlinear silicon photonics”. In: *Journal of Optics* 19.9 (2017), p. 093002. URL: `https://doi.org/10.1088/2040-8986/aa7a6d`.

[23] A. Muñoz de las Heras and I. Carusotto. “Unidirectional lasing in nonlinear taiji microring resonators”. In: *Physical Review A* 104.4 (2021), p. 043501.

[24] Alberto Muñoz de las Heras, Riccardo Franchi, Stefano Biasi, Mher Ghulinyan, Lorenzo Pavesi, and Iacopo Carusotto. “Nonlinearity-Induced Reciprocity Breaking in a Single Nonmagnetic Taiji Resonator”. In: *Physical Review Applied* 15.5 (2021), p. 054044.

[25] M. Parto, Y. G. N. Liu, B. Bahari, M. Khajavikhan, and D. N. Christodoulides. “Non-Hermitian and topological photonics: optics at an exceptional point”. In: *Nanophotonics* 10.1 (2021), pp. 403–423.

[26] Liang Feng, Zhifang J. Wong, Ren-Min Ma, Yuan Wang Wang, and Xiang Zhang. “Single-mode laser by parity-time symmetry breaking”. In: *Science* 346.6212 (2014), pp. 972–975.

[27] Bo Peng, Şahin Kaya Özdemir, Stefan Rotter, Hasan Yilmaz, Martin Liertzer, Faraz Monifi, Carl M. Bender, Franco Nori, and Lan Yang. “Loss-induced suppression and revival of lasing”. In: *Science* 346.6207 (2014), pp. 328–332.

[28] L. Jin and Z. Song. “Hybrid silicon microring resonators with controllable non-Hermitian coupling”. In: *Physical Review A* 97.1 (2018), p. 012121.

[29] H. Zhou, C. Peng, Y. Yoon, C.W. Hsu, K.A. Nelson, B. Zhen, and M. Soljačić. “Observation of bulk Fermi arc and polarization half charge from paired exceptional points”. In: *Science* 359.6379 (2018), pp. 1009–1012.

[30] K. Wang, A. Dutt, K.Y. Yang, C.C. Wojcik, J. Vučković, and S. Fan. “Observation of reflectionless transmission in non-Hermitian photonic lattices”. In: *Nature* 582.7813 (2020), pp. 198–202.

[31] S. Weimann, M. Kremer, Y. Plotnik, Y. Lumer, S. Nolte, K.G. Makris, M. Segev, and A. Szameit. “Topologically protected bound states in photonic parity–time-symmetric crystals”. In: *Nature Materials* 16.4 (2017), pp. 433–438.

[32] H. Zhao, S. Longhi, and L. Feng. “Non-Hermitian topological light steering”. In: *Science* 365.6458 (2019), pp. 1163–1166.

[33] J. Doppler, A.A. Mailybaev, J. Böhm, U. Kuhl, A. Girschik, F. Libisch, T.J. Milburn, P. Rabl, N. Moiseyev, and S. Rotter. “Dynamically encircling an exceptional point for asymmetric mode switching”. In: *Nature* 537.7618 (2016), pp. 76–79.

[34] H. Xu, D. Mason, L. Jiang, and J.G.E. Harris. “Topological energy transfer in an optomechanical system with exceptional points”. In: *Nature* 537.7618 (2016), pp. 80–83.

[35] Wen Chen, Şahin Kaya Özdemir, Güney E. Kiran, and Lan Yang. “Exceptional points enhance sensing in an optical microcavity”. In: *Nature* 548 (2017), pp. 192–196.

[36] Hossein Hodaei, Absar U. Hassan, Steffen Wittek, Hipolito Garcia-Gracia, Ramy El-Ganainy, Demetrios N. Christodoulides, and Mercedeh Khajavikhan. “Enhanced sensitivity at higher-order exceptional points”. In: *Nature* 548 (2017), pp. 187–191.

[37] Shaowu Chen, Libin Zhang, Yonghao Fei, and Tongtong Cao. “Bistability and self-pulsation phenomena in silicon microring resonators based on nonlinear optical effects”. In: *Optics express* 20.7 (2012), pp. 7454–7468.

[38] Thomas J. Johnson, Matthew Borselli, and Oskar Painter. “Self-induced optical modulation of the transmission through a high-Q silicon microdisk resonator”. In: *Optics Express* 14.2 (2006), pp. 817–831.

[39] Libin Zhang, Yonghao Fei, Yanmei Cao, Xun Lei, and Shaowu Chen. “Experimental observations of thermo-optical bistability and self-pulsation in silicon microring resonators”. In: *Journal of the Optical Society of America B* 31.2 (2014), pp. 201–206.

[40] Wim Bogaerts, Peter De Heyn, Tom Van Vaerenbergh, Koen De Vos, Saeedeh Kumar Selvaraja, Thomas Claes, Pieter Dumon, Dries Van Thourhout, and Roel Baets. “Silicon microring resonators”. In: *Laser & Photonics Reviews* 6.1 (2012), pp. 47–73.

[41] B. E. Little, S. T. Chu, H. A. Haus, J. Foresi, and J.-P. Laine. “Microring resonator channel dropping filters”. In: *Journal of Lightwave Technology* 15.6 (1997), pp. 998–1005.

[42] Amnon Yariv. “Universal relations for coupling of optical power between microresonators and waveguides”. In: *Electronics Letters* 36.4 (2000), pp. 321–322.

[43] Salamat Ali, Riccardo Franchi, Stefano Biasi, Bülent Aslan, and Lorenzo Pavesi. “Optimized photon routing with a silicon 3×3 waveguide coupler device”. In: *Optics Express* 33.6 (2025), pp. 14035–14047.

[44] R. Franchi. “The Taiji and infinity-loop microresonators: examples of non-Hermitian photonic systems”. PhD thesis. Università degli Studi di Trento, 2023.

[45] Bülent Aslan, Riccardo Franchi, Stefano Biasi, Salamat Ali, Davide Olivieri, and Lorenzo Pavesi. “Coherent control of (non-)Hermitian mode coupling: tunable chirality and exceptional point dynamics in photonic microresonators”. In: *Light: Science & Applications* (2024). to appear.

[46] Shanhui Fan, Wenjing Suh, and Jian Wang. “Temporal coupled-mode theory for the Fano resonance in optical resonators”. In: *Journal of the Optical Society of America A* 20.3 (2003), pp. 569–572.

[47] Pochi Yeh. *Optical Waves in Layered Media*. Wiley, 1988.

[48] Allan W. Snyder and John D. Love. *Optical Waveguide Theory*. Chapman and Hall, 1983.

[49] Richard A. Soref and B. R. Bennett. “Electrooptical effects in silicon”. In: *IEEE Journal of Quantum Electronics* 23.1 (1987), pp. 123–129.

[50] L. B. Soldano and E. C. M. Pennings. “Optical multi-mode interference devices based on self-imaging: principles and applications”. In: *Journal of Lightwave Technology* 13.4 (1995), pp. 615–627.

[51] Yifei Wang, Xue Fu, and Lan Yang. “Non-Hermitian Physics and Engineering in Silicon Photonics”. In: *Silicon Photonics IV*. Ed. by David J. Lockwood and Lorenzo Pavesi. Vol. 139. Topics in Applied Physics. See also arXiv:2109.15262. Cham: Springer, 2021.

[52] Zhiyuan Lin, Wange Song, Li-Wei Wang, Haoran Xin, Jiacheng Sun, Shengjie Wu, Chunyu Huang, Shining Zhu, Jian-Hua Jiang, and Tao Li. “Observation of topological transition in Floquet non-Hermitian skin effects in silicon photonics”. In: *Physical Review Letters* 133 (2024), p. 073803.

[53] Mingyuan Gao, Chong Sheng, Yule Zhao, Runqiu He, Liangliang Lu, Wei Chen, Kun Ding, Shining Zhu, and Hui Liu. “Quantum walks of correlated photons in non-Hermitian photonic lattices”. In: *Physical Review B* 110 (2024), p. 094308.

[54] Xilin Feng, Tianwei Wu, and Liang Feng. “Non-Hermitian hybrid silicon photonic switching”. In: *Nature Photonics* (2025). Early 2025; add volume/issue/pages when assigned.

[55] Graham T Reed, Goran Mashanovich, F Yand Gardes, and DJhttps Thomson. “Silicon optical modulators”. In: *Nature photonics* 4.8 (2010), pp. 518–526.

[56] P.-A. Absil, J. V. Hryniewicz, B. E. Little, P.-T. Ho, and P.-C. Chao. “Compact microring notch filters on silicon-on-insulator”. In: *IEEE Photonics Technology Letters* 12.7 (2000), pp. 974–976.

[57] Qianfan Xu, Bradley Schmidt, Sameer Pradhan, and Michal Lipson. “Micrometre-scale silicon electro-optic modulator”. In: *nature* 435.7040 (2005), pp. 325–327.

[58] Alfredo Pasquazi, Marco Peccianti, Luca Razzari, David J. Moss, Shayan Coen, Miro Erkintalo, Yoshitomo K. Chembo, Thomas Hansson, Sigurdur Wabnitz, Pascal Del'Haye, et al. "Micro-combs: A novel generation of optical sources". In: *Physics Reports* 729 (2018), pp. 1–81.

[59] Chong Wang, Zhoutian Fu, and Lan Yang. "Non-Hermitian optics and photonics: from classical to quantum domains". In: *Advances in Optics and Photonics* 15.2 (2023), pp. 442–589.

[60] Amnon Yariv, Yong Xu, Reginald K. Lee, and Axel Scherer. "Coupled-resonator optical waveguide: a proposal and analysis". In: *Optics Letters* 24.11 (1999), pp. 711–713.

[61] Allegra Calabrese, Fernando Ramiro-Manzano, Hannah M. Price, Stefano Biasi, Martino Bernard, Mher Ghulinyan, Iacopo Carusotto, and Lorenzo Pavesi. "Unidirectional reflection from an integrated Taiji microresonator". In: *Photonics Research* 8.8 (2020), pp. 1333–1341.

[62] R. Franchi, S. Biasi, F. Mione, B. Aslan, and L. Pavesi. "On the response of the taiji microresonator against small perturbation of the counter propagating mode". In: *Proceedings of SPIE*. Vol. 12004. 2022, p. 1200406.

[63] Lucas B Soldano and Erik CM Pennings. "Optical multi-mode interference devices based on self-imaging: principles and applications". In: *Journal of lightwave technology* 13.4 (1995), pp. 615–627.

[64] Herwig Kogelnik and R. V. Schmidt. "Switched directional couplers with alternating $\delta\beta$". In: *IEEE Journal of Quantum Electronics* 12.7 (1976), pp. 396–401.

[65] Ivan L. Garanovich, Stefano Longhi, Andrey A. Sukhorukov, and Yuri S. Kivshar. "Light propagation and localization in modulated photonic lattices and waveguides". In: *Physics Reports* 518.1–2 (2012), pp. 1–79.

[66] M. Tang, J. He, C. Xiang, W. Liu, H. Wang, W. Li, P. Yu, and J. E. Bowers. "Review of heterogeneous integration of III–V lasers on silicon". In: *Progress in Quantum Electronics* 66 (2019), pp. 1–50.

[67] Di Liang and John E. Bowers. "Recent progress in heterogeneous III–V-on-silicon photonic integrated circuits". In: *Light: Advanced Manufacturing* 2.1 (2021), p. 5.

[68] Antonio P. Maldonado, Michaël L. Povinelli, and Shanhui Fan. "Temporal coupled-mode theory in nonlinear resonant photonics: a review". In: *Journal of Applied Physics* 136.1 (2024), p. 011101.

[69] Zhichao Ruan and Shanhui Fan. “Temporal Coupled-Mode Theory for Fano Resonance in Light Scattering by a Single Obstacle”. In: *The Journal of Physical Chemistry C* 114.16 (2010), pp. 7324–7329.

[70] Zongfu Yu and Shanhui Fan. “Complete optical isolation created by indirect interband photonic transitions”. In: *Nature Photonics* 3.2 (2009), pp. 91–94.

[71] Hugo Lira, Zongfu Yu, Shanhui Fan, and Michal Lipson. “Electrically Driven Nonreciprocity Induced by Interband Photonic Transition on a Silicon Chip”. In: *Physical Review Letters* 109.3 (2012), p. 033901.

[72] Dimitrios L. Sounas and Andrea Alù. “Non-reciprocal photonics based on time modulation”. In: *Nature Photonics* 11.12 (2017), pp. 774–783.

[73] L. D. Tzuang, K. Fang, P. Nussenzveig, Shanhui Fan, and Michal Lipson. “Non-reciprocal phase shift induced by an effective magnetic flux for light”. In: *Nature Photonics* 8.9 (2014), pp. 701–705.

[74] Nicholas A. Estep, Dimitrios L. Sounas, Jason Soric, and Andrea Alù. “Magnetic-free non-reciprocity and isolation based on parametrically modulated coupled-resonator loops”. In: *Nature Physics* 10.12 (2014), pp. 923–927.

[75] Tayfun Dinc, Mohamed S. Mohamed, Anantha P. Chandrakasan, and Dina El-Damak. “Synchronized conductivity modulation to realize magnetic-free on-chip circulators and nonreciprocal amplifiers”. In: *Nature Communications* 8.1 (2017), p. 15313.

[76] Amirhossein Zarif, Alessandro Marchetti, Matteo Cherchi, Daniele Melati, and Andrea Melloni. “Non-reciprocity in a silicon photonic ring resonator with time-modulated regions”. In: *Optics Express* 32.15 (2024), pp. 26938–26952.

[77] Ramy El-Ganainy, Konstantinos G. Makris, Demetrios N. Christodoulides, and Ziad H. Musslimani. “Theory of coupled optical $\mathcal{PT}$-symmetric structures”. In: *Optics Letters* 32.17 (2007), pp. 2632–2634.

[78] Yidong D. Chong, Li Ge, Hui Cao, and A. Douglas Stone. “Coherent perfect absorbers: time-reversed lasers”. In: *Physical Review Letters* 105.5 (2010), p. 053901.

[79] Emil J. Bergholtz, Jan Carl Budich, and Flore K. Kunst. “Exceptional topology of non-Hermitian systems”. In: *Reviews of Modern Physics* 93 (2021), p. 015005.

[80] Qiang Lin, Oskar Painter, and Govind P Agrawal. “Nonlinear optical phenomena in silicon waveguides: Modeling and applications”. In: *Optics Express* 15.25 (2007), pp. 16604–16644.

[81] Rune S. Jacobsen et al. “Strain-induced $\chi^{(2)}$ in silicon waveguides”. In: *Optics Express* 14.12 (2006), pp. 5872–5877.

[82] Erman Timurdogan, Christopher V. Poulton, Michael J. Byrd, and Michael R. Watts. “Electric field-induced second-order nonlinear optical effects in silicon waveguides”. In: *Nature Photonics* 11.3 (2017), pp. 200–206.

[83] Alan D Bristow, Nir Rotenberg, and Henry M van Driel. “Two-photon absorption and Kerr coefficients of silicon for 850–2200 nm”. In: *Applied Physics Letters* 90.19 (2007), p. 191104.

[84] R. A. Soref and B. R. Bennett. “Electrooptical effects in silicon”. In: *IEEE Journal of Quantum Electronics* 23.1 (1987), pp. 123–129.

[85] Christina Manolatou, M. J. Khan, Shanhui Fan, P. R. Villeneuve, H. A. Haus, and J. D. Joannopoulos. “Coupling of modes analysis of resonant channel add/drop filters”. In: *IEEE Journal of Quantum Electronics* 35.9 (1999), pp. 1322–1331.

[86] G. Griffel. “Vernier effect in asymmetrical ring resonator filters”. In: *IEEE Photonics Technology Letters* 12.12 (2000), pp. 1642–1644.

[87] Qianfan Xu, Bradley Schmidt, Sameer Pradhan, and Michal Lipson. “Micrometre-scale silicon electro-optic modulator”. In: *Nature* 435.7040 (2005), pp. 325–327.

[88] Y. Li, L. Zhang, M. Song, S. Chen, and L. Yang. “Coupled-ring-resonator-based silicon modulator for enhanced performance”. In: *Optics Express* 16.17 (2008), pp. 13342–13348.

[89] Jian Teng, Peng Yao, Dongning Zhu, Guiqiang Duan, Hanlin Hu, and Bai-Ou Guan. “Ultrahigh Q silicon microring resonator sensor with narrow linewidth”. In: *Optics Express* 22.25 (2014), pp. 30988–30998.

[90] Simone Azzini, Davide Grassani, Matteo Galli, Marc Sorel, Marco J. Strain, Lorenzo G. Helt, John E. Sipe, Marco Liscidini, and David Bajoni. “Ultra-low power generation of twin photons in a compact silicon ring resonator”. In: *Optics Express* 20.19 (2012), pp. 23100–23107.

[91] Pascal Del’Haye, Alfred Schliesser, Oskar Arcizet, Tobias Wilken, Richard Holzwarth, and Tobias J. Kippenberg. “Optical frequency comb generation from a monolithic microresonator”. In: *Nature* 450.7173 (2007), pp. 1214–1217.

[92] Qiang Li, Tao Wang, Yikai Su, Min Yan, and Min Qiu. “Coupled mode theory analysis of mode-splitting in coupled cavity system”. In: *Optics Express* 18.8 (Apr. 2010), pp. 8367–8382.

[93] Yisheng Fang and Zhichao Ruan. "Temporal Coupled-Mode Theory for Light Scattering and Absorption by Nanostructures". In: *Fano Resonances in Optics and Microwaves: Physics and Applications*. Ed. by Eugene Kamenetskii, Almas Sadreev, and Andrey Miroshnichenko. Springer Series in Optical Sciences. Cham: Springer International Publishing, 2018, pp. 157–183.

[94] M. L. Gorodetsky and V. S. Ilchenko. "Optical microsphere resonators: optimal coupling to high-Q whispering-gallery modes". In: *Journal of the Optical Society of America B* 16.1 (Jan. 1999), pp. 147–154.

[95] Tobias J. Kippenberg, Sean M. Spillane, and Kerry J. Vahala. "Modal coupling in traveling-wave resonators". In: *Optics Letters* 27.19 (2002), pp. 1669–1671.

[96] Brent E. Little, Su-Ping Chu, Hermann A. Haus, James Foresi, and Jean-Pierre Laine. "Microring resonator channel dropping filters". In: *Journal of Lightwave Technology* 15.6 (1997), pp. 998–1005.

[97] Matteo Borselli, Tracy J. Johnson, and Oskar Painter. "Rayleigh scattering, mode coupling, and optical loss in silicon microdisks". In: *Optics Express* 13.5 (2005), pp. 1515–1530.

[98] Andreas Ø. Svela, Jonathan M. Silver, Leonardo Del Bino, Shuangyou Zhang, Michael T. M. Woodley, Michael R. Vanner, and Pascal Del'Haye. "Coherent suppression of backscattering in optical microresonators". In: *Light: Science & Applications* 9.1 (2020), p. 204.

[99] Hwaseob Lee, Ali Kecebas, Feifan Wang, Lorry Chang, Şahin K. Özdemir, and Tingyi Gu. "Chiral exceptional point and coherent suppression of backscattering in silicon microring with low loss Mie scatterer". In: *eLight* 3.1 (2023), p. 20.

[100] Ang Li and Wim Bogaerts. "Fundamental suppression of backscattering in silicon microrings". In: *Optics Express* 25.3 (2017), pp. 2092–2099.

[101] J. Kim, J. Notaros, and et al. "Reducing backscattering in silicon microrings by intentionally broken symmetry". In: *Optics Letters* 41.15 (2016), pp. 3439–3442.

[102] Herbert Goldstein, Charles Poole, and John Safko. *Classical Mechanics*. 3rd. San Francisco: Addison-Wesley, 2002.

[103] J. J. Sakurai and Jim Napolitano. *Modern Quantum Mechanics*. 2nd. Reading, MA: Addison-Wesley, 1995.

[104] Kyoung Hwan Kim, Minsu Jin, Jing Zhang, et al. "Direct observation of exceptional points in coupled photonic-crystal nanolasers". In: *Nature Communications* 7 (2016), p. 13893.

[105] A. Calabrese, F. Ramiro-Manzano, H. M. Price, A. Pitanti, M. Bernard, L. Pavesi, I. Carusotto, and F. Riboli. "Unidirectional reflection from an integrated "taiji" microresonator". In: *Photonics Research* 8.8 (2020), pp. 1333–1341.

[106] Yuto Ashida, Zongping Gong, and Masahito Ueda. "Non-Hermitian physics". In: *Advances in Physics* 69.3 (2020), pp. 249–435.

[107] Dominique S. Weiss, Arno H. M. van der Veen, et al. "Splitting of high-Q modes in microcavities due to coupling". In: *Optics Letters* 20.18 (1995), pp. 1835–1837.

[108] Michael Borselli, Trevor J. Johnson, and Oskar Painter. "Beyond Rayleigh scattering: surface-roughness induced splitting in microdisk resonators". In: *Applied Physics Letters* 85.17 (2004), pp. 3693–3695.

[109] F. Morichetti, C. Ferrari, A. Canciamilla, and A. Melloni. "Roughness induced backscattering in optical silicon waveguides". In: *Physical Review Letters* 104.3 (2010), p. 033902.

[110] S. Biasi, F. Ramiro-Manzano, F. Turri, G. Pucker, and L. Pavesi. "Hermitian and non-Hermitian mode coupling in a microdisk resonator due to stochastic surface roughness scattering". In: *IEEE Photonics Journal* 11.2 (2019), pp. 1–14.

[111] S. Biasi, R. Franchi, F. Mione, et al. "Interferometric method to estimate the eigenvalues of a non-Hermitian two-level optical system". In: *Photonics Research* 10.4 (2022), pp. 1134–1145.

[112] Gal Harari, Miguel A Bandres, Yaakov Lumer, Mikael C Rechtsman, Yi Dong Chong, Mercedeh Khajavikhan, Demetrios N Christodoulides, and Mordechai Segev. "Topological insulator laser: Theory". In: *Science* 359.6381 (2018), eaar4003.

[113] Tomoki Ozawa et al. "Topological photonics". In: *Rev. Mod. Phys.* 91 (1 Mar. 2019), p. 015006. URL: `https://link.aps.org/doi/10.1103/RevModPhys.91.015006`.

[114] Alberto Muñoz de las Heras and Iacopo Carusotto. "Unidirectional lasing in nonlinear Taiji microring resonators". In: *Physical Review A* 104.4 (2021), p. 043501.

[115] Riccardo Franchi, Stefano Biasi, Alberto Muñoz de las Heras, Mher Ghulinyan, Iacopo Carusotto, and Lorenzo Pavesi. "Influence of the bus waveguide on the linear and nonlinear response of a Taiji microresonator". In: *Optics Express* 29.19 (2021), pp. 29615–29629.

[116] Stefano Biasi, Filippo Mione, Riccardo Franchi, and Lorenzo Pavesi. "Interferometric method to estimate the eigenvalues of a non-Hermitian two-level optical system". In: *Photonics Research* 10.4 (2022), pp. 1134–1145.

[117] H. M. Price, Y. D. Chong, A. B. Khanikaev, et al. “Roadmap on topological photonics”. In: *Journal of Physics: Photonics* 4.3 (2022), p. 032501.

[118] H. B. Perets, Y. Lahini, F. Pozzi, M. Sorel, R. Morandotti, and Y. Silberberg. “Realization of quantum walks with negligible decoherence in waveguide lattices”. In: *Physical Review Letters* 100.17 (2008), p. 170506.

[119] Alberto Peruzzo et al. “Quantum walks of correlated photons”. In: *Science* 329.5998 (2010), pp. 1500–1503.

[120] Stefano Biasi, Giacomo Donati, Andrea Lugnan, et al. “Photonic neural networks based on integrated silicon microresonators”. In: *Intelligent Computing* 3 (2024), p. 0067.

[121] Alberto Lugnan, Shubham Aggarwal, Felix Brückerhoff-Plückelmann, et al. “Emergent self-adaptation in an integrated photonic neural network for backpropagation-free learning”. In: *Advanced Science* 12.2 (2025), p. 2404920.

[122] R. Menchon-Enrich, A. Llobera, V. J. Cadarso, J. Mompart, and V. Ahufinger. “Adiabatic passage of light in CMOS-compatible silicon oxide integrated rib waveguides”. In: *IEEE Photonics Technology Letters* 24.7 (2012), pp. 536–538.

[123] R. Menchon-Enrich, A. Llobera, J. Vila-Planas, V. J. Cadarso, J. Mompart, and V. Ahufinger. “Light spectral filtering based on spatial adiabatic passage”. In: *Light: Science & Applications* 2 (2013), e90.

[124] Vasileios Evangelakos, Emmanouil Paspalakis, and Dionisis Stefanatos. “Efficient light transfer in coupled nonlinear triple waveguides using shortcuts to adiabaticity”. In: *Scientific Reports* 13.1 (2023), p. 1368.

[125] Chul-Min Kim and Yeong-Jin Im. “Switching operations of three-waveguide optical switches”. In: *IEEE Journal of Selected Topics in Quantum Electronics* 6.1 (2000), pp. 170–174.

[126] Matthias Stegmaier and Wolfram H. P. Pernice. “Broadband directional coupling in aluminum nitride nanophotonic circuits”. In: *Optics Express* 21.6 (2013), pp. 7304–7315.

[127] A. Syahriar, H. Adam, D. Astharini, et al. “Analysis of three parallel waveguides using coupled mode theory and the method of lines”. In: *International Seminar on Application for Technology of Information and Communication*. IEEE. 2016, pp. 174–178.

[128] Chang-Min Kim and Young-Joon Im. “Switching operations of three-waveguide optical switches”. In: *IEEE Journal of Selected Topics in Quantum Electronics* 6.1 (2000), pp. 170–174.

[129] Ramamurti Shankar. *Principles of quantum mechanics*. Springer Science & Business Media, 2012.

[130] Alan L Jones. “Coupling of optical fibers and scattering in fibers”. In: *JOSA* 55.3 (1965), pp. 261–271.

[131] D Marcuse. “Coupled mode theory of round optical fibers”. In: *Bell System Technical Journal* 52.6 (1973), pp. 817–842.

[132] Amnon Yariv. “Coupled-mode theory for guided-wave optics”. In: *IEEE journal of Quantum Electronics* 9.9 (2003), pp. 919–933.

[133] C Paiva-Sánchez, E Burgos-Inostroza, O Jiménez, and A Delgado. “Quantum tomography via equidistant states”. In: *Physical Review A: Atomic, Molecular, and Optical Physics* 82.3 (2010), p. 032115.

[134] Y. Liu, H.-C. Luan, L. C. Kimerling, and J. Michel. “High-quality-factor silicon-on-insulator microring resonators using deep-UV lithography”. In: *Optics Letters* 25.8 (2000), pp. 591–593.

[135] Y. Zhang, H. Wang, and Y. Chen. “Design space exploration of microring resonators in silicon photonics”. In: *Journal of Lightwave Technology* 36.12 (2018), pp. 2764–2772.

[136] Q. Xu, S. Manipatruni, B. Schmidt, and M. Lipson. “12.5 Gbit/s carrier-injection-based silicon microring silicon modulators”. In: *Optics Express* 15.2 (2007), pp. 430–436.

[137] K. Preston, S. Manipatruni, B. Schmidt, and M. Lipson. “Performance guidelines for WDM interconnects based on silicon microring resonators”. In: *CLEO: Science and Innovations*. 2011, CThP4.

[138] Vivien R. Almeida, Carolyn A. Barrios, Roberto R. Panepucci, and Michal Lipson. “All-optical control of light on a silicon chip”. In: *Nature* 431.7012 (2004), pp. 1081–1084.

[139] A. W. Poon, Q. Xu, and S. Yamashita. “Electrically reconfigurable silicon microring resonator-based filter with waveguide-coupled feedback”. In: *Optics Express* 27.5 (2019), pp. 6848–6858.

[140] C.-Y. Hsu, C. Lee, M. Tsai, and H. Chang. “Gate-tuning of silicon microring resonator for WDM applications”. In: *Scientific Reports* 13 (2023), p. 49015.

[141] M. Zhang, B. Buscaino, C. Wang, A. Shams-Ansari, C. Reimer, R. Zhu, J. M. Kahn, and M. Lončar. “Broadband electro-optic frequency comb generation in a lithium niobate microring resonator”. In: *Nature* 568 (2019), pp. 373–377.

[142] Abdou E. Shetewy et al. “Demonstration of high-frequency self-pulsing oscillations in an active silicon micro-ring cavity”. In: *Scientific Reports* 14 (2024), p. 23823.

[143] Abdou E. Shetewy et al. “Characterization of self-pulsing in active silicon ring resonators”. In: *Proceedings of SPIE*. Vol. 12569. SPIE. 2023, p. 1256907.

[144] Francesco Morichetti, Andrea Melloni, et al. “The first demonstration of thermo-optic relaxation oscillations in silicon microrings with lateral p-i-n structures”. In: *Optics Express* 19.21 (2011), pp. 20662–20675.

[145] Biswajeet Guha et al. “Thermal nonlinear dynamics in high-Q silicon microring resonators”. In: *Optica* 4.2 (2017), pp. 218–225.

[146] Ryan Hamerly et al. “Conditions for Parametric and Free-Carrier Oscillation in Silicon Ring Cavities”. In: *Journal of Lightwave Technology* (2018). Available as arXiv:1802.00071.

[147] Wolfram H. P. Pernice, Mo Li, and Hong X. Tang. “Time-domain measurement of optical transport in silicon micro-ring resonators”. In: *Optics Express* 18.17 (2010), pp. 18438–18452.

[148] P. E. Barclay, Kartik Srinivasan, and Oskar Painter. “Nonlinear response of silicon photonic crystal microresonators excited via an integrated waveguide and fiber taper”. In: *Optics Express* 13.3 (2005), pp. 801–820.

[149] A. C. Turner-Foster, M. A. Foster, J. S. Levy, M. Lipson, and A. L. Gaeta. “Frequency comb generation in silicon microresonators”. In: *Optics Express* 22.4 (2014), pp. 4492–4499.

[150] Van Vaerenbergh, Thomas. “All-optical spiking neurons integrated on a photonic chip”. eng. PhD thesis. Ghent University, 2014, XLIX, 206.

[151] Mohammad Reza Bonyadi and Zbigniew Michalewicz. “Particle Swarm Optimization for Single Objective Continuous Space Problems: A Review”. In: *Evolutionary Computation* 25.1 (Mar. 2017), pp. 1–54.

[152] Dodd Gray, Ryan Hamerly, Meysam Namdari, Mircea-Traian C ătuneanu, Kambiz Jamshidi, Nate Bogdanowicz, and Hideo Mabuchi. “Thermo-Optic Multistability and Relaxation in Silicon Microring Resonators with Lateral Diodes”. In: *Phys. Rev. Appl.* 14 (2 Aug. 2020), p. 024073. URL: `https://link.aps.org/doi/10.1103/PhysRevApplied.14.024073`.

[153] Massimo Borghi, Davide Bazzanella, Mattia Mancinelli, and Lorenzo Pavesi. “On the modeling of thermal and free carrier nonlinearities in silicon-on-insulator microring resonators”. In: *Optics Express* 29.3 (2021), pp. 4363–4377.

[154] K. v. Klitzing, G. Dorda, and M. Pepper. "New method for high-accuracy determination of the fine-structure constant based on quantized Hall resistance". In: *Physical Review Letters* 45.6 (1980), pp. 494–497.

[155] D. R. Hofstadter. "Energy levels and wave functions of Bloch electrons in rational and irrational magnetic fields". In: *Physical Review B* 14.6 (1976), pp. 2239–2249.

[156] M. Hafezi, E. A. Demler, M. D. Lukin, and J. M. Taylor. "Robust optical delay lines with topological protection". In: *Nature Physics* 7.11 (2011), pp. 907–912.

[157] M. Hafezi, S. Mittal, J. Fan, A. Migdall, and J. M. Taylor. "Imaging topological edge states in silicon photonics". In: *Nature Photonics* 7.12 (2013), pp. 1001–1005.

[158] T. Ozawa et al. "Topological photonics". In: *Reviews of Modern Physics* 91.1 (2019), p. 015006.

[159] M. Jalali Mehrabad, S. Mittal, and M. Hafezi. "Topological photonics: Fundamental concepts, recent developments, and future directions". In: *Physical Review A* 108.4 (2023), p. 040101.

[160] D. Leykam, S. Mittal, M. Hafezi, and Y. D. Chong. "Reconfigurable Topological Phases in Next-Nearest-Neighbor Coupled Resonator Lattices". In: *Physical Review Letters* 121.2 (2018), p. 023901.

[161] S. Mittal, V. V. Orre, D. Leykam, Y. Chong, and M. Hafezi. "Photonic Anomalous Quantum Hall Effect". In: *Physical Review Letters* 123.4 (2019), p. 043201.

[162] B. Bahari, A. Ndao, F. Vallini, A. E. Amili, Y. Fainman, and B. Kanté. "Nonreciprocal lasing in topological cavities of arbitrary geometries". In: *Science* 358.6363 (2017), pp. 636–640.

[163] M. A. Bandres, S. Wittek, G. Harari, M. Parto, J. Ren, M. Segev, D. N. Christodoulides, and M. Khajavikhan. "Topological insulator laser: Experiments". In: *Science* 359.6381 (2018), eaar4005.

[164] G. Harari, M. A. Bandres, Y. Lumer, M. C. Rechtsman, Y. D. Chong, M. Khajavikhan, D. N. Christodoulides, and M. Segev. "Topological insulator laser: Theory". In: *Science* 359.6381 (2018), eaar4003.

[165] Y. Zeng, U. Chattopadhyay, B. Zhu, Y. Liu, L. Wang, X. Li, J. Han, R. Agarwal, C. Zhang, and A. Alù. "Electrically pumped topological laser with valley edge modes". In: *Nature* 578.7794 (2020), pp. 246–250.

[166] Y. G. N. Liu, P. S. Jung, M. Parto, S. Wittek, J. Huang, J. W. Yoon, S. Kim, H. Cao, M. Khajavikhan, and D. N. Christodoulides. "Gain-induced topological response via tailored long-range interactions". In: *Nature Physics* 17.6 (2021), pp. 704–709.

[167] Y. Ota, K. Takata, T. Ozawa, A. Amo, Z. Jia, B. Kante, Y. Arakawa, and S. Iwamoto. "Active topological photonics". In: *Nanophotonics* 9.3 (2020), pp. 547–567.

[168] A. Calabrese, F. Ramiro-Manzano, and H. Price. "Unidirectional reflection from an integrated "Taiji" microresonator". In: *Photonics Research* 8.8 (2020), pp. 1333–1341.

[169] W. E. Hayenga, M. Parto, J. Ren, S. Yin, A. Mirzaei, D. N. Christodoulides, and M. Khajavikhan. "Direct Generation of Tunable Orbital Angular Momentum Beams in Microring Lasers with Broadband Exceptional Points". In: *ACS Photonics* 6.8 (2019), pp. 1895–1901.

[170] Alberto Muñoz de las Heras. "Non-Hermitian and Topological Features of Photonic Systems". PhD Thesis. PhD thesis. Trento, Italy: Università di Trento, 2023.

[171] Jan Wiersig. "Enhancing the Sensitivity of Frequency and Energy Splitting Detection by Using Exceptional Points: Application to Microcavity Sensors for Single-Particle Detection". In: *Physical Review Letters* 112 (2014), p. 203901.

[172] Wolfgang Langbein. "No exceptional precision of exceptional-point sensors". In: *Physical Review A* 98 (2018), p. 023805.

[173] Hoi-Kwan Lau and Aashish A. Clerk. "Fundamental limits and non-reciprocal approaches in non-Hermitian quantum sensing". In: *Nature Communications* 9 (2018), p. 4320.